

---

# Transverse Spin Asymmetries at the COMPASS Experiment

Anselm Vossen



---

Physikalisches Institut  
Albert-Ludwigs-Universität Freiburg

---



---

# Transverse Spin Asymmetries at the COMPASS Experiment

Dissertation

zur  
Erlangung des Doktorgrades  
der  
Fakultät für Mathematik und Physik  
der  
Albert-Ludwigs-Universität  
Freiburg im Breisgau

vorgelegt von  
**Anselm Vossen**  
aus  
Freiburg im Breisgau

Freiburg, April 2008

---

Ein Artikel mit Ergebnisse aus dieser Arbeit soll unter dem Titel “Collins and Sivers Transverse Spin Asymmetries for Pions and Kaons on Deuterons” in Physics Letters B veröffentlicht werden.

Ein Vorabdruck ist elektronisch unter CERN-PH-EP/2008-00 oder hep-ex/0802.2160 verfügbar.

Dekan:

Prof. Dr. Jörg Flum

Leiter der Arbeit:

Prof. Dr. Kay Königsmann

Referent:

Prof. Dr. Kay Königsmann

Korreferent:

Prof. Dr. Karl Jakobs

Tag der Verkündung des Prüfungsergebnisses: 29.5.2008

# Contents

<b>1</b>	<b>Introduction</b>	<b>1</b>
<b>2</b>	<b>Theory</b>	<b>3</b>
2.1	Deep Inelastic Scattering . . . . .	3
2.1.1	Kinematical Variables . . . . .	4
2.1.2	Deep Inelastic Scattering Cross Section . . . . .	5
2.1.3	Factorization . . . . .	6
2.1.4	Field Theoretical Description . . . . .	6
2.1.5	Optical Theorem and Chiral Odd Amplitudes . . . . .	9
2.1.6	Independent Contributions to the Forward Compton Scattering Amplitude . . . . .	9
2.2	The Quark-Quark Correlation Matrix . . . . .	10
2.2.1	Light Cone Formulation . . . . .	10
2.2.2	Parametrization of $\Phi$ . . . . .	11
2.2.3	Parton Model Interpretation . . . . .	13
2.3	Soffer Bound on Transversity . . . . .	14
2.4	Vector-, Axial- and Tensor Charges . . . . .	14
2.5	Quark Transverse Momenta . . . . .	15
2.6	Sivers effect in DIS and Drell-Yan . . . . .	17
2.7	Fragmentation in Semi Inclusive DIS . . . . .	17
2.7.1	Collins Effect . . . . .	21
2.7.2	Sivers Effect . . . . .	21
2.8	Fragmentation into two Hadrons . . . . .	24
2.8.1	Partial wave analysis of $H_1^{\triangleleft}$ . . . . .	25

---

2.8.2	Models for $H_1^{\triangleleft}$ . . . . .	26
2.9	Single Spin Asymmetries in SIDIS . . . . .	30
2.9.1	One Hadron SSAs . . . . .	30
2.9.2	Two Hadron SSAs . . . . .	31
2.10	Parton Model independent Cross Section in the Born Approximation . . . . .	32
<b>3</b>	<b>The COMPASS Experiment</b>	<b>35</b>
3.1	The Polarized Target and Beam . . . . .	35
3.2	Particle Identification . . . . .	36
3.2.1	Muon Filters . . . . .	36
3.2.2	Calorimetry . . . . .	36
3.2.3	The RICH detector . . . . .	36
<b>4</b>	<b>Data Analysis</b>	<b>39</b>
4.1	Data selection . . . . .	39
4.1.1	Event Selection . . . . .	39
4.1.2	Hadron Selection . . . . .	41
4.1.2.1	One Hadron Analysis . . . . .	42
4.1.2.2	Two Hadron Analysis . . . . .	43
4.2	Kinematic Distributions . . . . .	43
4.2.1	One Hadron Analysis . . . . .	43
4.2.2	Two Hadron Analysis . . . . .	44
4.2.3	Statistics of the One Hadron Analysis . . . . .	51
4.2.4	Statistics of the Two Hadron Analysis . . . . .	53
4.2.5	Statistics for the leading Two Hadron Analysis . . . . .	53
4.3	Monte Carlo Simulation . . . . .	53
4.3.1	Event Generation . . . . .	54
4.3.2	Detector Description and Particle Propagation . . . . .	57
4.3.3	Reconstruction . . . . .	57
4.4	PID with RICH-1 . . . . .	58
4.4.1	Introduction to the Search for Optimized Cuts for PID . . . . .	62

---

4.4.2	Data Sets . . . . .	62
4.4.3	Attribute Selection . . . . .	62
4.4.4	Optimal Cuts from Multivariate Analysis . . . . .	64
4.4.5	Optimal Cuts from Grid search on MC . . . . .	66
4.4.6	Optimal Cuts from Grid search on Data . . . . .	67
4.4.7	Results for Different Cuts for PID . . . . .	68
4.5	Single Spin Asymmetries . . . . .	72
4.6	Estimators for Single Spin Asymmetries . . . . .	72
4.6.1	General Framework . . . . .	73
4.6.1.1	Influence of Detector Acceptances on the Extraction of Physical Amplitudes . . . . .	75
4.6.1.2	Corrections due to Kinematics and Experimental Setup	75
4.6.1.3	Corrections due to Finite Bin Size . . . . .	76
4.6.2	Standard Method . . . . .	77
4.6.3	Double Ratio Method . . . . .	78
4.6.4	Weighted Double Ratio Method . . . . .	78
4.6.5	Two Dimensional Fit to Double Ratios . . . . .	81
4.6.6	Two Dimensional Fit to Counts . . . . .	82
4.6.7	Analytic Description of the Acceptance with the Fourier Series .	85
4.6.8	Unbinned Maximum Likelihood Estimator . . . . .	86
4.6.9	Performance on Monte Carlo Data . . . . .	88
<b>5</b>	<b>Results</b>	<b>95</b>
5.1	One Hadron Asymmetries . . . . .	96
5.2	Two Hadron asymmetries . . . . .	108
5.3	Systematic Studies . . . . .	117
5.4	Discussion and Comparison with other Experiments . . . . .	117
5.4.1	Collins and Sivers Asymmetries . . . . .	118
5.4.2	Two Hadron Asymmetries . . . . .	118
5.5	Interpretation and Conclusion . . . . .	125
<b>6</b>	<b>Summary</b>	<b>135</b>

---

<b>A Appendix</b>	<b>137</b>
A.1 One Hadron Asymmetries . . . . .	137
A.1.1 Binning . . . . .	137
A.1.2 Sivers Asymmetries . . . . .	138
A.1.2.1 Leading one Hadron . . . . .	138
A.1.2.2 All one Hadron . . . . .	143
A.1.3 Collins Asymmetries . . . . .	148
A.1.3.1 Leading Hadrons . . . . .	148
A.1.3.2 All Hadrons . . . . .	153
A.2 Two Hadron Asymmetries . . . . .	158
A.2.1 All Two Hadron pairs . . . . .	158
A.2.1.1 Binning . . . . .	158
A.2.1.2 Asymmetries . . . . .	160
A.2.2 Leading Two Hadron Asymmetries . . . . .	165
A.2.2.1 Binning . . . . .	165
A.2.2.2 Asymmetries . . . . .	166
<b>List of Figures</b>	<b>186</b>
<b>List of Tables</b>	<b>190</b>
<b>References</b>	<b>198</b>
<b>B Acknowledgements</b>	<b>199</b>

# 1. Introduction

The field theory of the strong force, quantum chromodynamics, is one of the great advances in physics. It has been tested successfully from the GeV to the TeV scale. However, due to its non-abelian structure, the low energy region provides for many challenges for theorists and experimentalists alike. Because perturbative calculations are no more possible predictions have to be made in effective models and experimental backgrounds are hard to predict.

However, it is the soft scale that dominates the matter around us. The properties of nucleons that make up the visible matter are determined by dynamics at the soft scale. For example, most of the mass is generated by the field dynamics. And the composition of the nucleon spin is still unaccounted for. With the advent of the parton model in the 1960s many properties of the nucleon could be understood in a quite simple picture. However, only the inclusion of QCD and the field theoretical treatment of quarks and gluons allow for a consistent and complete approach to the description of the structure of the nucleon.

One finding was, that the spin structure of the nucleon at leading order without considering quark transverse momenta is determined by three functions that have a probabilistic interpretation in the parton model. These are conventionally named  $f_1$ ,  $g_1$  and  $h_1$ . The first one describes the distribution of unpolarized quarks in an unpolarized nucleon, whereas the second one describes the distribution of helicity of a longitudinally polarized parent nucleon among the quarks.

The third one, the so called transversity distribution function  $h_1$  was thought to be negligible in the phenomenology of DIS, since the interpretation in the parton model is usually done in a frame, where the nucleon is boosted in the longitudinal direction. This suggest that effects connected to transverse spin and transverse quark momenta can be neglected. However, since boosts break rotational symmetry,  $h_1$  provides independent information about the spin structure of the nucleon.

If we leave the collinear picture and allow transverse momenta of the quarks, more distribution functions of quarks exist. One of these, the so called Sivers function  $f_{1T}^\perp$ , describes the distribution of unpolarized quarks in a transversely polarized nucleon. It is strongly connected to the orbital angular momenta of the quarks, which might be another contribution to the nucleon spin.

At COMPASS, a fixed target experiment at CERN, transverse spin effects were measured for the first time on a deuterium target. Due to the chiral structure of  $h_1$  and the naïve T-oddness of the Sivers effect, a measurement in inclusive deep inelastic scattering (DIS) is impossible, which is a reason for the scarce experimental data on these important functions. Instead, semi inclusive DIS (SIDIS) has to be used, where at least one hadron in the final state is detected.

Particle identification of these final state hadrons allows for flavor separation. In this

work Collins and Sivers effects are extracted from the COMPASS data taken in 2003 and 2004. Furthermore, the data is analyzed for a signal of transversity in two hadron correlations. Chapter 2 gives a theoretical introduction to transversal spin effects. Then the COMPASS experiment is introduced in chapter 3. For the extraction of the results novel approaches for asymmetry extraction and particle identification are developed in chapter 4. They are evaluated on simulated data produced for this thesis. The extracted results are presented in chapter 5 along with an interpretation and comparison with other experiments. The work is summarized in chapter 6.

## 2. Theory

In this chapter, the theory of transverse single spin asymmetries (SSAs) and what they reveal about quark dynamics will be introduced. There are several good overviews published and this introduction is guided by the reviews in [1][2][3][4]. After the introduction of the basic notation, the quark-quark correlation matrix will be introduced in section 2.2. It is a field theoretical description of the quark dynamics in the nucleon and contains all information about the nucleon structure, which cannot be calculated perturbatively. Therefore it has to be measured. An appropriate parametrization will be presented in 2.2.2. It will be based upon a decomposition over a Dirac base. This base has to be related to measurable quantities as the nucleon spin and hadron momenta. For the parameters a probabilistic interpretation as parton densities in the parton model can be found as shown in sec. 2.2.3. These findings will be generalized to the case where quark transverse momenta exist or hadrons are detected in the final state. The measurement of azimuthal asymmetries will prove to be a way of accessing the parton densities connected to tensorial structures. Collins and Sivers asymmetries will be treated in detail as will be azimuthal asymmetries in the fragmentation into two hadrons, which provide another way to access the transverse spin structure of the nucleon.

### 2.1 Deep Inelastic Scattering

The primary tool in the investigation of the structure of the nucleon is Deep Inelastic Scattering (DIS) where a high-energy pointlike particle, for all practical purposes a lepton  $l$ , scatters off a nucleon  $N$  with momentum as depicted in figure 2.1 in the process

$$l + N \rightarrow l' + \mathcal{X}. \quad (2.1)$$

After scattering the nucleon goes into the unknown hadronic state  $\mathcal{X}$ . Here it is assumed, that the scattering reaction takes place by one-photon exchange, the so-called Born approximation. This approximation can be safely used in the kinematic range covered by the COMPASS experiment. Due to the small wavelength of the photon, the result of the scattering reaction depends solely on the internal structure of the nucleon [5]. In this work, the emphasis is on the analysis of the transverse spin structure of the nucleon. To anticipate this, the momentum and spin vectors of the target nucleon  $P$  and  $S$  are introduced, as are the momentum  $P_{\mathcal{X}}$  of the state  $\mathcal{X}$ . The four-momenta of the incoming and outgoing lepton are conventionally called  $l$  and  $l'$ .

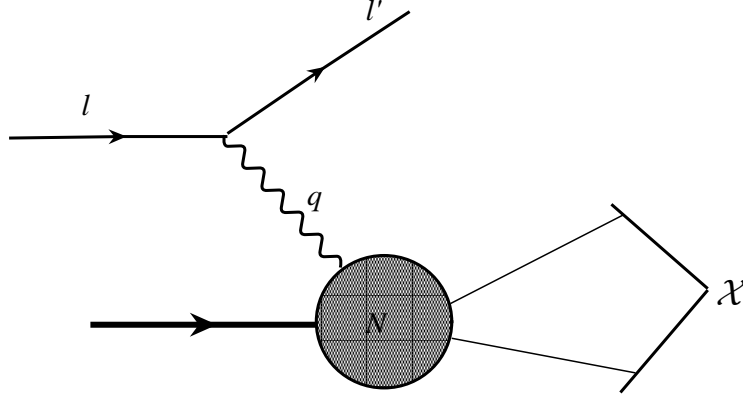


**Figure 2.1:** Deep Inelastic Scattering

### 2.1.1 Kinematical Variables

The kinematical degrees of freedom of the reaction are usually described by the set of lorentz invariant variables  $Q^2$ ,  $x_{Bj}$ ,  $\nu$  and  $y$  that are listed in table 2.1. If no confusion is possible, the subscript of  $x_{Bj}$  can be omitted.

**Table 2.1:** Definition of kinematic variables relevant for the DIS process

mass of the target nucleon	$M_N$
4-momentum of the incoming lepton $l$	$l^\mu = (E, \vec{l})$
4-momentum of the target nucleon $P$	$P^\mu = (E_N, \vec{P}_N)$
4-momentum of the outgoing lepton $l'$	$l'^\mu = (E', \vec{l}')$
4-momentum of the virtual photon $q$	$q = l - l'$
4-momentum of an outgoing hadron $P_h$	$P_h^\mu = (E_h, \vec{P}_h)$
neg. squared invariant mass of the virtual photon $Q^2$	$Q^2 = -q^\mu q_\mu$
energy transfer to the target $\nu$	$\nu = P^\mu q_\mu / M_N$
Bjorken scaling variable $x_{Bj}$	$x_{Bj} = \frac{Q^2}{2M_N \nu}$
fractional energy transfer of the virtual photon $y$	$y = \frac{P^\mu q_\mu}{P^\mu l'_\mu}$
fraction $z$ of the energy of the virtual photon carried by hadron $h$	$z = \frac{P_\mu P_h^\mu}{P^\mu q_\mu}$
transverse momentum of the hadron w.r.t. the virtual photon $P_\perp^h$	(not Lorentz-invariant)

Unless otherwise noted, from here on we take  $\hbar = c = 1$ . The coordinate system conventionally employed in DIS is a gamma-nucleon ( $\gamma^* N$ ) reference system, in which the z-axis coincides with the virtual photon direction and the x-z plane is the lepton scattering plane. The y-axis is orthogonal to it, so that a right-handed coordinate system is obtained (see fig. 2.2). To get a Cartesian coordinate system, there are two choices for the x-axis. Here it is chosen in such a way, that the direction of the scattered

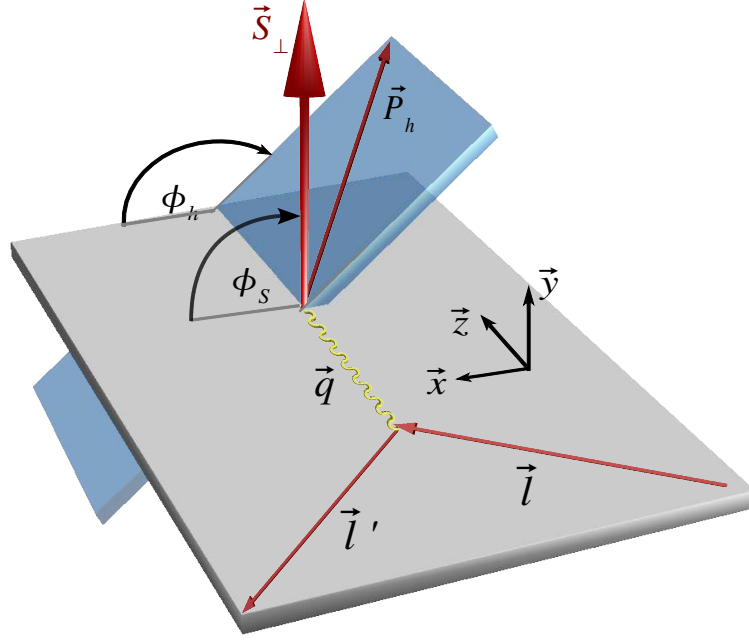


**Figure 2.2:** Coordinate System for the one hadron asymmetries. The hadron scattering plane is indicated in blue. For the computation of azimuthal asymmetries the projection of the nucleon spin transverse to the lepton scattering plane is used, which is called  $\vec{S}_\perp$ .

lepton is positive in  $x$ . Azimuthal angles are denominated  $\Phi$ , whereas polar angles are called  $\theta$ . For example, the azimuthal angle of an outgoing hadron  $h$  will be  $\Phi_h$ .

### 2.1.2 Deep Inelastic Scattering Cross Section

The Born approximation treats one-photon exchange in the scattering process between the lepton and the nucleon. The scattering of a lepton interacting with a photon can be computed at leading order in QED by either computing the Feynman tree level diagram or considering the electromagnetic current from the scattered lepton  $J^\mu(l-l') = \bar{u}(l')\gamma^\mu u(l)$ . Here the  $u$  denote the lepton spinors and  $\gamma^\mu$  Dirac gamma matrices. Without knowledge about the substructure of the nucleon, the scattering process can then be expressed as the interaction between the leptonic and the hadronic current. Following Fermi's golden rule, the cross-section can be expressed by the squared matrix element  $\mathcal{M}$  integrated over the phase space. Separating leptonic and hadronic current contributions in this expression leads to the description of the squared matrix element in DIS by the product of the leptonic tensor  $L^{\mu\nu}$  and the hadronic tensor  $W^{\mu\nu}$  [6]:

$$\overline{|\mathcal{M}|^2} = 4\pi M \frac{e^4}{q^4} L^{\mu\nu} W_{\mu\nu} \quad (2.2)$$

Since the leptonic tensor describes the purely electromagnetic transition of the lepton, which is a pointlike particle, it can be computed in QED and the coupling strength is

given by the elementary charge  $e$ . On the other hand the transition of the hadron to an unknown state, symbolically denoted by  $\mathcal{X}$  with total momentum  $P_{\mathcal{X}}$ , is dependent on soft QCD contributions. These are to be investigated. In terms of the unknown transition current  $J^\mu$  the hadronic tensor can be written as

$$2MW^{\mu\nu}(q, P, S) = \frac{1}{2\pi} \sum_{\mathcal{X}} \int \frac{d^3 P_{\mathcal{X}}}{(2\pi)^3 2P_{\mathcal{X}}^0} (2\pi)^4 \delta^{(4)}(q + P - P_{\mathcal{X}}) \langle P, S | J^\mu(0) | \mathcal{X} \rangle \langle \mathcal{X} | J^\nu(0) | P, S \rangle \quad (2.3)$$

with  $P, S$  momentum and spin of the nucleon. For the recasting of the integration measure see e.g. [7]. Here and in the following, a field theoretical approach is used, promoting the  $J^\mu$  to operators. The summation is carried out over all states  $\mathcal{X}$  and the four-momentum  $P_{\mathcal{X}}$  is integrated out. After using the translational invariance, the Fourier representation of the  $\delta$  function and completeness relations

$$2MW_{\mu\nu}(q, P, S) = \frac{1}{2\pi} \int d^4 \xi e^{iq\xi} \langle P, S | J^\mu(\xi) J^\nu(0) | P, S \rangle \quad (2.4)$$

is obtained [2]. Without an understanding of the internal dynamics of the nucleon it is impossible to further specify the hadronic tensor and it has to be parametrized by structure functions.

### 2.1.3 Factorization

As already realized by Bjorken, the phenomenology of DIS at sufficiently high  $Q^2$  can be explained by assuming that a photon scatters off a massless parton inside the nucleon. This kinematic regime is the so-called Bjorken limit which is defined by  $\nu, Q^2 \rightarrow \infty$ , with  $x_{Bj}$  fixed and is indicated in fig. 2.3. In this regime QCD becomes scale invariant up to logarithms of  $Q^2$  generated by radiative corrections [3]. Factorization theorems show that the measured soft matrix elements are process independent [8]. They have to be proven for each process. A consistent set of rules that describes the factorization is called a factorization scheme. The  $\overline{\text{MS}}$  scheme is such a set of rules, which has the advantage, that the parton distribution functions are defined directly in terms of hadronic matrix elements [8]. In DIS it is customary to set the factorization scale  $\mu^2$  at  $Q^2$ . Evolution of the quark distribution functions to different scales is done by the DGLAP<sup>1</sup> equations, if quark transverse momentum is neglected [9][10][11]. Otherwise the evolution equations have to be changed. At high  $Q^2$  the scale dependence becomes small and essentially logarithmic in  $Q^2$ , also with the inclusion of quark transverse momenta [3][12]. All quantities are in principles dependent on this scale. In contrast, at leading order in the Born approximation, the results are independent of the renormalization scheme.

### 2.1.4 Field Theoretical Description

The final state  $\mathcal{X}$  can be split into a quark plus a state  $X$  with momentum  $P_X$ . Using the  $\overline{\text{MS}}$  factorization scheme, the interacting hadronic current can be written in terms of the quark field<sup>2</sup>  $\Psi$  as  $J^\mu(\kappa - k) = \langle P, S | \bar{\Psi}(\kappa) \gamma^\mu \Psi(k) | X \rangle$ . The four-vectors  $k$  and

<sup>1</sup>Dokshitzer, Gribov, Lipatov, Altarelli, Parisi

<sup>2</sup>For both, the quark field and the corresponding operator the same variable  $\Psi$  will be used

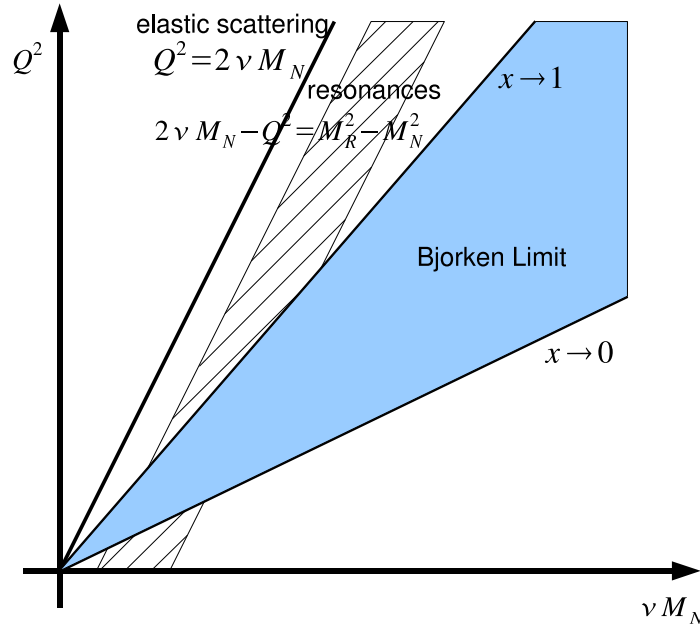


**Figure 2.3:** Kinematic regimes in lepton-nucleon scattering. The Bjorken variable  $x_{Bj}$  measures the inelasticity of a process. The energy transferred from the scattered lepton to the hadronic system can be computed as  $(P + q)^2 - M_N^2 = 2Pq(1 - x_{Bj})$ . For elastic processes  $x_{Bj}$  equals one. For smaller values of  $x_{Bj}$  resonances of the nucleon are formed. If even more energy is transferred, the Bjorken region is reached where in a first approximation deep inelastic scattering can be treated as the scattering of the virtual photon from quasi free quarks. In the figure the borders of this region for large  $x_{Bj}$  and small  $x_{Bj}$  are indicated. As  $x_{Bj} = 0$  is approached, photoproduction dominates and the so-called Regge regime is entered [3].

$\kappa$  designate the quark momenta before and after scattering, mirroring completely the description of the scattering beam particle. At tree level the hadronic tensor in equation 2.4 can then be expressed as

$$\begin{aligned}
2MW^{\mu\nu}(q, P, S) &= \frac{1}{2\pi} \sum_{q_f} e_{q_f}^2 \sum_X \int \frac{d^3\vec{P}_X}{(2\pi)^3 2P^0} \int \frac{d^3\kappa}{(2\pi)^3 \kappa^0} (2\pi)^4 \delta^{(4)}(P + q - \kappa - P_X) \\
&\quad \langle P, S | \bar{\Psi}(\kappa) \gamma^\mu \Psi(k) | X \rangle \langle X | \bar{\Psi}(k) \gamma^\nu \Psi(\kappa) | P, S \rangle \\
&= \frac{1}{2\pi} \sum_{q_f} e_{q_f}^2 \sum_X \int \frac{d^3\vec{P}_X}{(2\pi)^3 2P^0} \int \frac{d^3\kappa}{(2\pi)^3 k^0} (2\pi)^4 \delta^{(4)}(P + q - \kappa - P_X) \\
&\quad \langle P, S | \bar{\Psi}_i(0) | X \rangle \langle X | \Psi(0)_j | P, S \rangle (\gamma^\mu \not{k} \gamma^\nu)_{ij}.
\end{aligned} \tag{2.5}$$

Here and in the following the  $i, j$  are Dirac indices,  $\not{k} = \gamma^\mu \kappa_\mu$  is the Feynman slash and  $q_f$  is the quark flavor with charge  $e_{q_f}$ . The quark field  $\Psi$  contains the quark dynamics. One can choose to evaluate it at zero instead of  $k$ , as done in the last line, since the product of the unitary operators shifting the fields  $\Psi$  and  $\bar{\Psi}$  by  $-k$  is unity [5]. Rewriting equation 2.5 by using completeness relations of the states  $X$  and part of exponential representation of  $\delta^{(4)}$  to translate the field operator  $\Psi(0)$  one arrives at

$$\begin{aligned}
2MW^{\mu\nu}(q, P, S) &= \\
&\quad \sum_{q_f} e_{q_f}^2 \int d^4k \delta(k + q)^2 \Delta(k^0 + q^0) \cdot \\
&\quad \int \frac{d^4\xi}{(2\pi)^4} e^{i(P-k-P_X)\xi} \langle P, S | \bar{\Psi}(\xi)_i \Psi_j(0) | P, S \rangle \gamma_{ik}^\mu (\not{k} + \not{q})_{kl} \gamma_{lj}^\nu
\end{aligned} \tag{2.6}$$

where the relation  $k = \kappa - q$  for the outgoing quark is used and causality is observed due to the step function  $\Delta$ . The matrix element  $\langle P, S | \bar{\Psi}(\xi)_i \Psi_j(0) | P, S \rangle$  is now independent of the unobserved state  $X$ . It can be regarded as the unnormalized distribution of quarks within the nucleon in the state  $P, S$  and contains all the information about the soft part of the inclusive scattering reaction [13].

In addition one has to consider that the quark is propagating in the QCD background field  $A_\mu$  of the nucleon. Matrix elements of the form  $\langle P, S | \bar{\Psi}(\xi)_i \Psi_j(0) | P, S \rangle$  are connected to quark propagation from point 0 to point  $\xi$  in four-momentum space. In the case of inclusive DIS, the optical theorem introduced in the next chapter provides an intuitive explanation for this. The interaction is thus taking place on a path from 0 to  $\xi$ , This can be incorporated by inserting a so-called Wilson link [3]

$$\mathcal{L}(\xi) = \mathcal{P} \left( \exp i \int_0^\xi d\zeta^\mu A_\mu(\zeta) \right), \tag{2.7}$$

where  $\mathcal{P}$  means path ordering. It can be shown that the insertion of the Wilson link leads also to a gauge invariant expression [4]. However, in a collinear picture, where quark intrinsic transverse momentum  $k_\perp$  is neglected, it is possible to choose a gauge such that  $\mathcal{L}$  evaluates to unity; the light cone (LC) gauge. Therefore the link will be omitted in the following, until effects depending on  $k_\perp$  are treated. Then it becomes important when comparing measurements in the Drell-Yan and DIS processes.

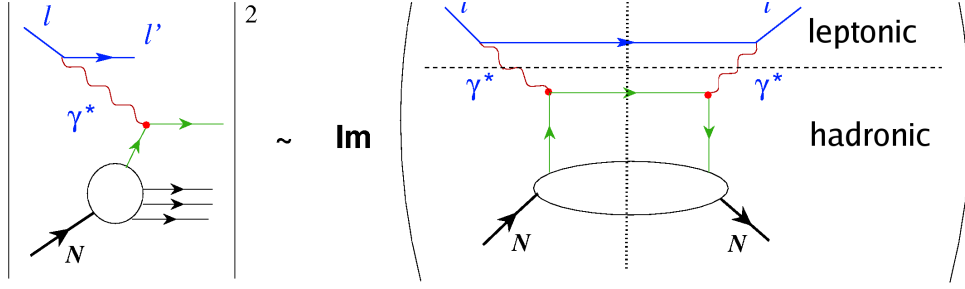


**Figure 2.4:** Illustration of the Optical Theorem. Squaring an amplitude is accomplished by multiplying with the complex conjugate which leads to a mirrored process. The on-shell and causality conditions for the outgoing particles allow the connection of the amplitude with the mirrored amplitude.

### 2.1.5 Optical Theorem and Chiral Odd Amplitudes

Via the optical theorem the hadronic tensor in equation 2.4 is related to the forward Compton scattering amplitude  $T_{\mu\nu}$  by [5]

$$W_{\mu\nu} \propto \frac{1}{\pi} \text{Im}(T_{\mu\nu}). \quad (2.8)$$

See figure 2.4 for a visualization.

This relationship can also be read from the equation 2.5 by identifying  $\Phi$  ( $\bar{\Phi}$ ) with incoming (outgoing) quark lines,  $\gamma^\mu$ ,  $\gamma^\nu$  with the quark-photon vertices and  $\not{k}$  with the propagation of a quark on the mass shell.

### 2.1.6 Independent Contributions to the Forward Compton Scattering Amplitude

In the helicity basis there are naïvely 16 independent amplitudes contributing to the forward Compton scattering amplitude. They are written in the following as  $\mathcal{A}_{\lambda_N \lambda, \lambda'_N \lambda'}$  and  $\lambda$ ,  $\lambda'$  ( $\lambda_N$ ,  $\lambda'_N$ ) are quark (nucleon) helicities. From helicity conservation the condition  $\lambda_N + \lambda = \lambda'_N + \lambda'$  follows. Parity invariance demands  $\mathcal{A}_{\lambda_N \lambda, \lambda'_N \lambda'} = \mathcal{A}_{-\lambda_N - \lambda, -\lambda'_N - \lambda'}$ . After applying these conditions three independent amplitudes survive.

$$\mathcal{A}_{++,++}, \quad \mathcal{A}_{+,-,+}, \quad \mathcal{A}_{+,-,-} \quad (2.9)$$

They are customary represented by the so-called handbag diagrams shown in fig. 2.5. Two amplitudes conserve the helicity of the quark line ( $\lambda = \lambda'$ ) but the third involves a flip of the quark helicity. This is forbidden in leading order inclusive DIS, because at the given energy scale quark masses can be neglected and then standard model processes apart from the weak force are chirality conserving. Chirality coincides for massless quarks with helicity. Therefore  $\mathcal{A}_{+,-,-}$  is a chiral odd quantity which can only be measured in a combination with another chiral odd quantity. The transversity distribution function to be defined in the following is proportional to the imaginary part of this amplitude. Already at this point it is clear that it cannot be measured in inclusive DIS unlike the unpolarized and helicity quark distribution function which are proportional to  $\text{Im}(\mathcal{A}_{++,++} + \mathcal{A}_{+,-,+})$  and  $\text{Im}(\mathcal{A}_{++,++} - \mathcal{A}_{+,-,+})$ , respectively.

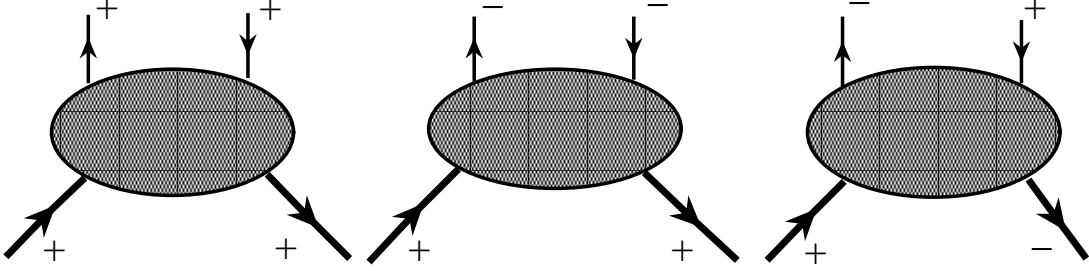


Figure 2.5: Handbag diagrams

## 2.2 The Quark-Quark Correlation Matrix

The hadronic tensor in equation 2.6 contains hard parts that can be calculated perturbatively and soft parts that have to be parameterized. If factorization is proven for the given process, the soft and hard parts can be separated, allowing the measurement of the soft parts. Putting the soft matrix elements together leads to the definition of the **Quark-Quark Correlation Matrix**[1]<sup>3</sup>.

$$\Phi_{ij}(k, P, S) = \int d^4\xi e^{ik\xi} \langle P, S | \bar{\Psi}(0)_j \Psi_i(\xi) | P, S \rangle. \quad (2.10)$$

This allows to write the hadronic tensor in a more compact way, clearly separating the soft parts contained in  $\Phi$  and the hard parts [1][2]:

$$2MW^{\mu\nu} = \sum_{q_f} e_{q_f}^2 \int \frac{d^4k}{(2\pi)^4} \delta((k+q)^2) \text{Tr} [\Phi \gamma^\mu (\not{k} + \not{q}) \gamma^\nu]. \quad (2.11)$$

The trace over the correlation matrix  $\Phi$  is

$$\text{Tr}(\Gamma\Phi) = \int d^4\xi e^{ik\cdot\xi} \langle PS | \bar{\Psi}(0) \Gamma \Psi(\xi) | PS \rangle \quad (2.12)$$

and its cyclicity can be used to rearrange arguments.

### 2.2.1 Light Cone Formulation

Deep inelastic scattering is dominated by contributions on the light cone (LC), while space like distances are excluded due to causality. That is, the hadronic tensor in equation 2.6 receives only significant contributions for  $\xi^2 \approx 0$ . This can be demonstrated in a simple picture. At high energies the quark mass can be neglected which means, that the quark moves along the 'handle' of the handbag diagram with the speed of light. The separation  $\xi$  between the outgoing and incoming quark is thus light like. The quark

<sup>3</sup>Following the notation in [1] the arguments 0 and  $\xi$  have been exchanged together with the sign of  $\xi$  with respect to eq. 2.6. Because of translational invariance this leads to the same result.

only leaves the light cone if a gluon is emitted along the way. But gluon radiation and gluon exchange with the target remnant is suppressed. The latter is known as higher twist contributions. They contain interdependent quark-gluon dynamics. Therefore it is instructive to look at the leading light cone projections of the quark fields. For this reason light cone coordinates are defined.

Taking an ordinary 4-vector  $a^\mu = (a_0, a_1, a_2, a_3)$ , the light cone representation is  $a = (a_+, a_-, a_\perp)$  with  $a_\pm = \frac{1}{\sqrt{2}}(a_0 \pm a_3)$  and  $a_\perp = (a_1, a_2)$ . The corresponding metric  $g_{\mu\nu}$  is given by  $g_{+-} = g_{-+} = 1$  and  $g_{ij} = -\delta_{ij}$ <sup>4</sup> [3]. Vectors on the light cone are orthogonal to themselves ( $a^\mu a_\mu = 0$  if  $a$  is on the light cone). The Sudakov-decomposition of  $a$  can be constructed [1] with the two light like vectors  $p^\mu$  and  $n^\mu$ , which contain only components in the '+' and '-' direction, respectively:

$$p^\mu = \frac{p}{\sqrt{2}}(1, 0, 0, 1) \quad (2.13)$$

$$n^\mu = \frac{1}{\sqrt{2}p}(1, 0, 0, -1). \quad (2.14)$$

The factor  $p$  selects a specific frame. Examples are  $p = M\sqrt{2}$ , the target rest frame and  $p \rightarrow \infty$ , which selects the infinite momentum frame [3][4]. By using the decomposition in terms of  $p^\mu$  and  $n^\mu$  it is not necessary to use a boost to a specific frame. In the Bjorken limit the momentum of the parent nucleon  $P^\mu$  and the virtual photon  $q^\mu$  can be expressed as

$$P^\mu = p^\mu + \frac{M^2}{2}n^\mu \approx p^\mu \quad (2.15)$$

and

$$\lim_{Bj} q^\mu = \left( \nu + \frac{1}{2}M^2 x_{Bj} \right) n^\mu - x_{Bj} p^\mu + \mathcal{O}\left(\frac{1}{Q^2}\right) \approx -x_{Bj} p^\mu. \quad (2.16)$$

The approximate relations are valid in the infinite momentum frame, where they become scale invariant.

Analogously the Dirac matrices  $\gamma^\pm = \frac{1}{2}(\gamma^0 \pm \gamma^3)$  are defined. They can be used to construct projectors on the light cone  $\mathcal{P}_\pm = \frac{1}{2}\gamma^\mp \gamma^\pm$ . Due to the choice of the coordinate system, the sign of the z-component of the outgoing quark momentum changes after the scattering of the virtual photon. This means that the leading light cone projection changes from the + to the - direction. Therefore the dominating part of the fragmentation function is determined by the - direction. With the parton model assumption of small  $k_\perp$  and  $k^2$  the Bjorken variable  $x = Q^2/(2Pq)$  can be interpreted as the light cone momentum fraction of the quark  $k^+/P^+$  [1] because in this case the on shell condition  $\delta((k+q)^2)$  becomes  $\frac{1}{Pq}\delta(k^+ - x)$ . Later also quark transverse momentum  $k_\perp$  will be considered.

### 2.2.2 Parametrization of $\Phi$

After this introduction the goal is to find a representation of the quark-quark correlation matrix in terms of measurable quantities. The most general decomposition of  $\Phi$  is in

---

<sup>4</sup><sub>i=1,2</sub>

terms of the Dirac matrices  $\Gamma = \{\mathbb{1}, \gamma^\mu, \gamma^\mu \gamma^5, i\gamma^5, i\sigma^{\mu\nu} \gamma^5\}$  into a scalar, vector, axial-vector, pseudo-vector and tensorial part. For instance, the vectorial part  $\mathcal{V}^\mu$  is given by tracing with  $\gamma^\mu$ :

$$\mathcal{V}^\mu = \frac{1}{2} \int d\xi e^{ik\xi} \langle P, S | \bar{\Psi}(0) \gamma^\mu \Psi(\xi) | P, S \rangle \equiv \text{Tr}(\gamma^\mu \Phi) \quad (2.17)$$

Under hermiticity, parity and time reversal invariance, the pseudo-vector part has to be zero and the kinematical quantities that can be used to build the vector, axial-vector and tensor part are  $P^\mu$ ,  $\lambda_N P^\mu$  and  $P^{[\mu} S_\perp^{\nu]5}$ , respectively, where  $\lambda_N$  is the helicity of the nucleon and  $S_\perp^\nu$  the transverse part of the nucleon spin vector. Here, only quantities that are of leading order in  $P^+$  in the infinite momentum frame are of interest. They can be identified with the leading twist contributions that can be interpreted in the parton model. Therefore the expansion is contracted with  $n^\mu$ , leading to traces of the light cone gamma matrices, e.g.  $\not{n} = \gamma^+$ . The leading twist contributions to the quark-quark correlation matrix are thus expansions in the light cone Dirac matrices  $\gamma^+$ ,  $\gamma^+ \gamma^5$  and  $i\sigma^{i+} \gamma_5$ . Taken together with the parton model assumption  $x = k^+/P^+$  and  $\delta(x - \frac{k^+}{P^+}) = P^+ \delta(k^+ - xP^+)$  the leading twist distribution functions corresponding to the unsuppressed parts of the quark-quark correlation matrices are<sup>6</sup>[1]

$$\begin{aligned} f_1(x) &= \frac{1}{2} \int \frac{d^4 k}{(2\pi)^4} \text{Tr}(\gamma^+ \Phi) \delta(k^+ - xP^+) \equiv \Phi^{[\gamma^+]} \\ &= \frac{1}{2} \int \frac{d^4 k}{(2\pi)^4} \int d\xi e^{ik\xi} \langle P, S | \bar{\Psi}(0) \gamma^+ \Psi(\xi) | P, S \rangle \delta(k^+ - xP^+) \\ g_1(x) &= \frac{1}{2} \int \frac{d^4 k}{(2\pi)^4} \int d\xi e^{ik\xi} \langle P, S | \bar{\Psi}(0) \gamma^+ \gamma^5 \Psi(\xi) | P, S \rangle \delta(k^+ - xP^+) \\ &\equiv \Phi^{[\gamma^+ \gamma^5]} \\ h_1(x) &= \frac{1}{2} \int \frac{d^4 k}{(2\pi)^4} \int d\xi e^{ik\xi} \langle P, S | \bar{\Psi}(0) \gamma^+ \gamma^1 \gamma^5 \Psi(\xi) | P, S \rangle \delta(k^+ - xP^+) \\ &\equiv \Phi^{[\gamma^+ \gamma^1 \gamma^5]} \end{aligned} \quad (2.18)$$

Note the definition of the integrated traces  $\Phi^{[\Gamma]}$ , where  $\Gamma$  is an arbitrary Dirac matrix [14][15]. These projections depending on the fractional momentum  $x = k^+/P^+$  can be expressed by densities of partons having the chiral quark field projections defined by  $\Gamma$  [14]. The next section will show how the specific operator combinations can be interpreted as parton densities. The projection with the condition  $k^+ = xP^+$  basically amounts to integrating out the small components of the quark field, which becomes apparent when using the Fourier representation of the  $\delta$ -function together with the LC-metric  $k \cdot \xi = k^+ \xi^- + k_\perp \xi_\perp + k^- \xi^+$ :

$$\Phi^{[\Gamma]}(x) = \int \frac{d\xi^-}{2\pi} e^{ixP^+ \xi^-} \langle P, S | \bar{\Psi}(0) \Gamma \Psi(0, \xi^-, \vec{0}_\perp) | P, S \rangle \quad (2.19)$$

<sup>5</sup>  $P^{[\mu} S_\perp^{\nu]} := P^\mu S_\perp^\nu - S_\perp^\mu P^\nu$

<sup>6</sup> setting  $\lambda_N = 1$  and  $S_\perp = (1, 0)$ , thus using only the trace over  $\gamma^+ \gamma^1 \gamma^5$  for  $h_1$ , where the trace over  $\gamma^+ \gamma^i \gamma^5$  would allow for two equations ( $i = 1, 2$ ). But only one of those is independent. Note that  $i\sigma^{i+} \gamma^5 = \gamma^+ \gamma^i \gamma^5$ .

In terms of the available kinematical variables the quark-quark-correlation matrix in leading order can now be written as

$$\Phi(x) = \frac{1}{2} (f_1(x)\not{P} + \lambda_N g_1(x)\gamma_5\not{P} + h_1(x)\not{P}\gamma_5\not{S}_\perp) \quad (2.20)$$

Here it becomes obvious that the parent nucleon polarization determines the measurability of a specific quark distribution function. Since the definition of  $p^\mu$  and  $n^\mu$  is only up to a factor  $p$  which depends on the frame of reference (eq. 2.15), the same is also true for  $\Phi$ .

### 2.2.3 Parton Model Interpretation

In the parton model interpretation of DIS quasi free quarks on the light cone are interacting with the virtual photon. These independent degrees of freedom of the quark field  $\Psi$  are the so-called “good” components  $\Psi_+$ . They can be projected out by the operator  $\mathcal{P}_+ = \frac{1}{2}\gamma^-\gamma^+$  [3]. The dependent degrees of freedom are the “bad” components  $\Psi_- = \mathcal{P}_-\Psi$ ,  $\mathcal{P}_- = \frac{1}{2}\gamma^+\gamma^-$ . Since the bad components are connected to more complicated quark-gluon correlations, they are generally associated with higher twist, which leads to the dominance of the good components over the bad components as  $P^+ \rightarrow \infty$ . In order to interpret the functions  $f_1(x)$ ,  $g_1(x)$  and  $h_1(x)$  in the parton model, they have to be described in terms of good quark fields. Using the identity  $\gamma^0\gamma^+ = \sqrt{2}\mathcal{P}_+ = \sqrt{2}\mathcal{P}_+\mathcal{P}_+$  the relevant operator combinations in 2.18 can be rewritten as

$$\bar{\Psi}\gamma^+\Psi = \sqrt{2}\Psi_+^\dagger\Psi_+ \quad (2.21)$$

$$\bar{\Psi}\gamma^+\gamma_5\Psi = \sqrt{2}\Psi_+^\dagger\gamma_5\Psi_+ \quad (2.22)$$

$$\bar{\Psi}\gamma^+\gamma^1\gamma_5\Psi = \sqrt{2}\Psi_+^\dagger\gamma^1\gamma_5\Psi_+ \quad (2.23)$$

Lastly, the projectors  $\mathcal{P}_{R,L} = \frac{1}{2}(1 \pm \gamma^5)$  and  $\mathcal{P}_{\uparrow,\downarrow} = \frac{1}{2}(1 \pm \gamma^1\gamma^5)$  are used which project out the helicity and transverse spin state. Now the operators appearing in the definition of  $g_1(x)$  and  $h_1(x)$  can be written as  $\gamma_5 = \mathcal{P}_R - \mathcal{P}_L$  and  $\gamma^1\gamma^5 = \mathcal{P}_\uparrow - \mathcal{P}_\downarrow$ . Inserting again a complete set of states  $\{|n\rangle\}$  the formulation of 2.18 that can be interpreted as parton density functions is

$$\begin{aligned} f_1(x) &= \frac{1}{\sqrt{2}} \sum_n \delta((1-x)P^+ - P_n^+) |\langle P, S | \Psi_+(0) | n \rangle|^2 \\ g_1(x) &= \frac{1}{\sqrt{2}} \sum_n \delta((1-x)P^+ - P_n^+) \cdot \\ &\quad \cdot \left( |\langle P, S | \mathcal{P}_R \Psi_+(0) | n \rangle|^2 - |\langle P, S | \mathcal{P}_L \Psi_+(0) | n \rangle|^2 \right) \\ h_1(x) &= \frac{1}{\sqrt{2}} \sum_n \delta((1-x)P^+ - P_n^+) \cdot \\ &\quad \cdot \left( |\langle P, S | \mathcal{P}_\uparrow \Psi_+(0) | n \rangle|^2 - |\langle P, S | \mathcal{P}_\downarrow \Psi_+(0) | n \rangle|^2 \right) \end{aligned} \quad (2.24)$$

From this formulation it can be seen, that  $f_1(x)$  is the probability to scatter off a quark with momentum fraction  $x$  and  $g_1(x)$  the probability difference to find a quark with helicity parallel and anti-parallel to the nucleon helicity.

The third one,  $h_1(x)$  is the probability difference to scatter off a quark with a transverse polarization parallel and anti-parallel to the nucleon transverse polarization. It has to be kept in mind that the assumption is  $\lambda_N = 1$  and  $S_\perp = (1, 0)$ . It contains  $i\sigma^{1+}\gamma_5$ , which makes it a chiral odd quantity.

Chiral oddness can be seen quite literally, since  $h_1(x)$  is connected to the third handbag diagram in fig. 2.5 where the quark flips its chirality between the left and the right handle. Since the hard part is conserving chirality up to negligible quark mass terms,  $h_1$  cannot be measured in inclusive DIS. Another chiral odd soft partner is needed to construct a process that is observable in hard scattering. This can be a chiral odd fragmentation function. Chiral odd parton distribution functions in spin  $\frac{1}{2}$  hadrons have also a different evolution behavior than chiral even ones. Because the handbag diagram corresponding to  $h_1(x)$  does not exist for gluons, there exists no transversity distribution for gluons with which  $h_1(x)$  could mix during evolution. The reason for the nonexistence of a gluon transversity is, that instead of a quark, a gluon has to go along the handle of the handbag diagram and flip its helicity. This, however, means a total spin flip of two units of the parent hadron, which is not possible for spin one half particles.

### 2.3 Soffer Bound on Transversity

From the definitions of the parton distribution functions in terms of the forward Compton scattering amplitudes in eq. 2.9 Soffer derived an inequality relation [16]:

$$f_1(x) + g_1(x) \geq 2|h_1(x)| \quad (2.25)$$

This is an important bound which must be respected by all models describing the leading twist functions.

### 2.4 Vector-, Axial- and Tensor Charges

The integration of  $\Phi(x)$  over  $x$  leads to a local matrix element

$$\int dx \Phi_{ij}(x) = \langle PS | \bar{\Psi}_j(0) \Psi_i(0) | PS \rangle \quad (2.26)$$

which can be parametrized like 2.20:

$$\Phi = \frac{1}{2} [g_V \not{P} + g_A \lambda_N \gamma^5 \not{P} + g_T \not{P} \gamma_5 \not{S}_\perp] \quad (2.27)$$

Here  $g_V$  is the vector charge,  $g_A$  the axial charge and  $g_T$  the tensor charge, which gives the deformation of the quark distribution in a polarized nucleon. Using the definition of the parton distribution function one gets for the different charges:

$$\int_{-1}^{+1} dx f_1(x) = g_V \quad (2.28)$$

$$\int_{-1}^{+1} dx g_1(x) = g_A \quad (2.29)$$

$$\int_{-1}^{+1} dx h_1(x) = g_T \quad (2.30)$$

This means that for example  $g_V$  is simply the valence quark number. Due to the evolution of  $h_1$ , which is different from the other parton distribution functions, the tensor charge evolution is also different to the one of  $g_V$  and  $g_A$  and it is expected, that this will lead to a vanishing charge at sufficiently high  $Q^2$  [17]. Measured values of the tensor charge can be compared with model calculations, for example from the lattice [18][19][20][21][22].

## 2.5 Quark Transverse Momenta

If one takes into account transverse motion of quarks, i.e. does not integrate over the quark dynamics inside the nucleon, one obtains extra degrees of freedom. With the formalism of the previous sections the inclusion of quark transverse momenta  $k_\perp$  is quite straightforward. The quark momentum is now given by

$$k^\mu \simeq xP^\mu + k_\perp^\mu \quad (2.31)$$

where the part  $k_\perp^\mu$  is zeroth order in  $P^+$  and thus suppressed by one power of  $P^+$  with respect to the longitudinal momentum. The quark-quark correlation matrix  $\Phi(x, \vec{k}_\perp)$  is then also dependent on the transverse momentum. Consequently the projection onto  $\gamma^+$  has a richer structure and reads

$$\Phi^{[\gamma^+]} = f_1(x, \vec{k}_\perp^2) - \frac{\epsilon_\perp^{ij} k_{\perp i} S_{\perp j}}{M} f_{1T}^\perp(x, \vec{k}_\perp^2). \quad (2.32)$$

The other projections also contain more parton distribution functions than in the collinear case. They are interesting in themselves, but will not be covered in detail in this thesis. It shall suffice to mention the additional distribution functions as they appear in the quark-quark correlation matrix. The leading twist expression for the correlation matrix expressed in available kinematical variables and parton distribution functions (PDF) becomes

$$\begin{aligned} \Phi(x, \vec{k}_\perp) = & \\ & \frac{1}{2} \left\{ f_1(x, \vec{k}_\perp^2) \not{P} + \left( \lambda_N g_{1L}(x, \vec{k}_\perp^2) - \frac{\vec{k}_\perp \cdot \vec{S}_\perp}{M} g_{1T}(x, \vec{k}_\perp^2) \right) \gamma^5 \not{P} \right. \\ & \left. \left( h_{1T}(x, \vec{k}_\perp^2) \gamma_5 \not{S}_\perp \not{P} + \left( \lambda_N h_{1L}^\perp(x, \vec{k}_\perp^2) - \frac{k_\perp \cdot S_\perp}{M} h_{1T}^\perp(x, \vec{k}_\perp^2) \right) \frac{\gamma_5 k_\perp \not{P}}{M} \right) \right\} \\ & + \frac{1}{2} \left( f_{1T}^\perp(x, \vec{k}_\perp^2) \frac{\epsilon_T^{ij} S_{\perp j} \vec{k}_\perp^i \not{P}}{M} + h_1^\perp(x, \vec{k}_\perp^2) \frac{i k_\perp \not{P}}{M} \right) \quad (2.33) \end{aligned}$$

where the last line contains the naïvely T-odd contributions and the notation for the distribution functions follows [14]. From 2.33 the three distribution functions  $f_1$ ,  $g_1$  and  $h_1$  can be recovered by integration over  $k_\perp$ . Generalizing from the definition of the integrated trace of the correlation matrix  $\Phi$  over Dirac structures  $\Gamma$ ,  $\Phi^{[\Gamma]}$  defined in 2.19, these traces now also contain the integral over transverse momenta:

$$\Phi^{[\Gamma]} = \int \frac{d\xi^- d^2\vec{\xi}_\perp}{2(2\pi)^3} e^{i(xP^+\xi^- - \vec{k}_\perp \cdot \vec{\xi}_\perp)} \langle P, S | \bar{\Psi}(0) \Gamma \Psi(0, \xi^-, \vec{\xi}_\perp) | P, S \rangle \quad (2.34)$$

It can be seen, that, as before, the different projections define probability distributions of partons with a specific chiral projection. The projection  $\Phi^{[\gamma^+]}$  is the probability to find an unpolarized quark, which can be symbolized by  $\mathcal{P}_{q/N}$  to use the notation of [1]. Thus  $f_1(x, \vec{k}_\perp^2)$  is the probability of finding an unpolarized parton in an unpolarized nucleon. Since the occurrence of  $f_{1T}^\perp(x, \vec{k}_\perp^2)$  is connected to transverse polarization of the parent nucleon,  $S_\perp$ , this PDF can be interpreted as the probability to find an unpolarized parton in a transversely polarized nucleon. More precisely [23]

$$\begin{aligned} \mathcal{P}_{q/N^\uparrow}(x, \vec{k}_\perp) - \mathcal{P}_{q/N^\downarrow}(x, \vec{k}_\perp) &= \mathcal{P}_{q/N^\uparrow}(x, \vec{k}_\perp) - \mathcal{P}_{q/N^\uparrow}(x, -\vec{k}_\perp) \\ &= -2 \frac{|\vec{k}_\perp|}{M_N} \sin(\Phi_k - \Phi_S) f_{1T}^\perp(x, \vec{k}_\perp^2). \end{aligned} \quad (2.35)$$

This is the so-called Sivers function, which can be measured in the Sivers effect [24][25]. After its proposition in 1990 its existence has been disputed by Collins [26] before it became widely accepted [27][28]. Due to its connection with generalized parton distributions (GPDs), measurement of the Sivers function might provide insight into quark orbital angular momentum, which is a part of the proton spin puzzle [29]. The reason it does not exist in a simple model is the term  $\frac{\epsilon_{\perp}^{ij} k_{\perp i} S_{\perp j}}{M}$ . As mentioned, this is forbidden by standard T-invariance. However, since the nucleon is a composite system, the time reversal operator might be realized in a way that allows for these 'naïve' T-odd functions to exist [30]. One possibility is, that hadronic initial state interactions might lead to nontrivial phases, allowing functions like  $f_1(x, \vec{k}_\perp^2)$  similarly to naïve T-odd fragmentation functions. These will be revisited later. But in the case of hadronic initial state-interactions, the Sivers effect should only be measurable in Hadron-Hadron interactions. Measurement in semi-inclusive leptonproduction, as claimed by the HERMES experiment, favor a different model [31][32]. Another observation obtained from eq. 2.33 is that due to the presence of transverse momentum, the different PDFs mix in the probabilistic interpretation. For example the probability to find a quark with the same helicity as the nucleon is given by the projection on  $\gamma^+ \gamma_5$  as in the collinear case. But in the presence of quark transverse momentum and transverse spin of the nucleon the relation

$$\begin{aligned} \Phi^{[\gamma^+ \gamma_5]} &= \mathcal{P}_{q/N}(x, \vec{k}_T) \lambda(x, \vec{k}_\perp) \\ &= \lambda_N g_1(x, \vec{k}_\perp) + \frac{\vec{k}_\perp \cdot \vec{S}_\perp}{M} g_{1T}(x, \vec{k}_\perp^2) \end{aligned} \quad (2.36)$$

is obtained.

DIS observables are implicitly integrated over quark transverse momenta. In order to measure for example the quantity  $f_{1T}^\perp(x, k_\perp)$  semi inclusive measurements are necessary which are the topic of the next section. There the transverse momentum of the parton can be transferred to the transverse momentum of the fragmenting hadron, which is an observable. This allows the measurement of  $f_{1T}^\perp(x, k_T)$  through the Sivers-effect.

## 2.6 Sivers effect in DIS and Drell-Yan

The presence of quark transverse momenta also allows for nontrivial paths of the Wilson link in eq. 2.7. The Wilson link is equivalent to summing up all gluon contributions on the quark path from 0 to  $\xi$ , and thus making  $\Phi$  gauge invariant. For this reason it is also called the gauge link. It can be shown analytical that the link may allow  $\Phi$  to be naïve T-odd [4]. Since it is a formal treatment of gluon interactions with the fragmenting quark, it is also possible to derive this result from models with final- or initial state interactions with gluons. The fact, that these effects are intrinsically related to transverse momenta is also intuitively clear, because the emission or absorption of gluons leads to transverse momentum.

One interesting conclusion of this duality is, that the sign of the Sivers effect is different in the Drell-Yan (DY) and the DIS process. Formally this result can be derived from the gauge link, where nontrivial paths are allowed in the presence of transverse momenta, which are different in DY and DIS. On an intuitive level, it can be explained by the fact, that in DY the quark gluon interaction is expected in the initial state, since there are no hadrons left in the final state. In contrast, in DIS the interaction between the two hadrons is expected in the final state. In principle, the gauge link can differ for each process, calling in question the generalizability of transverse momentum dependent parton distribution functions and the factorization for the spin-dependent cross section in DIS. However, there is reason to believe, that the differences between the processes can be reduced to simple relations as above. And indeed, recently a set of factorization formulas was presented for SIDIS and DY at low transverse momentum [33]<sup>7</sup>.

## 2.7 Fragmentation in Semi Inclusive DIS

In order to measure the chiral odd transversity function or  $k_\perp$  dependent distribution functions one has to go to semi inclusive DIS, where in addition to the scattered lepton at least one other hadron is detected in the final state.

As mentioned earlier, chiral odd amplitudes are suppressed in the inclusive DIS cross-section. For the measurement of the Sivers effect, the reason is twofold. Firstly in the inclusive DIS cross-section the  $\vec{k}_\perp$  dependence is integrated out. Secondly the Sivers function is naïve T-odd, therefore in most models the wave function of a second hadron is needed that interferes with the detected one, to obtain a non-vanishing Sivers effect. The process under consideration is thus

$$l + N \rightarrow l' + h + X \tag{2.37}$$

---

<sup>7</sup>Large transverse momenta lead to large double logarithms in the hard part, which must be resummed to make reliable predictions [33]

where hadron  $h$  with momentum  $P_h$  in the current fragmentation region is detected and the final state  $X$  remains undetected. It is convenient to work, instead of the  $\gamma^*N$  collinear frame, in a frame where the produced hadron and the target nucleon are collinear. Usually the transverse momenta in the first frame are denoted with the subscript  $\perp$  whereas for the second frame  $T$  is used.

Therefore one has  $\vec{P}_\perp = \vec{q}_\perp = 0$  and  $\vec{P}_{h\perp} \simeq -z\vec{q}_T$  up to  $1/Q^2$  corrections [1]. The two systems differ by a boost, that introduces effects that can be ignored at leading order [34].

Analogous to the hadronic tensor for inclusive DIS from eq. 2.5 the hadronic tensor for the process 2.37 becomes

$$2MW^{\mu\nu} = \frac{1}{(2\pi)^4} \sum_a e_a^2 \sum_X \int \frac{d^3\vec{P}_X}{(2\pi)^3 2E_X} \int \frac{d^4k}{(2\pi)^4} \int \frac{d^4\kappa}{(2\pi)^4} \cdot (2\pi)^4 \delta^4(P - k - P_X) (2\pi)^4 \delta^4(k + q - \kappa) (2\pi)^4 \delta^4(\kappa - P_h - P_X) \cdot [\bar{\Xi}(\kappa; P_h, S_h) \gamma^\mu \Phi(k; P, S)]^* [\Xi(\kappa; P_h, S_h) \gamma^\mu \Phi(k; P, S)] \quad (2.38)$$

where  $\Phi(k; P, S)$  describes the structure of the nucleon and  $\Xi(\kappa; P_h, S_h)$  the fragmentation of a quark with momentum  $\kappa$  into a hadron  $h$  with momentum  $P_h$  and spin  $S_h$  plus an undetected state  $X$  with energy  $E_X$  and momentum  $P_X$ .  $\Xi(\kappa; P, S)$  is given by the matrix element of the quark field  $\Psi$ :  $\Xi(\kappa; P_h, S_h) = \langle 0 | \Psi(0) | P_h, S_h, X \rangle$ . Integration over  $E_X$  was already carried out.

According to eq. 2.5 the matrix element  $\Phi(k; P, S)$  is given by  $\langle X | \Psi(0) | PS \rangle$ . If the helicities of the scattering quark and the parent nucleon are neglected, it represents one half of a handbag diagram like those shown in figure 2.5

The expression  $\bar{\Xi}(\kappa; P_h, S_h) \gamma^\mu \Phi(k; P, S)$  can be seen as the current of the quark which interacts with the scattered lepton. But in contrast to 2.5 the quark does not go back into the nucleon. Instead it fragments. In this formula the parton model assumption is already used, namely, that the current can be divided into two soft parts, described by the matrix elements  $\Phi$  and  $\Xi$ . These can then be treated independently by assuming a quasi free quark that scatters and then fragments, if factorization holds. Without the validity of factorization, parton model quantities lose their generalizability. In the presence of soft gluon exchanges, factorization becomes difficult to prove and additional effects have to be taken into account. For example the mentioned sign change of the Sivers effect in Drell-Yan and SIDIS.

Similarly to the quark-quark correlation matrix, we can form the fragmentation matrix  $\Xi(\kappa; P_h, S_h)$  (averaging over color and in LC gauge):

$$\Xi(\kappa; P_h, S_h)_{ij} = \sum_X \int d^4\xi e^{i\kappa \cdot \xi} \langle 0 | \Psi_i(\xi) | P_h S_h, X \rangle \langle P_h S_h, X | \bar{\Psi}_j(0) | 0 \rangle \quad (2.39)$$

where the integration over  $P_X$  (see again eq. 2.5) is contained in  $\sum_X$  [14].

The hadronic tensor at leading order can then be expressed as the product of quark dynamics inside the nucleon and the fragmentation in the hadronic final state [1][14]:

$$2MW^{\mu\nu} = \sum_a e_a^2 \int \frac{dk^- d^2\vec{k}_\perp}{(2\pi)^4} \frac{d\kappa^+ d^2\vec{\kappa}_\perp}{(2\pi)^4} \delta^2(\vec{k}_\perp + \vec{q}_\perp - \vec{\kappa}_\perp) Tr[\Phi\gamma^\mu\Xi\gamma^\nu] \Big|_{k^+=xP^+, \kappa^- = P_h^-/z} \quad (2.40)$$

Note the  $\delta$ -function that ensures the transfer of the outgoing quark momentum to the fragmentation process, so that transverse momentum dependent parton distribution functions can be measured in semi inclusive DIS. The light cone momentum fraction carried by hadron  $h$  is denoted by  $z$  and is the same variable as in table 2.1. Here one difference with regard to parton distribution functions, which was already mentioned in section 2.2.1 can be seen. Due to the change in direction of the fragmenting quark, the rôles of positive and negative light cone directions and projections have to be exchanged, when comparing  $\Xi$  and  $\Phi$ . Also  $\gamma^+$  and  $\gamma^-$  have to be exchanged.

Equation 2.40 is similar to 2.5 except that  $\not{k}$  describing the propagation of the quark along the handle is replaced by the fragmentation matrix  $\Xi$ . As before  $\gamma^\mu$  and  $\gamma^\nu$  are the vertex factors from the one-photon exchange with the scattered beam particle. A graphical representation thereof is shown in fig. 2.6 which extends the handbag diagrams in fig. 2.5 to include fragmentation.

Following the leading order analysis of  $\Phi$  presented earlier,  $\Xi$  can be decomposed over a Dirac base using the kinematical quantities available in fragmentation. These are in principle the momentum with regard to the fragmenting quark and the polarization of the produced hadron. But since it is difficult to measure the polarization of the hadrons in the final state, the focus is on the production of unpolarized hadrons. Therefore the fragmentation functions depending on  $S_h$  are averaged out.

Analogous to the treatment of  $\Phi$  in section 2.2, the Dirac structures surviving at leading order are the vectorial, the axial-vectorial and the tensorial part. They are isolated by forming the traces over the Dirac structures  $\gamma^-$ ,  $\gamma^-\gamma^5$  and  $i\sigma^{i-}\gamma^5$ . The coefficient functions are this time the different fragmentation functions, which can be interpreted in a partonic picture. Since the hadron spin is averaged out, the axial-vector part also vanishes. In detail, with  $\vec{\kappa}' = z\vec{\kappa}'_T$ :

$$\Xi^{[\gamma^-]} = D_1(z, \vec{\kappa}'_T, z) \quad (2.41)$$

$$\Xi^{[i\sigma^{i-}\gamma^5]} = \frac{1}{M_h} \epsilon_T^{ij} \kappa_{Tj} H_1^\perp(z, \kappa'_T) \quad (2.42)$$

The integrated trace over the quark-quark correlation matrix  $\Xi$  is defined in analogy to eq. 2.19 [1]

$$\begin{aligned} \Xi^{[\Gamma]} &\equiv \frac{1}{4z} \int \frac{d\kappa^+ d\kappa^-}{(2\pi)^4} Tr(\Gamma\Xi) \delta(\kappa^- - P_h^-/z) \\ &= \frac{1}{4z} \sum_X \int \frac{d\xi^+ d^2\vec{\xi}_T}{(2\pi)^3} e^{i(P_h^i \xi^+ / z - \vec{\kappa}_T \cdot \vec{\xi}_T)} \\ &\quad \times Tr(\langle 0 | \Psi(\xi^+, 0, 0_\perp) | P_h S_h, X \rangle \langle P_h S_h, X | \bar{\Psi}(0) \Gamma | 0 \rangle). \end{aligned} \quad (2.43)$$

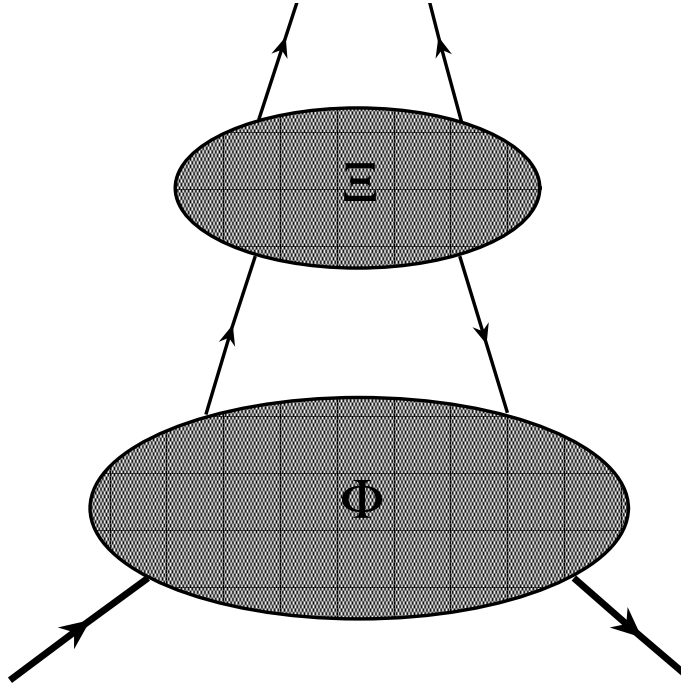


**Figure 2.6:** Feynman diagram like notation for the spin averaged SIDIS hadronic tensor at leading twist. The lower blob contains the nucleon dynamics, described by the quark-quark correlation matrix. The upper blob the fragmentation process, described by the fragmentation matrix. The lines are the quarks. The two blobs are only connected by the single quark line, provided fragmentation holds and if only the leading twist contribution is considered in which there is no gluon radiation from the scattered quark. As in the case of the forward scattering amplitudes in fig. 2.5, which is the lower blob, the diagrams are symmetric with respect to the vertical axis and represent the squared matrix element described by the correlation matrices. Taking advantage of this symmetry allows to find a probabilistic interpretation.

### 2.7.1 Collins Effect

As shown in section 2.2.3, the tensorial part at leading twist, given by  $i\sigma^{i-}\gamma^5 = \gamma^-\gamma^i\gamma^5$ , can be interpreted in a chiral base for the quark fields by using the projectors on the different chirality states  $\mathcal{P}_{\uparrow,\downarrow} = \frac{1}{2}(1 \pm \gamma^1\gamma^5)$ . With this follows  $\Xi^{[i\sigma^{i-}\gamma^5]} = \mathcal{N}_{h/q}(z, \vec{\kappa})s_{\perp}^i(z, \vec{\kappa})$ , where  $\vec{s}'$  is the spin of the fragmenting quark and  $\mathcal{N}_{h/q}(z, \vec{\kappa})$  the probability for a quark  $q$  to fragment into a hadron  $h$ . The azimuthal angles of the quark in the initial state and after the interaction with the virtual photon are related by  $\Phi_{s'} = \Phi_s + \pi$  due to the change of direction along the  $z$ -axis in the photon-nucleon system of the quark, for a detailed explanation see [1]. By fixing  $i$  for example to 1, the magnitude of  $\Xi^{[i\sigma^{i-}\gamma^5]}$  is given by the component of  $\vec{\kappa}$  that is transversal, here  $\kappa_2$  due to the Levi-Civita-symbol in equation 2.42. The number of transversely polarized quarks fragmenting into unpolarized hadrons is thus dependent on the azimuthal angle between  $\vec{\kappa}$  and  $s'$ . From equation 2.42 a modulation by  $\frac{|\vec{\kappa}_T|}{M_h} \sin(\Phi_{\kappa} - \Phi_{s'})$  can be derived. This is called the 'Collins Effect', since it was first predicted by Collins [26]. The fragmentation function  $H_1^{\perp}$  is called the 'Collins Fragmentation function'. Like the Sivers distribution function it is T-odd since the corresponding kinematical Dirac structure would be forbidden under time invariance. However, final state effects may allow these naïve T-odd functions. The Collins effect has a descriptive interpretation in the Lund string fragmentation model, as noted by X. Artru [35]: If a transversely polarized quark fragments to form an unpolarized hadron, it is connected to the color-charged nucleon remnant by a color flux tube. The flux tube stretches and eventually breaks down, forming a quark/antiquark pair with the quantum numbers of the vacuum. If the transverse direction is chosen as the quantization axis, this means orbital angular momentum  $L_y = 1$  and spin  $S_y = -1$ . Together with the fragmenting quark that has spin  $s_y = \frac{1}{2}$ , the produced antiquark forms a scalar hadron. Due to the conservation of orbital angular momentum, this scalar particle has a preferred direction of momentum. This mechanism is illustrated in figure 2.7.

In order to observe the Collins effect, the azimuthal angle of the fragmenting quark spin  $\Phi_{s'}$  has to be related to an observable. A first step is to use the relation  $\Phi_{s'} = \pi - \Phi_s$ . Then it can be assumed that the initial quark spin  $s$  is parallel to the spin of the parent nucleon  $S$ . The direction of momentum of the detected hadron  $P_h$  can be substituted for the one of the quark momentum  $\kappa$ , so that  $\Phi_{\kappa} = \Phi_h$ . This leads to a modulation of the cross section which is dependent on the Collins angle  $\Phi_{\text{Coll}} = \Phi_h + \Phi_S - \pi$  and the amplitude of the effect is proportional to the fraction of quarks which is indeed polarized parallel to the nucleon spin. Here the assumption is a transversely polarized nucleon.

### 2.7.2 Sivers Effect

Using the transverse momentum dependent expression for the hadronic tensor in eq. 2.40, there is another single spin asymmetry which can be observed in SIDIS of an unpolarized beam off a transversely polarized target. Namely the Sivers effect which is connected to the Sivers function described in sec. 2.5. The vectorial Dirac structure of the Sivers function expressed in eq. 2.32 causes the coupling to the corresponding fragmentation functions which are obtained from the vectorial part of the fragmentation correlation

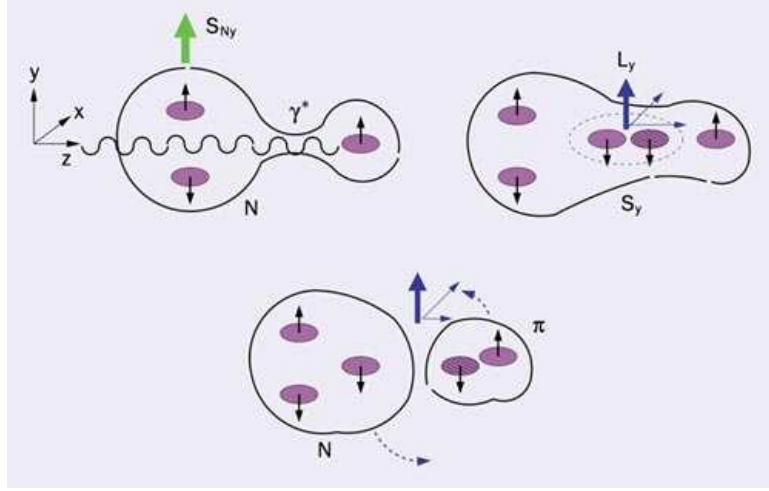


**Figure 2.7:** Illustration of the Collins mechanism from [35].

matrix. This is, as seen in eq. 2.41, at leading order the unpolarized fragmentation function  $D_1$ .

Due to the dependence of the amplitude of the Sivers function on  $\frac{\epsilon_{\perp}^{ij} k_{\perp i} S_{\perp j}}{M}$  and the transfer of the initial state quark transverse momentum  $\vec{k}_{\perp}$  to the final state quark transverse momentum  $\vec{\kappa}_{\perp}$ , which is expressed in the term  $\delta^2(\vec{k}_{\perp} + \vec{q}_{\perp} - \vec{\kappa}_{\perp})$  of eq. 2.40, a single spin asymmetry exists. The azimuthal dependence of the cross-section is of the form  $\sin(\Phi_{\kappa} - \Phi_S)$ . Here  $\Phi_S$  is the azimuthal angle of the parent nucleon and  $\Phi_{\kappa}$  can be obtained from the the azimuthal angle of the hadron  $\Phi_h$ . The angular combination  $\Phi_h - \Phi_S$  is called the Sivers angle  $\Phi_{\text{Siv}}$ . Due to the orthogonality with respect to the Collins effect, described in sec. 2.7.1, the two effects can be disentangled in practice. One important aspect of the Sivers effect is, that it provides an insight into quark angular momentum. If the Sivers effect exists, the angular momentum carried by the quarks has to be non-zero. Furthermore quark angular momentum can explain the Sivers effect quite nicely as Burhardt noted [29]. If a quark with angular momentum in the direction of the polarization of the parent nucleon is considered, then this quark appears shifted in momentum space depending on which side of the axis of rotation the nucleon is probed by the virtual photon. At a fixed momentum fraction  $x_{Bj}$  the unpolarized quark distribution function in a transversely polarized nucleon therefore appears deformed and shifted. This asymmetry with respect to the transverse axis of rotation then leads to an azimuthal asymmetry in the produced hadron momenta if final state interactions between the fragmenting quark and the nucleon remnant are taken into account. The reason is simply, that the strong force acting on a quark is higher if it is further away. See figure 2.8.

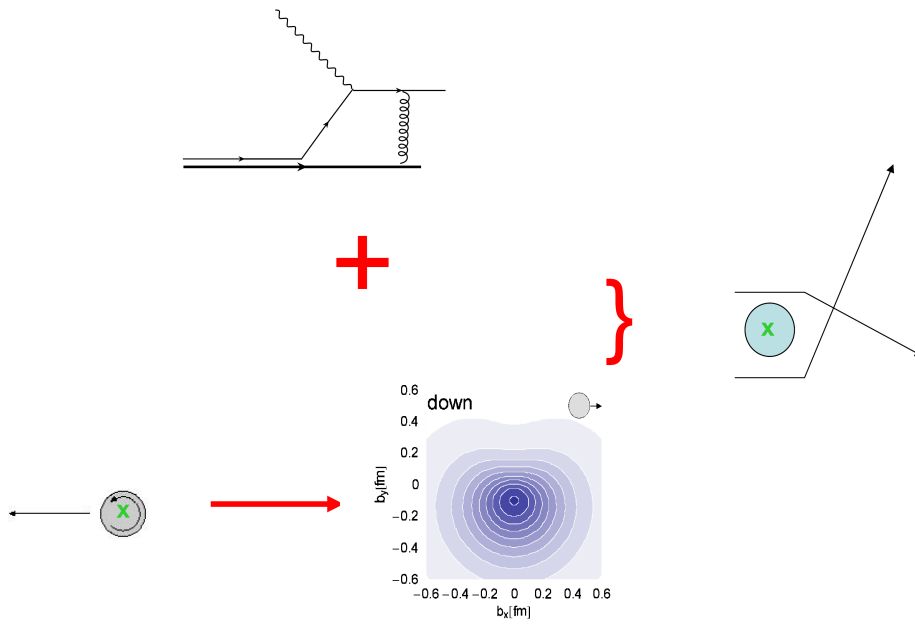


**Figure 2.8:** Illustration of the Sivers effect. The virtual photon comes from the left and in the photon-nucleon center of mass system the nucleon moves to the left. The polarization vector points into the plane. This leads to a deformation of the quark distribution function in impact parameter space. Together with a final state interaction of the outgoing quark, this causes a left-right asymmetry of the outgoing hadron. Burkardt et. al. christened this effect “Chromodynamic Lensing” [29]. Here the visualization of the quark distribution in impact parameter space is taken from [36]. It shows the distribution of the down quarks in the proton as computed from lattice QCD integrated over  $x_{Bj}$ . At variance to the other pictograms, the virtual photon direction points into the plane and the nucleon spin to the right as indicated.

## 2.8 Fragmentation into two Hadrons

The Collins effect is probably the most prominent probe of the transversity distribution. However, due to the explicit dependence on the intrinsic quark transverse momentum, as seen in eq. 2.41, the analysis of this channel exhibits some difficulties [37]. Subleading twist has to be included and the modeling of the Collins fragmentation function is difficult, because an understanding of microscopic phases of channels leading to the same detected hadron is necessary. Another way that was proposed is to look for a SSA originating from a channel, where transversity couples to the two hadron interference fragmentation function  $H_1^{\triangleleft}$  [38][39][40][41]. This SSA, where two unpolarized hadrons in the current fragmentation region are detected in SIDIS, is an independent channel in which to measure transversity. In principle, due to the existence of a second hadron, the expansion of the fragmentation matrix is richer and there are many more fragmentation functions possible. But the presence of the additional degree of freedom makes it possible to integrate over the intrinsic quark  $\kappa_{\perp}$ , and still retain a non-vanishing effect. This is very advantageous, since now collinear factorization can be used. Moreover, one can assume that it is enough to describe the residual interaction between the produced two hadrons to model  $H_1^{\triangleleft}$  because the interaction between other hadrons occurs at higher order. This makes modeling much easier [38]. The process in question is thus

$$l + N \rightarrow l' + h_1 + h_2 + X. \quad (2.44)$$

It is convenient to parametrize the relevant kinematics by the vectors

$$P_h = P_1 + P_2 \quad R = \frac{1}{2}(P_1 - P_2) \quad (2.45)$$

and the dimensionless variable  $\zeta = 2R^-/P_h^-$ , which describes how the total momentum of the pair is split into the two single hadrons. The light cone momentum fraction of the fragmenting quark carried by the hadron pair,  $z = P_h^-/k^-$ , simplifies to  $z = (P \cdot P_h)/(P \cdot q) = z_1 + z_2$  in the absence of intrinsic quark momenta.

With these definitions the fragmentation correlation matrix can be written in terms of matrix elements for the fragmentation into two hadron as [34]

$$\Xi(z, R) = z^2 \sum_X \int \frac{d\xi^+}{2\pi} \langle 0 | \psi(\xi) | P_h, R; X \rangle \langle X; P_h, R | \bar{\psi}(0) | 0 \rangle |_{\xi^- = \vec{\xi}_T = 0} \quad (2.46)$$

which is analogous to eq. 2.39 for the one hadron case at leading twist and integrated over transverse momenta. After a decomposition over a Dirac structure, the traces of the tensorial and vectorial part analogous to eq. 2.41, which play a role in the measurement of transverse single spin asymmetries, read with the invariant mass of the hadron pair  $M_{\text{Inv}} = |P_h|$ :

$$\Xi^{[\gamma^-]} = D_1(z, \zeta, M_{\text{Inv}}) \quad (2.47)$$

$$\Xi^{[i\sigma^{i-}\gamma^5]} = \frac{\epsilon_T^{ij} R_{Tj}}{M_{\text{Inv}}} H_1^{\triangleleft}(z, \zeta, M_{\text{Inv}}). \quad (2.48)$$

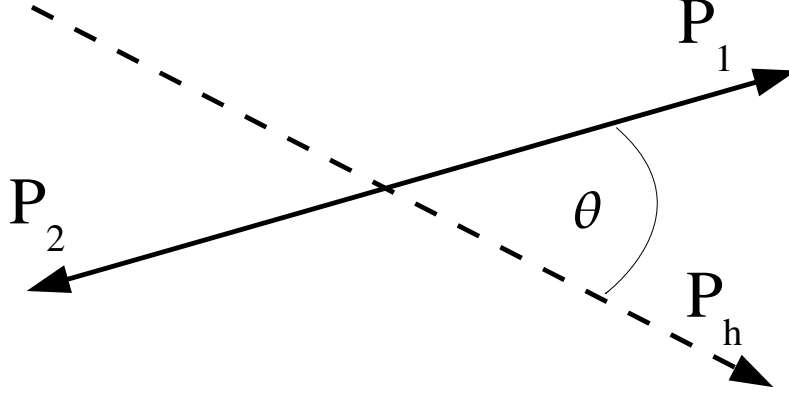


**Figure 2.9:** Definition of the angle  $\theta$  in the center of mass system of the hadron pair

By comparing with section 2.7.1 it is obvious, that  $H_1^{\triangleleft}$  describes the probability for a transversely polarized quark to fragment into an unpolarized hadron pair. It is also naïve T-odd and chiral odd and couples to the transversity distribution. As for the Collins effect, the part of the cross section proportional to  $h_1 \cdot H_1^{\triangleleft}$  exhibits a dependence on an azimuthal angle. In the case of the two hadron fragmentation on  $\Phi_R$  of the form  $\sin(\Phi_R + \Phi_S - \pi) \frac{|\vec{S}_\perp| |\vec{R}_T|}{M_{\text{Inv}}}$ .

### 2.8.1 Partial wave analysis of $H_1^{\triangleleft}$

Using partial wave analysis, further knowledge about the inner structure of  $H_1^{\triangleleft}$  can be gained. To this end, the correlation function  $\Xi$  is expressed in the center of mass parameter  $\cos \theta$ . The polar angle  $\theta$  is illustrated in fig. 2.9 and gives the angle between  $P_h$  and  $P_1$  in the center of mass system (CM) of the two hadrons.

With this angle,  $\zeta$  in the center of mass system can be written as

$$\zeta \stackrel{CM}{=} \frac{1}{M_{\text{Inv}}} \left( \sqrt{M_1^2 + |\vec{R}|^2} - \sqrt{M_2^2 + |\vec{R}|^2} - 2|\vec{R}| \cos \theta \right) \quad (2.49)$$

where

$$|\vec{R}| = \frac{1}{2} \sqrt{M_{\text{Inv}}^2 - 2(M_1^2 + M_2^2) + (M_1^2 + M_2^2)/M_{\text{Inv}}^2}. \quad (2.50)$$

The variable  $\zeta$  depends in the CM-frame only linearly on  $\cos \theta$ , which allows to expand a function of  $\zeta$  in the basis of Legendre polynomials. Expressing the vector  $\vec{R}$  in CM parameters also leads to an introduction of a  $\sin \theta$  factor into eq. 2.48. After expansion into partial waves, the interference fragmentation function becomes

$$\frac{2|\vec{R}|}{M_{\text{Inv}}} H_1^{\triangleleft}(z, \zeta(\cos(\theta)), M_{\text{Inv}}^2) = H_{1,ut}^{\triangleleft,sp}(z, M_{\text{Inv}}^2) + H_{1,lt}^{\triangleleft,pp}(z, M_{\text{Inv}}^2) \cos(\theta) \quad (2.51)$$

Comparing coefficients with the decay matrix  $\mathcal{D}(\theta, \Phi_R)_{jm, j'm'} = Y_j^m Y_j^{m'}$ , where the  $Y$  are spherical harmonics, shows the meaning of the sub- and superscripts. The combination  $sp$  denotes the interference between an “unpolarized” hadron pair in a relative s-wave and a transversely polarized pair in a relative p-wave, thus the subscript  $ut$ . The combination  $pp$  and  $lt$  for super- and subscript, respectively, signifies the interference between hadron pairs that are both in a p-wave, but one longitudinally and the other transversely polarized. The expansion can be truncated after the first three terms, if one considers, that at low invariant mass hadron pairs are mainly produced in the s-wave channel or in the p-wave channel. This set is also the minimal set required to describe all the polarization states of the system in the CM frame for relative partial waves with  $L=0,1$ . The  $ss$  term is unpolarized, i. e. does not depend on the target polarization. Experimentally relevant at COMPASS is first of all  $H_{1,ut}^{\triangleleft, sp}$ , which contributes with a factor of  $\sin \theta$  to the cross section. As shown later (sec. 4.2) the COMPASS acceptance makes the measurement of the part depending on  $H_{1,lt}^{\triangleleft, pp}$  much more difficult. The p-wave term can be seen as the fragmentation of spin-one particles, i.e. the  $\rho$  for  $\pi$ -pair production.

In a visual way, the fragmentation function  $H_1^{\triangleleft}$  corresponds to the upper blob in fig. 2.6, its chiral odd nature makes it possible to carry away the quark helicity at the handbag handles. This is done by having a hadron pair with different relative orbital angular momentum at each handle. At lowest order, there are two possibilities to do so, giving the  $sp$  and  $pp$  interference.

### 2.8.2 Models for $H_1^{\triangleleft}$

Collins and Ladinsky used the linear sigma model to make the first predictions for  $\pi$ - $\pi$  correlations as a probe for the fragmentation of polarized quarks [42]. The insights gained from the partial wave analysis in the previous section then inspired model predictions for  $H_1^{\triangleleft}$  based on the interference of meson pairs (pions and kaons) in relative s- and p-waves [37][43]. Notable is a common strong dependence on the invariant mass of the hadron pair because the relative partial waves of the meson pairs are determined by the resonance they were produced from. Exemplarily for predictions of effects at COMPASS kinematics are the models by Jaffe, Jin and Tang [44] and Radici, Jakob and Bianconi [37]. Jaffe and collaborators estimate the final state interactions of the meson pairs from meson-meson phase shift data obtained from [45]. From these it is known, that s- and p-wave production channels interfere strongly in the mass region around the  $\rho$ , the  $K^*$  and the  $\Phi$  meson resonances. As an example fig. 2.10 shows the phase shifts for the experimentally most relevant region around the  $\rho$ -meson. Radici et al. use a quark spectator model to predict the amplitude of  $H_{1,ut}^{\triangleleft, sp}$ . Figure 2.11 shows the processes that were considered. Later Bacchetta and Radici refined this model, by using Monte-Carlo simulations to fix some parameters [46]. The resulting predictions for asymmetries at COMPASS are shown in fig. 2.12. Compared to a future proton target (fig. 2.13), the expected asymmetries with the current deuterium target are decreased due to a cancellation between u- and d-quark contributions.

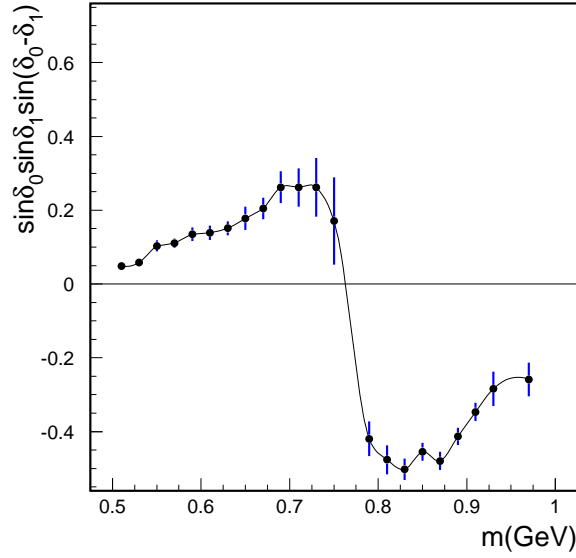


**Figure 2.10:** Phase shifts from p-wave resonances and non-resonant s-wave background [45].

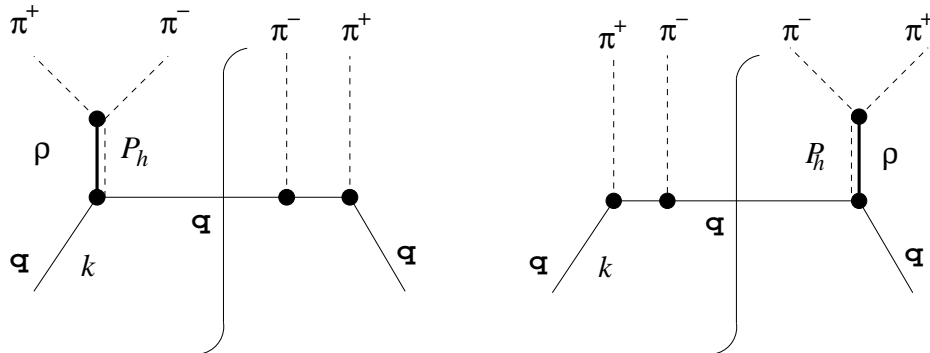


**Figure 2.11:** Diagrams considered in the predictions of [37] and [46]. They describe the interference between two pions produced in a p-wave through a  $\rho$  decay and an s-wave. The quark line labeled  $\mathbf{q}$  represents the handle of a handbag diagram.

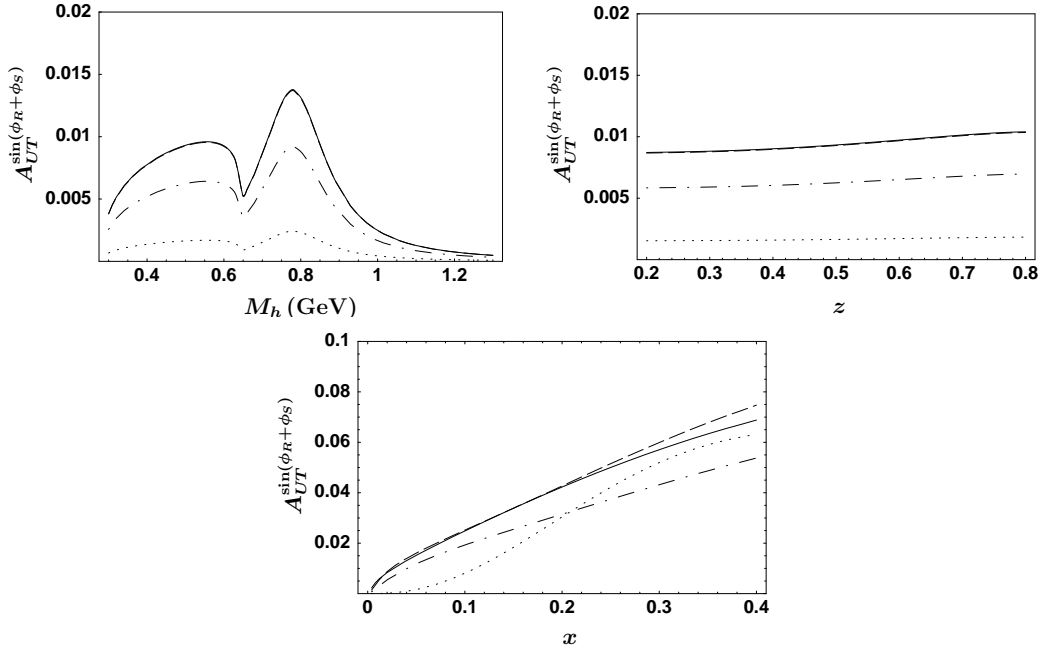


**Figure 2.12:** Predictions of [46] for a deuterium target at COMPASS kinematics in  $x_{Bj}$ ,  $z$  and the invariant mass of the hadron pair ( $M_h$ ). The different lines correspond to different models of the transversity function: Solid line from [47], dotted line from [48], dash-dotted line from [49] and dashed line from [50]. In the invariant mass plot, an effect is expected close to the  $\rho$  resonance. In  $x_{Bj}$  the asymmetry becomes greater in the valence quark region. Compared to a proton target, the expected magnitude is decreased due to a cancellation between u- and d-quark contributions.

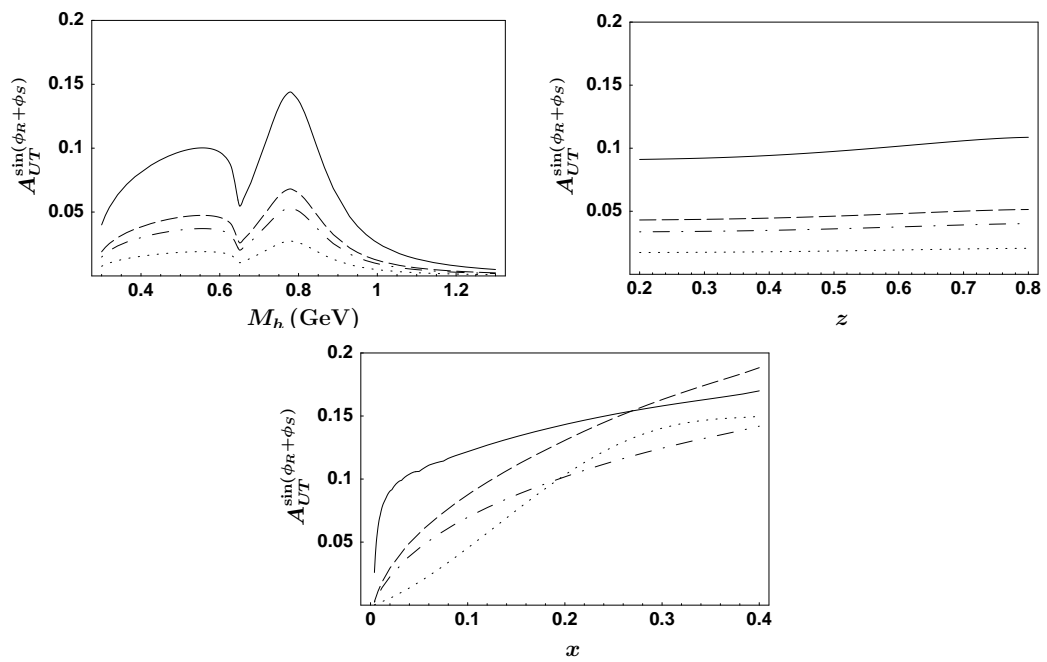


**Figure 2.13:** Predictions of [46] for a proton target at COMPASS kinematics. The different lines correspond to different models of the transversity function as in fig. 2.12. In comparison with the predictions for a deuterium target shown in fig. 2.12, the scale is magnified.

## 2.9 Single Spin Asymmetries in SIDIS

The last section introduced the basic mechanism for single spin asymmetries due to the Collins effect, the Sivers effect and the two hadron interference fragmentation function  $H_1^\triangleleft$ . Now the results are compiled into asymmetries that are expressed in quantities accessible in an experiment.

### 2.9.1 One Hadron SSAs

The full SIDIS cross section has been compiled by Mulders and Tangerman [14]. If only the Collins and Sivers mechanisms are considered, the cross section for one hadron production can be written as [51]

$$d\sigma \sim \sum_{q_f} e_{q_f}^2 \left\{ \frac{1}{2} [1 + (1-y)^2] x_{Bj} \left[ q \otimes D_{1q} + |\vec{S}_\perp| \sin(\Phi_{\text{Siv}}) q_{1T}^\perp \otimes D_{1q} \right] + (1-y) |\vec{S}_\perp| \sin(\Phi_{\text{Coll}}) x_{Bj} h_{1q} \otimes H_{1q} \right\}. \quad (2.52)$$

Here  $y$  is the fractional energy transfer of the lepton as defined in tbl. 2.1, the sum is performed over all quark flavors and  $e_{q_f}$  signifies the charge of a quark of flavor  $q_f$ ,  $q$  its unpolarized distribution function,  $q_{1T}$  its Sivers and  $h_{1q}$  its transversity distribution function. The convolution integral is performed over the transverse momentum of the fragmenting quark. Assuming that a fraction  $z$  of the intrinsic transverse momentum  $\vec{k}_T$  of the quark is transferred to the detected hadron, the convolution between the transverse momentum dependent (TMD) distribution and fragmentation functions ( $DF$  and  $FF$ ) can be written as

$$DF \otimes FF = \int d^2 \vec{k}_T DF(x, \vec{k}_T) \cdot FF(z, \vec{\kappa}_T - z \vec{k}_T). \quad (2.53)$$

With the common Gaussian ansatz for the transverse momentum dependence of the transversity distribution and the unpolarized fragmentation function, the convolution can be reduced to a product, with an extra factor depending on the mean transverse momentum [52][53].

If these are absorbed into the definition of the functions, the following asymmetry can be build to extract  $h_1(x) \cdot H_1(z, \kappa_T)$  and  $f_{1T}^\perp \cdot D_1(z)$ .

$$\begin{aligned} A_T^h &= \frac{d\sigma(\vec{S}_\perp) - d\sigma(-\vec{S}_\perp)}{d\sigma(\vec{S}_\perp) + d\sigma(-\vec{S}_\perp)} \\ &= |\vec{S}_\perp| \cdot D_{NN} A_{\text{Coll}} \cdot \sin \Phi_{\text{Coll}} + |\vec{S}_\perp| \cdot A_{\text{Siv}} \cdot \sin \Phi_{\text{Siv}} \end{aligned} \quad (2.54)$$

The factor

$$D_{NN} = \frac{1-y}{1-y+y^2/2} \quad (2.55)$$

is the transverse spin transfer coefficient from the initial to the struck quark [1]. The azimuthal asymmetries are evaluated in a reference frame, where both, photon and nucleon momenta, are parallel to the z-axis. In this reference system the target spin and

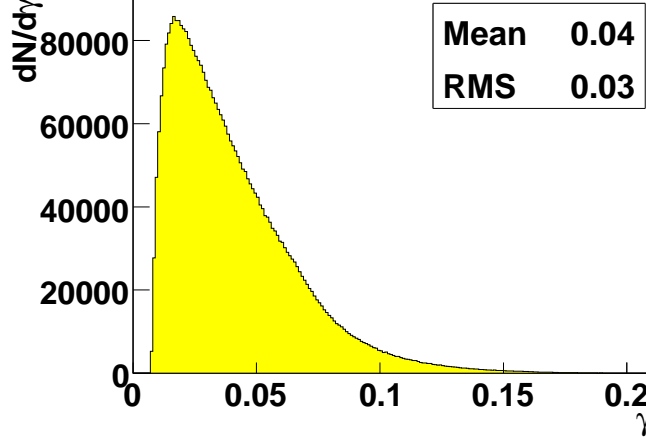


**Figure 2.14:** Distribution of the kinematic factor  $\gamma = \frac{2Mx_{Bj}}{Q}$ . Depending on the scattering process kinematics, the target spin and virtual photon vectors are not perpendicular resulting in a dilution of transverse target spin asymmetries. The size of this effect is given by  $\gamma$  and is negligible at COMPASS kinematics.

virtual photon vectors are not necessarily perpendicular since the polarization vector of the nucleon lies in a plane transverse to the z-axis in the lab system, Therefore, depending on the scattering process kinematics, there could be an effect on  $|\vec{S}_\perp|$ . However, this is suppressed by a factor of  $\gamma = \frac{2Mx_{Bj}}{Q}[1]$ . Figure 2.14 shows the distribution of  $\gamma$  for COMPASS, which is small.

### 2.9.2 Two Hadron SSAs

Similar to the one hadron case the two hadron Asymmetry to extract  $h_1(x) \cdot H_1^\triangleleft(z, M_{\text{Inv}})$  is

$$A_T^{2h} = \frac{d\sigma_{2h}(\vec{S}_\perp) - d\sigma_{2h}(-\vec{S}_\perp)}{d\sigma_{2h}(\vec{S}_\perp) + d\sigma_{2h}(-\vec{S}_\perp)} = |\vec{S}_\perp| \cdot D_{NN} A^{\text{RS}} \cdot \sin(\Phi_R + \Phi_S - \pi). \quad (2.56)$$

Here, a slightly different definition of  $\vec{R}$  is employed. The reason is that for the analysis of single spin asymmetries where one looks for azimuthal asymmetries several coordinate systems are commonly used. They differ by boosts along the z-axis and have in common that the photon and the nucleon are collinear. Using the Sudakov decomposition for photon and nucleon momentum as shown in equations 2.13 and 2.14, the difference in the coordinate systems can be reduced to the choice of the parameter  $p$ . For the extraction of azimuthal asymmetries, this does not make a difference, because the directions perpendicular to the boost are unaffected by it. This is true for the extraction of the one hadron asymmetries.

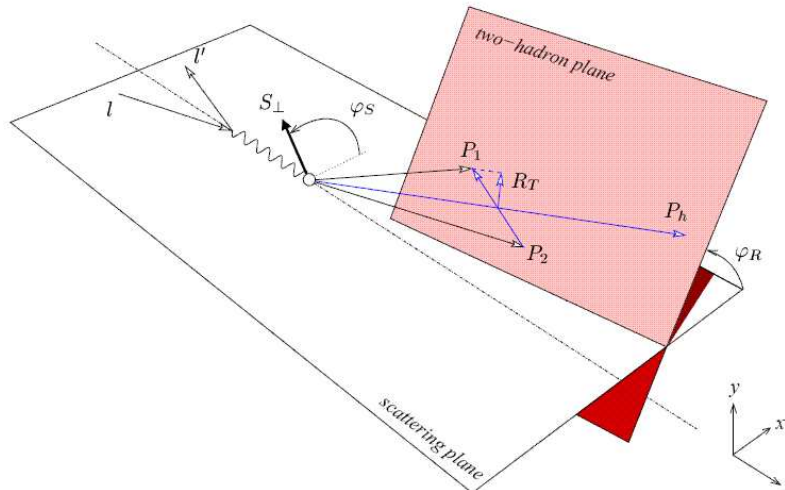


**Figure 2.15:** Coordinate System for the two hadron asymmetries.

However, in the two hadron case, using the definition of  $\vec{R}$  in eq. 2.45, introduces a dependence of the asymmetry on a boost along the  $z$ -axis, because  $\vec{R}$  is a linear combination of the momentum vectors of the two hadrons. Since these vectors are affected differently by the boost,  $\vec{R}$  will rotate also in the azimuthal plane. So, at variance to the definition of  $\vec{R}$  in sec. 2.8, for the analysis the definition

$$\vec{R} = \frac{z_2 \vec{p}_1 - z_1 \vec{p}_2}{z_1 + z_2}. \quad (2.57)$$

is used. The terms  $\vec{p}_1$ ,  $\vec{p}_2$  are the momenta of the two hadrons measured again in the coordinate system of fig. 2.2. The resulting vector  $\vec{R}$  is depicted in fig. 2.15. Scaling the momenta in the given way makes the definition approximately invariant against boosts along the photon direction, allowing to treat  $\Phi_R$  in the same way as  $\Phi_h$ . This becomes apparent when using the collinear approximation for the fragmenting hadron. Then the fractional energy  $z$  is a good approximation of the fractional momentum of the hadron in  $z$  direction. The normalization of the two hadron momenta to the same momentum in  $z$  direction then leads to invariance with regards to boosts in this direction.

## 2.10 Parton Model independent Cross Section in the Born Approximation

The SSAs described so far are effects that can be measured for an unpolarized beam scattering off a transversely polarized target. In addition to Collins and Sivers asymmetries, there are more SSAs with one hadron in the final state in this setup which also depend on the azimuthal angles of spin and hadron momentum. The number of SSAs gets augmented when considering the experimentally relevant configuration of a longitudinal polarized beam and a transversely polarized target.

With the one-photon approximation there are in general eight spin dependent modulations allowed in the one hadron leptoproduction process  $l + n^\uparrow \rightarrow l' + h + X$  cross section where a lepton  $l$  scatters off a transversely polarized nucleon  $n^\uparrow$  to produce one hadron  $h$  and an undetected state  $X$  [54][55].

In terms of structure functions  $F$  the general cross section can be written as [56]

$$\begin{aligned}
\frac{d\sigma}{dx dy dz d\Phi_h d\Phi_S dP_{h\perp}^2} &= (1 - y + y^2) \frac{\alpha^2}{xyQ^2} \\
&\left\{ F_{UU} + D^{\cos \Phi_h} \cos \Phi_h F_{UU}^{\cos \Phi_h} + D^{\cos(2\Phi_h)} \cos(2\Phi_h) F_{UU}^{\cos 2\Phi_h} + \lambda_b D^{\sin \Phi_h} \sin \Phi_h F_{LU}^{\sin \Phi_h} \right. \\
&+ |\vec{S}_\perp| \left[ D^{\sin(\Phi_h - \Phi_S)} \sin(\Phi_h - \Phi_S) F_{UT}^{\sin(\Phi_h - \Phi_S)} + D^{\sin(\Phi_h + \Phi_S)} \sin(\Phi_h + \Phi_S) F_{UT}^{\sin(\Phi_h + \Phi_S)} \right. \\
&+ D^{\sin(3\Phi_h - \Phi_S)} \sin(3\Phi_h - \Phi_S) F_{UT}^{\sin(3\Phi_h - \Phi_S)} + D^{\sin \Phi_S} \sin \Phi_S F_{UT}^{\sin \Phi_S} + \\
&D^{\sin(2\Phi_h - \Phi_S)} \sin(2\Phi_h - \Phi_S) F_{UT}^{\sin(2\Phi_h - \Phi_S)} \left. \right] \\
&+ |\vec{S}_\perp| \lambda_b \left[ D^{\cos(\Phi_h - \Phi_S)} \cos(\Phi_h - \Phi_S) F_{LT}^{\cos(\Phi_h - \Phi_S)} + D^{\cos \Phi_S} \cos \Phi_S F_{LT}^{\cos \Phi_S} \right. \\
&\left. + D^{\cos(2\Phi_h - \Phi_S)} \cos(2\Phi_h - \Phi_S) F_{LT}^{\cos(2\Phi_h - \Phi_S)} \right] \left. \right\}. \tag{2.58}
\end{aligned}$$

This formulation is independent from the parton model and follows from general symmetry arguments. Terms that are only present with a longitudinal polarization of the target have been omitted as well as terms of the order  $\mathcal{O}(\gamma = \frac{2Mx}{Q})$  which are connected to kinematic corrections that are small at COMPASS kinematics, see fig. 2.14. The different depolarization factors  $D$  are functions of  $y$  and given as:

- $D^{\cos \Phi_h} = D^{\sin \Phi_S} = D^{\sin(2\Phi_h - \Phi_S)} = \frac{(2-y)\sqrt{1-y}}{1-y+\frac{1}{2}y^2}$
- $D^{\cos(2\Phi_h)} = D^{\sin(\Phi_h + \Phi_S)} = D^{\sin(3\Phi_h - \Phi_S)} = \frac{1-y}{1-y+\frac{1}{2}y^2}$
- $D^{\sin \Phi_h} = D^{\cos \Phi_S} = D^{\cos(2\Phi_h - \Phi_S)} = \frac{y\sqrt{1-y}}{1-y+\frac{1}{2}y^2}$
- $D^{\sin(\Phi_h - \Phi_S)} = 1$
- $D^{\cos(\Phi_h - \Phi_S)} = \frac{y(1-\frac{1}{2}y)}{1-y+\frac{1}{2}y^2}$

The subscripts of the structure functions indicate the polarization of beam and target (U unpolarized, T transverse, L longitudinal),  $\alpha$  is the fine structure constant,  $\lambda_b$  the beam helicity and  $\vec{S}_T$  the transverse polarization vector of the target.

Since the cross-section describes one hadron production, the structure functions are dependent on  $x$ ,  $z$ ,  $|P_T|$  and  $Q^2$ . In the parton picture, the dependence on  $\sin(\Phi_h - \Phi_S)$  is due to the Sivers and the dependence on  $\sin(\Phi_h + \Phi_S)$  is due to the Collins effect<sup>8</sup>.

<sup>8</sup>Note that the Collins angle is defined as  $\Phi_h + \Phi_S - \pi$ . This leads to a sign change if the structure functions are to be interpreted in the parton model.

That means that at leading twist  $F_{UT}^{\sin(\Phi_h - \Phi_S)}$  can be written as the convolution of the Sivers function with the unpolarized fragmentation function and  $F_{UT}^{\sin(\Phi_h + \Phi_S)}$  as the convolution of the transversity distribution function with the Collins fragmentation function. However, for the extraction of asymmetries this interpretation does not play a role.

Since the SSAs are orthogonal angular combinations they should not play a rôle for the extraction of Collins and Sivers asymmetries. The situation gets more complicated when considering the acceptance of the spectrometer. When measuring the SSAs the acceptance is convoluted with the cross section leading to possible correlations between the different modulations. This makes a more sophisticated treatment of the extraction necessary, which will be discussed in detail in sec. 4.6.

Considering the two hadron electroproduction cross section in the process  $l + n \rightarrow l' + h_1 + h_2 + X$  there are also several other modulations allowed. They depend on the azimuthal angles between the polarization, the angle  $\Phi_h$  of one hadron and the vector  $R_T$  as defined in sec. 2.8. However, only the modulation with  $\sin(\Phi_S + \Phi_R)$  survives after integrating out intrinsic transverse momentum [38]. The depolarization factor of this asymmetry is the same as for the Collins effect. This is because the hard scattering part of both effects is the same. They differ only in the fragmentation of the struck quark.

The extraction of Collins, Sivers and two Hadron Asymmetries from COMPASS data taken in the years 2003 and 2004 will be the topic of the analysis presented in this work.

## 3. The COMPASS Experiment

The analysis presented in the following chapters is based on data collected during the years 2003 and 2004 by the COMPASS<sup>1</sup> experiment. This experiment is set up at the end of the M2 beamline of the SPS<sup>2</sup> at CERN. COMPASS consists of a large angle (LAS) and a small angle open field spectrometer (SAS). Each part contains a dipole magnet, SM1 and SM2, respectively, a set of tracking detectors and calorimetry. Particle identification capabilities are provided by a Ring Imaging Čerenkov (RICH) detector. An extensive description of the setup can be found in [57]. Here only a brief introduction to the main components of the relevant setup, shown in fig. 3.1, will be given as far as they pertain to the analysis.

### 3.1 The Polarized Target and Beam

Due to the broad physics program, the COMPASS experiment is dedicated to, there are setups using muon and hadrons beams. The data analyzed in the following was taken with a muon beam scattering off a transversely polarized target. This configuration accounted for about 20% of the effective running time during the years 2003 and 2004. The muons, originating from the decay of pions and kaons which in turn were produced by scattering protons off a beryllium target, exhibit a natural longitudinal polarization [58]. However, as mentioned in sec. 2.9.2, this can be ignored for the purpose of this analysis. The beam exhibits a typical spill structure, reflecting 4.8s of spill extraction of protons from the SPS during a 16.8s cycle. Muons in the beam have an average energy of 160 GeV with a deviation of 3-5% [57]

To achieve a high luminosity a thick solid state target consisting of two oppositely polarized cylindrical cells is used [59]. As the target material deuterated lithium ( $\text{Li}^6\text{D}$ ) was chosen due to its favorable dilution factor and high polarizability. It can be considered to be an effective deuterium, thus isoscalar target. To estimate its dilution by non-polarizable material  $^6\text{Li}$  is treated as a three body system of  $\alpha+p+n$  from which the p,n pair is aligned with the nuclear  $^6\text{Li}$  spin 86,6% of the time. So one would expect the dilution factor to be about 50%. Considering that the target cell also contains  $^3\text{He}/^4\text{He}$  cooling mixture fluid and that it is dependent on kinematics of the scattering process, one arrives at a value of approximately  $f = 0.38$  for this analysis [51][60].

The configuration of two oppositely polarized target cells allows for the cancellation of beam flux, acceptance effects of the spectrometer and target spin independent asymmetries. To this end it is also necessary to take data with reversed target polarization.

---

<sup>1</sup>COmmon Muon Proton Apparatus for Structure and Spectroscopy

<sup>2</sup>Super Proton Synchrotron

Using the technique of dynamic nuclear polarization [61] the polarization of the target material longitudinal with respect to the beam direction is achieved.

To obtain transverse polarization the target is first brought into a stable longitudinal mode, where the spin configuration is then held frozen by cooling below 90 mK. Using a transverse dipole-magnet field of 0.5 T, the target spins are then rotated adiabatically into the desired configuration. By these techniques polarizations of about 50 % percent for the target are obtained. Compared to the longitudinal mode, the changeover to the opposite polarization configuration takes significantly longer, since a spin rotation by means of magnets is impossible and the target has to be re-polarized. Therefore it is necessary to mind possible effects due to changes over time in the spectrometer acceptance when combining data taking periods for asymmetry extraction during data analysis.

## 3.2 Particle Identification

For the extraction of single spin asymmetries it is necessary to accurately identify the particles in a SIDIS event. This section describes the parts of the spectrometer that are used for particle identification. An accurate identification of the scattered muon is necessary to reconstruct the inclusive DIS variables whereas the identification of produced hadrons by calorimetry and the Ring Imaging Čherenkov detector allows to reconstruct the SIDIS parameters of interest for different hadron types.

### 3.2.1 Muon Filters

To identify muons COMPASS has two sets of muon wall detectors. They are insulated from passing hadrons by electromagnetic and hadronic calorimeters and passive  $\mu$  filters. These consist of iron absorbers in the LAS and blocks of concrete in the SAS. Both sets of detectors are installed at the very downstream ends of the small angle and the large angle parts of the spectrometer. They allow a reliable identification of the muons, especially the scattered muon required to reconstruct the kinematic variables of inclusive DIS.

### 3.2.2 Calorimetry

COMPASS features two hadronic calorimeters which are used to discern hadrons and non hadronic background. Muons can be identified by using the muon filters described in sec. 3.2.1. While both, the large and small angle part of the spectrometer are equipped with a hadronic calorimeter only the small angle part behind the second spectrometer magnet (SM2) includes an electromagnetic calorimeter. The electromagnetic calorimeter was not fully operational during the time the data was taken, therefore it was not used for this analysis.

### 3.2.3 The RICH detector

The COMPASS RICH detector RICH-1 is a large size **R**ing **I**maging **Č**herenkov detector. With a length of about 3 m and a Volume of 80 m<sup>3</sup> filled with  $C_4F_{10}$  gas, it allows

---

for the collection of a sufficient number of Čherenkov photons due to its low chromaticity and a high refractive index. Choosing  $C_4F_{10}$  as the radiator gas makes the detection of hadrons up to momenta of about 40 GeV possible. The achieved resolutions on the Čherenkov angles of the detected photons allow to separate pions and kaons at the  $2.5\sigma$  level up to 43 GeV by a maximum likelihood method described in sec. 4.4.

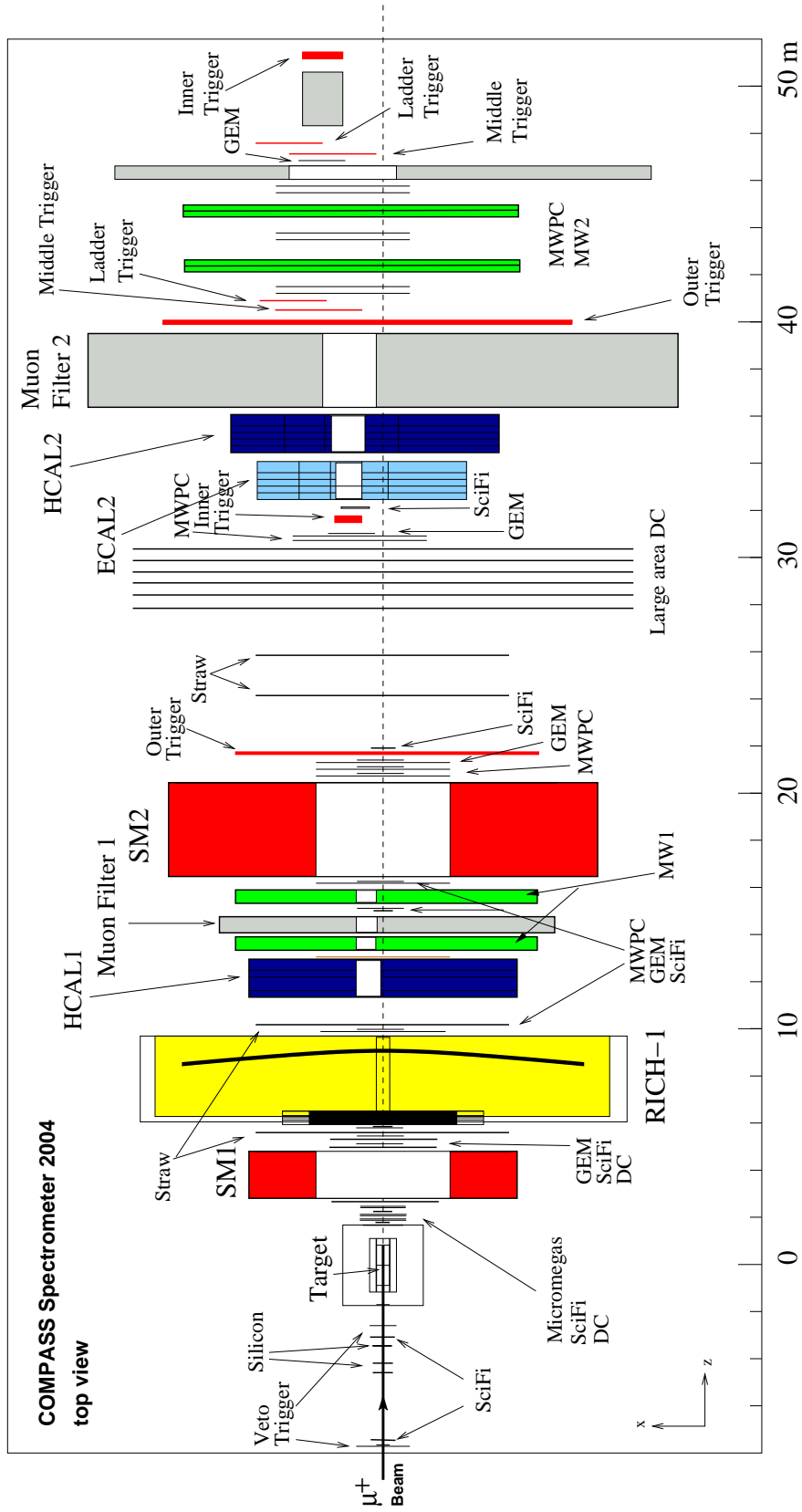


**Figure 3.1:** The COMPASS spectrometer consists of a large angle (LAS) and a small angle spectrometer (SAS). Each part contains a dipole magnet, SM1 and SM2, respectively, a set of tracking detectors and calorimetry.

## 4. Data Analysis

The extraction of Single Spin Asymmetries from the 2003-2004 transverse data is the main part of this work. This section presents the event selection and asymmetry extraction along with systematic studies.

Single spin asymmetries were extracted on four distinct samples. Collins and Sivers asymmetries were extracted on the “all hadron” and “leading hadron” sample. The first one contains all hadrons in an event, surviving specific cuts, whereas the second one constitutes a subset of these hadrons for which only the leading hadron in an event was considered. Here the term leading hadron signifies the hadron carrying the largest energy fraction from the scattering process. Accordingly, the two hadron asymmetry defined in eq. 2.56 was extracted from all hadron pairs in an event and a sample consisting only of pairs of leading and subleading hadrons. For these pairs, [39] and [62] predict an enhancement of the signal.

Furthermore, a Monte Carlo simulation of the detector was set-up and performed as described in sec. 4.3. Special attention was given to the simulation of the RICH-1 detector and the effects of the magnetic field in the target region for transverse spin configurations. This was the first time that a Monte Carlo simulation for the COMPASS setup with transverse setting was performed where both RICH-1 and target magnetic field were correctly treated.

Using accurately simulated data made the verification of the RICH-1 studies on data possible. In these studies strategies to arrive at the optimal particle identification performance based on the available data are tested. They are presented in sec. 4.4.

Simulated events were also used to investigate the performance of different methods of asymmetry extraction. Here the use of simulated events was especially important to evaluate the effects of varying acceptances on the measured asymmetries in sec. 4.6.

### 4.1 Data selection

From the data recorded a subset is selected where quality and kinematics allows reliable estimation of physical quantities. The quality criteria and kinematic cuts are the topic of the following sub-sections. They can be divided into event selection and subsequent hadron selection.

#### 4.1.1 Event Selection

The data taken with transverse target spin is divided in pairs of periods taken closely together in time with opposite target spin configuration. During each period the target

Year	Period	Target polarization
2003	P1G	$\downarrow\uparrow$
2003	P1H	$\uparrow\downarrow$
2004	W33	$\uparrow\downarrow$
2004	W34	$\downarrow\uparrow$
2004	W35	$\downarrow\uparrow$
2004	W36	$\uparrow\downarrow$

**Table 4.1:** Data taking periods. For historic reasons the periods taken in the year 2003 are named P1G and P1H according to the database slots in which they were saved. In the year 2004 a naming scheme was adapted that corresponds roughly to the week of data acquisition. For the analysis the periods P1G/P1H, W33/W34 and W35/W36 were combined.

spin was stable and corresponds to about one week of data acquisition. Target spin asymmetries are extracted for each of these pairs and then combined using the weighted mean. Table 4.1 shows the periods used for this analysis.

From these the good runs and good spills are selected. They are determined by looking at specific quality monitors [51][63][64][65][66]. From this sample deep inelastic scattering events are selected by using the cut  $Q^2 > 1 \text{ GeV}^2$  on the photon virtuality and the cut  $W > 5 \text{ GeV}$ , where  $W$  is the mass of the final hadronic state,  $W^2 = (P + q)^2$ , to avoid the region of hadronic resonances (see figure 2.3). Further cuts are made to ensure that from the hadron sample the relevant physics signal can be extracted. Requiring the relative energy in the muon scattering process  $y$  to fulfill  $0.1 < y < 0.9$  limits the corrections necessary due to radiative corrections (higher cut) but warrants that the energy loss of the scattered beam particle is high enough to allow for reliable event reconstruction (lower cut).

A track that is reconstructed in the scintillating fibers and silicons upstream of the target is considered to be a beam track originating from the incoming muon if the track time is within three standard deviations of the times measured by the beam momentum station and the trigger time [51]. Its momentum is being reconstructed in the beam momentum station. If there are several candidates a backtracking algorithm is employed. As for tracking, also for vertexing a Kalman fit is used [67]. Only so-called primary vertices that have an ingoing beam track are considered. From these the vertex with the maximum number of tracks is taken as the “best primary vertex”. If two candidates for the best primary vertex have the same number of tracks associated with them, the one with the smallest  $\chi^2$  value in the vertex fit is utilized. It is also required that this vertex lies within the target and that the extrapolated beam track crosses both target cells. This ensures equal flux for both target cells.

Among the outgoing positive tracks, additional candidates to the scattered muon tagged by CORAL are selected by requiring at least three or five hits after muon wall one or muon wall two, respectively. Furthermore, the amount of traversed material has to correspond to at least 30 radiation lengths. There has to be exactly one candidate for

the scattered muon and the reduced  $\chi^2$  for the beam and scattered muon candidate has to be less than 10, otherwise the event is discarded.

In principle candidates for the scattered muon are lost that exited the spectrometer without crossing sufficient material, a problem described in [68]. If the scattered muon passed through holes in the hadron absorbers and a particle originating in the primary vertex is mistaken for the scattered muon, the event is incorrectly reconstructed and has to be rejected. To solve this problem, tracks are extrapolated to the downstream end of the spectrometer at 50 m and cuts are made on the extrapolated  $x_e$  and  $y_e$  coordinates based on geometrical considerations. For tracks having the last hit before SM2 ( $z$  position  $< 20$  m), the cut is:

$$\sqrt{(x_e - 45 \text{ cm})^2 + y_e^2} > 10 \text{ cm} \quad (4.1)$$

If the track has its last hit after SM2

$$\begin{aligned} \sqrt{(x_e - 35 \text{ cm})^2 + y_e^2} > 15 \text{ cm or} \\ |x_e - 55 \text{ cm}| > 13 \text{ cm and } |y_e| > 3 \text{ cm} \end{aligned} \quad (4.2)$$

is required.

The laboratory coordinate system used here has its origin at the nominal target position with the  $z$ -axis pointing downstream along the beam, the  $y$ -axis upwards and the  $x$ -axis is chosen such that the coordinate system is right handed.

#### 4.1.2 Hadron Selection

For both, the one and two hadron analyses all outgoing particles of the primary vertex, that were not identified as muons in the preceding step, are considered for the hadron selection if they survive the following cuts.

- Particles have to be identified as pions or kaons as described in section 4.4.
- The amount of material traversed in the spectrometer has to be smaller than 10 radiation length.
- The last hit of the track has to be after SM1. This rejects tracks that were only reconstructed in the fringe field of SM1.
- A good resolution in the measured azimuthal angles is ensured by requiring
  - in the one hadron analysis the transverse momentum of the particle with respect to the virtual photon direction to be larger than 0.1 GeV.
  - in the two hadron analysis the size of the vector  $R_T$ , the transverse projection of  $\vec{R}$  defined in eq. 2.45 to be larger than 0.05 GeV.
- The reduced  $\chi^2$  of the fit of the particle trajectory to the detector hits has to be less than 10.

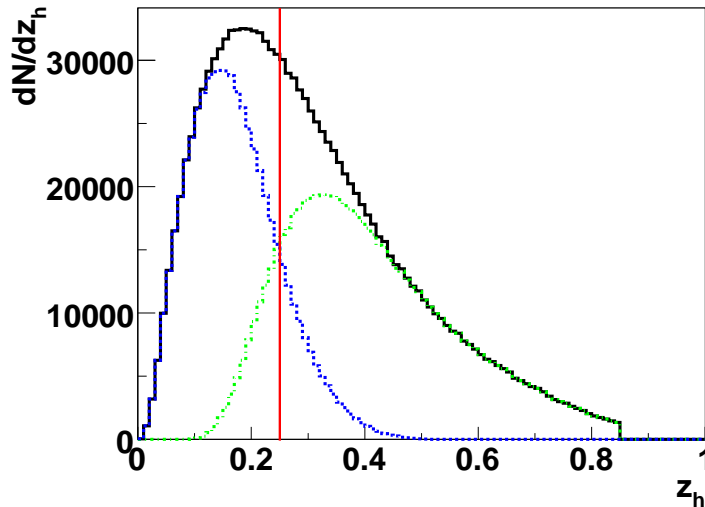


**Figure 4.1:** MC: Distributions of identified leading hadrons (black curve), correctly identified leading hadrons (dashed-dotted green curve) and incorrectly identified leading hadrons (blue dotted curve). The vertical red curve indicates the cut  $z_h > 0.25$  for the leading hadron sample.

#### 4.1.2.1 One Hadron Analysis

For the one hadron asymmetries a lower limit of 0.2 for the relative energy  $z$  of the hadron is demanded if all hadrons are considered. The underlying reasoning is that in the string fragmentation process hadrons with a higher energy are more sensitive to the properties of the struck quark spin [51][69]. Therefore the analysis is also carried out using only the leading hadron, that is the hadron with the highest  $z$  in the event. Here a lower cut of 0.25 on  $z$  is applied. Figure 4.1 shows the  $z$  distribution of leading and non-leading hadrons from Monte Carlo. For  $z > 0.25$  the fraction of leading hadrons in the sample dominates. The hadronic calorimeters are also used for the selection of hadrons. As can be seen in the responses of the hadronic calorimeter shown in figures 4.2 and 4.3 there is a contamination of non hadronic particles in the sample of hadrons which are left after the above cuts were applied. This contamination is removed by requiring that if a cluster in one of the hadronic calorimeters is associated with a track of a hadron candidate, the cluster energy has to be above the threshold indicated and the cluster has to be unique, i.e. there is no other cluster associated with the same track. Due to the limited acceptance of the calorimeters, particles with no associated clusters in either calorimeters are also considered to be hadrons. In the leading hadron analysis the calorimeters are also used to discard events with neutral particles that are potentially leading but for which a track cannot be reconstructed. To this end, clusters are searched for in the calorimeters without an associated track. If the maximum energy of the leading hadron in the event is smaller than the energy of the found cluster with

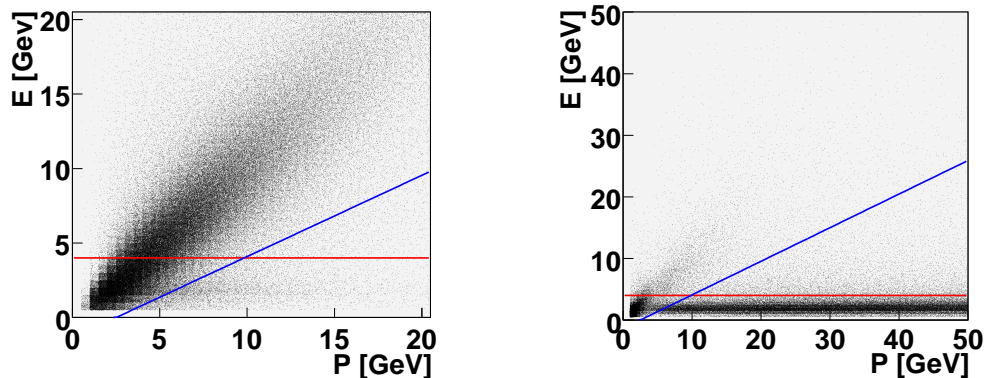


**Figure 4.2:** Correlation between energy measured in HCAL1 and momentum measured in the spectrometer for all outgoing particles of the primary vertex (left) and for particles tagged as muons (right). In blue the cut of the two hadron analysis, in red the cut of the one hadron analysis.

two times the resolution of the cluster energy subtracted, it is assumed that a neutral hadron in the event has been the leading particle and the event is skipped.

#### 4.1.2.2 Two Hadron Analysis

For the two hadron correlation the cut on the relative energy of the hadrons is  $z_1, z_2 > 0.1$  and in addition  $z_1 + z_2 < 0.9$  to avoid the kinematic region of exclusive meson production. In correspondence to the leading one hadron analysis, the leading two hadron analysis uses additionally a cut of  $z_1 + z_2 > 0.25$ . Since the cut on  $z$  is lower than for the one hadron analysis there is a considerable amount of soft pions that would be cut away by the constant cut described previously. Therefore a linear cut is applied as indicated in figs. 4.2 and 4.3. The selection of the leading hadron pair is analog to the selection of the leading hadron.

## 4.2 Kinematic Distributions

After the cuts described previously for the all hadron analysis were applied the remaining events cover the kinematic range in the  $Q^2, x_{Bj}$  domain as shown in fig. 4.4.

### 4.2.1 One Hadron Analysis

The spectra of the transverse momentum of the produced hadron and the relative energy transfer of the scattered muon  $y$  are shown in figs. 4.5 and 4.6. Figures 4.11 and 4.12 illustrate the distribution of the factor  $D^{\cos(\Phi_h + \Phi_s)}$ , which is the depolarization factor employed in the Collins and two-hadron analysis. It is a function of  $y$  and therefore correlated with  $x_{Bj}$  in an event.

The spectrum of the relative momentum fraction  $z$  is shown in fig. 4.7. It does not show an excess of exclusively produced particles.

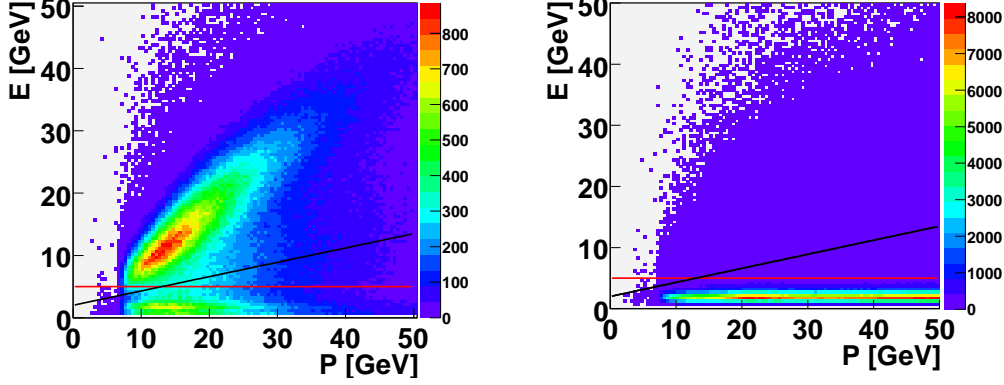


**Figure 4.3:** Correlation between energy measured in HCAL2 and momentum measured in the spectrometer for all outgoing particles of the primary vertex (left) and for particles tagged as muons (right). In black the cut of the two hadron analysis, in red the cut of the one hadron analysis.

#### 4.2.2 Two Hadron Analysis

At variance to the one hadron case, the distribution of the sum of the  $z$  of the hadron pairs in the two hadron analysis (fig. 4.8) shows a peak due to exclusively produced particles which decay. This motivates the cut on  $z_1 + z_2 < 0.9$ . Figure 4.9 shows the distribution of  $R_T$  and fig. 4.13 the distribution of the angle  $\theta$  for all hadron pairs. The importance of  $\theta$ , which is the polar angle in the center of mass system of the hadron pair is explained by the partial wave expansion explained in sec. 2.8.1, because at COMPASS kinematics, the two hadron interference fragmentation function  $H_1^{\triangleleft}$  is modulated with  $\sin \theta$ . The distribution observed, shows, that COMPASS is sensitive to the part  $H_{1,ut}^{\triangleleft,sp}$  of the two-hadron interference fragmentation function and that the signal is even enhanced by the COMPASS acceptance as compared to a flat acceptance. A flat  $\sin \theta$  distributions might lead to a cancellation of the effect since the counts used in the extraction of the asymmetry are integrated over  $\theta$ . The invariant mass spectra for the two-hadron analysis are shown in fig. 4.10. In the  $K^+K^-$  and  $\pi^+\pi^-$  spectra the peaks corresponding to the  $\rho$  and  $\phi$  vector mesons can be seen clearly. On the other hand the  $K^*$  peak can be seen in the combinations  $K^+\pi^-$  and  $\pi^+K^-$ . However, due to the low cut on  $z$ , the background below the vector meson resonances is higher than for the cuts used in the one hadron analysis. For this case the mass region around the  $\rho$  is shown in fig. 4.19. Since models for  $H_1^{\triangleleft}$  predict a signal for the interference of a vector meson resonance with non-resonance background, the invariant mass distributions are important for a prediction of the size of such an effect.

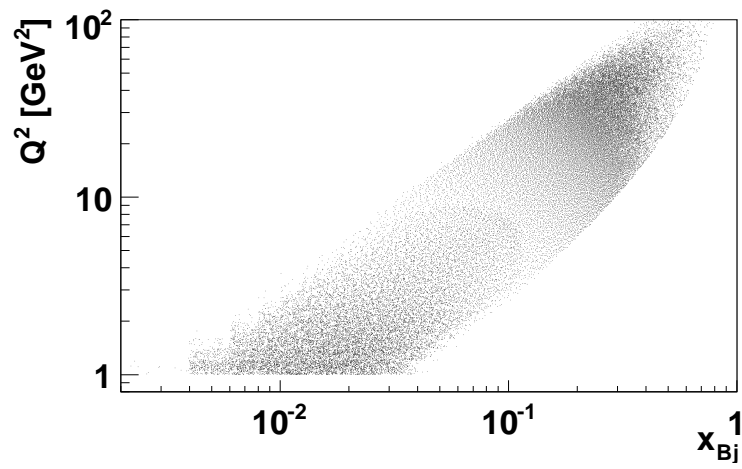


Figure 4.4:  $Q^2$  vs.  $x_{Bj}$  distribution of the all one hadron sample

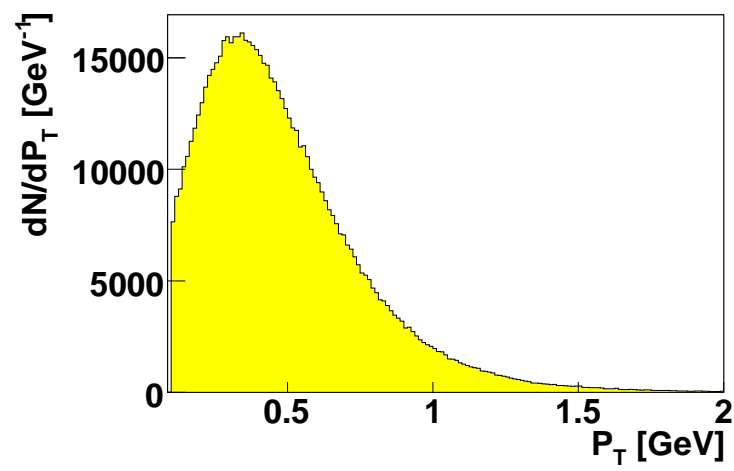


Figure 4.5:  $P_T$  spectrum of the all one hadron sample

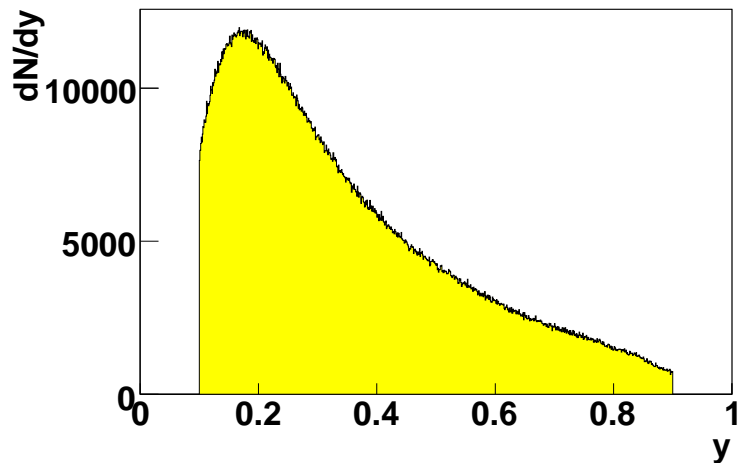


Figure 4.6:  $y$  spectrum of the all one hadron sample

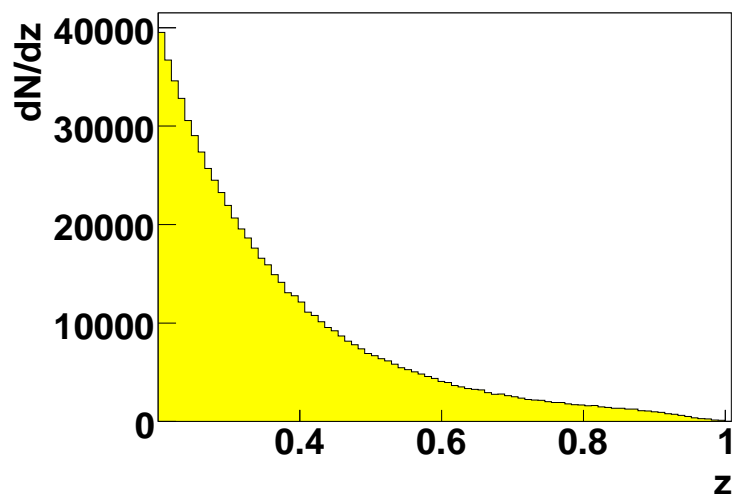
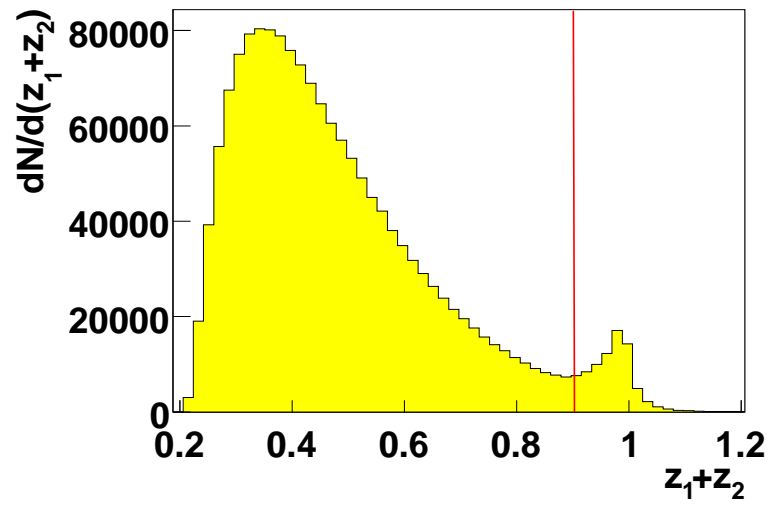
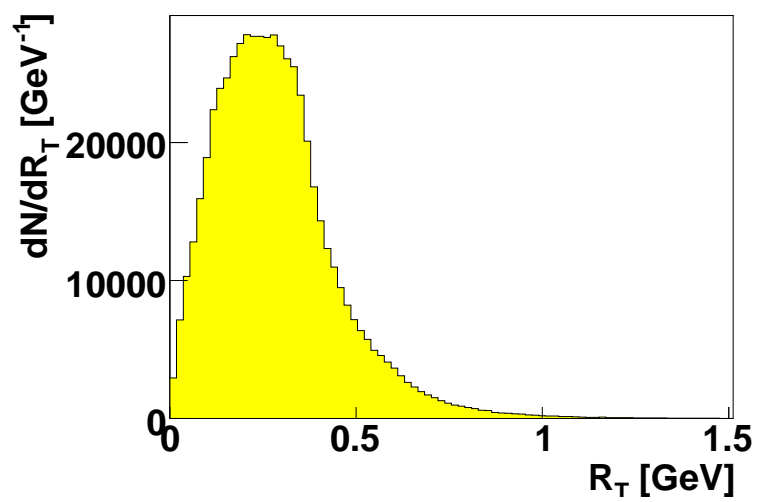


Figure 4.7:  $z$  spectrum of the all one hadron sample



**Figure 4.8:** Distribution of sum of  $z$  of the hadron pair before  $z_1 + z_2$  cut. This cut is indicated by the red line.



**Figure 4.9:**  $R_T$  spectrum

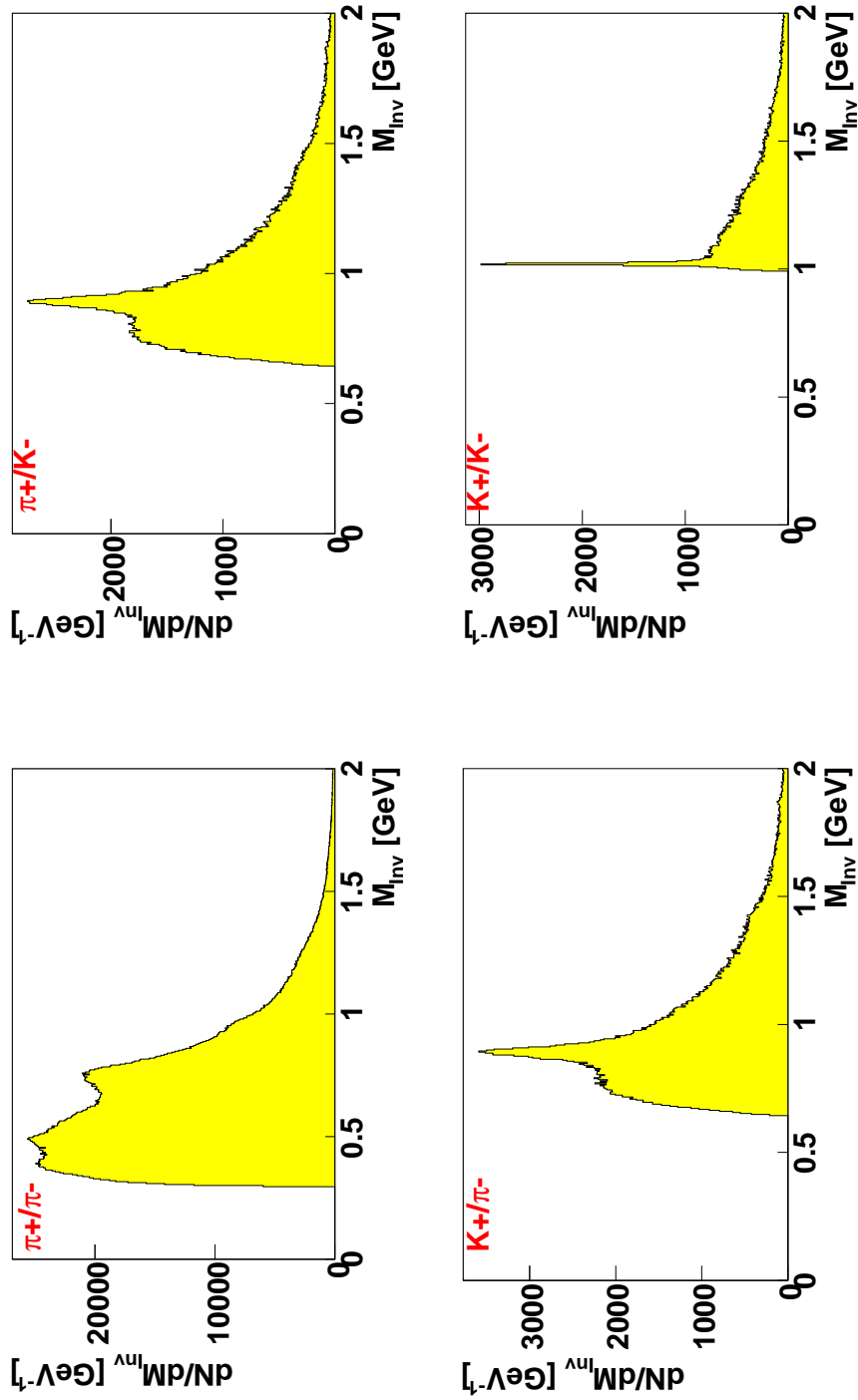


Figure 4.10: Invariant mass spectrum of the two hadron analysis for different particle combinations

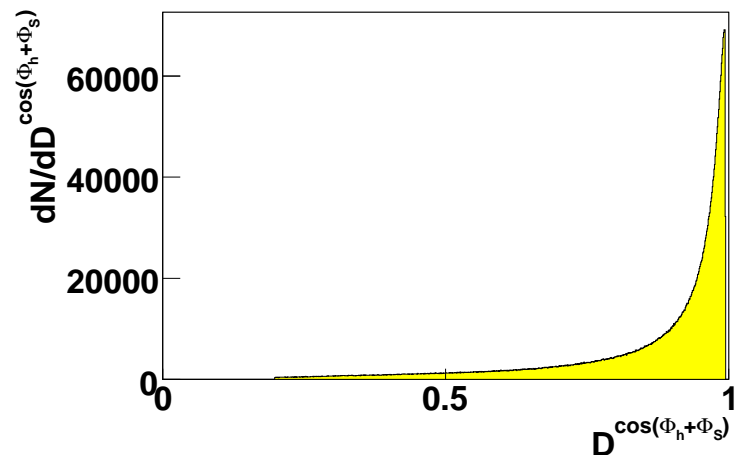


Figure 4.11:  $D^{\cos(\Phi_h + \Phi_s)}$  spectrum of the all one hadron sample

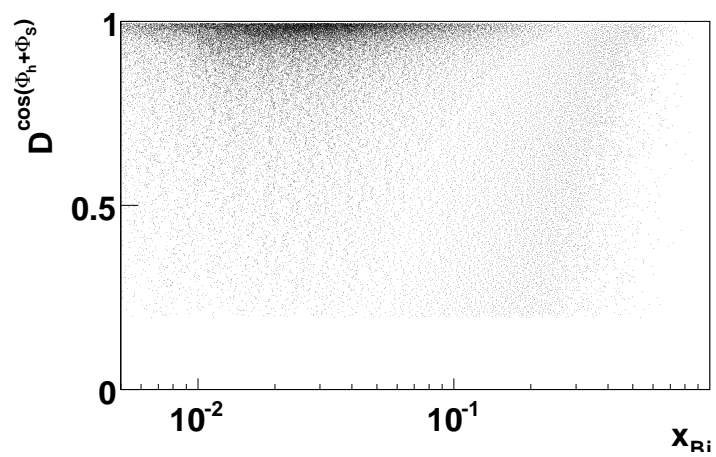
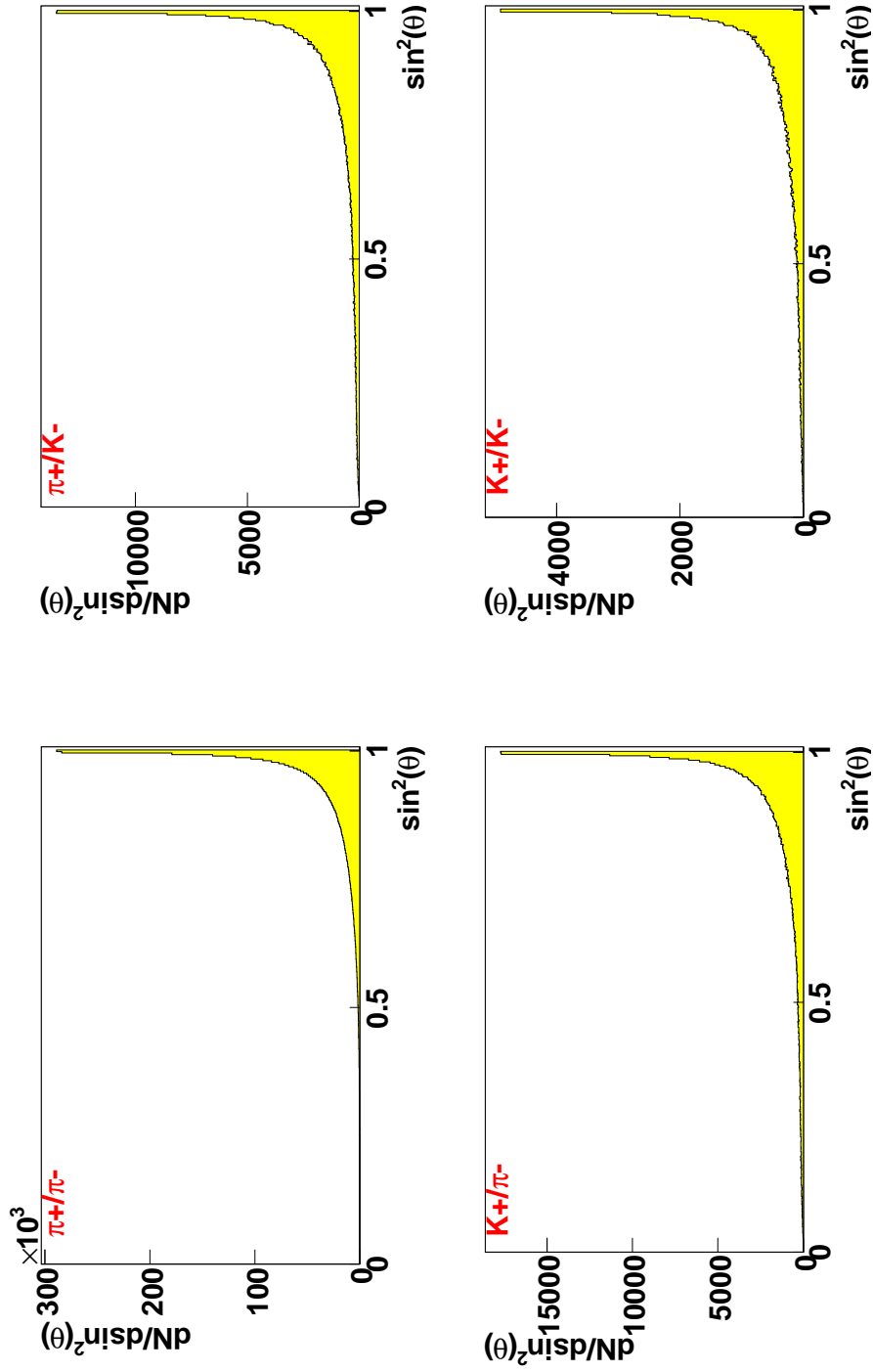


Figure 4.12:  $D^{\cos(\Phi_h + \Phi_s)}$  Vs.  $x_{Bj}$  distribution of the all one hadron sample



**Figure 4.13:** The  $\sin^2(\theta)$  spectrum for different particle combinations. Since  $|d \cos \theta| = |\sin \theta d \theta|$  it gives the distribution of the  $\theta$  dependent factor in the partial wave expansion of  $H_{1,ut}^{\langle \lambda, sp \rangle}$ .

### 4.2.3 Statistics of the One Hadron Analysis

As an example for the effect of the various cuts, the tables 4.2-4.4 show the fraction of events and particles left after each cut for the data taken in weeks 35/36. Tables 4.5 and 4.6 show the number of events left for each data taking period used in this analysis.

Cut	events/ $10^7$	fraction left
No cut	1.49869	1
With best primary vertex	1.49869	1
Beam found	1.49221	0.99
Scattered muon found	1.35197	0.90
$Q^2 > 1 \text{ GeV}^2$	1.35059	0.90
$W > 5 \text{ GeV}$	1.26815	0.84
$0.1 < y < 0.9$	1.22928	0.82
Cross cell	0.939278	0.63
Vertex in target	0.831625	0.55

**Table 4.2:** Events statistics for the period W35-36

Cut	particles/ $10^7$	fraction left
Number of particles	2.02403	1
Material traversed	2.00682	0.99
Track quality	1.95623	0.97
Hits after SM1	1.8905	0.93
$P_T > 0.1 \text{ GeV}$	1.63562	0.81
$z < 1$	1.63503	0.81
$z > 0.2$	0.528004	0.26
Cluster energy in HCAL	0.494642	0.24
Pos. hadrons.	0.271168	0.13
Neg. hadrons	0.223474	0.11

**Table 4.3:** Hadron statistics for the period W35-36; the initial number of particles in the first row is after the application of cuts of table 4.2.

Cut	pos. particles	fraction left	neg. particles	fraction left
Number of particles	2.71168 $10^6$	1	2.23474 $10^6$	1
No RICH information	133387	0.049	105805	0.047
Identified as pions	2.08439 $10^6$	0.769	1.79618 $10^6$	0.803
Identified as kaons	411383	0.151	275053	0.123
Protons	82520	0.030	57702	0.026
Pions after cuts	2.02902 $10^6$	0.748	1.755 $10^6$	0.785
Kaons after cuts	360924	0.133	235140	0.105

**Table 4.4:** RICH statistics for the period W35-36; the initial number of particles in first row is after the application of cuts of table 4.3.

Period		All $\pi$ sample		Leading $\pi$ sample	
		pos. $\pi/10^6$	neg. $\pi/10^6$	pos. $\pi/10^6$	neg. $\pi/10^6$
2003	P1G/P1H	1.71138	1.48719	1.09893	0.92631
2004	W33/W34	1.53985	1.33044	0.98499	0.82454
2004	W35/W36	2.02902	1.755	1.29858	1.08878

**Table 4.5:** Final statistics for pions for the years 2003, 2004

Period		All K sample		Leading K sample	
		pos. K.	neg. K.	pos. K.	neg. K.
2003	P1G/P1H	310937	203908	236133	143780
2004	W33/W34	273133	177190	208317	125122
2004	W35/W36	360924	235140	274771	165873

**Table 4.6:** Final statistics for kaons for the years 2003, 2004

#### 4.2.4 Statistics of the Two Hadron Analysis

In the following tables the statistics are given for the identified two hadron analysis compared with the statistics for the corresponding unidentified two hadron case for the observed 3 periods (P1G/P1H, W33/W34 and W35/W36).

	Unidentified	$\pi$ - $\pi$	%	$\pi$ -K	%	K- $\pi$	%	K-K	%
P1G-P1H	1802571	1236359	68,6	78123	4,3	101043	5,6	28210	1,6
W33-W34	1508689	1076871	71,4	68477	4,5	87036	5,8	24973	1,7
W35-W36	1953694	1416340	72,5	90885	4,7	115561	5,9	33053	1,7
Total	5264954	3729570	70,8	237485	4,5	303640	5,8	86236	1,6

**Table 4.7:** Statistics for all identified hadron-pairs in comparison with the statistics for the unidentified case.

#### 4.2.5 Statistics for the leading Two Hadron Analysis

Table 4.8 and table 4.9 give the statistics for the leading two hadron analysis.

	$\pi^+/\pi^-$	$\pi^-/\pi^+$	$\pi^+/\pi^+$	$\pi^-/\pi^-$	$\pi^+/K^-$	$\pi^-/K^+$	$\pi^+/K^+$	$\pi^-/K^-$
P1G/P1H	301675	296050	175346	138082	11810	14996	9358	6045
W33/W34	274313	268435	158017	122707	10819	13268	8241	5285
W35/W36	361785	353555	206960	162233	14278	17376	11093	7075
Total	937773	918040	540323	423022	36907	45640	28692	18405

**Table 4.8:** Statistics for leading  $\pi/\pi$  and  $\pi/K$  pairs

	$K^+/\pi^-$	$K^-/\pi^+$	$K^+/\pi^+$	$K^-/\pi^-$	$K^+/K^-$	$K^-/K^+$	$K^+/K^+$	$K^-/K^-$
P1G/P1H	43532	31582	25252	14738	10569	9536	1692	906
W33/W34	38414	28541	22390	12930	9397	8822	1445	734
W35/W36	51536	37816	29629	16783	12548	11455	2020	1051
Total	133482	97939	77271	44451	32514	29813	5157	2691

**Table 4.9:** Statistics for leading  $K/\pi$  and  $K/K$  pairs

### 4.3 Monte Carlo Simulation

The term 'Monte Carlo simulation' or just Monte Carlo (MC) for short, in this context designates the simulation of a number of events whose properties are random variables,

reflecting the quantum mechanical nature of the underlying processes. The corresponding probability densities are taken from calculations where possible, otherwise from models tuned on data. For example, parton distribution functions are parametrized using experimental data from a multitude of experiments, see e.g. [8][70]. In contrast, contributions at the hard scale can be calculated at fixed order. In a second step, the events are then propagated through the detector, giving rise to detector responses, which are in a third step used as inputs to the event reconstruction. The whole process is often called 'Monte Carlo chain' even though 'Monte Carlo' in the name designates only the use of Monte Carlo techniques in the computation, e.g. integration. Since the detector response can be treated exactly as the detector response during real data taking, simulated data allows the verification of the reconstruction algorithms and the comparison between physics inputs and measured signals. Thus MC has become an essential tool in the understanding of experimental data. It is basically the only viable way to study complicated cuts in phase space. These cuts in the phase space of the process under study come about due to limited acceptances and efficiencies of the spectrometer.

### 4.3.1 Event Generation

For the generation of deep inelastic scattering events two different generators were used: LEPTO [71][72] and PYTHIA[73]. Both event generators use leading order matrix elements to determine the cross-section of the elementary hard lepton-quark scattering. Since this is a simple event topology at an energy high enough to apply perturbative techniques a computation from first principles is possible, taking the measured parton distribution functions (PDFs) into account. PDFs are determined by global fits to experimental data. Necessary evolution in  $Q^2$  is done using the DGLAP equations. The detailed event topology including initial and final state radiation is created by using heuristic approaches like parton showers and backward evolution, since an approach from first principles by matrix elements would lead to computational intractable problems. Sudakov factors, determining the splitting of the partons within a parton shower, are again computed with the DGLAP kernels. Lastly the fragmentation and decay into observable hadrons is modeled.

Both LEPTO and PYTHIA use the Lund string model for the later process as implemented in the formerly separately published program JETSET [69]. The Lund string fragmentation model is very popular and widely used to model the fragmentation process. Among its main hallmarks are collinear and infrared safety. Basics of the string model stem from a quite intuitive picture grounded in the confinement property of QCD. After the scattering there exists a number of colored quarks generated in the final and initial state radiation in the parton showers and from the target remnant. Depending on the struck parton, the parton remnant can be treated as a diquark object, or a quark plus diquark. Produced quarks are connected by so-called color flux tubes. This tube like configuration is again dictated by the confinement properties of QCD. And the string constant, i.e. the amount of energy per unit length within these tubes is determined to be about  $\kappa \approx 1\text{GeV}/\text{fm}$  by hadron spectroscopy experiments. The value of  $\kappa$  effectively corresponds to a 'mass density' along the string [73]. As the  $q$  and  $\bar{q}$  move apart, the potential energy stored in the string increases, eventually leading to the

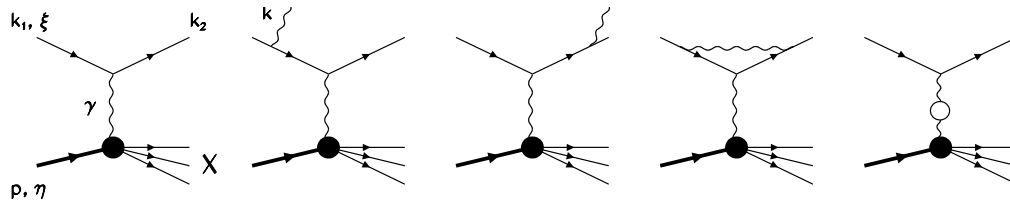


**Figure 4.14:** Feynman diagrams contributing to the Born and radiative corrected cross-sections in lepton-nucleon scattering. The letters denote the four-momenta and polarizations of corresponding particles. Figure taken from [74]

creation of another  $q\bar{q}$  pair. This process is repeated as long as the invariant mass of the string is big enough and only colorless, on-shell mesons remain, each corresponding to a small string with a quark at the one end and an antiquark at the other. Their mass is generated by the field strength of the remaining string. The required distance between the quarks is achieved in the Lund model by evoking the idea of quantum mechanical tunneling. This leads to a flavor invariant transverse momentum spectrum for the  $q\bar{q}$  pairs and a suppression of heavy quark production of  $u : d : s : c \approx 1 : 1 : 0.3 : 10^{-11}$  [73]. For the creation of baryons, more complicated processes have to be evoked. One example is the 'popcorn' scenario, where diquarks as such do not exist but quarks and antiquarks are produced one after another and then form hadrons [69]. For the analysis presented here baryons do not play a major role. The specific parameters of the model are tuned such that it is consistent with fragmentation functions measured mainly in  $e^+e^-$  collisions.

In the end, the output of the event generator is a list of produced hadrons together with the corresponding kinematics.

For this analysis, the event kinematics of the respective MC-generator were corrected with RADGEN to observe the possible radiation of a real photon in the initial or final state [74][75]. Otherwise the radiative tails from the elastic and quasi-elastic peaks and the continuous spectrum would not be reproduced correctly. Furthermore RADGEN incorporates loop corrections coming from effects of vacuum polarization and exchange of an additional virtual photon. The Feynman diagrams corresponding to the corrections of the born cross-section are shown in fig. 4.14.

Since MC generators are original work these results are not necessarily identical to what is present in real physics data and the results should be treated with care. However, the given generators have been extensively tested with the COMPASS experimental setup e.g. [76][77] and the agreement of simulated events with data is satisfactory in the relevant kinematical domain and for attributes important to the PID as illustrated in fig. 4.15.

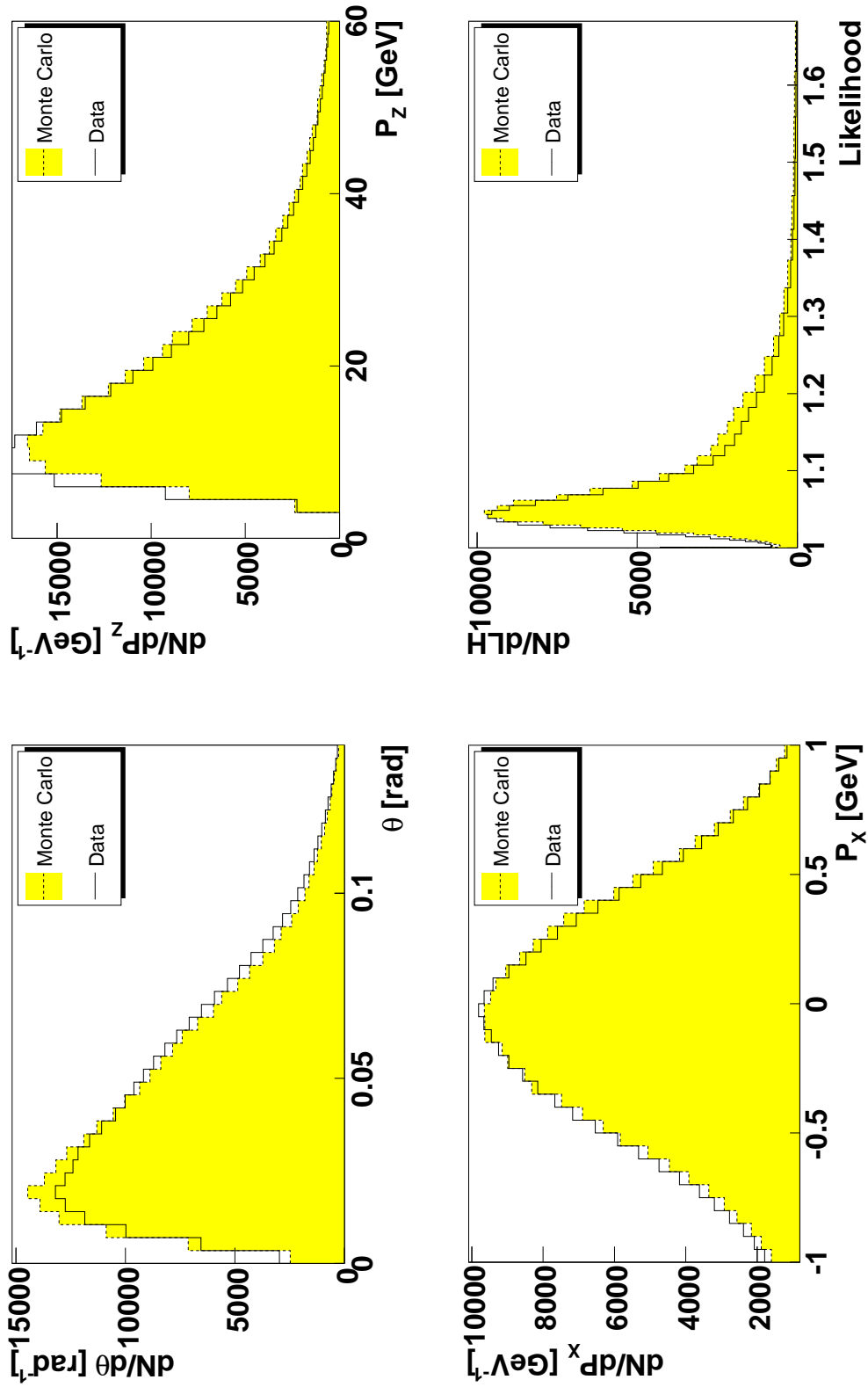


**Figure 4.15:** Comparison of data and Monte Carlo for values important to the PID: Polar angle  $\theta$ , longitudinal momentum  $P_z$ , transversal momentum in x-direction  $P_x$ , and kaon likelihood for hadrons after cuts for the “all hadron” analysis.

### 4.3.2 Detector Description and Particle Propagation

Detector description and particle propagation were done using COMGEANT [78]. This is an interface to GEANT3.21 which was adapted to the COMPASS experiment [79][80]. GEANT<sup>1</sup> is a system of detector description and simulation tools which has become the de-facto standard for high energy experiments and in other fields where the passing of particles through material has to be simulated. GEANT takes the geometry and the initial set of particles as input. Then the software tracks the particles through the material given by the detector setup description by sampling the free path from the mean free path length for each possible physical process in the respective material. The particle is then moved by the determined distance and the interaction simulated by computing energy loss, creating new particles etc. Multiple scattering and magnetic fields are taken into account when moving the particle. If one of the particles hits active detector material, information required to produce the detector signal has to be recorded. Examples are the amount of deposited energy and the exact position of interaction from which the electronics channel can be inferred. In the end enough information for the digitization of the simulated events is available. The output of this complicated simulation of the geometry implemented by COMGEANT is saved to so-called ZEBRA files [81], which can then be read by the COMPASS reconstruction software CORAL described in the next section. It is a modular software package combining the knowledge about the actual electronics and provides a digitization step. Thereafter the flow of the simulated data through the software is exactly the same as for real data. This allows to treat the simulated data in exactly the same way and use the same tools as with real data. The addition of generator information, the so-called MC-truth, allows verification of reconstruction and analysis steps.

Putting the actual digitization of the MC-chain into the reconstruction and not the simulation software allows to test different digitalizations without redoing the time consuming particle tracking through the detector. As an example, the efficiency of the RICH-1 CsI photocathodes had to be chosen as to reproduce real data, specifically the number of photons detected per event. Since these efficiencies are an input to the reconstruction software, several configurations could be tested without redoing the simulation.

### 4.3.3 Reconstruction

The reconstruction software CORAL<sup>2</sup>[82] combines analysis routines needed to construct events from detector input, real data or MC. These are for example the vertex reconstruction, beam reconstruction, particle identification and tracking. The reconstruction scheme for real and MC data is shown in fig. 4.16. After the digitization or decoding for Monte Carlo or real data, respectively, reconstruction of tracks and momentum of particles takes place. Several competitive track reconstruction programs have been used in COMPASS. The RECON algorithm taken from the precursor experiment SMC [83], the program for Track Finding and Fit in COMPASS (TRAFFIC) and also a cellular automaton [84]. For all algorithms, the COMPASS environment provides

---

<sup>1</sup>GEometryANdTracking

<sup>2</sup>COmpass REconstruction and AnaLysis software

a challenge due to its geometry aimed to provide large angular acceptance. Because of this requirement the first spectrometer magnet SM1 was constructed with a large gap size, thus causing a strong fringe field in the area around the magnet. The presence of the magnetic field of the target solenoid complicates the task of tracking even more. This is especially true for the algorithms using straight line models. In the end a modified version of TRAFFIC was adopted, combining the original algorithm with a track look-up-table called “Dico”. This new algorithm got the name TRAFFDiC and provides excellent performance [85]. Where possible, straight line segments are used to fit particle tracks in different projections. The use of projections is mandated by the fact, that most tracking detectors do not give information about space-points but only points in a specific two-dimensional projection. Track segments of several projections are combined to a representation in space and then connected in a bridging step. For fitting and track parameter estimation Kalman filter and fit methods are used where possible [86]. Kalman fitting was also used for the vertexing in CORAL. Where necessary, e.g. to bridge over difficult regions, the track parameters were determined with the help of the dictionary.

#### 4.4 PID with RICH-1

The sample of charged hadrons selected so far consists mainly of Pions and Kaons. To separate them, the output of the Ring Imaging Čerenkov detector RICH-1 is utilized by the reconstruction software RICHONE, which is part of CORAL. Depending on its velocity, a charged particle will emit Čerenkov radiation if its velocity is above the Čerenkov threshold, that is above the speed of light in the radiator. For a particle of mass  $m$ , and radiator refractive index of  $n$  the momentum threshold can be computed as  $m/\sqrt{n^2 - 1}$ . Using the nominal values of RICH-1, pions and kaons have a velocity above this thresholds for momenta greater then 2.6 GeV and 9.1 GeV respectively. They then emit radiation under an angle  $\Theta$  which is dependent on the velocity  $\beta$  of the particle and the refractive index  $n$  of the medium with the relation

$$\cos \Theta = \frac{1}{n\beta}. \quad (4.3)$$

Together with the momentum obtained by the track curvature measured in the spectrometer the mass of the particle can be determined. For 7eV photons the nominal refractive index of the radiator gas  $C_4F_{10}$  is 1.0015 at nominal conditions. It is dependent on the pressure and temperature of the gas, which can change slightly [77][87]. Also, contaminations of the gas degrade and change the optical properties. However, due to the improved temperature and pressure monitoring and sophisticated cleaning procedures, computation of the refractive index could be substantially improved for the data used in this analysis [57]. In a data preproduction step the real refractive index is computed from pions in saturation ( $\beta \approx 1$ ) from data samples distributed evenly in time. For the final production these values are corrected based on the measured gas properties. Since the real refractive index is only known after a production, the particle likelihoods, which are used for PID, are saved together with their derivatives with respect to the refractive index. For an analysis of a first production these derivatives are then used to correct the likelihoods. Thereafter the values of the refractive index vary

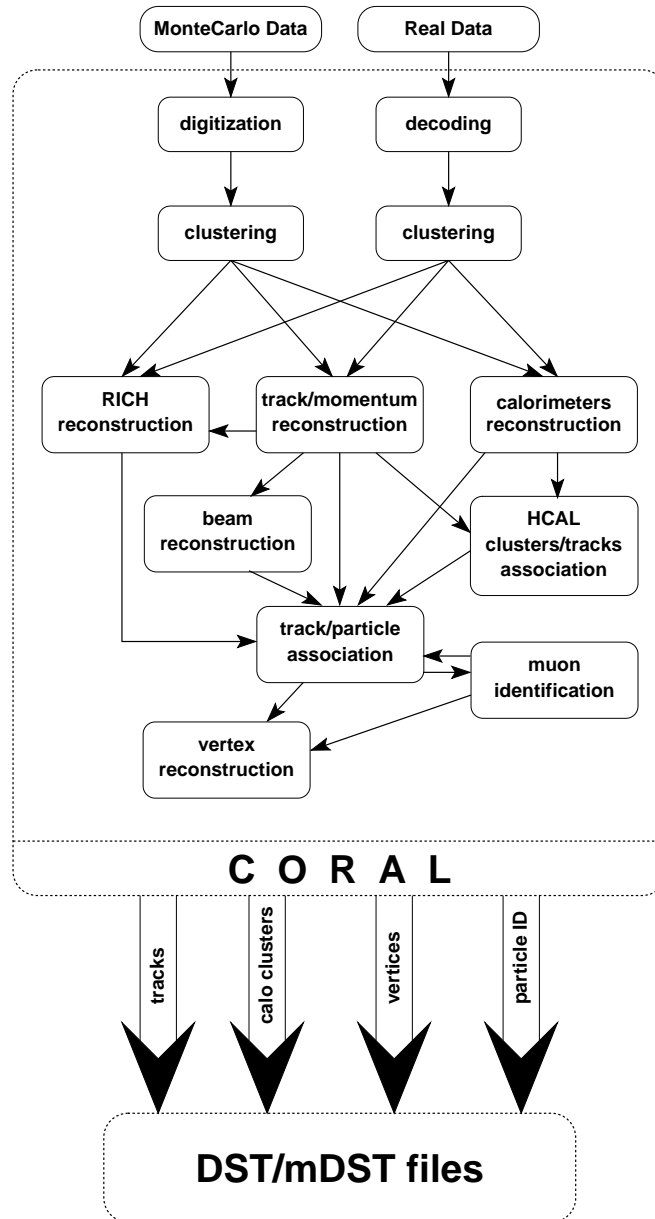


Figure 4.16: CORAL reconstruction scheme from [57]

only very little from the actual values, on the 0.5% level. So errors introduced by using the linearly corrected values for the particle likelihoods are negligible. Data taken in 2003 used in this analysis has been reproduced so that the real refractive index could be used for the new production. For data taken in 2004 small run by run variations are corrected by using the above mentioned derivatives.

For a fixed refractive index the mirror geometry is such, that photons emitted under a polar angle  $\Theta^{\text{photon}}$  from a particle track lie on concentric circles on the photon detector surface. The position of the ring depends on the angle of the incoming track. That means also, that the detector surface limits the angular acceptance of RICH-1.

After a Hough transformation to the  $\Theta^{\text{photon}}, \phi^{\text{photon}}$  plane, where  $\phi$  is the azimuthal angle of the emitted photon relative to the particle direction, the photons belonging to the same particles lie on lines, the photons belonging to the same ring can be found by looking for peaks in the projection on  $\Theta^{\text{photon}}$ . A Gaussian distribution around  $\Theta^{\text{ring}}$  is a reasonable signal description in the  $\Theta^{\text{photon}}, \phi^{\text{photon}}$  plane for fixed  $\phi^{\text{photon}}$ , if  $\Theta^{\text{ring}}$  is the expected polar angle for a given mass hypothesis [88].

For a fixed  $\Theta^{\text{photon}}$  the width of the Gaussian  $G$  is dependent on  $\phi^{\text{photon}}$  and  $\beta$ . Together with the background parametrization  $B$ , the likelihood function for a given mass hypothesis can therefore be written as

$$L_N^{\text{photon}} = \prod_{k=1}^{N^{\text{photon}}} \left[ (1 - \epsilon)G(\Theta_{\text{rec},k}^{\text{photon}}, \phi_{\text{rec},k}^{\text{photon}}) + \epsilon B(\Theta_{\text{rec},k}^{\text{photon}}) \right]. \quad (4.4)$$

In order to compare likelihood values of different particles, the normalized likelihood  $L = \sqrt[N^{\text{photon}}]{L_N^{\text{photon}}}$  is introduced.

An accurate calculation of the likelihood of a given mass hypothesis requires an adequate background description. This is not an easy task, since in addition to the electronics noise, which can be assumed to be distributed evenly on the detector surface, there are a number of other background sources. For example Čerenkov photons emitted by other particles of the same event and recorded because of the memory time of the photon chambers and the beam halo. For these sources the description is not so evident and background models had to be extracted from data and MC. In turn this background description can be used in the description of the RICH-1 detector during simulation. Figure 4.17 shows the reconstructed Čerenkov angles versus the particle momentum. Pion, kaon and proton bands are clearly visible. In order to identify a given particle the likelihood for the different mass hypotheses  $\pi$ ,  $K$  or proton is calculated with eq. 4.4. based on the incoming track parameters [88][89]. For this analysis only hadrons identified as pions and kaons were used. Of course the likelihoods do have an error associated with them. Since it is difficult to evaluate it from first principles, the decision boundaries, or cut values, are chosen such, that a figure of merit (FOM) is maximized on a sample for which the real particle identity is sufficiently well known. This will be addressed in the next section.

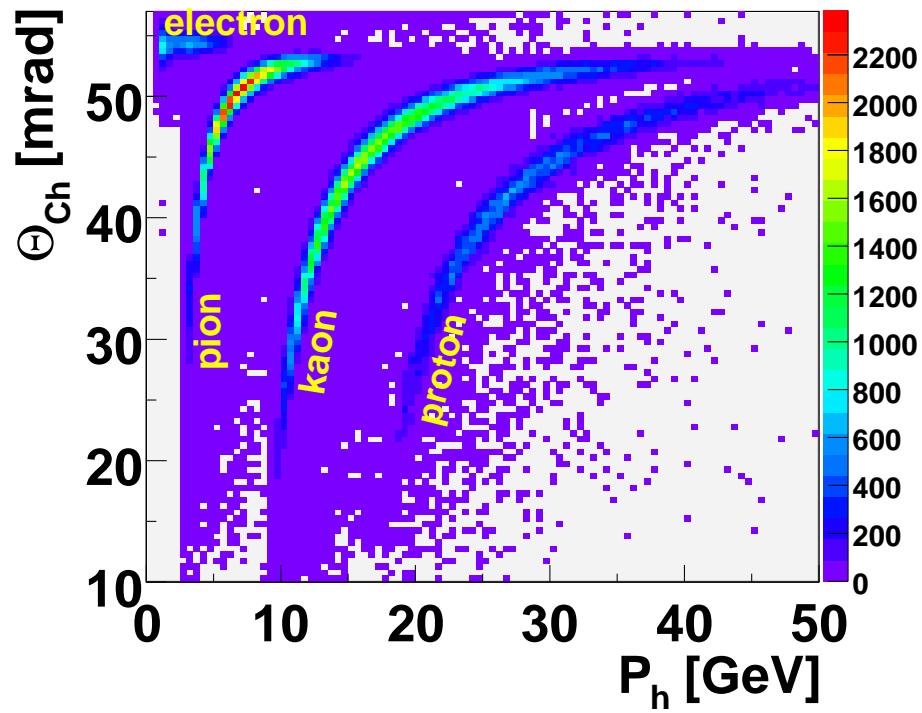


**Figure 4.17:** The correlation of the reconstructed Čerenkov angle with the measured momentum for pions, kaons, protons and electrons. The pion band is suppressed by a factor of 10 and the proton band is enhanced by a factor of 6, also the criteria for the identification are different than the ones used for the analysis. Figure from [90]

#### 4.4.1 Introduction to the Search for Optimized Cuts for PID

For optimal particle identification performance with RICHONE, a set of cuts  $\vec{c}$  has to be found that optimize the particle identification rate with respect to charged pions and kaons. This subsection sketches the strategies explored to find optimal attributes to which cuts can be applied and the optimal cut values. The objective function that has to be maximized is chosen as

$$f(\vec{c}) = S(\vec{c}) \cdot \frac{S(\vec{c})}{S(\vec{c}) + B(\vec{c})}. \quad (4.5)$$

For a fixed number of charged particles passing RICH-1, the signal  $S(\vec{c})$  is defined as the number of particles correctly identified. Accordingly, the background  $B(\vec{c})$  is the number of misclassified particles when applying the cuts  $\vec{c}$ . Then the figure of merit is the fraction of signal events times the number of signal events as defined in eq. 4.5. It is a trade-off between the demand for a high signal purity on the one hand, and a high efficiency on the other hand. The curves in 4.18 show the trade-off of these two indicators for the case of a multivariate method for PID. Two different sets of attributes were used, which will be explained later. Examples for multivariate methods are neural networks and decision trees.

In addition to multivariate methods a more traditional cut optimization method was used, where for the most relevant, physical motivated cuts a grid search is employed. In the following, these two strategies for optimal PID cuts will be described.

#### 4.4.2 Data Sets

In order to investigate the performance of the PID, it is necessary to correctly label signal and background events. There are two strategies for this. Firstly, using the Monte Carlo data described in sec. 4.3, for which the real PID is known, and secondly using known physical processes. In the last approach, the  $\rho$  and  $\phi$  resonances in the invariant mass spectrum of two particle combinations are taken as signal events for pions and kaons, respectively, because the  $\rho$  meson decays almost always into  $\pi^+\pi^-$  and the  $\phi$  into  $K^+K^-$ . The data used was taken in 2004 during the periods W33 and W34 and the same cuts as used for the all hadron analysis were applied. To obtain a purer sample, it is possible to use exclusive events. Results obtained from the exclusive samples have been found to be compatible with the results from non-exclusive data. However, since the analysis uses semi-inclusive events where the dependence on the azimuthal angles of spin and hadrons is different from the semi-inclusive case [91] the PID was optimized on non-exclusive sample. This ensures that the background and the kinematics will be similar.

#### 4.4.3 Attribute Selection

A priori, the set of attributes to which the cuts  $\vec{c}$  are applied in order to maximize  $f(\vec{c})$  is unknown and has to be found. However, the likelihoods computed according to eq. 4.4 are supposed to contain all the knowledge that can be obtained from the kinematical variables and the RICH-1 signal. In order to investigate if the signal quality can be

improved, by augmenting the number of parameters on which cuts are defined, well established strategies are followed. The general approach is described in [92]. Here only a brief description based on MC data is sketched. The results from data are similar, and are given in the end for the figure of merit from data.

There are two ways to evaluate if an attribute or feature is valuable for classification. Either the performance together with a given classifier is measured or by evaluating how much information is contained in an attribute about the class, independently of the used classifier. In this case, classes are signal and background.

The classification of pions and kaons can be treated separately. Since an accurate classification of kaons is more important, due to the lower number of kaons as compared to pions (about 12% vs. 77% of all identified hadrons after cuts), the focus will be on the identification of kaons, pions can be treated analogously and for them only the result will be listed.

An obvious example of criteria used to evaluate the importance of a certain attribute for classification is the correlation with the class. If for a given attribute value, the given particle is always a kaon, one should use it for classification. This can be quantified with a measure from information theory: The information gain that is associated with an attribute. The information gain is the difference in information that is contained in the outcome of the classification if the value of the attribute is known as opposed to the case, where it is not known. Another way to put this is, that one looks at the entropy difference between the initial set and the sets where the attribute has a specific value, assuming that a good attribute sorts between the classes of interest [93]. Information is measured in bit and the maximum information contained in the outcome of a yes/no decision is 1 bit. The best attribute determines completely the outcome of the decision. The information contained in the outcome would thus be 0 bit. Here the information gain is obviously  $1 - 0 = 1$  bit. In general the information of a random draw with  $n$  possible outcomes  $v_i$  with probability  $P(v_i)$  is

$$\text{Info}(P(v_1), \dots, P(v_n)) = \sum_{i=1}^n -P(v_i) \log_2 P(v_i). \quad (4.6)$$

Given that an attribute partitions the set of examples that are to be classified into  $v$  partitions, where each contains  $p_i$  positive and  $n_i$  negative examples (signal or background) and the whole set contains  $p$  positive and  $n$  negative ones, the remaining information after the value of the attribute  $A$  is determined, is

$$\text{Remainder}(A) = -\frac{\sum_{i=1}^n p_i + n_i}{p + n} \text{Info} \left( \frac{p_i}{p + n}, \frac{n_i}{p + n} \right). \quad (4.7)$$

This is just the information contained in the subsamples, where the probability for a negative or positive outcome of a random draw is  $\frac{p_i}{p+n}$  and  $\frac{n_i}{p+n}$ , respectively weighted by the fraction of events in the subsample.

The information contained in the initial sample can be computed with eq. 4.6 as

$$\text{Info}_{\text{Init}} \left( \frac{p}{p+n}, \frac{n}{p+n} \right) = \frac{-p}{p+n} \log_2 \frac{p}{p+n} - \frac{-n}{p+n} \log_2 \frac{n}{p+n}. \quad (4.8)$$

Therefore the information gain of the attribute  $A$  is  $\text{Info}_{\text{init}} - \text{Remainder}(A)$ .

In order to use attributes in a decision as in cuts or the above information gain computation, a proper discretization has to be chosen. This discretization, of course, also determines the possible cut values used later in the analysis. Again, there are several strategies [92]. The most straightforward one is to chose equal discretization steps or equal frequency in each bin. Since cut points define attributes, the information gain measure described above can also be used to choose them.

In order to apply these automated methods for the evaluation of the attributes, it is advisable to normalize the values. Also a decorrelation step can reduce the number of attributes. An integrated tool that realizes a workbench for the most popular methods for data mining is the weka environment [94]. This tool was used to evaluate several methods for attribute selection and optimal cuts. The information gain selection gave the following values for the information contained in the set of the attributes pion likelihood (LH), kaon LH, fit angle, ring  $\chi^2$ , proton LH, hadron  $\theta$  and hadron momentum with respect to kaon identification, if evaluated on MC data:

- pion LH: 0.16 bit
- kaon LH: 0.14 bit
- fit angle: 0.1 bit
- ring  $\chi^2$ : 0.014 bit
- proton LH: 0.00422 bit
- hadron  $\theta$ : 0.0007 bit
- hadron momentum: 0.0005 bit

The fit angle is the Čerenkov angle from the fit to the identified ring. Since it is already used in the computation of the likelihoods, it does not provide significant extra information. In addition to the aforementioned possible attributes also others that could have effects on the identification performance like the hadron momenta in x,y and z direction, the particle multiplicities and other global event properties where used. These were also combined in a nonlinear way to form attributes that might be useful for classification. However, they did not allow for a better identification performance of the classifiers tried and which are described in the following.

#### 4.4.4 Optimal Cuts from Multivariate Analysis

Some popular multivariate methods where tested with the enlarged attribute set as input parameters.

- The Ripper algorithm for automated cut finding
- Support-Vector Machines (SVMs)

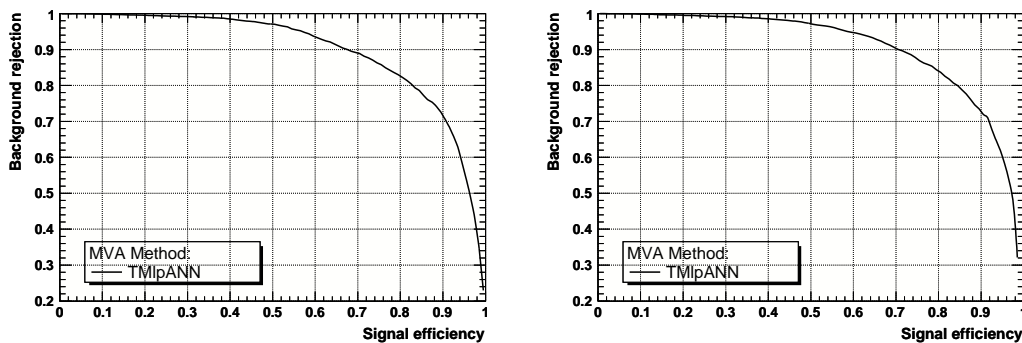


**Figure 4.18:** Signal efficiency vs. background rejection curve without (left) and with hadron momentum, hadron  $\theta$ , ring  $\chi^2$  and fit angle (right). Performances were evaluated on Monte Carlo data using a neural network as an example of a multivariate method. There is no significant gain from using the enlarged attribute set.

- Multivariate methods as implemented in TMVA<sup>3</sup> [95], the most important being
  - Neural Networks
  - Boosted Decision Trees (normal and decorrelated)
  - Principal Component Analysis (PCA)

TMVA is part of the ROOT software for data analysis [96]. To account for the different frequencies in the occurrence of the pions and kaons in the sample and for the different weighting of signal and background in eq. 4.5 adequate cost matrices were used. An in-depth analysis of the strategy used can be found in [92]. The comparison of the performance of the different classifiers implemented in TMVA for a typical set of attributes is shown in fig. 4.18.

As mentioned earlier, training and test sets are taken from simulated (Monte Carlo) or experimental data, for which the term 'real data' will be used. One encounters thus a typical problem in the use of multivariate methods in high energy physics, namely that it is very difficult to obtain training data that is correctly labeled and with a correct distribution in the relevant variables. Real data can be used, but with the trade-off that many examples are labeled incorrectly. Noisy data can make it unfeasible to use specific classifiers, e.g. Support-Vector-Machines (SVMs)[97]. Here noisy data leads to an increased number of support vectors, making training and classification inefficient. For simulated data the truth is known but the agreement with real data is difficult to achieve and to evaluate. Thus, when using Monte Carlo, it is important to know, how a classifier reacts to shifted inputs<sup>4</sup>. For both, simulated and real data, it was found that the best performance is achieved with a small set of attributes, namely the likelihood

<sup>3</sup>Toolkit for MultiVariate Data Analysis with ROOT

<sup>4</sup>For a discussion with respect to neural networks and SVMs, see [98].

Particle	LH over BG	LH over 2nd Max	Momentum Margin [GeV]
$\pi$	1.05	1.004	0.2
$K$	1.1	1.014	1.2

**Table 4.10:** Optimal parameter set for pions and kaons

values with the hadron  $\theta$  and the hadron momentum. A further enlargement only leads to worse performance. Performances were evaluated with the cuts used later on for the extraction of the single spin asymmetries. Differences between a setup where only the likelihoods were used as an input to the classification and the use of a bigger parameter set are minimal. These results are consistent with the results of the information gain computation.

#### 4.4.5 Optimal Cuts from Grid search on MC

The inclusion of more attributes than the given likelihoods does not merit a significant improvement of performance. It is of the same order as fluctuations between different MC versions and uncertainties in the MC, which are difficult to quantify. Therefore the approach presented in the following aims to optimize simple cuts on the likelihoods and particle momenta. Physical meaningful cuts to extract pions/kaons are:

- The pion/kaon likelihood has to be the greatest of all likelihoods and bigger than the background likelihood.
- Cut on the pion/kaon likelihood to suppress background.
- Cut on the ratio between the pion/kaon likelihood and the second highest likelihood for a mass hypothesis in the event.
- Cut on the minimal hadron momentum. The *momentum margin* between the Čherenkov threshold and the required hadron momentum ensures that a minimal number of photons is emitted.
- Cut on the maximal hadron momentum at 43 GeV since for higher momenta the difference between the expected values for the ring angle for the pion and kaon mass hypothesis differ by less than  $2\sigma$ , where  $\sigma$  is the resolution.

The simplest strategy to find the optimum values with respect to eq. 4.5 is a grid search in parameter space. In this case the parameter space is three-dimensional: the likelihood over background for the particle, the momentum over the Čherenkov threshold and the ratio to the second highest likelihood in the event. To find an optimal parameter set for pions and kaons, different grids with decreasing grid spacing were used. A coarse binning was used to find the approximate point of the optimum and finer ones to find the exact location of the optimum. The parameter set found by this technique is shown in tbl. 4.10.

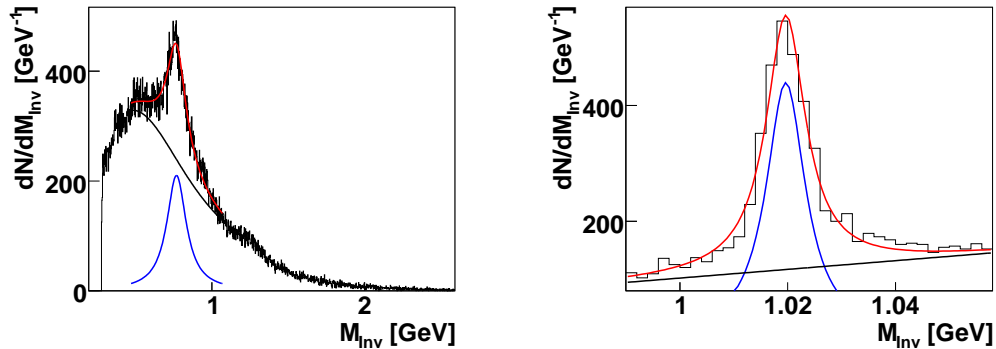


**Figure 4.19:** Exemplary fit to the  $\rho$  and  $\phi$  signal and background. In blue the vector meson signal, in black the background. The red line is the combination. For the grid search on data, the reduced  $\chi^2$  for the  $\rho$  fit is between 1.4 and 1.6. For the fit to the  $\phi$  signal between 0.95 and 1.1.

The performance of the particle identification on MC data of these cuts is within the errors compatible with the performance found from the multivariate methods, which were trained on the same parameter set. It has to be compared with the cuts found from data.

#### 4.4.6 Optimal Cuts from Grid search on Data

For the estimation of optimal cuts from real data, the strategy employed is quite straightforward and follows the procedure of cut finding with Monte Carlo data: For pions and kaons a cut on the likelihood over the background and on the ratio to the second highest likelihood in the event is made. Furthermore a cut on the margin of the hadron momentum over the Čerenkov threshold is made which directly reflects on the number of emitted photons. At variance to Monte Carlo data, the number of correctly identified particles has to be estimated from the size of the  $\rho$  and  $\phi$  resonances. Therefore invariant mass spectra are reconstructed separately for all identified pairs of pions and kaons of opposite charge. Then, to estimate signal and background in the region of the resonances, the signal is fitted with a Breit-Wigner-function and the background with an appropriate model. In the case of the  $\rho$  another Breit-Wigner-function is used, whereas for the narrower  $\phi$  resonance a linear fit is sufficient. Usually finding a model for the background is quite difficult. In this case, since the signal has to come from the resonance region, also the background description has to be valid only in this region. The signal region has been selected by the values for the mass and the width  $\Gamma$  of the  $\rho$  and  $\phi$  resonances as documented by the particle data group [99]. For the  $\rho$  the mass is taken to be 0.77 GeV and  $\Gamma = 0.151$  GeV and for the  $\phi$  1.02 GeV and  $\Gamma = 0.044$  GeV is used. Exemplary, the fit to the  $\rho$  and  $\phi$  resonances are shown in fig. 4.19.

The number of correctly and incorrectly identified particles that is used in the figure of merit (eq. 4.5) can then be estimated by the area under the background and signal

Particle	Likelihood over BG	LH over LH of 2nd Max	Momentum Margin [GeV]
$\pi$	1.01	1.001	0.35
K	1.06	1.00001	0.8

**Table 4.11:** Optimal cuts as computed from data.

Particle	Likelihood over BG	LH over LH of 2nd Max	Momentum Margin [GeV]
$\pi$	1.03	1.002	0.5
K	1.04	1.003	1

**Table 4.12:** Cuts used for the analysis.

curves. To this end, the signal is computed by taking the integral over the Breit-Wigner-function and the background by subtracting the signal from the mass spectrum in a region corresponding to  $\pm 2\Gamma$  around the maximum. As in the case where the optimal cuts were determined from MC data, a grid search is employed. For each point in the grid a separate fit is performed and the  $\chi^2$  over the number of degrees of freedom and figure of merit computed. The error on the figure of merit is computed by assuming that the error on the signal is to a good approximation given by  $\sqrt{S}$ , where  $S$  is computed from the area under the fit to the signal. The error on the background  $B$  is taken as  $\sqrt{B}$  and the error on the figure of merit obtained by error propagation.

The resulting cuts are shown in table 4.11. For the presented grid search, the reduced  $\chi^2$  for the  $\rho$  fit is between 1.4 and 1.6. For the fit to the  $\phi$  signal it is between 0.95 and 1.1.

#### 4.4.7 Results for Different Cuts for PID

In this section, the results on Monte Carlo and real data for the different cut strategies presented are given. The evaluation on MC has the advantage that purities and efficiencies for the particle identification can be investigated without being restricted to particles originating from a resonance decay. For example, in the two hadron analysis the performance of the PID can be evaluated over the full range of the invariant mass of the produced meson pair. Whereas for real data one is restricted to the masses of the respective vector mesons. The resulting figures of merit are shown in tbl. 4.13 and the purities in figs. 4.21 and 4.22. They are consistent with the ones obtained from real data presented in [100]. However, in [100] the performance of the PID for positive kaons was better than for negative ones as shown in fig. 4.20.

This trend cannot be reproduced on Monte Carlo data and could be attributed to the way the purities are evaluated from data or to the suppression of the production of a pure sea object  $K^-$  in comparison to  $K^+$  production. Furthermore, the evaluation of the figure of merit for kaons from non-exclusive  $\phi$  production is afflicted with large errors, of the order of 100%. This is because the signal count is low and the background large. From MC it is possible to enrich the sample with kaons, which reduces the errors. For the pion identification, the cuts obtained from data and Monte Carlo are compatible within the errors. But for kaon identification there are differences. Here, the cuts

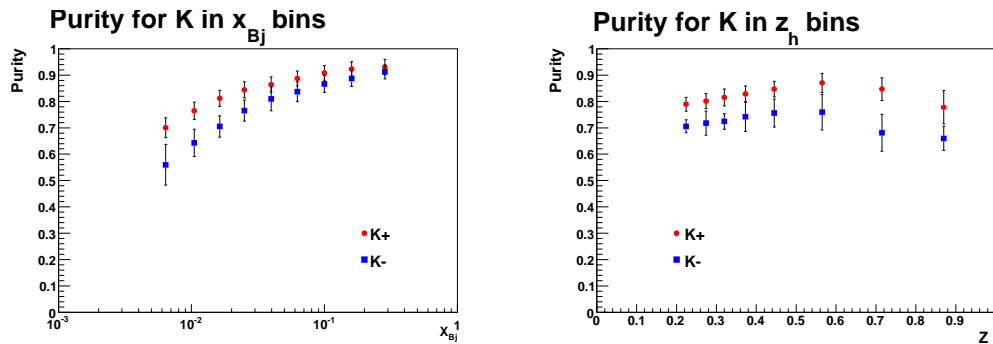
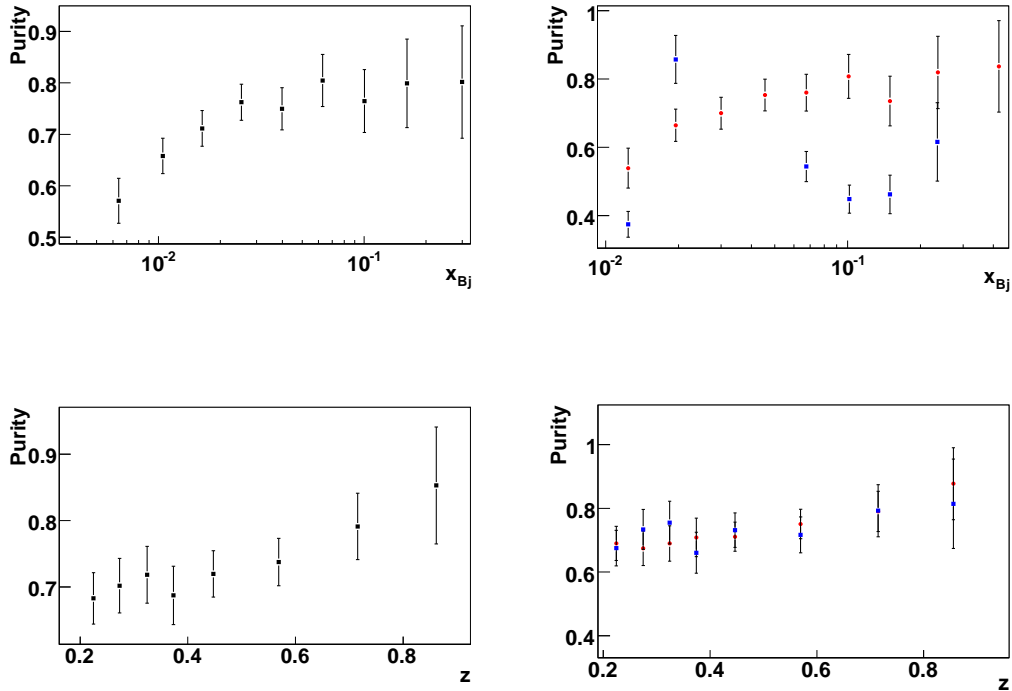


**Figure 4.20:** Purities of kaon identification evaluated on data using the cuts in tbl. 4.12. The trend is similar to the purities computed from Monte Carlo and presented in this thesis. However, the dependence of the purity on the kaon charge is not present in simulated data. Plots from [100].

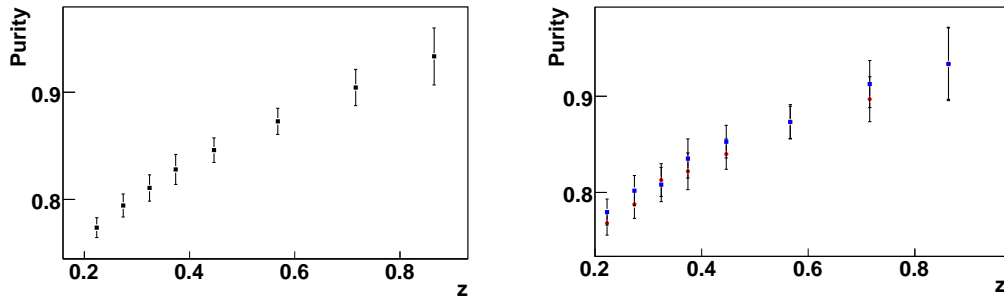
obtained from MC perform far better on Monte Carlo than the cuts optimized on data, but worse in the identification of particles in data. This behavior is either rooted in the inaccurate modeling of kaon production in Monte Carlo, or in the fact that kaons not originating from  $\phi$  production are poorly classified by cuts optimized for those from  $\phi$  production. Due to the need for a cross-check, a third set of cuts was chosen for the final analysis (see table 4.12). Results obtained on this set are also listed in tbl. 4.13. Mostly, the performance is comparable within the errors. An exception is the kaon identification which is a little bit worse on data and significantly worse on Monte Carlo.

When evaluating multivariate methods one does not only obtain purities and efficiencies at a single cut value but also so-called ROC<sup>5</sup> curves. They show the background rejection ratio at a given value for the signal efficiency and are produced by cutting on the output of the classifier, which reflects the confidence of the classification. In these curves the ideal operating point for the given analysis can be chosen. This is an advantage with respect to a simple cut-based approach. In this analysis, the best performance was achieved with neural networks and boosted decision trees. Exemplarily the results on MC data obtained with a neural network for different attribute sets are shown in fig. 4.18. From these plots and the ratio of pions to kaons in the training and test MC file of about 6.5:1 one can easily estimate the possible purities and efficiencies by multiplying the background rejection at the working point with the fraction of kaons in the sample. Using cuts on the classifier output as to maximize the figure of merit in eq. 4.5 one gets purities in the kaon sample of around 70%. Higher efficiencies are reached for higher values of  $x_{Bj}$  whereas for the smallest  $x_{Bj}$  bins the efficiency is only around 50%. At a cut point on the classifier output corresponding to a signal efficiency of about 70 % the figure of merit is within the errors equal to the one obtained with the cuts used in this analysis.. Since the use of multivariate methods does not merit a significant improvement for the PID, the analysis uses the simple cuts on particle likelihoods and momentum.

<sup>5</sup>Receiver Operating Characteristic

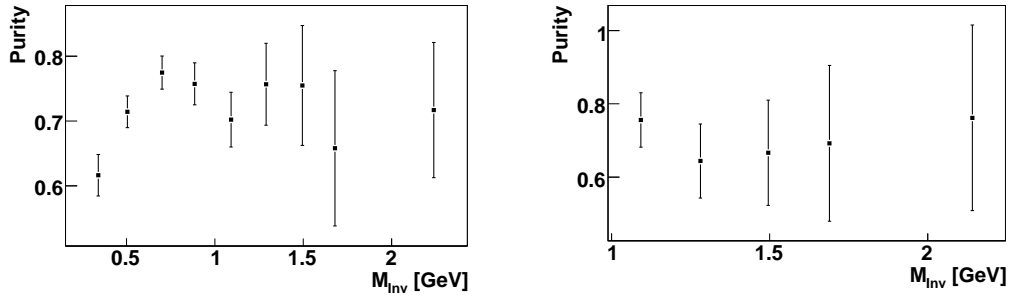


All (black squares on the left), positive (red dots) and negative (blue squares) kaons



All (black squares on the left), positive (red dots) and negative (blue squares) pions

**Figure 4.21:** Purities of kaon and pion samples after PID. Results are obtained from Monte Carlo data with optimal cuts determined on real data. The purity in  $P_T$  is constant for pions (around 85 %) and kaons (around 70%). Binned in  $x_{Bj}$ , the purity for pions is approximately constant at 85%. The increase of the purities with  $z$  and  $x_{Bj}$ , which is correlated with  $Q^2$ , can be explained with the higher momentum of the detected particle. Because a high momentum particle emits more Čherenkov photons than a low momentum particle, the PID is also more reliable.



All pions (left) and kaons (right)

**Figure 4.22:** Purities of pions (left) and kaon (right) samples after PID. Same sample as in fig. 4.21.

Data Set	Method	Figure of Merit $S^*S/(S+B)$
Monte Carlo	Cuts from MC	$3635 \pm 63$
Monte Carlo	Cuts from Data	$2906 \pm 59$
Monte Carlo	Cuts for Cross Check	$2590 \pm 55$
Data	Cuts from MC	$0.25 \pm 0.3$
Data	Cuts from Data	$0.37 \pm 0.34$
Data	Cuts for Cross Check	$0.34 \pm 0.31$

**Table 4.13:** Results for the different cuts to identify kaons. For the evaluation on data, the weeks 33 and 34 were used. The cuts for the “all hadron” analysis were applied.

## 4.5 Single Spin Asymmetries

From the selected hadron sample, single spin asymmetries are extracted. They are divided into one hadron asymmetries and two hadron asymmetries. In the first case, the distribution of single hadrons is analyzed to extract Collins and Sivers asymmetries and in the second case, the distribution of hadron pairs to access the transversity distribution. Both can be treated in the same framework, as was demonstrated in chapter 2.

- *One Hadron Asymmetries:* The two relevant azimuthal modulations of the cross-section in the one hadron analysis are dependent on the sin of  $\Phi_{\text{Coll}}$ , the Collins angle and  $\Phi_{\text{Siv}}$  the Sivers angle. This has already been shown with eq. 2.52 on page 30, along with a naive extraction scheme. Both can be written in terms of linear independent combinations of the azimuthal angles  $\Phi_h$  and  $\Phi_S$ :  $\Phi_{\text{Siv}} = \Phi_h - \Phi_S$  and  $\Phi_{\text{Coll}} = \Phi_h - (\pi - \Phi_S) = \Phi_h - \pi + \Phi_S$  as was explained in sec. 2.7.1.
- *Two Hadron Asymmetries:* In the Two Hadron case, the relevant azimuthal modulation of the cross-section is dependent on  $\sin(\Phi_S + \Phi_R)$ . The angle  $\Phi_R$  is depicted in fig. 2.15. Section 2.9.2 treats the extraction of the asymmetry which is similar to the extraction of the one hadron Collins asymmetry after exchange of  $\Phi_h$  with  $\Phi_R$ .

## 4.6 Estimators for Single Spin Asymmetries

After the selection of a hadron sample the amplitudes of the respective asymmetries have to be extracted. In this section the general framework, challenges and different estimators for asymmetry extraction are presented. In detail these are

- The *standard method*: In the presence of stable acceptances that do not influence the asymmetry extraction, this is the most straightforward method.
- The *double ratio method*: Its demand for detector stability is not as strict as for the standard method. In the presence of small asymmetries it gives stable results. This method is used in the further analysis.
- The *weighted double ratio method*: In a further development a method is presented that allows the weighting of events.
- *Two dimensional double ratio*: This method avoids biases of the extracted asymmetries due to the detector acceptance by using a binning in two independent azimuthal angles.
- *Two dimensional fit to counts*: In addition to the advantages of the two dimensional double ratio, a two dimensional fit to counts allows the incorporation of Poissonian statistics. Because the fit is directly to counts, statistical effects are better understood.

- *Unbinned maximum likelihood method:* This method is developed from first principles. By construction it is unbiased and best suited for low number of counts.

Each of these approaches has different advantages based on the assumptions regarding expected asymmetries and spectrometer acceptances. For historical reasons, the double ratio method was selected for this analysis. However, in the light of new analyses which will be performed on current and future COMPASS data, new and enhanced approaches like the unbinned maximum likelihood method have been developed and evaluated in the frame of this thesis. This is done by testing the algorithms on simulated data, in which arbitrary asymmetries can be injected. Based on these results presented at the end of this section, the optimal algorithms for a given analysis with respect to expected bias and complexity can be selected.

### 4.6.1 General Framework

With respect to the asymmetry extraction procedure, the one and two hadron case can be treated analogously. Because in both cases two momenta are used, the scattered muon momentum and  $\vec{P}_h$  or  $\vec{R}^6$ , the cross-sections and asymmetries depend in principle on six variables. The standard set of variables chosen here are  $x_{Bj}$ ,  $y$ ,  $z$ ,  $|P_\perp^h|^2$ ,  $\Phi_s$  and  $\Phi_h$  in the one hadron case or  $\Phi_R$  in the two hadron case. Then the density of counts at the kinematics point  $\vec{x} = (x_{Bj}, y, z, |P_\perp^h|^2)$  is proportional to the product of detector acceptance and effective physical cross-section:

$$\frac{d}{d\vec{x} d\Phi_k d\Phi_S} N_{\text{cell},\uparrow\downarrow}(\vec{x}, \Phi_k, \Phi_S) \propto n_{\text{cell}} \cdot A_{\text{cell},\uparrow\downarrow}(\vec{x}, \Phi_k, \Phi_S) \frac{d}{d\vec{x} d\Phi_k d\Phi_S} \sigma_{\uparrow\downarrow}(\vec{x}, \Phi_k, \Phi_S, f, P_{\text{Target}}) \quad (4.9)$$

where  $\Phi_k = \Phi_h$  in the one hadron case and  $\Phi_k = \Phi_R$  in the two hadron case and  $f, P_{\text{Target}}$  designate dilution factor and target polarization respectively. Since the flux is the same on both target cells during one period of data taking, only the number of target nucleons for the respective cell  $n_{\text{cell}}$  appears. One distinguishes count rates for upstream and downstream cell (cell=u,d) and polarizations up and down ( $\uparrow\downarrow$ ). Usually the dependence on one kinematic variable is of interest, the other ones are integrated out. Let w.l.o.g.<sup>7</sup> the remaining kinematic variable be  $x_{Bj}$ , and one considers a bin with  $x_k < x_{Bj} < x_{k+1}$ , then the count density depends only on the azimuthal angles  $\Phi_k$  and  $\Phi_S$ . If the acceptance dependence on  $\vec{x}$  is neglected eq. 4.9 becomes:

$$\frac{d}{d\Phi_k d\Phi_S} N_{\text{cell},\uparrow\downarrow}(\Phi_k, \Phi_S) \propto A_{\text{cell},\uparrow\downarrow}(\Phi_k, \Phi_S) \int_{y,z,|P_\perp^h|^2} \int_{x_k}^{x_{k+1}} n_{\text{cell}} \frac{d}{d\vec{x} d\Phi_k d\Phi_S} \sigma_{\uparrow\downarrow}(\vec{x}, \Phi_k, \Phi_S, f, P_{\text{Target}}) \quad (4.10)$$

The above expression will be the starting point for all estimators of azimuthal spin modulations of the polarized cross-section developed in the following. In the so-called

<sup>6</sup>At variance with  $\vec{P}_h$ ,  $\vec{R}$  depends on two momenta measured in the final state. However, in the extraction of the asymmetries, they can be treated analogously.

<sup>7</sup>without loss of generality

“binned” methods, the modulations are extracted by fitting to histograms. These contain counts in angular bins  $\Phi_k^i$  and  $\Phi_S^j$  with a fixed width:

$$N_{\text{cell},\uparrow\downarrow}(\Phi_k^i, \Phi_S^j) = \int_{\Phi_k^i}^{\Phi_k^{i+1}} \int_{\Phi_S^j}^{\Phi_S^{j+1}} \frac{d}{\Phi_k d\Phi_S} N_{\text{cell},\uparrow\downarrow}(\Phi_k, \Phi_S) \quad (4.11)$$

Since the modulations due to Collins and Sivers asymmetries are orthogonal functions of  $\Phi_h$  and  $\Phi_S$ , it is also possible to extract each separately, integrating out the other one. Therefore the Collins and Sivers angles are used as parameters and w.l.o.g. the Sivers dependence is integrated out:

$$N_{\text{cell},\uparrow\downarrow}(\Phi_{\text{Coll}}^i) = \int_{\Phi_{\text{Coll}}^i}^{\Phi_{\text{Coll}}^{i+1}} \int_{\Phi_{\text{Siv}}} \frac{d}{\Phi_{\text{Coll}} d\Phi_{\text{Siv}}} N_{\text{cell},\uparrow\downarrow}(\Phi_{\text{Coll}}, \Phi_{\text{Siv}}) \quad (4.12)$$

If the binning is in two azimuthal angles, the method will be called “two-dimensional” or 2D for short. In the later case, where one angular dependence is integrated out, the method is called a 1D method. Then it is assumed, that the acceptance is not only approximately constant in one angular bin, but also that its dependence on the angle that is integrated out does lead to a bias of the extracted amplitude.

Before integrating over any kinematic variable count rates and counts are proportional to the effective cross-section, which can be divided into a target spin independent and a target spin dependent part:

$$\sigma_{\uparrow\downarrow}(\vec{x}, \Phi_k, \Phi_S, f, P_{\text{Target}}) = \sigma_{XO}(x, y, z, |P_{\perp}^h|, \Phi_k) \pm f P_{\text{Target}} \sigma_{XT}(x, y, z, |P_{\perp}^h|, \Phi_k, \Phi_S), \quad (4.13)$$

since the COMPASS beam exhibits a natural longitudinal polarization  $X \in \{O, L\}$ . The target spin dependent part comprises the dilution factor and the polarization of the target  $P_{\text{Target}}$ . That this splitting is correct becomes clear from looking again at eq. 2.58. Since the spin dependent modulations contain the term  $\Phi_S$ , rotating  $\Phi_S$  by  $\pi$  leads to a change in the sign of the modulation while the acceptance factor stays. This implies, that the angle  $\Phi_S$  is computed assuming a fixed target polarization, here spin up. Consequently the ratio of effective cross-section and unpolarized cross-section can be written as

$$\begin{aligned} \frac{\sigma_{\uparrow\downarrow}(\vec{x}, \Phi_k, \Phi_S, f, P_{\text{Target}})}{\sigma_{XO}(x, y, z, |P_{\perp}^h|, \Phi_k)} &= 1 \pm \frac{f P_{\text{Target}} \sigma_{XT}(x, y, z, |P_{\perp}^h|, \Phi_k, \Phi_S)}{\sigma_{XO}(x, y, z, |P_{\perp}^h|, \Phi_k)} \\ &= 1 \pm \sum_{i=0}^8 f P_{\text{Target}} D^{\text{mod}_i}(y) \text{mod}_i(\Phi_k, \Phi_S) A^{\text{mod}_i} \\ &\equiv g^{\uparrow\downarrow} \end{aligned} \quad (4.14)$$

if the terms depending only on  $\Phi_h$  (e.g. Cahn asymmetry) are neglected.

Here  $g^{\uparrow\downarrow}$  is defined for convenience. It will be used later on to refer to the ratio  $\sigma_{\uparrow\downarrow}/\sigma_{XO}$ . The  $\text{mod}_i$  are the polarization dependent functions with which the cross-section is modulated. In the one hadron case these are:  $\text{mod}_{\{1,2,\dots,8\}} = \{\sin(\Phi_h - \Phi_S), \sin(\Phi_h + \Phi_S), \sin(3\Phi_h - \Phi_S), \sin(\Phi_S), \sin(2\Phi_h - \Phi_S), \cos(\Phi_h - \Phi_S), \cos(\Phi_S), \cos(2\Phi_h - \Phi_S)\}$ . The asymmetries  $A^{\text{mod}_i}$  are the amplitudes of these modulations. They contain the structure

functions  $F^{\text{mod}_i}$  divided by the spin independent part of eq. 2.58. Omitted is the factor of proportionality, which contains the global kinematic factor. But if for the extraction of asymmetries only ratios of counts are used, this can be neglected, otherwise, if the counts are used directly, it has to be accounted for. The estimators presented in the following compute  $A^{\text{mod}_i}$  from which transversity or the Sivers function can only be extracted, if the unpolarized part is known.

But before using the measured number of counts, the dependence on the unknown acceptance function has to be considered, which is generally expressed by equations 4.9-4.12. For different estimators the assumptions about the separability of convoluted acceptance and cross-section functions are different. If the acceptance function depends on a variable that is integrated out it can give contributions to the physical asymmetries which are to be extracted. In the following  $N(\Phi_i)$  is defined as in eq. 4.12 and  $N(\Phi_i, \Phi_j)$  as in eq. 4.11.

#### 4.6.1.1 Influence of Detector Acceptances on the Extraction of Physical Amplitudes

When using eq. 4.12 to project the counts on one azimuthal angle the dependence of the detector acceptance on the angle that is integrated out may lead to biased results [101]. The acceptance of the COMPASS spectrometer, which can be estimated from charged hadron production, exhibits a strong dependence on  $\Phi_S$  as shown in fig. 4.23. When Fourier transforming the acceptance functions, the  $\sin \Phi_s$  and  $\cos(2\Phi_s)$  ( $s_1$  and  $c_2$ ) components are of the order of 0.2, each corresponding to 40% effects on the measured asymmetries. When applying the addition theorems of trigonometric functions one can show analytically, that this leads to a mixing of the different asymmetries extracted with a 1D fit. For instance, when extracting Collins asymmetries, the extracted values are shifted by  $c_2$  times the value for the Sivers asymmetry and vice versa. If the expected values for both asymmetries are large, this can become a problem.

#### 4.6.1.2 Corrections due to Kinematics and Experimental Setup

The extracted asymmetry has to be corrected for the respective depolarization factor  $D^{\text{mod}_i}$ ,  $P_{\text{Target}}$  the target polarization and  $f$ , the dilution factor, which accounts for the fact that not every virtual photon scatters off a transversely polarized nucleon. It can naively be thought of as the fraction of polarizable nucleons in the target. As described in section 3.1 the COMPASS deuteron target consists of  ${}^6\text{LiD}$  with a dilution factor of about  $f \approx 0.38$ , which is dependent on the kinematics of the event and the position of the primary vertex for a non isotropic target. In principle the dilution factor can be computed for each event by considering the ratio of the  $F_2$  structure functions of deuteron and other isotopes together with radiative corrections [60]. However, as will be shown in this section, there is no significant effect on the results.

In all schemes presented in the following the extracted asymmetry is corrected with the mean depolarization, target polarization and dilution factors. Only the weighted double ratio method investigates the influence of these factors in an event-by-event weighting.

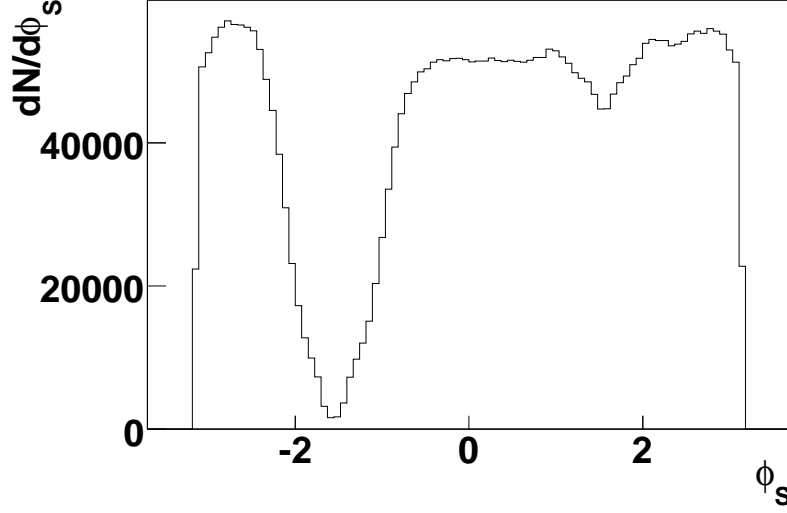


**Figure 4.23:** Distribution of  $\Phi_S$  for all events after cuts in the weeks 33 and 34.

#### 4.6.1.3 Corrections due to Finite Bin Size

For any “binned” method, that is a method that uses a binned histogram to which the azimuthal modulations are fitted, one has to account for effects due to the finite bin size [54]. Because the fit is done to the value at the center of the bin or at the center of gravity, one has to compare the mean value of the fit function over the bin range with the value of the function at the point of evaluation. Alternatively the value of the integral of the fit function can be fitted to the value of the bin. But since the relation of the integral to the value of the function in the middle of the bin can be determined analytically the added complexity can be avoided by correcting the obtained amplitudes with the “true” value of the function at the point of evaluation divided by the mean value. The “true” value is chosen such that the integral over the bin equals the bin content. For the one dimensional case this approach can be illustrated by considering the function

$$f(\Phi) = 1 + a \cos(\Phi) + b \sin(\Phi) \quad (4.15)$$

The mean value of  $f(\Phi)$  in a bin  $(\Phi_i, \Phi_{i+1})$  is

$$\langle f(\Phi) \rangle_{i,i+1} = \frac{1}{\Delta\Phi} \int_{\Phi_i}^{\Phi_{i+1}} f(\Phi) d\Phi. \quad (4.16)$$

For  $n$  bins, the bin width is  $\Delta\Phi = 2\pi/n$ . The standard fit is done to the mean value of  $f(\Phi)$  at the center of the bin. But the “true” height of the function at the center of the bin is given by

$$f(\Phi_i + \Delta\Phi/2) = 1 + a \cos(\Phi_i + \Delta\Phi/2) + b \sin(\Phi_i + \Delta\Phi/2). \quad (4.17)$$

The two values  $\langle f(\Phi) \rangle_{i,i+1}$  and  $f(\Phi_i + \Delta\Phi/2)$  are not equal. Their difference depends on the number of bins. For the limiting case  $n \rightarrow \infty$  the difference vanishes and for the

other cases the relation between the real amplitudes,  $a$  and  $b$ , and the amplitudes as extracted from the fit,  $a_{\text{fit}}$  and  $b_{\text{fit}}$ , can be analytically determined to be:

$$a_{\text{fit}} = a \frac{2}{\Delta\Phi} \sin \frac{\Delta\Phi}{2} \quad b_{\text{fit}} = b \frac{2}{\Delta\Phi} \sin \frac{\Delta\Phi}{2}. \quad (4.18)$$

Evaluating these relations leads to a correction factor  $a_{\text{fit}}/a = b_{\text{fit}}/b$  in the one dimensional case with 16 bins of 0.9936. Albeit the correction is very small, this changes for the two dimensional fits presented in sec. 4.6.5. Here, due to the higher overall bin number, the number of bins in each direction is chosen as eight. This corresponds to 64 bins overall. Then the amplitudes given in the full cross-section in eq. 2.58 can be described in the general form [54]

$$f(\Phi_h, \Phi_S) = 1 + \sum_{k=-1}^3 (a_k \sin(k\Phi_h - \Phi_S) + b_k \cos(k\Phi_h - \Phi_S)). \quad (4.19)$$

Using the same logic as before the correction factors can be extracted as

$$\begin{aligned} a_{k,\text{fit}} &= a_k \frac{2}{k\Delta\Phi_h} \sin \frac{k\Delta\Phi_h}{2} \frac{2}{\Delta\Phi_S} \sin \frac{\Delta\Phi_S}{2} \\ b_{k,\text{fit}} &= b_k \frac{2}{k\Delta\Phi_h} \sin \frac{k\Delta\Phi_h}{2} \frac{2}{\Delta\Phi_S} \sin \frac{\Delta\Phi_S}{2}. \end{aligned} \quad (4.20)$$

For the eight times eight binning used in the following, the correction factor evaluates to 0.87735. If the center of gravity of a bin no longer corresponds to the middle of the bin, extra caution has to be taken. Then in principle the calculation has to be redone with respect to the center of gravity of each bin.

### 4.6.2 Standard Method

Assuming independence of the acceptances of  $\Phi_h$ ,  $\Phi_S$  and  $\vec{x}$  the spin dependent asymmetries can be extracted by taking the normalized difference of the counting rates:

$$\frac{N_{\text{cell}}^{\uparrow}(\Phi_k) - r_{\text{cell}} N_{\text{cell}}^{\downarrow}(\Phi_k)}{N_{\text{cell}}^{\uparrow}(\Phi_k) + r_{\text{cell}} N_{\text{cell}}^{\downarrow}(\Phi_k)} = 1 + A_{\text{cell}}^{\text{mod}_i} \langle D^{\text{mod}_i} f P_{\text{Target}} \rangle (\Phi_k) \quad (4.21)$$

$\langle D^{\text{mod}_i}(y) f P_{\text{Target}} \rangle$  denotes the average of the corresponding correction factors due to kinematics and experimental conditions. Additionally, one has to assume independence of the structure functions on  $Q^2$ . The fit is performed for each function of interest  $\text{mod}_i$  and the weighted average of the result in each cell is computed. To balance differing counting rates, the factor  $r_{\text{cell}}$  is chosen as  $N_{\text{total}}^{\uparrow}/N_{\text{total}}^{\downarrow}$ . Since the  $\text{mod}_i$  are orthogonal, the different asymmetries can be extracted by fitting with the respective function. For the fit, the data is binned in 16 equidistant bins of  $\Phi_k$  and then fitted by  $\sin \Phi_{\{\text{Coll}, \text{Siv}, \text{RS}\}}$  at the bin center. Using 16 bins ensures, that binning effect can be neglected (see 4.6.1.3 and [54]).

Using eq. 4.21 is the so-called standard method which has been used for the very first analysis of azimuthal asymmetries by the COMPASS collaboration.

### 4.6.3 Double Ratio Method

For this analysis, the so-called double-ratio method is used, where one does not use the difference of the counting rates in the numerator of eq. 4.21 but the product of ratios

$$\text{DR}(\Phi_k) = \frac{N_U^\uparrow(\Phi_k)N_D^\uparrow(\Phi_k)}{N_U^\downarrow(\Phi_k)N_D^\downarrow(\Phi_k)} \quad (4.22)$$

where it is assumed, that the counts are in kinematic bins. Using the double ratio has the advantage, that it is robust against changes in the acceptance as long as the acceptance stays constant in one bin of  $\Phi_k$  and the ratio of acceptances stays constant between two periods of opposite polarization, that is

$$\frac{a_U^\uparrow}{a_U^\downarrow} = R \cdot \frac{a_D^\uparrow}{a_D^\downarrow}. \quad (4.23)$$

for each bin of  $\Phi_k$ . Here  $a_{\text{cell}}^{\text{polarization}}$  stands for the acceptance in one bin for the specified cell and polarization configuration. Eq. 4.23 is a reasonable assumption because for the extraction of single spin asymmetries two periods are combined during which the spectrometer can be assumed to be stable and which are close together in time. For a constant R-ratio there are no systematic effects expected using the standard or the double ratio method [102]. If the R-ratio changes in the different  $\Phi_k$  bins, this is not the case anymore for the standard method. But if the asymmetries are small it is still true for the double ratio method.

The double ratio method exhibits a somewhat higher statistical error then the standard one, if the counts between the two periods are unbalanced. However this is outweighed by the better stability. The validity of eq. 4.23 is called the R-test and is monitored for the analyzed data and was found to be well within the statistical errors [102].

The expectation value of the double ratio is obviously  $E\{\text{DR}\} = 1$ . This can be used to extract one specific modulation  $\text{mod}_i$  by Taylor expanding DR:

$$\begin{aligned} \text{DR}(\Phi_k) &= \frac{N_U^\uparrow(\Phi_k) \cdot N_D^\uparrow(\Phi_k)}{N_U^\downarrow(\Phi_k) \cdot N_D^\downarrow(\Phi_k)} \\ &= \frac{c_U^\uparrow \cdot c_D^\uparrow}{c_U^\downarrow \cdot c_D^\downarrow} \cdot \frac{a_U^\uparrow(\Phi_k) \cdot a_D^\uparrow(\Phi_k)}{a_U^\downarrow(\Phi_k) \cdot a_D^\downarrow(\Phi_k)} \cdot \frac{(1 + A^{\text{mod}_i} \sin \Phi_k)^2}{(1 - A^{\text{mod}_i} \sin \Phi_k)^2} \\ &\approx C \cdot \frac{a_U^\uparrow(\Phi_k) \cdot a_D^\uparrow(\Phi_k)}{a_U^\downarrow(\Phi_k) \cdot a_D^\downarrow(\Phi_k)} \cdot (1 + 4A^{\text{mod}_i} \sin \Phi_k) \end{aligned} \quad (4.24)$$

The  $c_{\text{cell}}^{\text{polarization}}$  are the respective factors of proportionality and  $A^{\text{mod}_i}$  the asymmetry that is to be extracted. Standard and double ratio method are described in detail in [102].

### 4.6.4 Weighted Double Ratio Method

Since the fit is done to binned data, where each event has a different weight in the asymmetry extraction, there is a somewhat more clever way to extract the asymmetries.

Instead of using the mean values for  $f$ ,  $P_{\text{Target}}$  and depolarization factor one can weight each event with the respective factor. Looking at equation 2.58 for the full cross-section there is also a factor of  $\frac{1-y+y^2}{xyQ^2}$  which varies from event to event for both, the polarized and the unpolarized part. If a kinematical binning other than in  $x$  is chosen, this means, that events with low  $xQ^2$  have a higher weight in the evaluation of the asymmetries. This is not ideal since Collins and Sivers effects are expected to be higher for partons in the valence region. With the restriction to the correction factors that pertain only to the polarized cross-section  $\sigma_{XT}$  the double ratio can be written as

$$\begin{aligned} \text{DR}(\Phi_k) &= \frac{N_U^\uparrow(\Phi_k) \cdot N_D^\uparrow(\Phi_k)}{N_U^\downarrow(\Phi_k) \cdot N_D^\downarrow(\Phi_k)} \\ &\approx \frac{(1 + \frac{(\sum DfP_{\text{Target}})^\uparrow_U}{N_U^\uparrow} A^{\text{mod}_i} \sin \Phi_k)(1 + \frac{(\sum DfP_{\text{Target}})^\uparrow_D}{N_D^\uparrow} A^{\text{mod}_i} \sin \Phi_k)}{(1 - \frac{(\sum DfP_{\text{Target}})^\downarrow_U}{N_U^\downarrow} A^{\text{mod}_i} \sin \Phi_k)(1 - \frac{(\sum DfP_{\text{Target}})^\downarrow_D}{N_D^\downarrow} A^{\text{mod}_i} \sin \Phi_k)}. \end{aligned} \quad (4.25)$$

The relative depolarization factor  $D$  is given by the ratio of the depolarization factor of the Sivers and Collins asymmetries, respectively ( $D^{\sin(\Phi_h - \Phi_s)}$  and  $D^{\sin(\Phi_h + \Phi_s)}$ ) and the global factor  $1 - y + y^2$ . Here it is assumed, that the global factors cancel in the double ratio and they are not included, leading to a less cumbersome notation. For the distribution of the double ratio of the factor  $\frac{1}{xyQ^2}$  over all  $\Phi_k$  bins, see fig. 4.26. If the coefficients  $N_i^j / (\sum DfP_{\text{Target}})_i^j$  are called  $k_i^j$  and the function  $A^{\text{mod}_i} \sin \Phi$  that is to be extracted  $x$ , the above equation can be written in a shorthand notation:

$$\text{DR} \frac{k_U^\uparrow k_D^\uparrow}{k_U^\downarrow k_D^\downarrow} = \frac{(k_U^\uparrow + x)(k_D^\uparrow + x)}{(k_U^\downarrow - x)(k_D^\downarrow - x)} \quad (4.26)$$

When solving for  $x$  one can take advantage of the fact that the expectation value of DR is 1 as is the expectation value of  $\frac{k_U^\uparrow k_D^\uparrow}{k_U^\downarrow k_D^\downarrow}$ . So one can assume that  $(\text{DR} \frac{k_U^\uparrow k_D^\uparrow}{k_U^\downarrow k_D^\downarrow} - 1)x^2 = 0$ , especially for small asymmetries  $A^{\text{mod}_i}$  which means, that the above equation reduces to a linear one which can easily be solved for  $x$ . See fig. 4.24 for the distribution of  $\text{DR} \frac{k_U^\uparrow k_D^\uparrow}{k_U^\downarrow k_D^\downarrow}$ .

The solution  $x$  is a function of the azimuthal angle  $\Phi$  and is then fitted with  $A^{\text{mod}_i} \sin \Phi$  to extract the asymmetry. The difference with respect to the normal double ratio method, where the mean value of each correction factor is used, is dependent on the deviation of this factor in the respective bin. Since for each  $\Phi_k$  bin an individual weight is computed, an improvement of the statistical error is expected. The size of this effect is dependent on the deviation of the weights. To get an idea of the sizes of the effect, a more straightforward way to extract the asymmetry is considered. Eq. 4.26 can be solved for  $x = A^{\text{mod}_i} \sin \Phi_k$ . Each bin in  $\Phi_i$  gives one value for  $A^{\text{mod}_i}$ . These can then be averaged to get an estimate of the asymmetry  $A^{\text{mod}_i}$ . Since in the weighted method, each measurement of  $x_i$  at an angle of  $\Phi_i$  is weighted, the error is smaller than for the standard method, where each measurement is assigned the same weight.

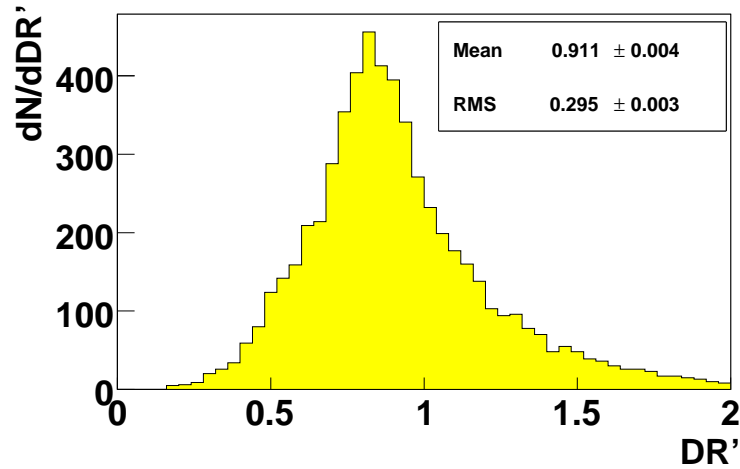


Figure 4.24: Distribution of the factor  $DR' = DR \frac{k_U^\dagger k_D^\dagger}{k_L^\dagger k_D^\dagger}$

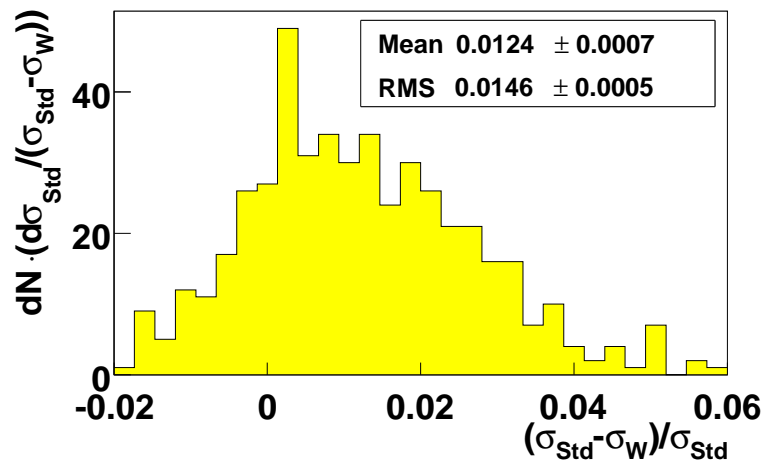
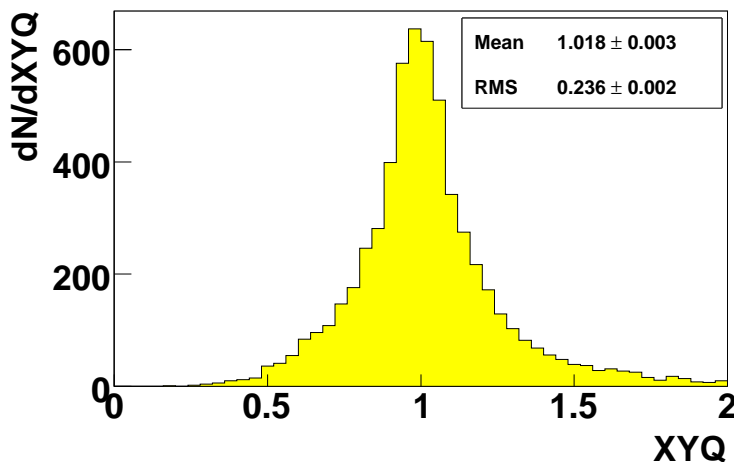


Figure 4.25: Normalized difference of errors on the asymmetry between weighted and standard method. For this sample the ordered two hadron asymmetries extracted from the data taken in the weeks 33 and 34 was considered



**Figure 4.26:** Variation of the double ratio of the global factor  $\frac{1}{xyQ^2}$ ,  $XYQ = \frac{(\frac{1}{xyQ^2})_U^{\dagger}(\frac{1}{xyQ^2})_D^{\dagger}}{(\frac{1}{xyQ^2})_U^{\dagger}(\frac{1}{xyQ^2})_D^{\dagger}}$ . For this sample the ordered two hadron asymmetries extracted from the data taken in the weeks 33 and 34 was considered. A minimum number of events of ten for each  $N_i^j$  was required.

However, taking into account only different polarizations and relative depolarization factors as indicated in eq. 4.25 amounts only to a 1.2% reduction in the statistical error as shown in fig. 4.25. However, there are also other variables that play a rôle in the asymmetry extraction and that vary from event to event, for example the depolarization factor. But since each event can be weighted individually, not only the appropriate kinematics for each event can be taken into account but also the acceptance function of the spectrometer to cancel the impact on the extraction of the physical amplitudes.

#### 4.6.5 Two Dimensional Fit to Double Ratios

Section 4.6.1.1 addressed the possibility of a bias introduced in the results of one dimensional methods due to effects between physical modulations of the cross-section and modulations due to the spectrometer acceptance function. One way to solve this problem is to appropriately weigh the events, which makes knowledge about the spectrometer acceptance necessary. Another way is to use a two dimensional fit in  $\Phi_h$  and  $\Phi_S$ . Here the additional degree of freedom in the cross-section given by a second angle is not integrated out and the bias introduced by this integration is avoided. Counting the degrees of freedom of the differential cross-section and comparing with the number of variables with respect to which the asymmetry extraction procedure is kept differential shows, that all degrees are conserved. For binned methods, the degrees of freedom equates to the number of variables with respect to which the counts are binned. Additionally, only with two dimensional methods one has access to the correlation coefficients between different asymmetries. These correlations are introduced

on variables which are independent on the physical level, like the Collins and Sivers asymmetries, by the convolution with the spectrometer acceptance. In a way, using one dimensional methods for asymmetry extraction has to be justified by evaluating the correlation coefficients by means of a two dimensional approach. This has been done in [51][54]. Following this argumentation, the two hadron asymmetries have to be extracted with a binning in three angles. Conventionally the angles  $\Phi_S$ ,  $\Phi_R$  and  $\Phi_h$ , the azimuthal angle of one of the hadron is chosen. Considering all three angles would make the extraction of the asymmetries of interest for this analysis much more complicated. These depend only on  $\Phi_R$  and  $\Phi_S$ . Since in addition, the dependence of the cross-section on the other angular combinations vanishes after intrinsic transverse momentum is integrated out, the two hadron asymmetry is extracted with a one dimensional fit [2][38]. Thus also avoiding problems with low number of counts due to the requirement of a specific hadron pair in the final state.

#### 4.6.6 Two Dimensional Fit to Counts

When using the double ratio method in the one or two dimensional case, the errors on the extracted asymmetries are determined assuming Gaussian distribution of the counts in one bin and Gaussian error propagation. However, the distribution of the double ratio does not have to follow a Gaussian distribution. This is especially true in the case of a low number of counts, where even the Gaussian assumption for the individual factors does not hold anymore. One possibility is to not consider such events in the fit. Another way is to fit directly to counts [103]. Using a two dimensional binning in  $\Phi_h$  and  $\Phi_S$ , the number of counts in a given bin  $j$  can be described by

$$N_{j,\text{cell}}^{\uparrow\downarrow} = F_{\text{cell}}^{\uparrow\downarrow} n_{\text{cell}} \sigma_0 \tilde{a}_{j,\text{cell}}^{\uparrow\downarrow} g_j^{\uparrow\downarrow}(\vec{A}, P_{\text{Target}}, f). \quad (4.27)$$

Here  $F$  is the muon flux,  $n$  the number of target nucleons,  $\sigma_0$  the unpolarized cross-section,  $\tilde{a}$  the acceptance,  $\vec{A}$  the vector of asymmetry amplitudes,  $f$  the dilution factor,  $g^{\uparrow\downarrow}$  the normalized cross-section defined in eq. 4.14 and  $P_{\text{Target}}$  the target polarization. The target cell is designated by  $\text{cell} = \{u, d\}$ . Both cells can be in one of the two configurations  $\uparrow$  or  $\downarrow$ . The bin number is  $j = \{1, 2, \dots, 64\}$  for a eight by eight binning. According to eq. 4.14,  $g_j^{\uparrow\downarrow}$  gives the modulation of the cross-section in each bin  $j$ . It can be parametrized as:

$$g_j^{\uparrow\downarrow} = 1 \pm \sum_i A_i \sin(\Phi_j^i) \quad (4.28)$$

$A_i$  and  $\Phi_j^i$  correspond to the eight modulations of the cross-section in eq. 2.58 evaluated for the bin  $j$ . Because the fit is performed to counts instead of double ratios, the unpolarized asymmetries only depending on  $\Phi_h$  can also be included, leading to

$$g_j^{\uparrow\downarrow} = 1 + \sum_i A_{i'} \sin(\Phi_j^{i'}) \pm \sum_i A_i \sin(\Phi_j^i). \quad (4.29)$$

However, discriminating a modulation due to a physical asymmetry only depending on the angle  $\Phi_h$  from a modulation of the acceptance is difficult because the analytic difference is only in the cross term  $\sum_{i'} A_{i'} \sin(\Phi_j^{i'}) \sum_i A_i \sin(\Phi_j^i)$  which would be present in the later case. Since the measured polarized asymmetries are small this is a not a significant correction.

If the sign of the polarized amplitude is positive or negative depends on the polarization in the corresponding cell and period. The dependence of  $g_j^{\uparrow\downarrow}$  on  $f$  and  $P_{\text{Target}}$  will be omitted in the following, because the correction for the attenuation of the amplitudes will be done separately as in the methods described before. Left is the dependence on the sign of the polarization, that is on  $\uparrow\downarrow$ . Since from the number of counts one cannot discern  $n_{\text{cell}}$ ,  $\sigma_0$  and  $\tilde{a}_{j,\text{cell}}^{\uparrow\downarrow}$  the normed acceptance

$$a_{j,\text{cell}}^{\uparrow\downarrow} = n_{\text{cell}}\sigma_0\tilde{a}_{j,\text{cell}}^{\uparrow\downarrow} \quad (4.30)$$

is defined. This leaves for a  $m$  by  $m$  binning  $4m^2 + 12$  free parameters and  $4m^2$  data points.

That more constraints are needed to determine the asymmetries becomes clear by the fact, that there are no constraints on the acceptances in each bin. Therefore modulations of the cross-section and acceptance effects cannot be distinguished. The necessary constraints on the acceptance are given by the double ratio as defined before. A reasonable assumption implies that the ratio

$$C = \frac{a_{ju}^{\uparrow}a_{jd}^{\uparrow}}{a_{ju}^{\downarrow}a_{jd}^{\downarrow}} \quad (4.31)$$

stays constant for all bins  $j$ . An even stricter constraint is that the ratio of acceptances stays constant for each cell, resulting in the constraints

$$C_u = \frac{a_{ju}^{\uparrow}}{a_{ju}^{\downarrow}} \quad C_d = \frac{a_{jd}^{\uparrow}}{a_{jd}^{\downarrow}}. \quad (4.32)$$

The flux parameter is linear dependent on the other parameters, thus there are four types of equations left to describe the number of counts for the two cells in each polarization state, when using the constraints from eq. 4.31:

$$\begin{aligned} N_{ju}^{\uparrow} &= C \frac{a_{jd}^{\downarrow}a_{ju}^{\downarrow}}{a_{jd}^{\uparrow}} g_j^{\uparrow}(\vec{A}) & N_{jd}^{\downarrow} &= a_{jd}^{\downarrow} g_j^{\downarrow}(\vec{A}) \\ N_{ju}^{\downarrow} &= a_{ju}^{\downarrow} g_j^{\downarrow}(\vec{A}) & N_{jd}^{\uparrow} &= a_{jd}^{\uparrow} g_j^{\uparrow}(\vec{A}) \end{aligned} \quad (4.33)$$

For the constraints in eq. 4.32 there exist a similar system of equations, but with less free parameters:

$$\begin{aligned} N_{ju}^{\uparrow} &= C_u a_{ju}^{\downarrow} g_j^{\uparrow}(\vec{A}) & N_{jd}^{\downarrow} &= C_d a_{jd}^{\uparrow} g_j^{\downarrow}(\vec{A}) \\ N_{ju}^{\downarrow} &= a_{ju}^{\downarrow} g_j^{\downarrow}(\vec{A}) & N_{jd}^{\uparrow} &= a_{jd}^{\uparrow} g_j^{\uparrow}(\vec{A}) \end{aligned} \quad (4.34)$$

Both, eqs. 4.33 and 4.34 are a nonlinear system of equations. A well known way to find a solution of these is the Levenberg-Marquardt (LM) algorithm [104][105]. The LM-algorithm solves the problem of minimizing  $\|\vec{F}(\vec{a})\|^2$ , with respect to the vector

of arguments  $\vec{a}$  of the general function  $\vec{F}(\vec{a})$ . This is done iteratively by solving the linearized version of the problem

$$\min_{\vec{a}} \|\vec{F}(\vec{a}_k) J(\vec{a}_k) (\vec{a} - \vec{a}_k)\|^2. \quad (4.35)$$

Here  $J$  denotes the Jacobian of  $F$ . A solution can be found by rearranging eq. 4.35 to

$$J^T J(\vec{a}_k - \vec{a}) = J^T F(\vec{a}_k). \quad (4.36)$$

Solving eq. 4.36 iteratively amounts to the well known Gauss-Newton method. A better convergence in regions further away from the minimum can be obtained by using the form

$$(J^T J + \lambda I) (\vec{a}_k - \vec{a}) = J^T F(\vec{a}_k). \quad (4.37)$$

The term  $\lambda I$  is a damping term, where  $I$  is the identity matrix. For high values of  $\lambda$  the LM algorithm is effectively a gradient-descent method. Additionally, the algorithm operates only in a trust-region to improve stability [106][107]. Equation 4.37 can be solved without performing the computationally costly matrix inversion by using the pseudo inverse. For this analysis the implementation of the Levenberg-Marquardt algorithm of the GNU Scientific Library (GSL) has been used [108]. The choice of  $F$  has to be taken, such that a solution of 4.35 is also a solution of 4.33 and 4.34, respectively, in the maximum likelihood sense. Assuming a Gaussian distribution of the number of counts, this is achieved by using a least squares fit [109]. If  $N_j$  is the number of counts in one bin and the fit function evaluated in that bin is  $f_j(\vec{a})$  the target function is chosen as

$$F_j = (N_j - f_j(\vec{a}))/\sigma_j, \quad (4.38)$$

where  $\sigma_j$  is the error on the number of counts  $N_j$ . With the Gaussian assumption, the error can be approximated for sufficiently high number of counts by  $\sigma_j = \sqrt{N_j}$ . Then 4.35 is equal to a least squares fit of  $f_j(\vec{a})$  to  $N_j$ . Since the assumption is, that  $N_j$  follows a normal distribution with the mean  $f_j(\vec{a})$ , minimizing the sum of the squares of the difference  $\sum \|(N_j - f_j(\vec{a}))/\sigma_j\|^2$  is equivalent to the maximization of the log likelihood: The probability of  $N_j$  given the parameters  $\vec{a}$  is given by

$$P(\vec{a}) = \frac{1}{\sigma \sqrt{2\pi}} e^{-(N_j - f_j(\vec{a}))^2 / (2\sigma_j^2)}. \quad (4.39)$$

Assuming independence of the distributions in each bin, the log likelihood of  $\vec{a}$  is given by

$$\sum_j -\frac{(N_j - f_j(\vec{a}))^2}{2\sigma_j^2} + \text{const.} \quad (4.40)$$

Minimizing 4.35 thus corresponds to maximizing the likelihood of the parameter vector  $\vec{a}$ . With the Gaussian assumption and the factor -2 the log likelihood in eq. 4.40 corresponds to the deviance and follows a  $\chi^2$  distribution. If the number of counts in one bin is too low to make this assumption, the derivation of the  $F_j$  has to be made with the Poisson probability. This is given for bin number  $i$  as

$$P(\vec{a}) = \frac{e^{-f_j(\vec{a})} f_j(\vec{a})^{N_j}}{N_j!}. \quad (4.41)$$

Computing the log likelihood with this probability distribution instead of eq. 4.39 leads to the minimization of the corresponding deviance given as

$$\sum_j 2(f_j(\vec{a}) - N_j) + 2N_j \ln(N_j/f_j(\vec{a})). \quad (4.42)$$

Because eq. 4.42 follows also a  $\chi^2$  distribution, eqs. 4.42 and 4.39 are “compatible” with each other [99]. The target function  $F_j$  can be chosen appropriately for the observed number of counts in one bin. For the analysis a threshold of ten events is chosen. Above,  $F_j = f_j(\vec{a}) - N_j$  and below  $F_j = \sqrt{2} \sqrt{f_j(\vec{a}) - N_j - N_j \ln(f_j(\vec{a})/N_j)}$  is used. Using this term ensures that minimizing  $F_j$  in the quadratic sense as in eq. 4.35 also minimizes eq. 4.42 and that the relation between the two forms is the same as in the case of a Gaussian distribution. In the later case the minimization of 4.39 is replaced by a minimization of 4.38. The prediction for the number of counts in a specific bin  $f_j$  is dependent on the cell and the polarization as in eqs. 4.33 and 4.34

#### 4.6.7 Analytic Description of the Acceptance with the Fourier Series

In the previously described asymmetry extraction method the spectrometer acceptance was described by a coefficient in each angular bin. This description makes it necessary to fit to binned histograms. It is also counterintuitive, since the resulting acceptance function is discontinuous<sup>8</sup> and each acceptance coefficient is independent from the ones in neighboring bins.

From data it is known, that the acceptance can efficiently be described by trigonometric functions, for example by a Fourier series. There are numerous advantages to this approach: Firstly the influence on the physical asymmetries extracted from the measured asymmetries can be taken into account. The analysis done in [101] shows that only the Fourier coefficients up to the order two, meaning up to the frequency  $2/(2\pi)$  lead to a significant bias when extracting asymmetries with a one dimensional fit. Secondly there are less parameters in the fit. Instead of having to fit  $3m^2$  amplitude coefficients to solve eqs. 4.33, only the relevant Fourier coefficients have to be fitted. As before,  $m$  is the number of bins in one dimension. Good results have already been obtained by including the coefficients up to the third order, so up to the frequency  $3/(2\pi)$ . Then the number of parameters is independent of  $m$  and equals  $3(1 + 3^2)$ , which will become clear in the following.

The solution of eqs. 4.33 and 4.34 requires that the number of equations is equal or greater than the number of parameters. The number of equations can decrease if the number of counts is too low. If the fit relies on the Gaussian assumption this would be the case for a number of counts less than ten. Then the equations for the respective bin and the corresponding acceptances are deleted because even if the number of counts in this angular bin is high enough there are not enough constraints left to determine the acceptance coefficients related to the angular bin and provide information about the physical amplitudes. Therefore the equations and parameters related to that bin are deleted. Since for each angular bin four equations and three parameters are deleted, it can happen, that there are not enough equations left to solve for the parameters.

<sup>8</sup>It is described by a coefficient in each angular bin

This problem is overcome by the Fourier ansatz for the acceptance. First of all, the number of parameters is far less, allowing the deletion of far more equations. Furthermore each coefficient is related to all angular bins. Therefore only the one equation has to be deleted for which there were not enough events counted. Less parameters should also mean faster and better convergence. However, the aforementioned dependence of the estimated number of counts in each bin on many Fourier coefficients leads to less non-zero entries in the Jacobian in eq. 4.37. The high correlation between the parameters makes the solution harder.

For the one hadron analysis, two distinct approaches were used for the description of the acceptance with Fourier coefficients. In the first factorizability of the acceptance dependence on  $\Phi_h$  and the dependence on  $\Phi_S$  was assumed. Then the acceptance in each angular bin can be described as the product of the acceptance functions in  $\Phi_h$  and  $\Phi_S$  which are in turn described by one-dimensional Fourier series:

$$Acc(c_k^h, s_k^h, c_k^S, s_k^S, \Phi_h, \Phi_S) = \frac{1}{\sqrt{2\pi}} \left( c_0^h + \sum_{k=1}^{MAX_F} (c_k^h \cos(k\Phi_h) + s_k^h \sin(k\Phi_h)) \right) \cdot \frac{1}{\sqrt{2\pi}} \left( c_0^S + \sum_{k=1}^{MAX_F} (c_k^S \cos(k\Phi_S) + s_k^S \sin(k\Phi_S)) \right). \quad (4.43)$$

The normalization chosen here is such that it is the same for the Fourier transformation and the inverse operation. Plancherel's and Parseval's theorem can then also be written without prefactors. At this point the normalization can be chosen arbitrarily. But when using the Fourier series for the spectrometer acceptance description in the unbinned maximum likelihood fit, described in the next section, this is not the case anymore. A more general formulation is the two-dimensional discrete Fourier transform (DFT) leading to the following form:

$$Acc(a_0, c_{kl}, s_{kl}, \Phi_h, \Phi_S) = \frac{1}{2\pi} \left( a_0 + \sum_{\substack{k=0, l=0 \\ k \neq 0 \vee l \neq 0}}^{MAX_F} c_{kl} (\cos(k \cdot \Phi_h) \cos(l \cdot \Phi_S) - \sin(k \cdot \Phi_h) \sin(l \cdot \Phi_S)) + s_{kl} (\sin(k \cdot \Phi_h) \cos(l \cdot \Phi_S) + \cos(k \cdot \Phi_h) \sin(l \cdot \Phi_S)) \right) \quad (4.44)$$

The number of coefficients  $MAX_F$  has to be chosen such that the acceptance can be described adequately. And it has to exceed the frequency of the acceptance modulation mainly causing the correlation effects between the different physical amplitudes. Section 4.6.9 covers the results for asymmetry extraction on Monte Carlo data for different values of  $MAX_F$ .

#### 4.6.8 Unbinned Maximum Likelihood Estimator

The asymmetry extraction methods presented previously are approximations of the maximum likelihood estimator [109]. They are valid in the limit of high number of

counts. For low number of counts, either the Gaussian assumption is not valid or the number of angular bins has to be chosen so low, that binning effects cannot be excluded anymore. A solution is to form the extended maximum likelihood for the asymmetry values  $\vec{A}$ . The probability density function (PDF)<sup>9</sup> of finding an event at the angular coordinate  $(\Phi_h, \Phi_S)$  is  $Acc(\Phi_h, \Phi_S)g^{\uparrow\downarrow}(\vec{A})$ . The normalization of  $Acc$  is chosen in the sense of eqs. 4.33, that is including all terms that are independent from the physical asymmetries. With this the extended likelihood can be formed:

$$L(\vec{A}) = \prod_j^N Acc(\Phi_h^j, \Phi_S^j)g^{\uparrow\downarrow}(\vec{A})\frac{e^{-\mu}\mu^N}{N!} \quad (4.45)$$

The product goes over all  $N$  observed events  $j$  with angular coordinates  $(\Phi_h^j, \Phi_S^j)$ . For a given choice of  $Acc$  and  $\vec{A}$  the number of expected events is  $\mu$ . Thus the additional term  $\frac{e^{-\mu}\mu^N}{N!}$  extending the regular likelihood function is the Poissonian probability of finding  $N$  events with  $\mu$  events theoretically expected. Without this term,  $L$  would go to infinity for  $Acc \rightarrow \infty$ . For a given acceptance function  $Acc(\Phi_h, \Phi_S)$   $\mu$  can be computed as

$$\mu = \int_0^{2\pi} \int_0^{2\pi} Acc(\Phi_h, \Phi_S)g^{\uparrow\downarrow}(\Phi_h, \Phi_S, \vec{A})d\Phi_h d\Phi_S \quad (4.46)$$

With  $Acc(a_0, c_{kl}, s_{kl}, \Phi_h, \Phi_S)$  from the DFT in eq. 4.44, neglecting cross terms with the physical modulations, one obtains for  $\mu$ :

$$\mu \approx 2\pi a_0 \quad (4.47)$$

because the integral over the non-constant parts is zero when integrated from 0 to  $2\pi$ . If the cross terms are considered, these have to be computed for each physical modulation  $\text{mod}_i(\Phi_h, \Phi_S)$  as  $\mu_{\text{mod}_i} = A^{\text{mod}_i} \int_0^{2\pi} \int_0^{2\pi} Acc(\Phi_h, \Phi_S)\text{mod}_i(\Phi_h, \Phi_S)$ .

However, due to the simple form of the  $\text{mod}_i$  this can be done in a straightforward manner. If w.l.o.g. only the physical relevant cases of the Collins and Sivers asymmetry are considered, then  $\text{mod}_i \in \{\sin(\Phi_S + \Phi_h), \sin(\Phi_S - \Phi_h)\}$ . Using the addition theorems

$$\sin(\Phi_h \pm \Phi_S) = \sin(\Phi_h) \cos(\Phi_S) \pm \cos(\Phi_h) \sin(\Phi_S) \quad (4.48)$$

for the Collins and Sivers modulations the problem reduces to the computation of integrals of the form

$$c_{kl}A_{\text{Coll/Siv}} \int_0^{2\pi} \int_0^{2\pi} ([\cos(k\Phi_h) \cos(l\Phi_S) - \sin(k\Phi_h) \sin(l\Phi_S)] \cdot [\sin(\Phi_h) \cos(\Phi_S) \pm \cos(\Phi_h) \sin(\Phi_S)]) d\Phi_h d\Phi_S \quad (4.49)$$

and

$$s_{kl}A_{\text{Coll/Siv}} \int_0^{2\pi} \int_0^{2\pi} ([\sin(k\Phi_h) \cos(l\Phi_S) + \cos(k\Phi_h) \sin(l\Phi_S)] \cdot [\sin(\Phi_h) \cos(\Phi_S) \pm \cos(\Phi_h) \sin(\Phi_S)]) d\Phi_h d\Phi_S. \quad (4.50)$$

<sup>9</sup>the difference to parton distribution function will be clear from the context

Since all terms which contain  $\cos(\Phi_i) \sin(\Phi_i)$  or for which  $k, l \neq 1$  evaluate to zero only the product of the modulation  $\sin(\Phi_h + \Phi_S)$  with the terms in the acceptance function of eq. 4.44 connected to the coefficient  $s_{11}$  contributes. Using the above relations, one arrives at  $\mu_{\text{Coll}} = \frac{1}{2\pi} A_{\text{Coll}} s_{11} 2\pi^2$ . Generally, all modulations that depend on the difference of  $m\Phi_h$  and  $n\Phi_S$  lead to a vanishing effect on  $\mu$ . If modulations only depending on one angle are taken into account additional terms  $\mu_{\text{mod}(n\Phi_i)}$  appear. They are

- $\mu_{\cos(\Phi_S)} = \frac{1}{2\pi} A^{\cos(\Phi_S)} 2\pi^2 (c_{01} + s_{01})$
- $\mu_{\sin(\Phi_S)} = \frac{1}{2\pi} A^{\sin(\Phi_S)} 2\pi^2 (s_{01} - c_{01})$

for the polarized asymmetries and

- $\mu_{\cos(\Phi_h)} = \frac{1}{2\pi} A^{\cos(\Phi_h)} 2\pi^2 (c_{10} + s_{10})$
- $\mu_{\cos(2\Phi_h)} = \frac{1}{2\pi} A^{\cos(2\Phi_h)} 2\pi^2 (c_{20} + s_{20})$
- $\mu_{\sin(\Phi_h)} = \frac{1}{2\pi} A^{\sin(\Phi_h)} 2\pi^2 (s_{10} - c_{10})$

for the unpolarized ones.

Instead of maximizing eq. 4.45 it is computationally easier to minimize the normalized logarithmic likelihood:

$$\begin{aligned}
 -\ln L(\vec{A}, a_0, c_{kl}, s_{kl}, C_u, C_d) &= \sum_i \left( -\ln \left( \text{Acc}(\Phi_h, \Phi_S, a_0, c_{kl}, s_{kl}, C_u, C_d) \right. \right. \\
 &\quad \left. \left. - \ln \left( g^{\uparrow\downarrow}(\Phi_h, \Phi_S, \vec{A}) \right) + \mu(a_0, C_u, C_d) - \ln(\mu(a_0, C_u, C_d)) \cdot N \right) \right). \tag{4.51}
 \end{aligned}$$

Depending on the index  $i$  the correct form of  $\mu$ ,  $\text{Acc}$  and  $g$  has to be chosen. For the implementation corresponding to the acceptances relying on the assumption in eq. 4.32 the acceptances in one polarization depend on the acceptances of the same cell in the other polarization configuration via the proportionality factor  $C_{u,d}$ . This relation is also valid for the expected number of events in one cell. For the minimization of eq. 4.51 the Fletcher-Reeves conjugate gradient method was chosen [110]. This is a popular example of a conjugate gradient algorithm using line searches to avoid the solution of a quadratic problem in each step. For the solution the minimum is iteratively searched for along a line. The direction of the line is defined by conjugate gradients. At the starting point the gradient of the function is chosen as the direction in which to search. For subsequent steps, the new direction is a conjugate of the old one and the gradient of the function at the new point. This method is only slightly more complicated than usual gradient descent methods, but converges much faster.

#### 4.6.9 Performance on Monte Carlo Data

Different strategies for asymmetry extraction can be studied and compared using Monte Carlo data with artificial asymmetries. The data was already presented in this chapter. In order to impose artificial asymmetries, the events were weighted according to the

generated kinematics. For the extraction the reconstructed kinematics were used. Then the extracted asymmetries were compared with the injected ones. According to eq. 2.58, the weighting function was chosen as

$$\begin{aligned}
w(\Phi_h, \Phi_S) = & \\
1 \pm \frac{fP_{\text{Target}}}{D_{\text{upol}}} & \left( D^{\sin(\Phi_h - \Phi_S)} \sin(\Phi_h - \Phi_S) A_{\text{Collins}}^{\sin(\Phi_h - \Phi_S)} + D^{\sin(\Phi_h + \Phi_S)} \sin(\Phi_h + \Phi_S) + \right. \\
A_{\text{Sivers}}^{\sin(\Phi_h + \Phi_S)} & + D^{\sin(3\Phi_h - \Phi_S)} \sin(3\Phi_h - \Phi_S) A^{\sin(3\Phi_h - \Phi_S)} + D^{\sin \Phi_S} \sin \Phi_S A^{\sin \Phi_S} + \\
D^{\sin(2\Phi_h - \Phi_S)} \sin(2\Phi_h - \Phi_S) & A^{\sin(2\Phi_h - \Phi_S)} D^{\cos(\Phi_h - \Phi_S)} \cos(\Phi_h - \Phi_S) A^{\cos(\Phi_h - \Phi_S)} + \\
D^{\cos \Phi_S} \cos \Phi_S A^{\cos \Phi_S} & + D^{\cos(2\Phi_h - \Phi_S)} \cos(2\Phi_h - \Phi_S) A^{\cos(2\Phi_h - \Phi_S)} \left. \right).
\end{aligned} \tag{4.52}$$

The depolarization factors  $D^f$  are dependent on  $y$ , the fractional energy transfer from the scattered muon, for which the generated value was used, too. In the case of the unbinned maximum likelihood method weights are more complicated to implement. Therefore this method was tested with a simpler data generation method:

- Values for  $\Phi_h$  and  $\Phi_S$  were generated in the interval  $[0, 2\pi)$  randomly according to a uniform distribution.
- For each event  $(\Phi_h, \Phi_S)$  a random number  $v$  in the interval  $[0, 2]$  was generated according to a uniform distribution.
- If the evaluation of  $w(\Phi_h, \Phi_S) \cdot \text{Acc}(\Phi_h, \Phi_S)$  was smaller than  $v$ , the event was discarded, otherwise kept.

The acceptance function  $\text{Acc}(\Phi_h, \Phi_S)$  was first taken to be constant and in a second set of tests to be

$$1 + c \cdot \cos(2\Phi_S) + s \cdot \sin(\Phi_S) \tag{4.53}$$

with  $c = 0.25$  and  $s = 0.6$ . This function is plotted in fig. 4.27. It reproduces qualitatively the experimental acceptance function in  $\Phi_S$  which is also shown in fig. 4.27. The acceptance dependence on  $\Phi_h$  is rather weak. So it is expected, that a function of the above form will allow to check for unwanted effects due to the convolution of the physical amplitudes with the acceptance. Since the approach, of fitting the acceptance approximately with a truncated Fourier series is the same in the maximum likelihood approach and the least squares fit described above, the validity of this form can be tested on the full Monte Carlo data. Supplementary checking the maximum likelihood on the simplified Monte Carlo data gives additional confidence in this approach.

## Results for the different Fit Methods

Twelve Monte Carlo runs with about  $10^6$  events each were taken to extract the asymmetries for pions, kaons, protons and unidentified particles with three bins in  $x_{Bj}$  and two bins in  $z$  and  $P_t$ . In order to ensure, that the Gaussian assumption for the event counts

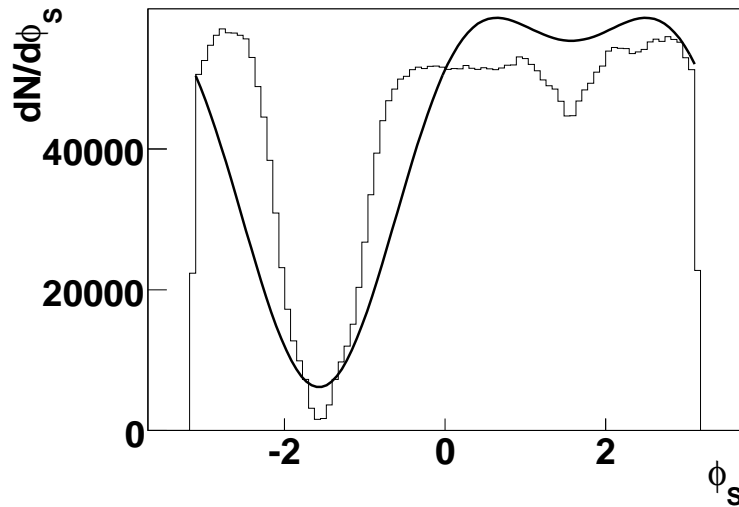


**Figure 4.27:** Artificial acceptance function generated by  $1 + 0.25 \cdot \cos(2\Phi_S) + 0.6 \sin(\phi_S)$  and  $\Phi_S$  distribution of all events after cuts in the weeks 33 and 34.

can be used, a minimum count of five<sup>10</sup> was required. Only those asymmetries were considered in the evaluation, that could be reconstructed with all methods, leaving 320 asymmetries. Even though there are no asymmetries expected for protons, the Collins asymmetry was injected there as well. Subsequently the distribution of the deviations between the reconstructed asymmetries and the injected ones normalized to the error on the reconstructed asymmetry for different methods was plotted. In a somewhat loose terminology they are called “pulls” in the following and are defined as

$$\text{Pull} := \frac{A_{\text{Reconstructed}} - A_{\text{Injected}}}{\sigma_{\text{Reconstructed}}}. \quad (4.54)$$

The correlation between the deviations is expected to be small, since they all depend on different data, the distribution is expected to be Gaussian. A mean different from zero hints to a bias in the method, whereas a root mean square error (RMS) of the distribution different from one to wrongly assigned errors. The RMS approximates the standard deviation of the distribution and will therefore also be called  $\sigma$  in the following. As expected all methods presented were able to extract an injected Collins signal correctly if all other physical amplitudes were set to zero. In a second run, Sivers and other possible asymmetries were injected to test the predicted correlation between the two amplitudes due to the detector acceptance. Figure 4.28 shows the pull distributions for the 1D, 2D and least squares method in the case of 20% Collins and a 30% Sivers asymmetry.

As can be seen, a significant deviation of the mean can be observed for the one-dimensional method. The magnitude of this effect is consistent with the magnitude

<sup>10</sup>Instead of ten as for real data due to the limited statistics

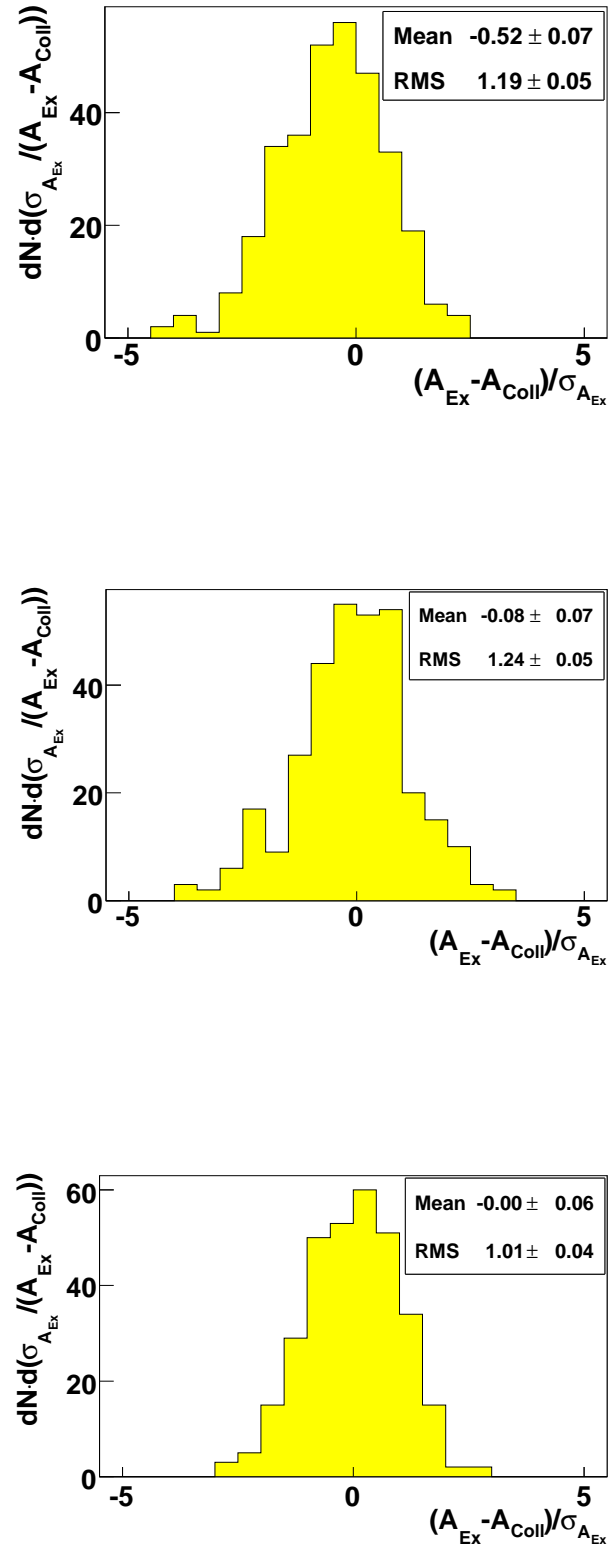


**Figure 4.28:** Results for 1D double ratio (top), 2D double ratio (middle) and least squares fit to counts. A 20% Collins asymmetry and 30% Sivers asymmetry was injected.

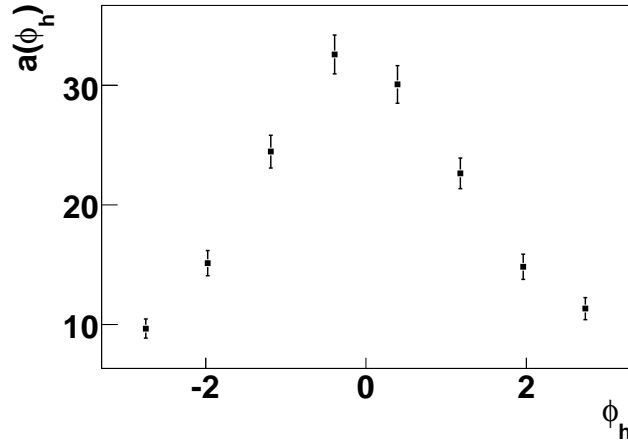


**Figure 4.29:** Acceptances computed with assumptions 4.32 extracted from least squares fit for the  $x_{B_j}$  bin  $0.05 - 1$  and the upstream cell. The y-axis is in an arbitrary scale. It was summed over the angle  $\phi_S$  so that the result can be compared with the acceptance function extracted in an independent analysis [90]. The agreement is reasonable.

predicted in [101]. Furthermore, the least squares method seems to be performing better than the standard double ratio two-dimensional fit. The RMS is closer to one and the deviation from the mean smaller. A special test was done for low statistics, therefore the pulls were additionally computed with twice as many kinematic bins, leaving about 30% of the event counts below the limit of five events. Of course, these low event counts are distributed unevenly between the different particle species.

Pulls were also computed for the method described in section 4.6.6. Again, the cases with high and low number of counts are considered. If low numbers of events are allowed, the least squares fit using Gaussian errors is biased with a mean of  $-0.11 \pm 0.06$ . A similar bias can be observed for the standard two-dimensional method ( $-0.14 \pm 0.07$ ). This bias can be removed if Poissonian errors are used and the mean is compatible with zero ( $0.03 \pm 0.07$ ). Since the fit also gives the coefficients for the acceptances in each bin an additional check can be done. Results were computed for both assumptions 4.31 and 4.32 about the relation of the acceptance functions in the two cells for the different polarization. In Monte Carlo data both constraints are fulfilled by construction. Thus any conclusions taken from the results depend on the fulfillment of the constraints in real data. Fig. 4.29 shows the results for these coefficients, which can be compared with the acceptances extracted from data.

The tests have also been carried out for the least squares fit with acceptances described by truncated Fourier series, for both, the acceptance described by a factorized discrete Fourier transformation (DFT) and a full DFT. They show that already a maximal

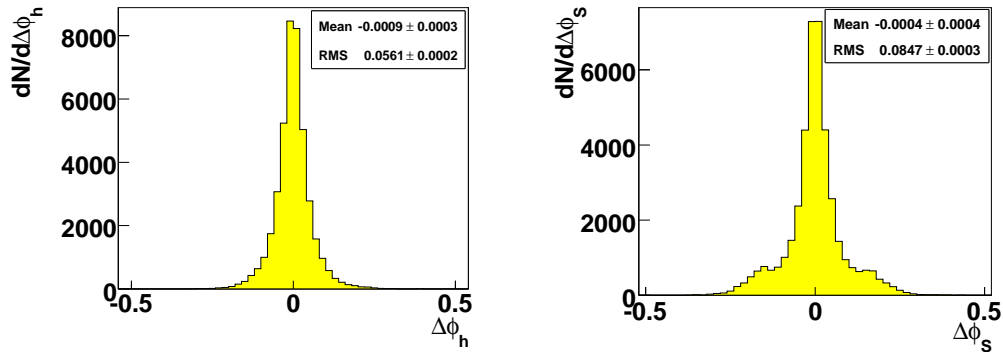


**Figure 4.30:** Deviation of the mean of  $\phi_h$  (left) and  $\phi_S$  from the center of each bin. The bin width is  $\Delta\Phi = 2\pi/8$ . The units on the x-axis is radian.

frequency  $\text{Max}_F$  of three is sufficient to obtain similar results as in the least squares method, where the acceptance is described by a coefficient in each angular bin. However the results using the factorized description of eq. 4.43 exhibit a bias of around one standard deviation, which is not present in the method using the full DFT. So it can be concluded, that the acceptance description cannot be factorized. For all tests the corrections for finite bin sizes as described in sec. 4.6.1.3 were used. Furthermore, the fits were not performed at the center of the bin, but at the mean value of the entries. Without this procedure, biases of about  $1.5 \sigma$  were observed. Fig. 4.30 shows the deviation of the mean value of  $\Phi_h$  and  $\Phi_S$  for Monte Carlo data used.

### Results for Unbinned Maximum Likelihood Fit

According to the findings of the previous paragraph, the full DFT is chosen as the appropriate description of the acceptance. Using this in the unbinned maximum likelihood fit described in section 4.6.8 leads to the accurate extraction of the injected 10 % Collins asymmetry if a flat acceptance was chosen. If the acceptance function 4.53 was used, the mean was one standard deviation away from zero. Even though this is still acceptable, a possible bias could have been introduced due to the non-convergence to the global minimum because the starting values for the acceptance coefficients were not optimal. Since the physical asymmetry is only a small correction to the detector acceptance good starting values can be obtained by Fourier transforming the given count rates. If there are still problems with the convergence, an EM<sup>11</sup>-algorithm can be used to iteratively find the correct values. For the given results only fixed starting values were used, which were oriented at the acceptance function. Another possible source of a bias is the use of the simplified expression for the expected number of events  $\mu$  in eq. 4.47.

<sup>11</sup>Expectation-Maximization

### Summary of Results on Monte Carlo Data

A multitude of different methods to extract the physical asymmetries was presented. As shown, each can be used to produce reliable results, given that the necessary pre-conditions are fulfilled. In the presence of enough statistics and small asymmetries, the one-dimensional method can be used. The drawback here is, that in principle, a two dimensional fit has to be made to extract the magnitude of the correlations between the parameters. This way, biases introduced by the detector acceptance can be excluded. If the correlations are small, the one dimensional fit has the advantage of being well understood and having only small binning effects, because the bin size can be chosen smaller than in a two dimensional method. With the two dimensional method using the double ratio in eq. 4.22 the correlation coefficients can be determined. In the presence of large amplitudes, a two dimensional method is necessary unless the acceptance is known exactly. The least squares fit has the advantage, that the distribution of the target values can be easily incorporated. Because the fit is directly to the number of counts, one can assume Gaussian or Poissonian distribution as necessary. In the presence of small numbers of counts the maximum likelihood method can be used. The feasibility of the Fourier approach in the description of the spectrometer acceptance was demonstrated. Due to the lower number of parameters as opposed to the use of coefficients in each angular bin, this approach can also be used when the number of equations in the least squares fit is reduced due to low statistics. Furthermore, the description of the acceptance in terms of trigonometric functions is more natural, considering that the physical modulations to be extracted are of the same form.

## 5. Results

This section will present the results obtained from data taken in the years 2003 and 2004. Data taking was divided in periods of about one week of effective beam time. Periods, in which the target cells were in opposite polarization configurations and which have been taken close together in time, were combined to extract raw asymmetries. Due to the smallness of the extracted asymmetries and therefore small correlation between the different asymmetries [51] the use of the one-dimensional fit is justified. The raw asymmetries were corrected with the mean values for depolarization factor, target polarization and dilution factor of the target to compute the final asymmetries. To produce the results a weighted mean of asymmetries from combinations taken close in time was computed. These were the periods P1H and P1G taken in 2003 and the combination of the periods W33/W34 and W35/W36 respectively taken in the year 2004. Results were obtained for Collins and Sivers asymmetries for all hadrons and leading hadrons. As described in chapter 4, the reasoning for the leading hadron analysis is the expectancy, that the leading hadron is more sensitive to the properties of the struck quark than the other hadrons in the event to which less energy was transferred. For the two hadron case results were obtained for all pairs in which one particle was positive and the other one negative. Since the computation of the two hadron asymmetries requires the ordering of the pair, the positively charged particle was taken as the first and the negatively charged particle as the second particle. Another possibility to impose ordering is according to the kinematic variable  $z$  of each hadron. Much like in the one hadron case, combining the leading and subleading hadron in each event can lead to an enhancement of the signal as compared with all oppositely charged combinations [39][62]. It also leads to more possible combinations. The binning chosen and numerical values for the asymmetries are listed in the appendix. In figs. 5.1-5.12 asymmetries for one hadron asymmetries are shown. Two hadron asymmetries are depicted in figs. 5.13-5.15 for all hadron pairs and in figs. 5.16-5.21 for leading pairs.

### 5.1 One Hadron Asymmetries

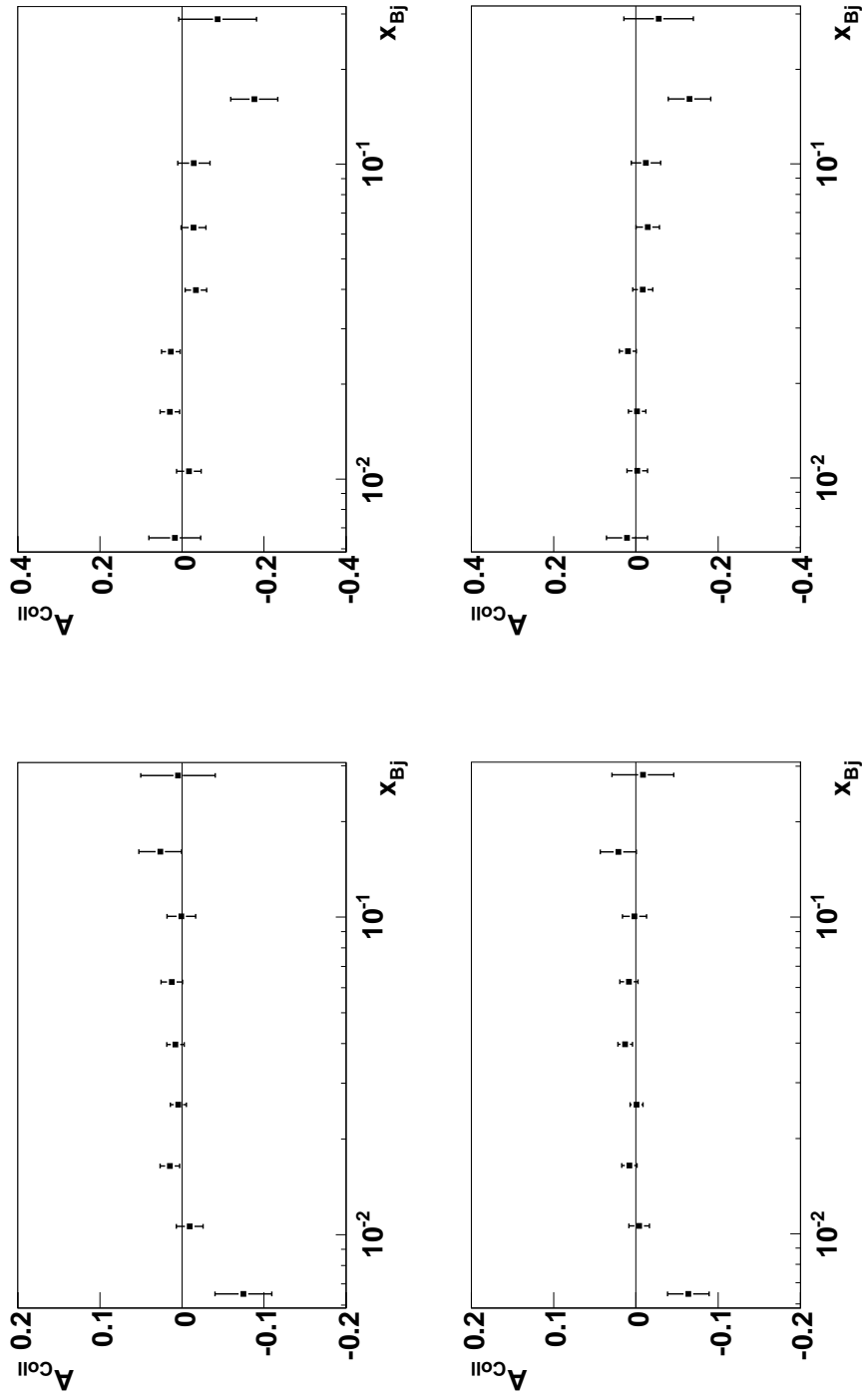


Figure 5.1: Collins asymmetries for leading (top) and all (bottom)  $\pi^+$  (left) and  $K^+$  (right) in  $x_{Bj}$  binning

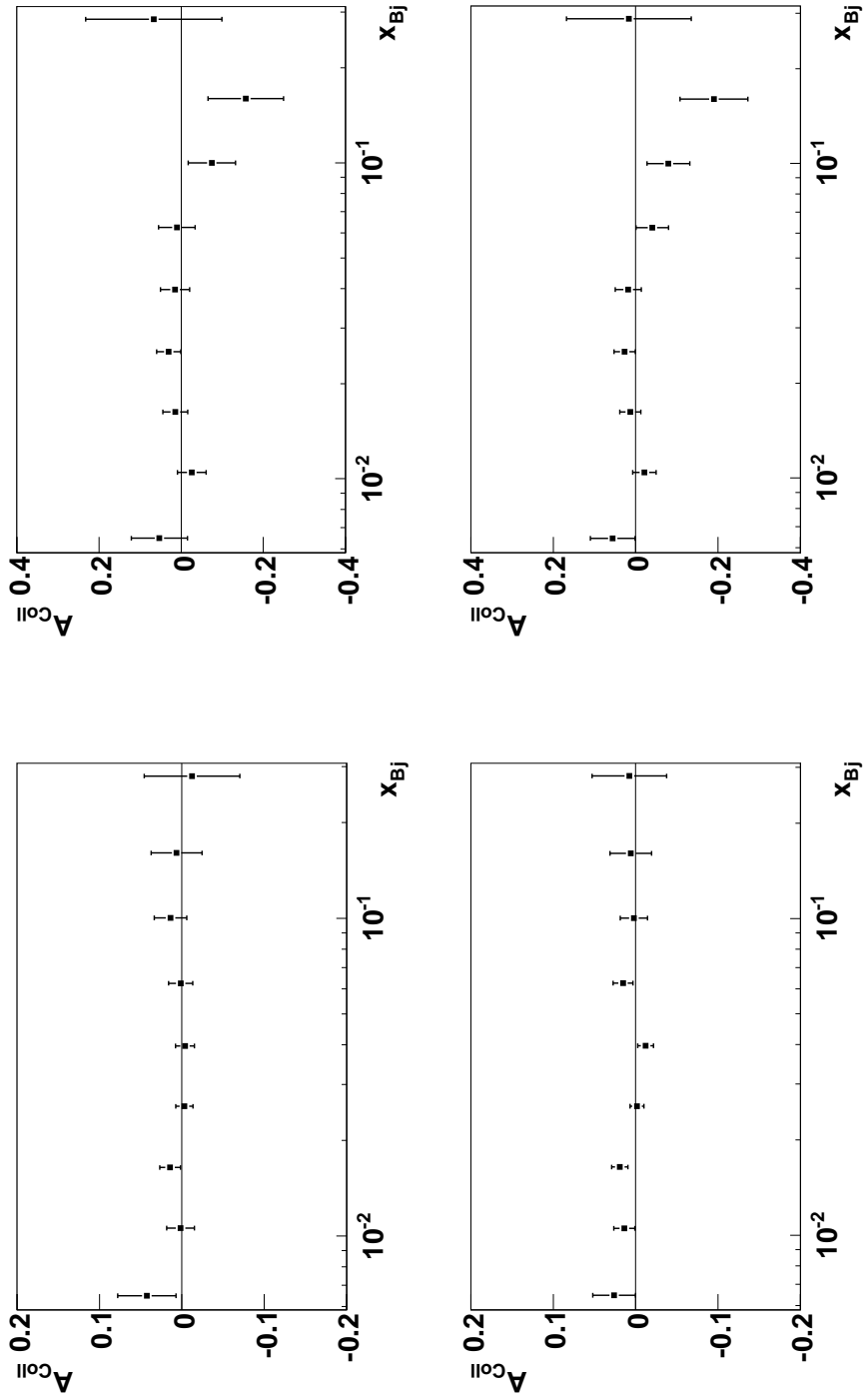
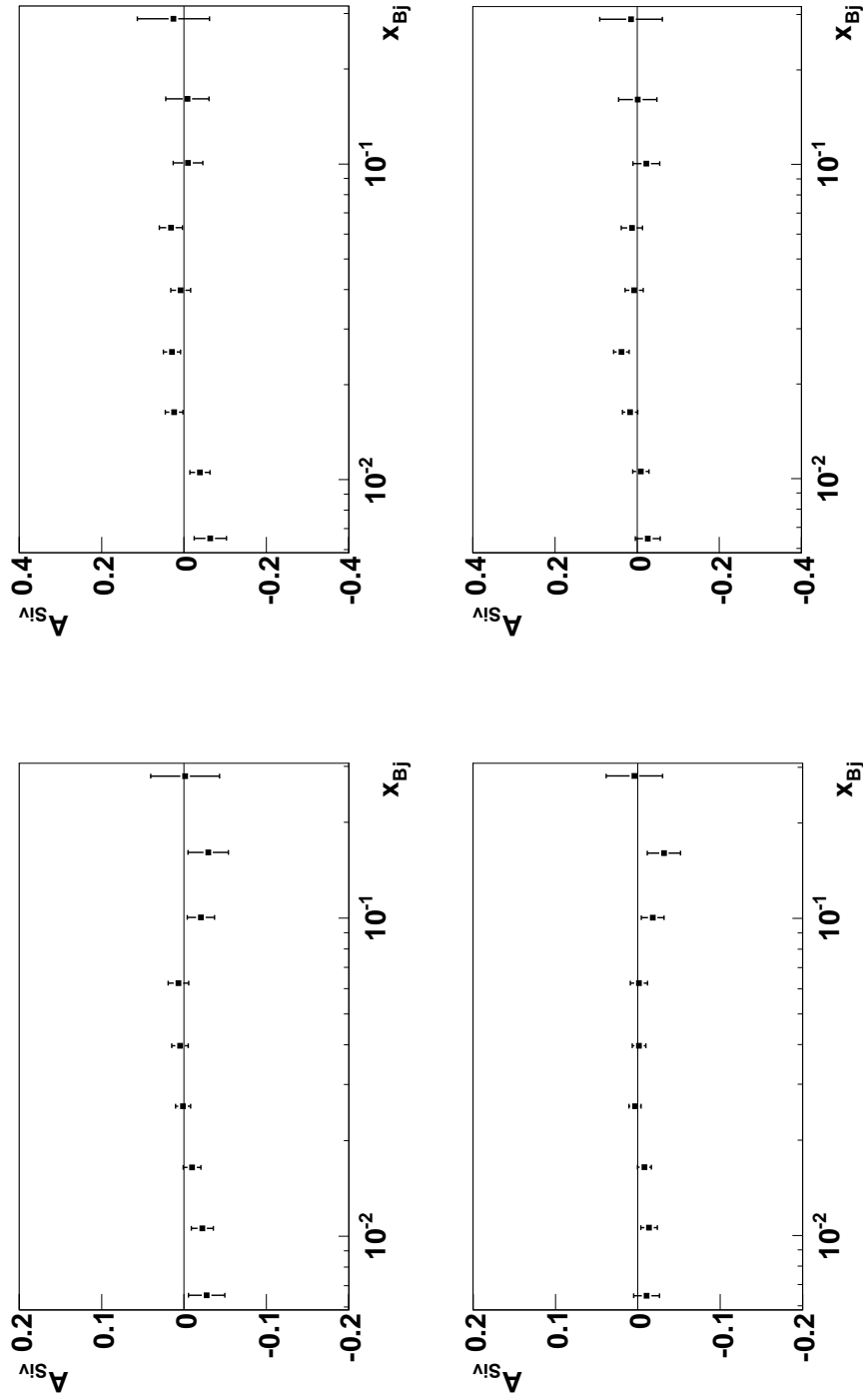


Figure 5.2: Collins asymmetries for leading (top) and all (bottom)  $\pi^-$  (left) and  $K^-$  (right) in  $x_{Bj}$  binning



**Figure 5.3:** Sivers asymmetries for leading (top) and all (bottom)  $\pi^+$  (left) and  $K^+$  (right) in  $x_{Bj}$  binning

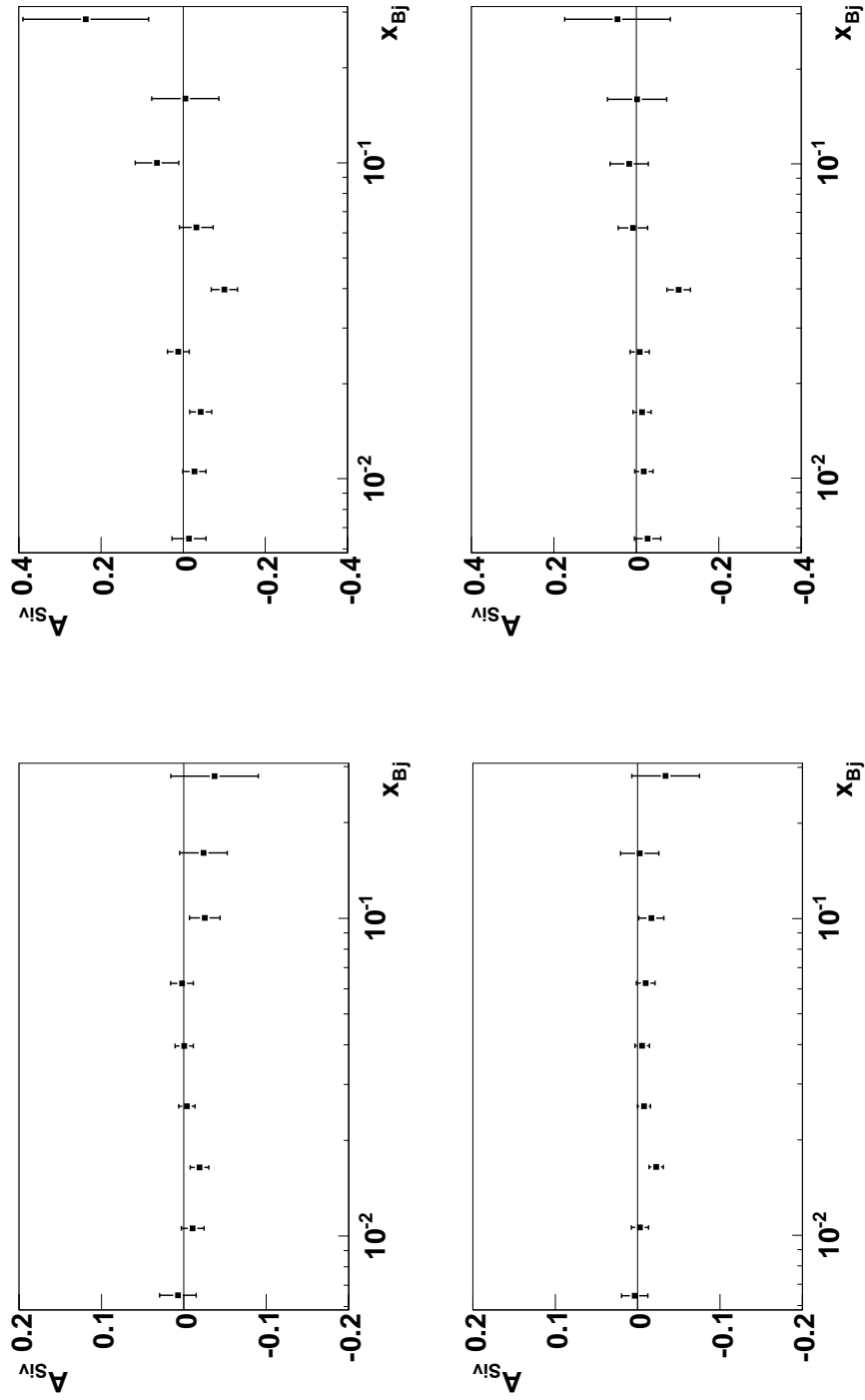


Figure 5.4: Sivers asymmetries for leading (top) and all (bottom)  $\pi^-$  (left) and  $K^-$  (right) in  $x_{Bj}$  binning

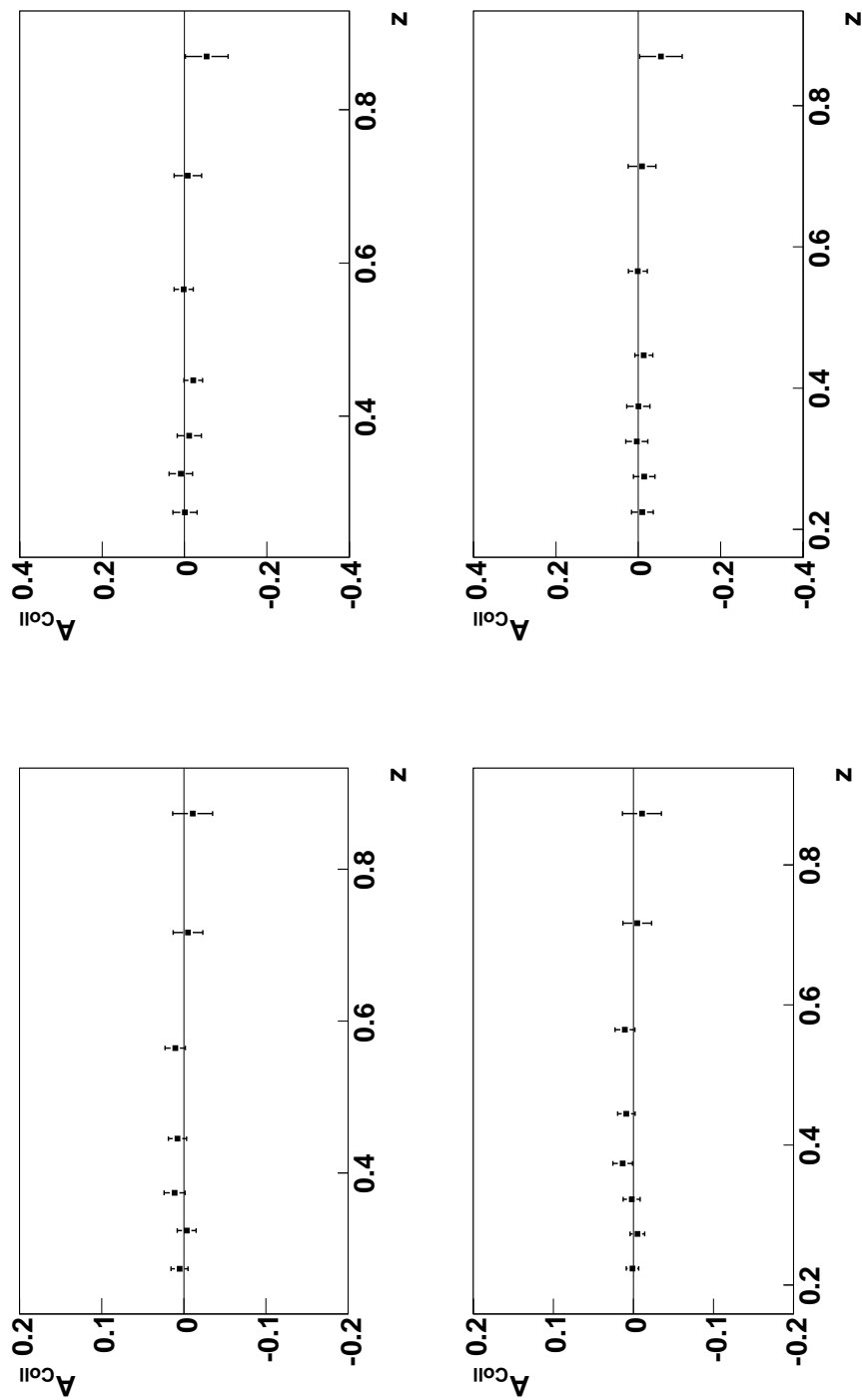


Figure 5.5: Collins asymmetries for leading (top) and all (bottom)  $\pi^+$  (left) and  $K^+$  (right) in  $z$  binning

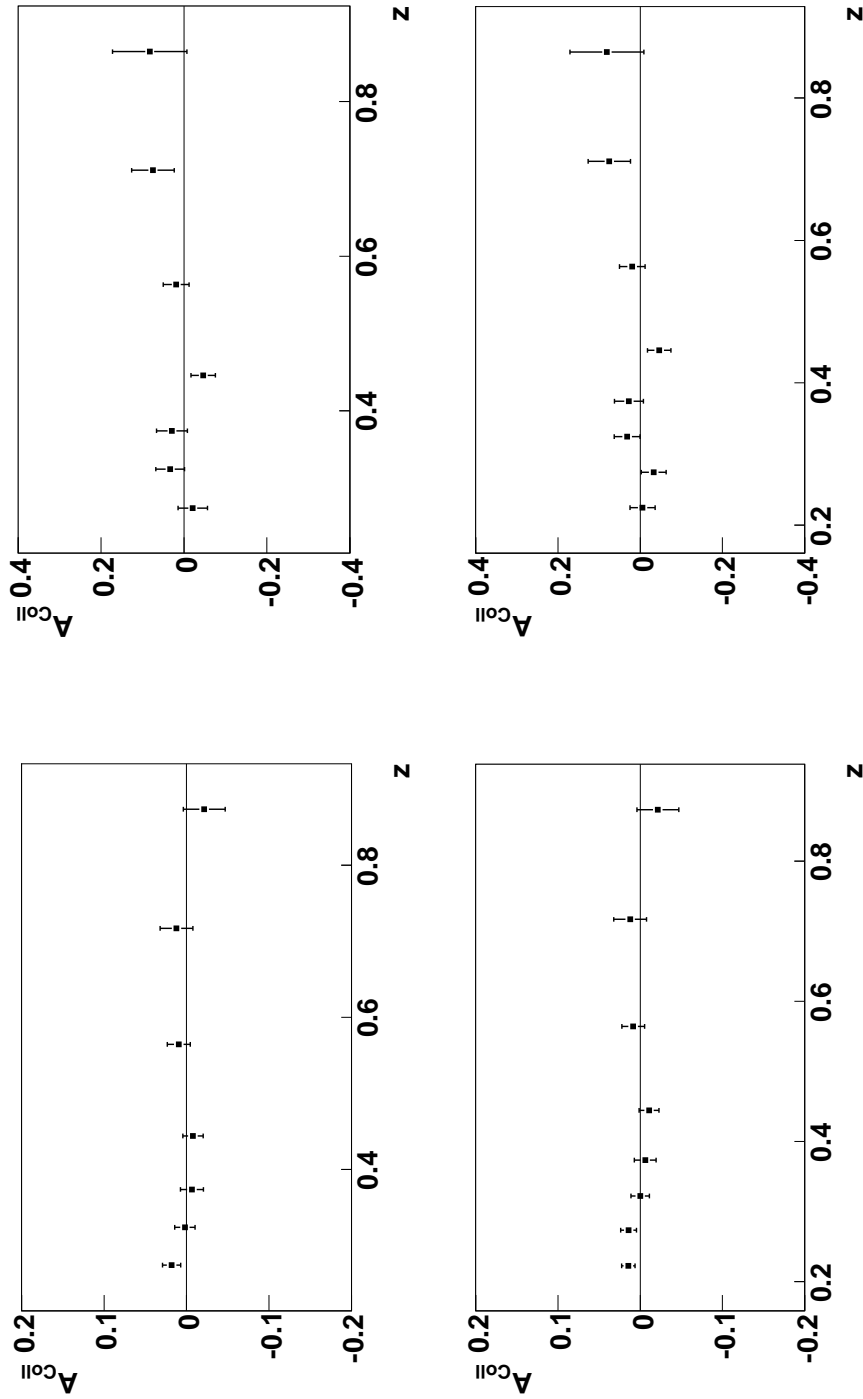


Figure 5.6: Collins asymmetries for leading (top) and all (bottom)  $\pi^-$  (left) and  $K^-$  (right) in  $z$  binning

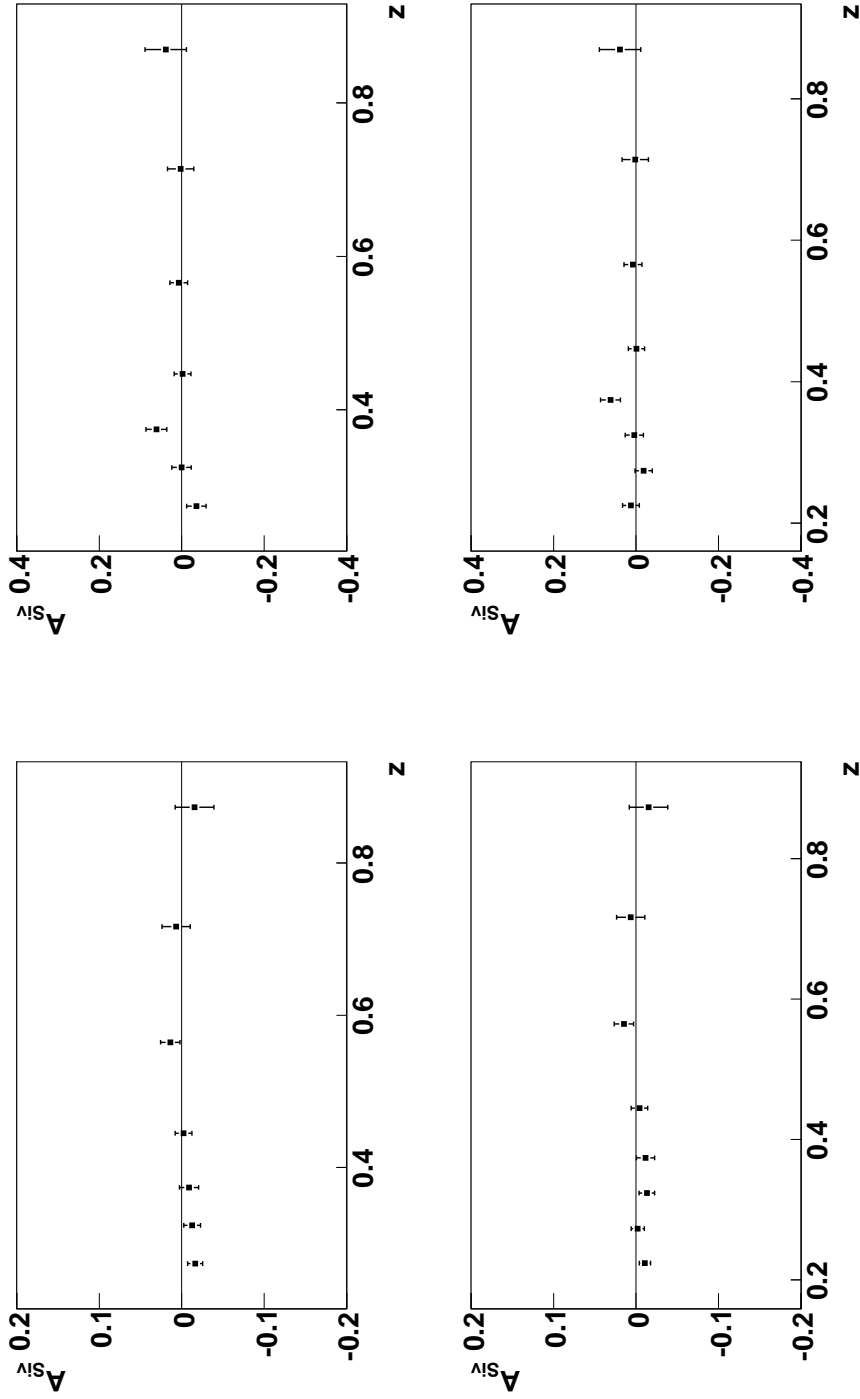


Figure 5.7: Sivers asymmetries for leading (top) and all (bottom)  $\pi^+$  (left) and  $K^+$  (right) in  $z$  binning

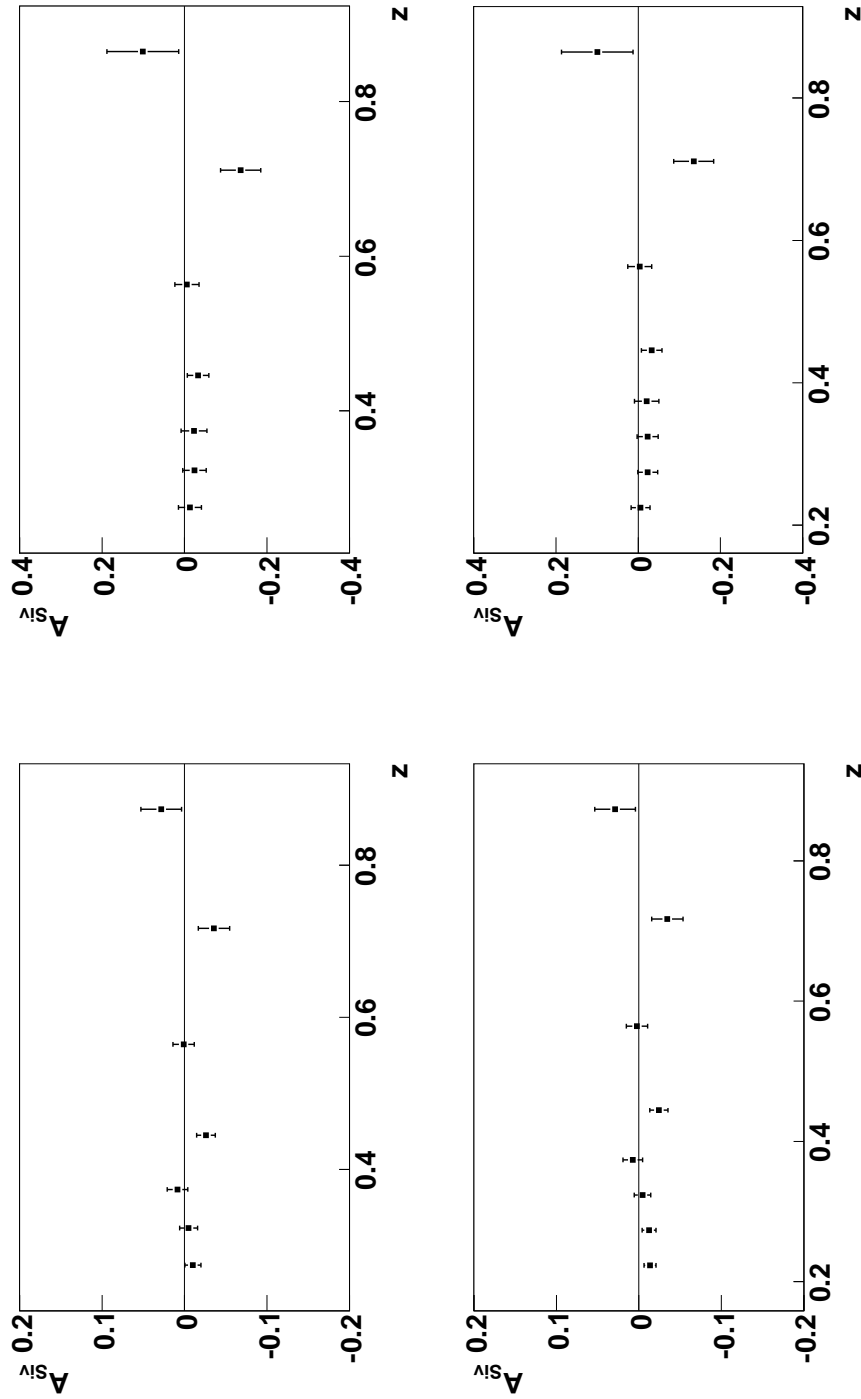
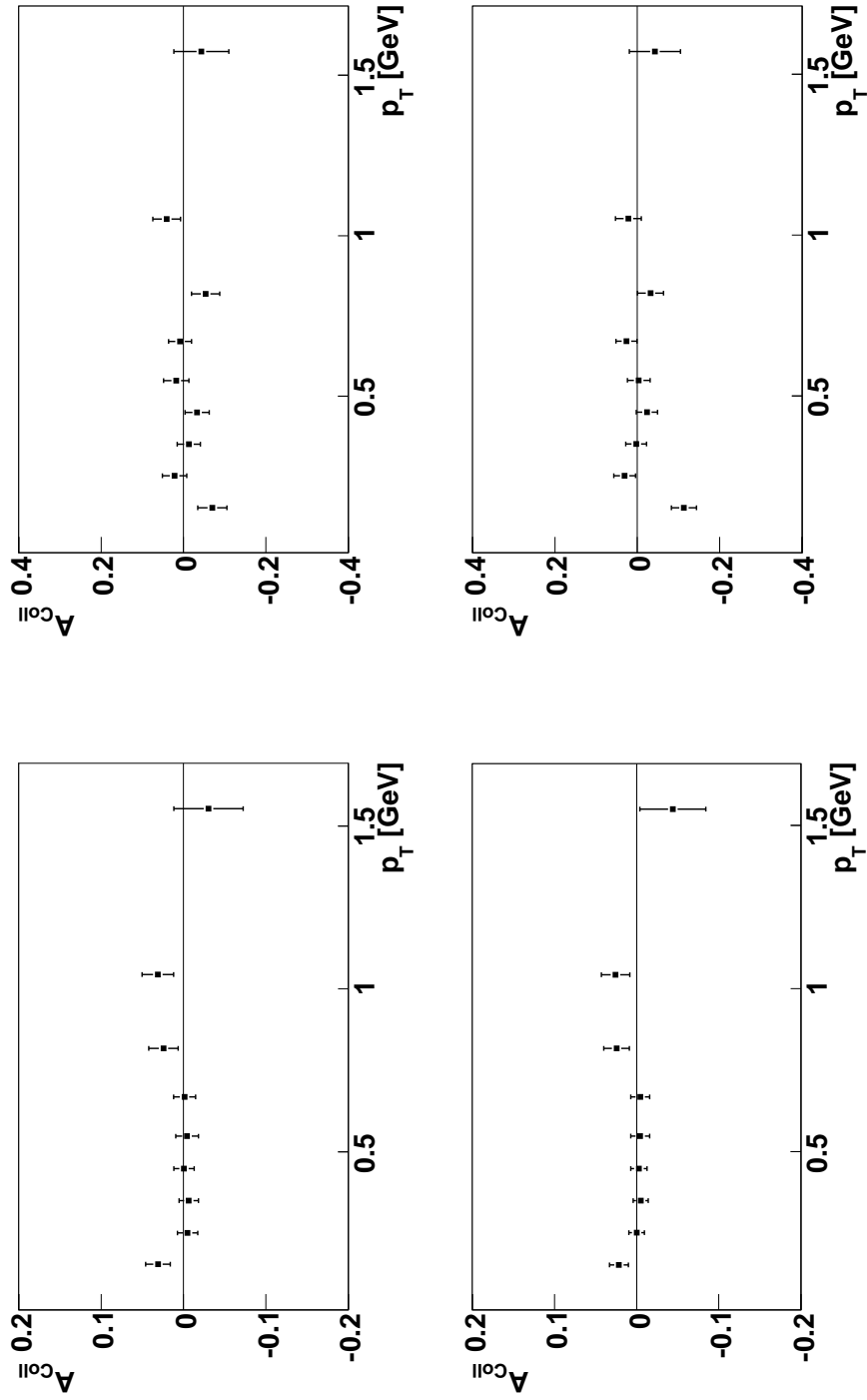


Figure 5.8: Sivers asymmetries for leading (top) and all (bottom)  $\pi^-$  (left) and  $K^-$  (right) in  $z$  binning



**Figure 5.9:** Collins asymmetries for leading (top) and all (bottom)  $\pi^+$  (left) and  $K^+$  (right) in  $p_T$  binning

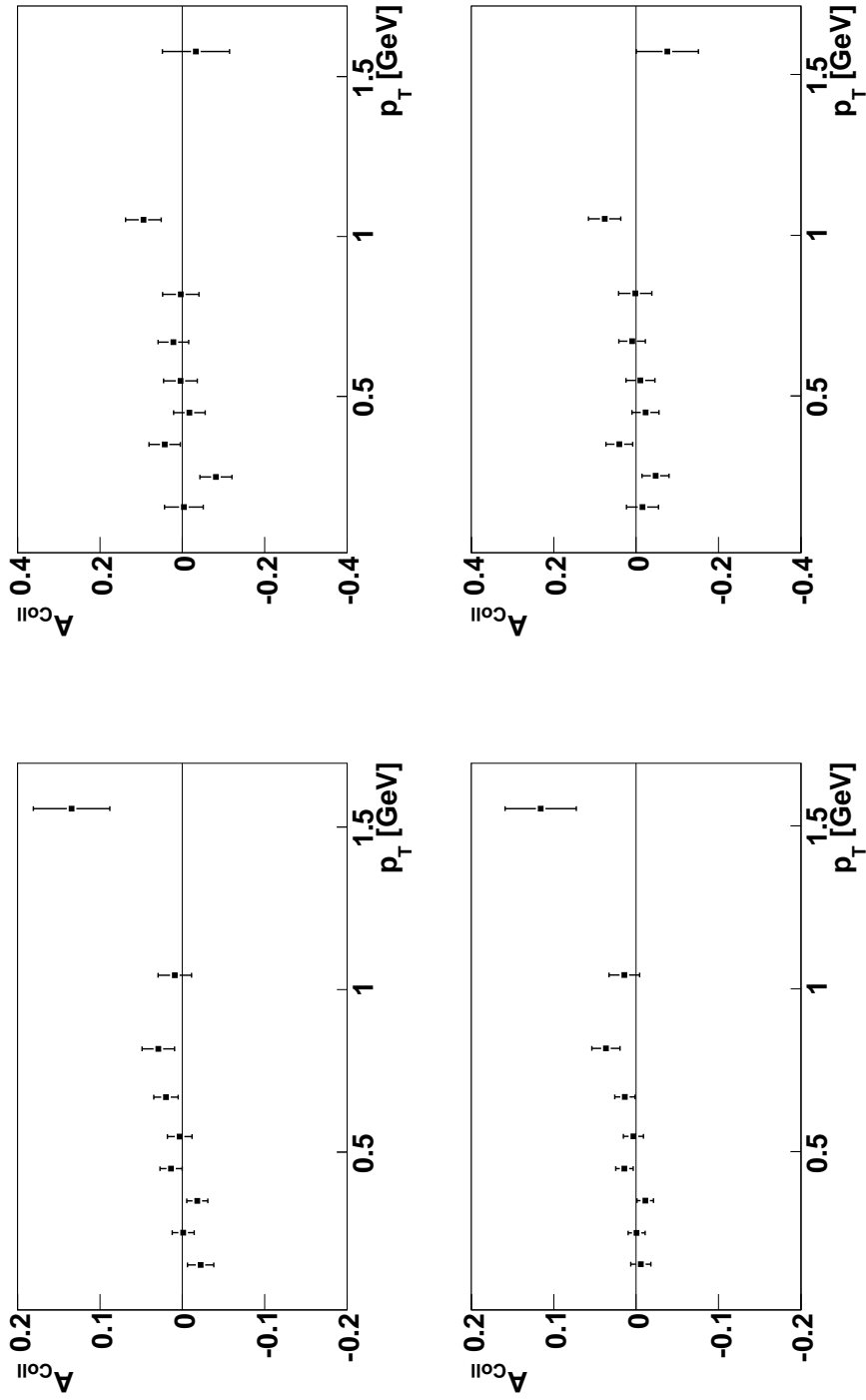
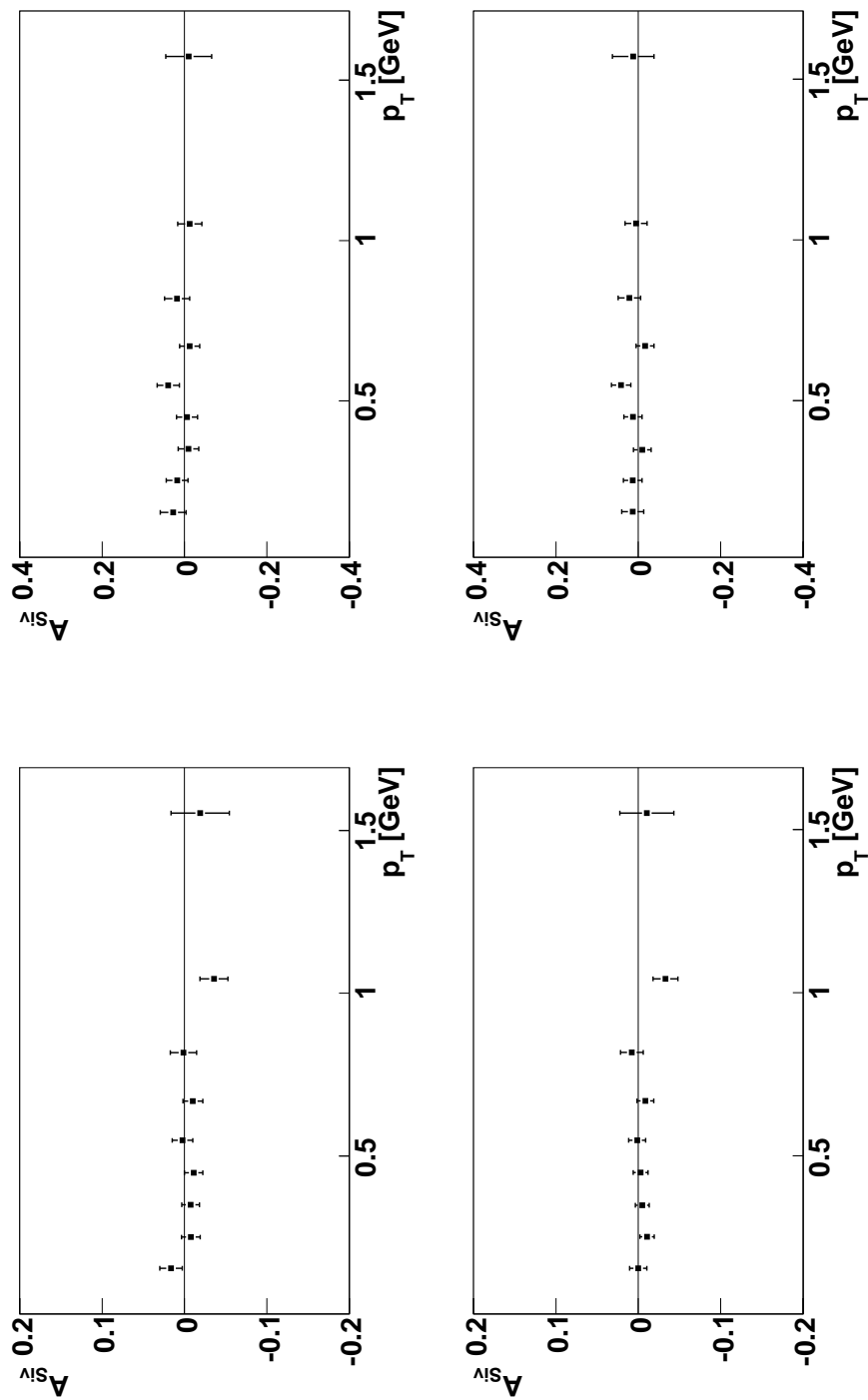


Figure 5.10: Collins asymmetries for leading (top) and all (bottom)  $\pi^-$  (left) and  $K^-$  (right) in  $p_T$  binning



**Figure 5.11:** Sivers asymmetries for leading (top) and all (bottom)  $\pi^+$  (left) and  $K^+$  (right) in  $p_T$  binning

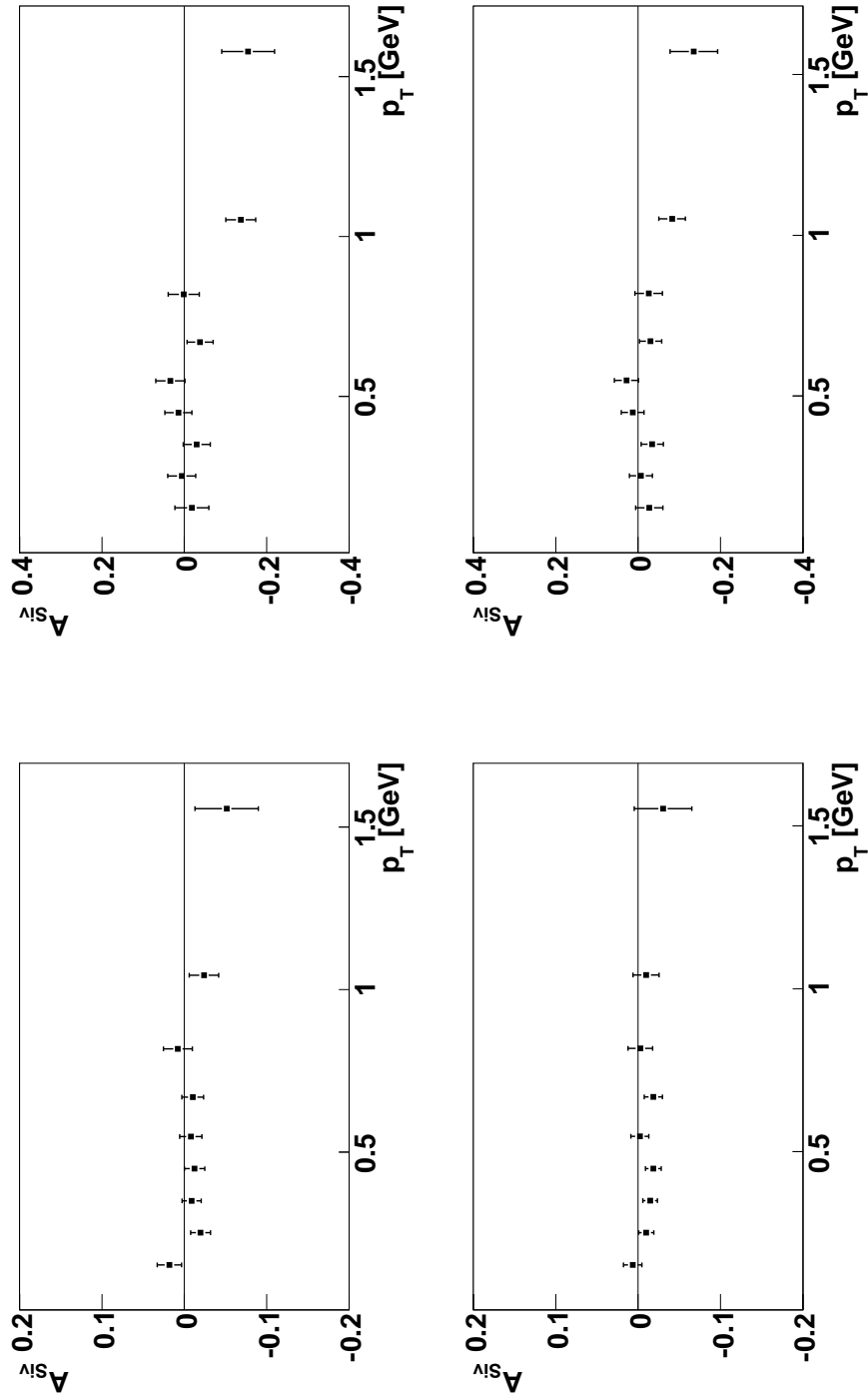


Figure 5.12: Sivers asymmetries for leading (top) and all (bottom)  $\pi^-$  (left) and  $K^-$  (right) in  $p_T$  binning

## 5.2 Two Hadron asymmetries

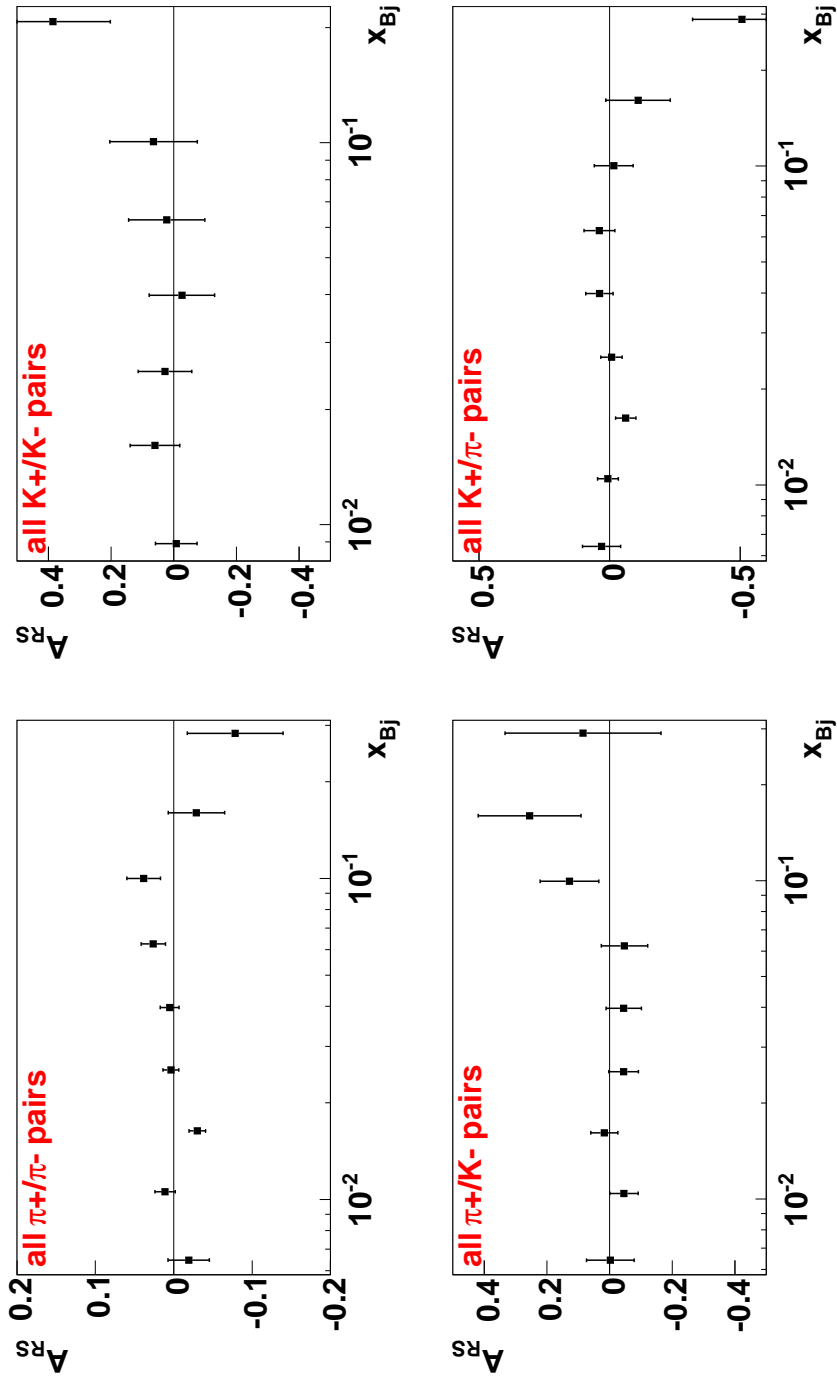
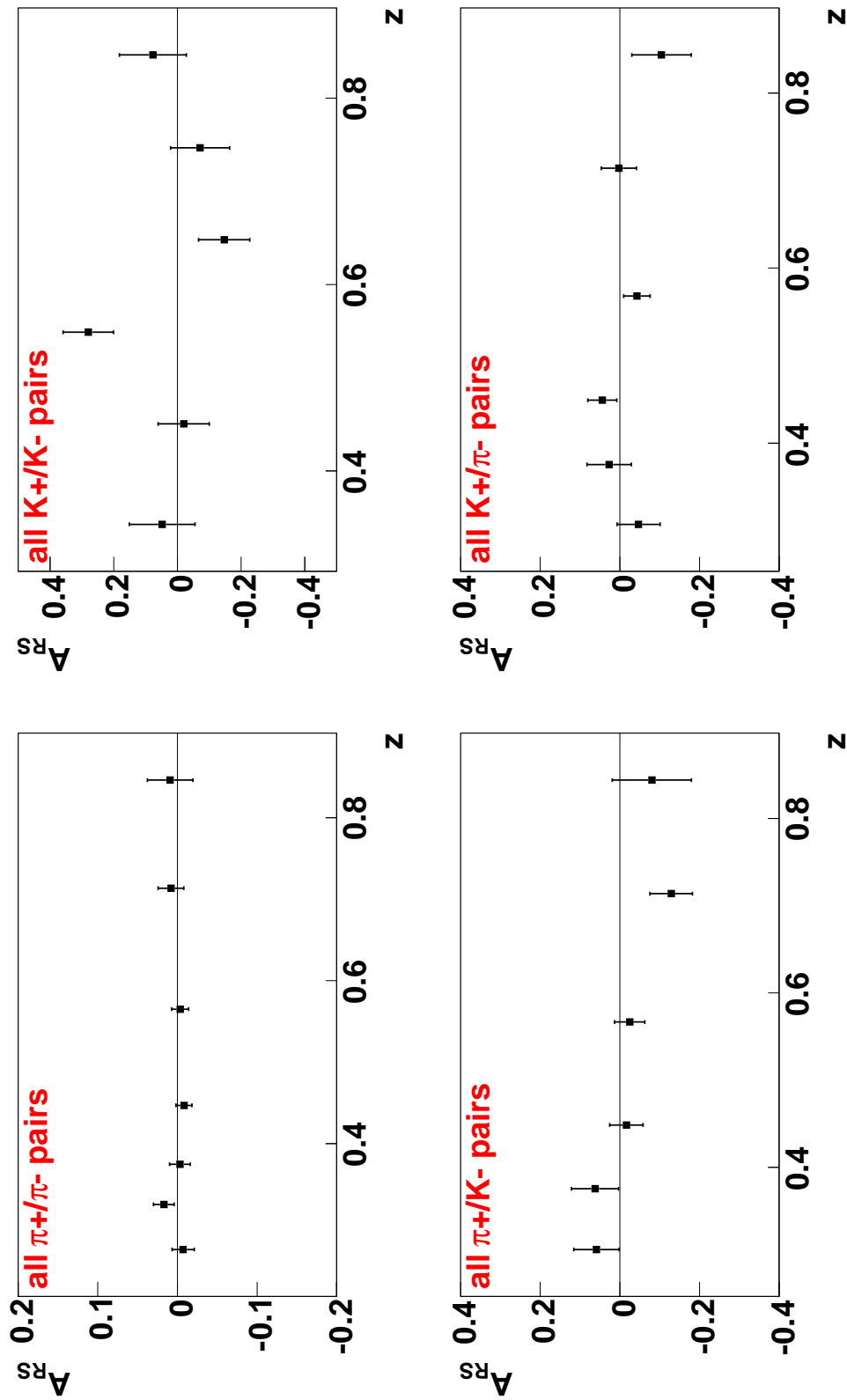
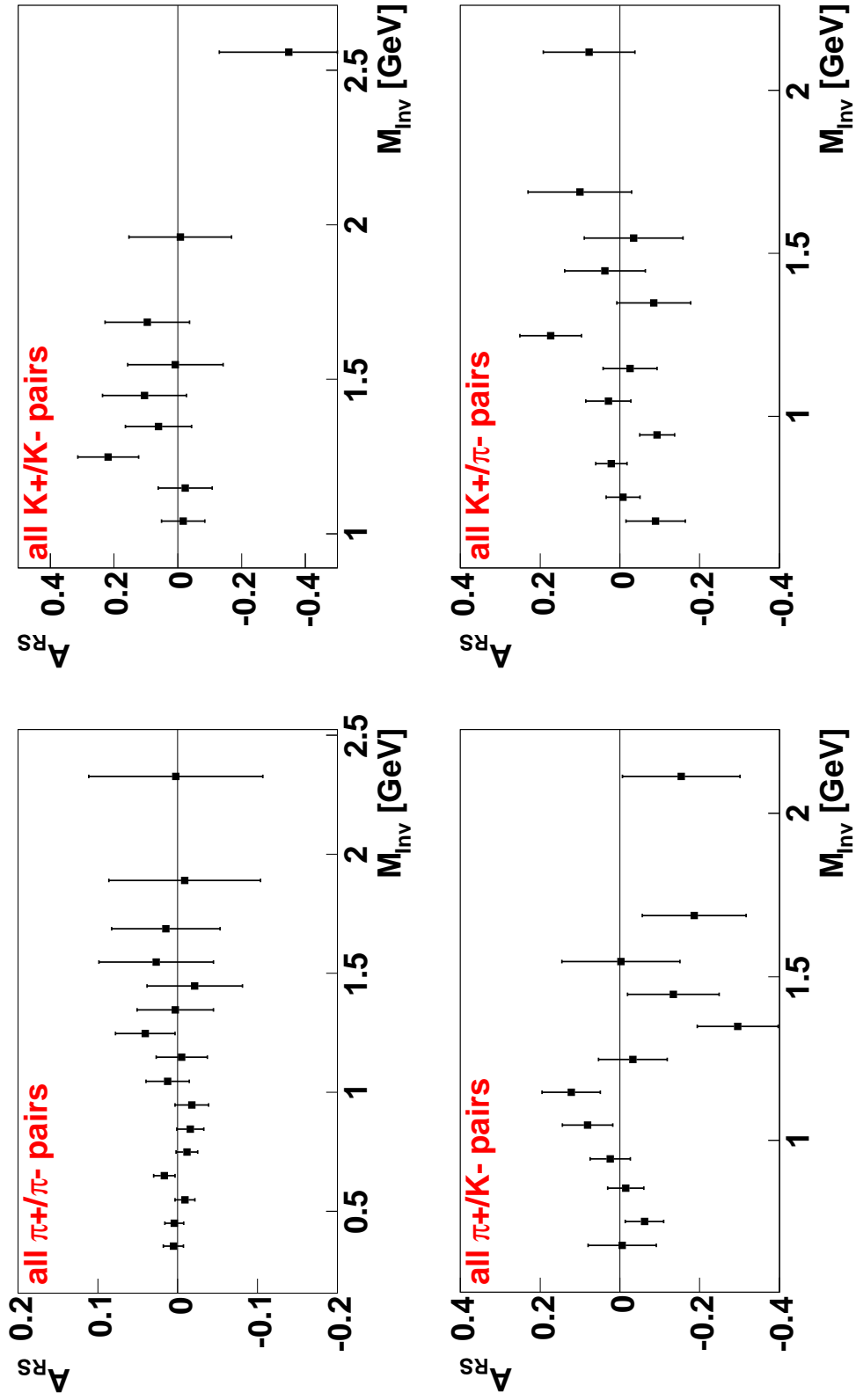


Figure 5.13: Two hadron asymmetries in  $x_{Bj}$  binning. Notice the scale on the combination  $K^+/\pi^-$

Figure 5.14: Two hadron asymmetries in  $z$  binning

Figure 5.15: Two hadron asymmetries in  $M_{\text{Inv}}$  binning

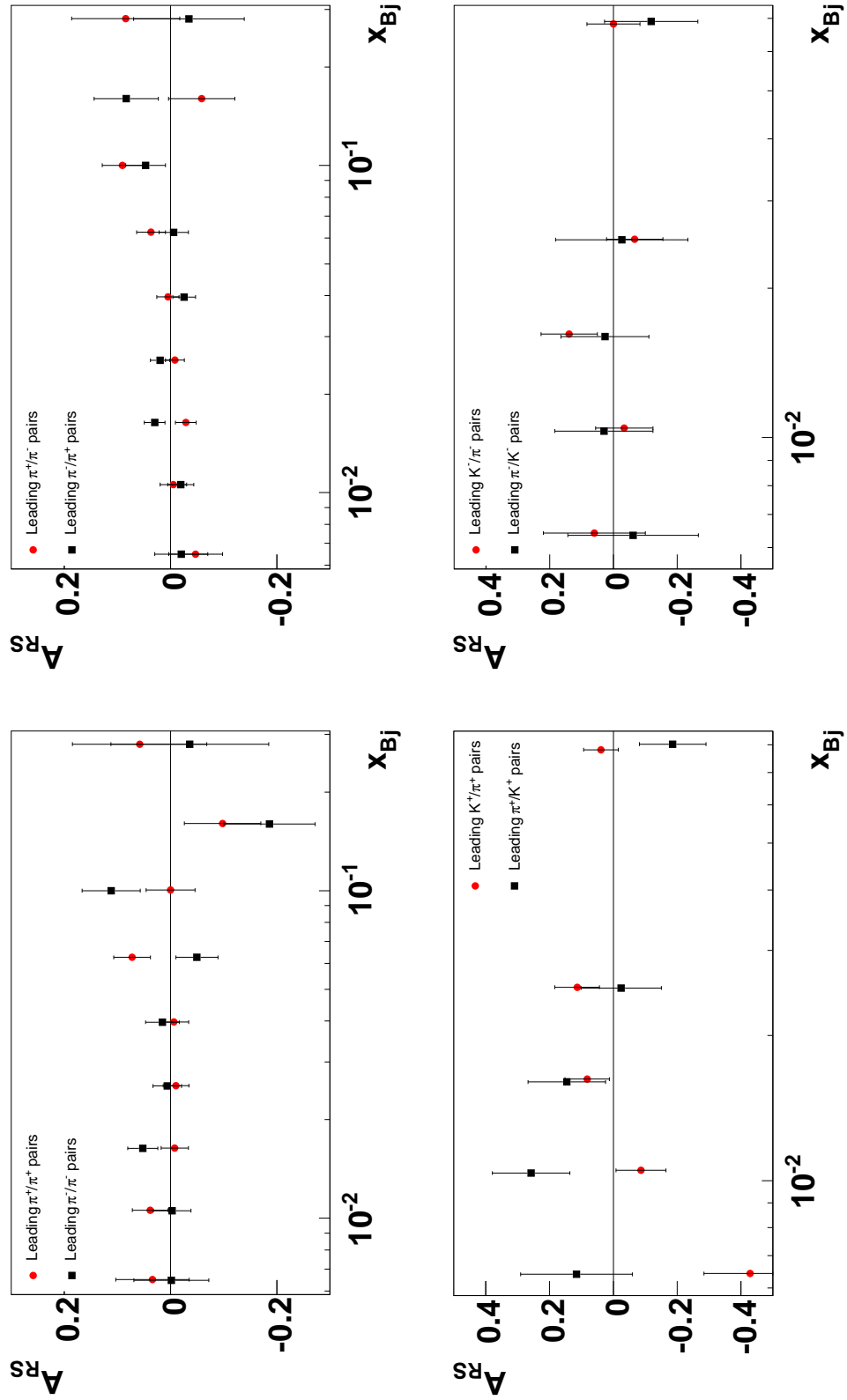
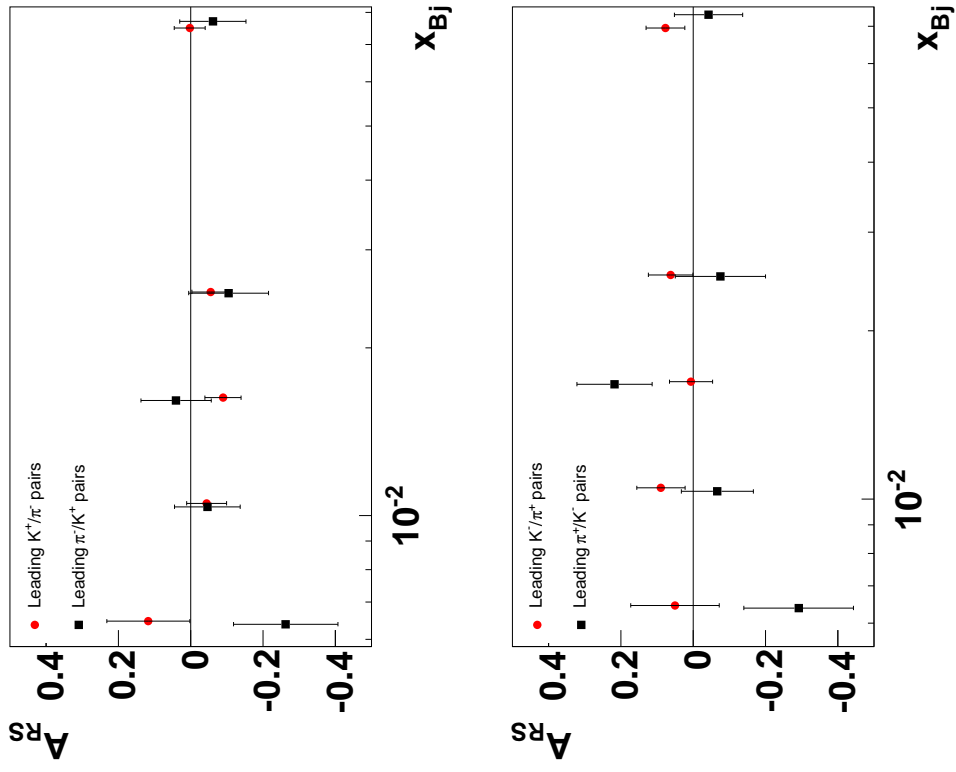


Figure 5.16: Leading two hadron asymmetries in  $x_{Bj}$  binning

Figure 5.17: Leading two hadron asymmetries in  $x_{Bj}$  binning

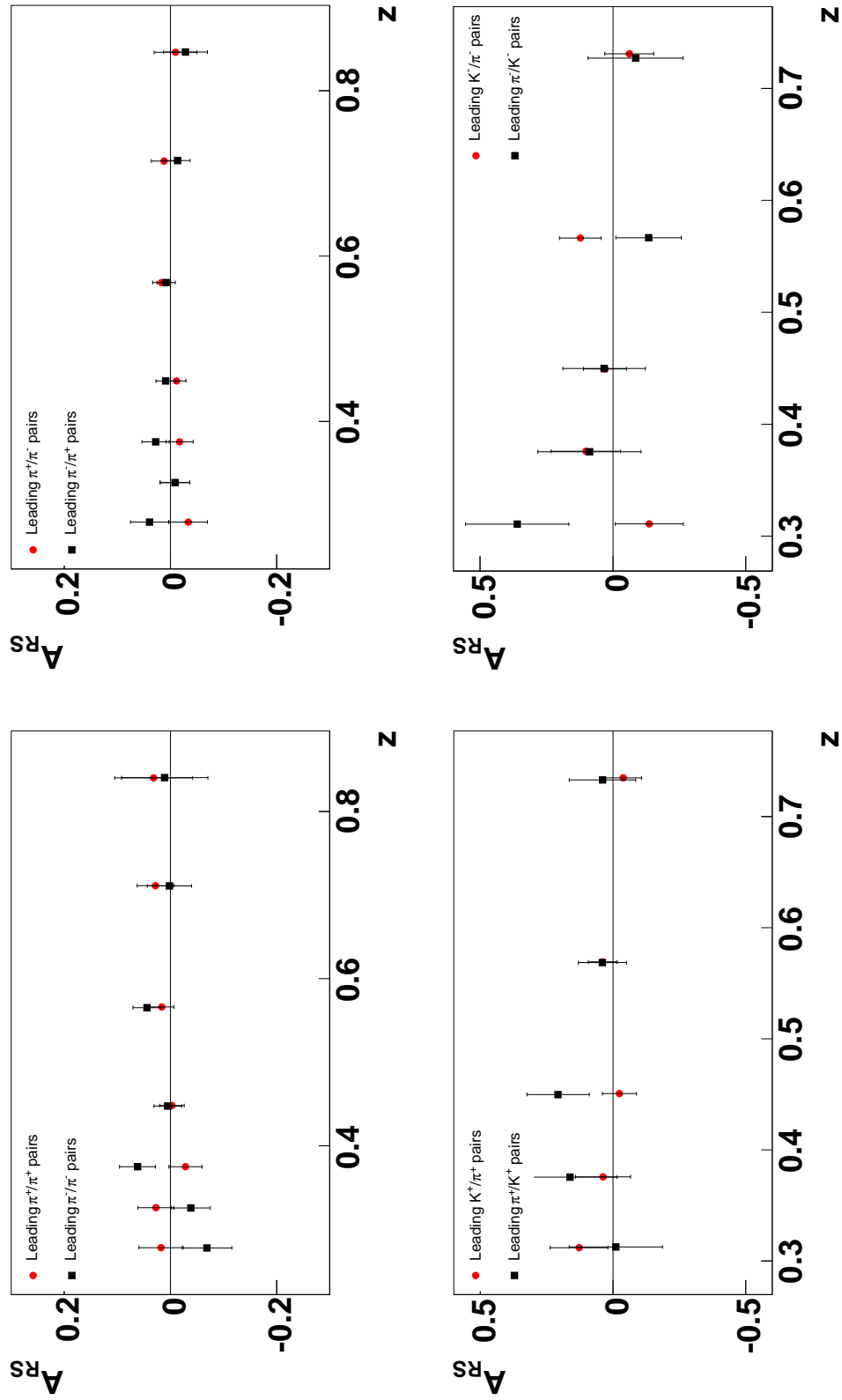
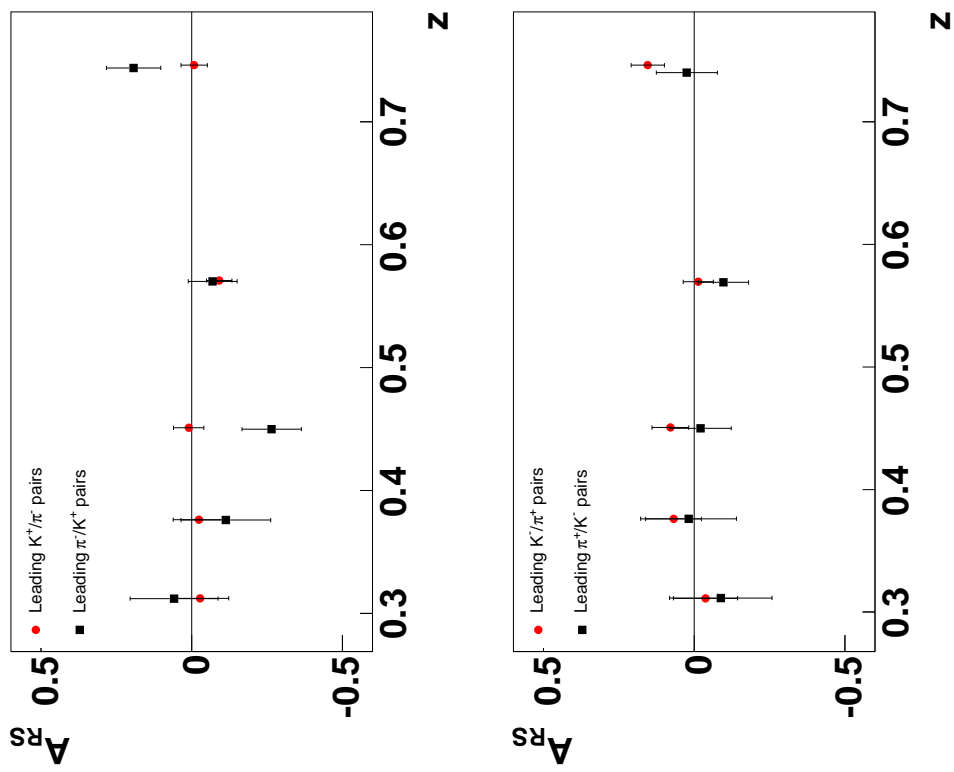


Figure 5.18: Leading two hadron asymmetries in  $z$  binning

Figure 5.19: Leading two hadron asymmetries in  $z$  binning

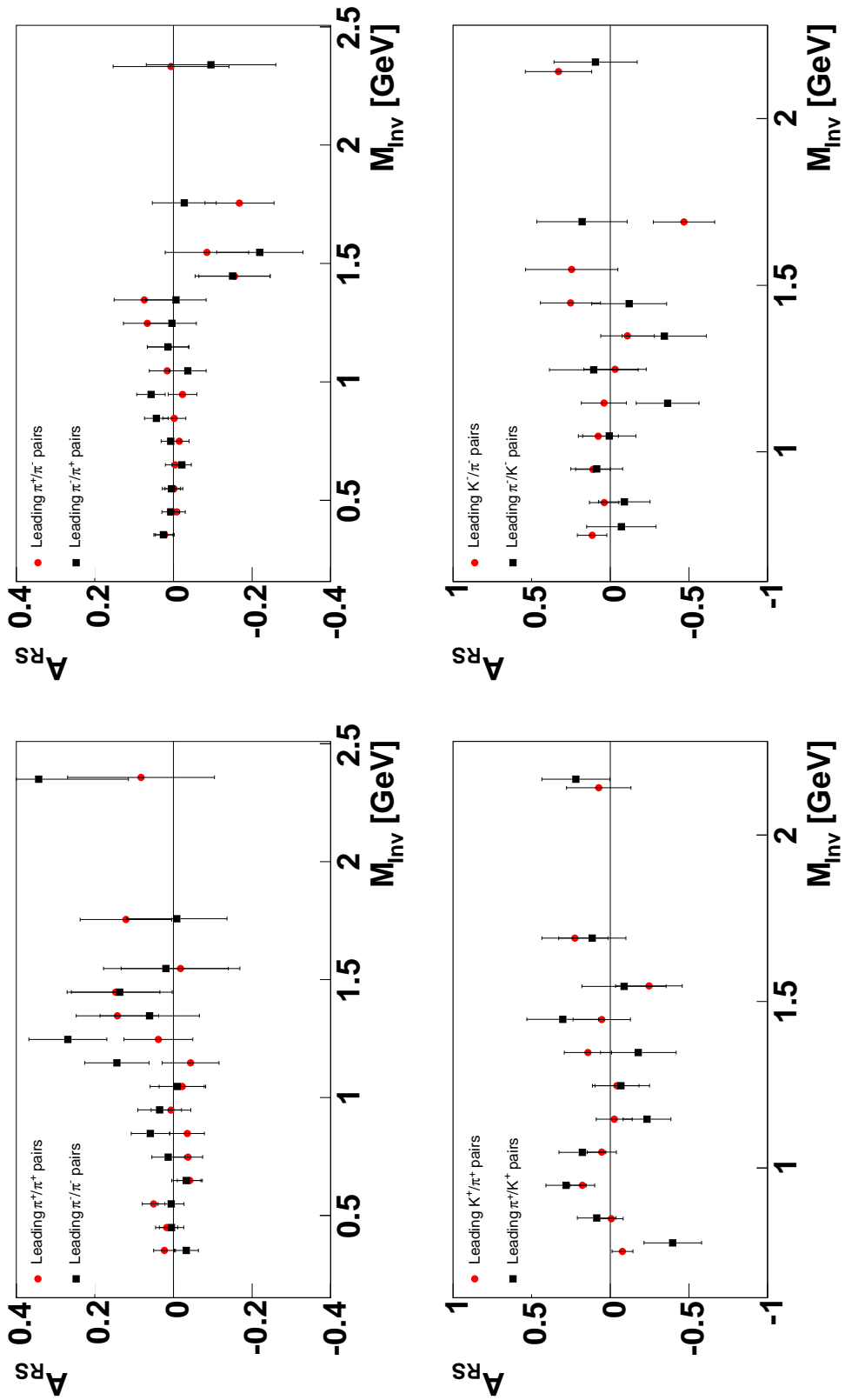


Figure 5.20: Leading two hadron asymmetries in  $M_{Inv}$  binning

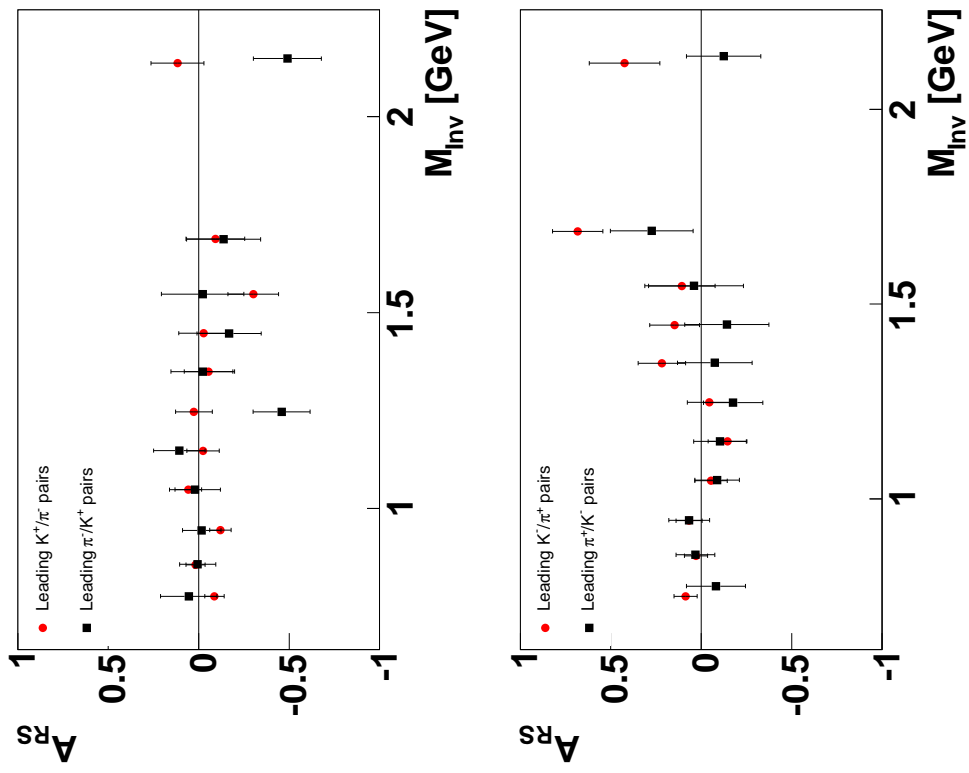


Figure 5.21: Leading two hadron asymmetries in  $M_{Inv}$  binning

### 5.3 Systematic Studies

To exclude any sizable systematic error a multitude of studies was performed [51][111]. The most important among these are listed in the following. They can be divided into studies that yield real asymmetries and which are:

- Compatibility of sub-periods
- Compatibility of different estimators
- Splitting the target cells so that real asymmetries are preserved
- Splitting the detector in segments
- Splitting periods in time
- Trigger dependent asymmetries

In these studies, the data was combined in a way so that physical asymmetries are expected. Studies which were performed that give false asymmetries are:

- Scrambling data
- Splitting the target cell so that real asymmetries are canceled

For these studies the data was combined such that no asymmetry is expected. Furthermore the double ratio, given in eq. 4.22 was monitored. Only a double ratio value, that stays constant in time for each angular bin can give the confidence that systematic effects due to varying spectrometer acceptances can be neglected. For all the above tests, it was ensured that all deviations from the expected values agree well within the statistical errors. The combined results of all systematic studies performed is, that the systematic errors are considerably smaller than the statistical errors.

### 5.4 Discussion and Comparison with other Experiments

In the beginning of this chapter, the COMPASS results for transverse single spin asymmetries with particle identification were shown. Collins and Sivers asymmetries were extracted separately for identified  $\pi^+/\pi^-$  and  $K^+/K^-$  and two hadron asymmetries for identified pairs of charged pions and kaons. The measured asymmetries are within the statistical errors compatible with zero. To be more sensitive to the properties of the fragmenting quark, the same asymmetries were also extracted for subsamples containing only the leading hadrons in the event. No significant differences can be observed between the leading sample and the sample containing all hadrons in an event. Since the asymmetries can be expressed as a convolution of quark distribution function and fragmentation function their smallness can be caused either by a small distribution or fragmentation function. Because the COMPASS collaboration uses a deuterium target another interpretation is a cancellation between contributions from neutron and proton. This will be discussed in sec. 5.5. To investigate if the fragmentation function

or respective distribution function is small compared with the statistical errors, measurements by other experiments can give valuable input. Fragmentation functions are measured by the BELLE experiment. BELLE uses colliding  $e^+e^-$  beams at a center of mass energy of about 10 GeV and investigates the fragmentation into hadrons. Figure 5.22 shows asymmetries computed from charged pion pair production which correspond to the product of the Collins fragmentation functions of quark and antiquark.

#### 5.4.1 Collins and Sivers Asymmetries

Experiments measuring Collins and Sivers asymmetries are performed at Jefferson Lab (JLab) and DESY<sup>1</sup>. The experiments at RHIC situated at Brookhaven National Lab also aim at a transversity measurement albeit using collisions of polarized protons. Both, the RHIC and JLab experiments are still at an early stage thus leaving the HERMES<sup>2</sup> experiment at DESY for a comparison. HERMES uses a gaseous target of polarized protons off which an electron beam scatters. The experiment benefited of a beam with a momentum of 27.6 GeV. Therefore HERMES measures at higher values of  $x_{Bj}$  at a comparable mean 4-momentum transfer than COMPASS. But the most important difference is the use of a proton target instead of a deuterium one. With this target, the HERMES collaboration extracted the transverse single spin asymmetries shown in figs. 5.23 and 5.24.

They show significant Collins and Sivers effects. If these asymmetries are not attributed to higher twist effects, one can conclude, that the convolution of the transversity distribution function of the proton and Collins fragmentation function exists. Because the Sivers effect is connected to the unpolarized fragmentation function, the measurements point to a Sivers distribution function with a significantly higher amplitude than measured at COMPASS. In contrast to the results presented in this work, HERMES' kinematical range is limited. For low values of  $x_{Bj}$  the statistic is limited which becomes apparent in the number of kinematic bins. Furthermore an analysis of the leading subsample has not been done. For a comparison between the two experiments it is instructive to look at the extracted Collins and Sivers asymmetries for identified kaons. The  $K^-$  asymmetries are expected to depend only on kinematics, because in both cases its constituent quarks can only originate from the sea. In contrast, the  $K^+$  contains a u-quark and the u-quark distribution is not the same in proton and deuteron. The comparison for Collins asymmetries is shown in fig. 5.25 and for Sivers in fig. 5.26. As expected the  $K^+$  asymmetries differ. The difference is more pronounced for the Sivers asymmetries. Here it seems as if the COMPASS data are a good continuation in the  $x_{Bj}$  region dominated by sea quarks. The agreement of the  $K^-$  asymmetries is very good, which is an exciting result because it shows, that both experiments measure the same effect in the sea-quark region.

#### 5.4.2 Two Hadron Asymmetries

The measurement of single spin asymmetries with two hadrons in the final state probes the convolution of the transversity distribution function with the two hadron interference fragmentation function. The later was also measured at BELLE and analysis has

<sup>1</sup>Deutsches Elektronen SYnchrotron

<sup>2</sup>HERa MEasurement of Spin

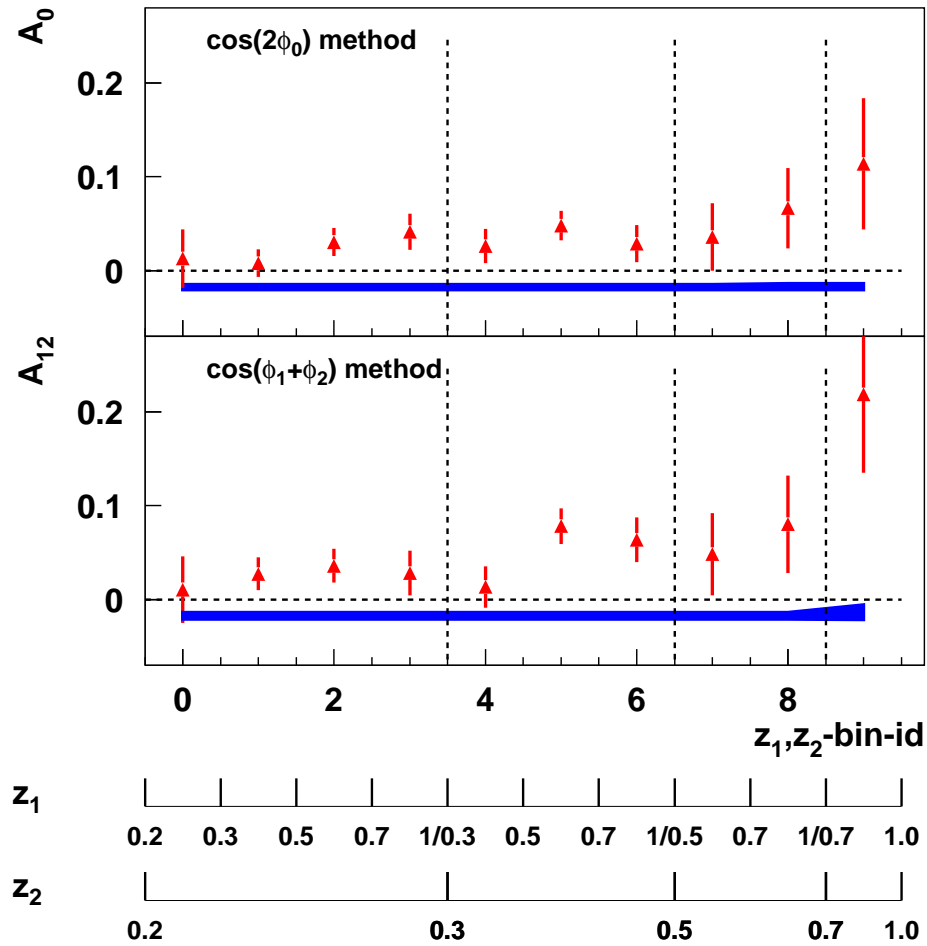


**Figure 5.22:** Collins fragmentation function measured by the BELLE experiment. The two plots correspond to two techniques to extract the asymmetries. In the upper one the product of the Collins fragmentation functions for quarks and antiquarks is measured. In the lower one a convolution of the two functions over transverse momenta is measured but unlike the first, this measurement does not require knowledge of the thrust axis of the measured jets. The lower scales show the boundaries of the bins in  $z_1$  and  $z_2$ . The shaded band shows the size of the systematic errors. Figure taken from [112].

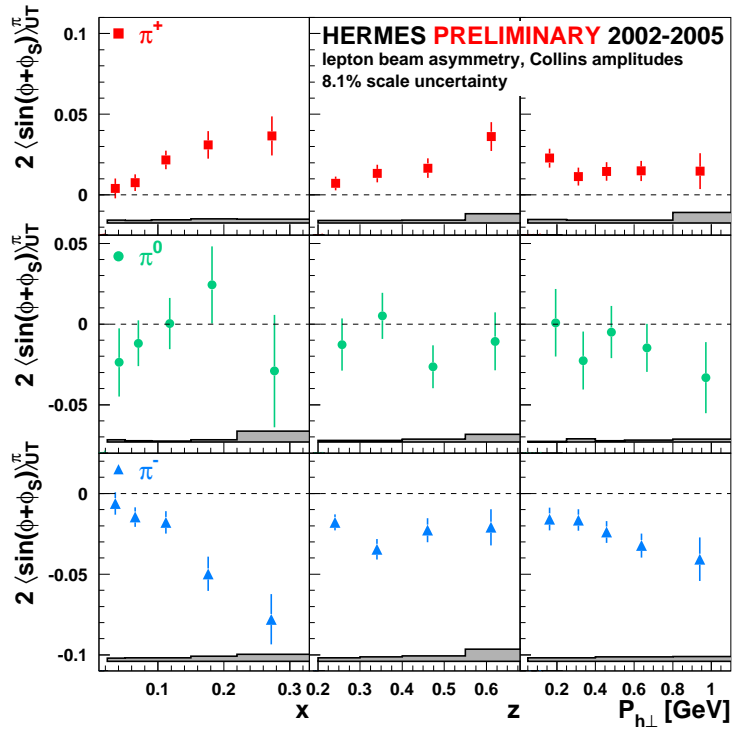


**Figure 5.23:** Collins asymmetries for identified pions measured by the HERMES experiment. In addition to the error bars, representing the statistical errors, there is a 8.1% scale uncertainty due to the target polarization uncertainty. The error bands represent the maximal systematic uncertainty. For historical reasons, the definition of the Collins angle by the HERMES collaboration differs by  $\pi$  from the definition used by the COMPASS collaboration. This causes a sign change of the extracted asymmetries. The asymmetries are extracted by computing moments which have to be multiplied by the indicated factor of 2 to compare them to the COMPASS results. Figure taken from [113].

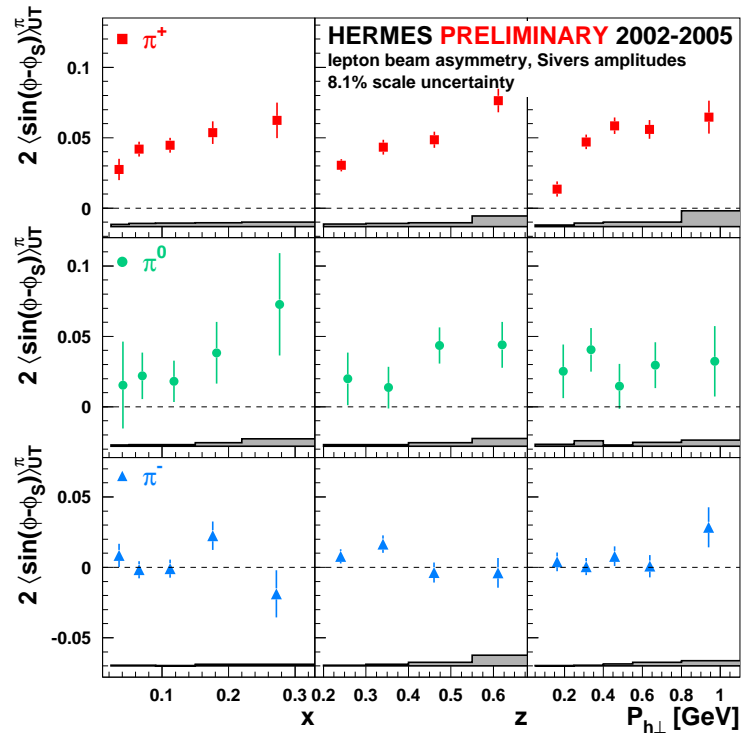


**Figure 5.24:** Sivers asymmetries for identified pions measured by the HERMES experiment. In addition to the error bars, representing the statistical errors, there is a 8.1% scale uncertainty due to the target polarization uncertainty. The error bands represent the maximal systematic uncertainty. The asymmetries are extracted by computing moments which have to be multiplied by the indicated factor of 2 to compare them to the COMPASS results. Figure taken from [113].

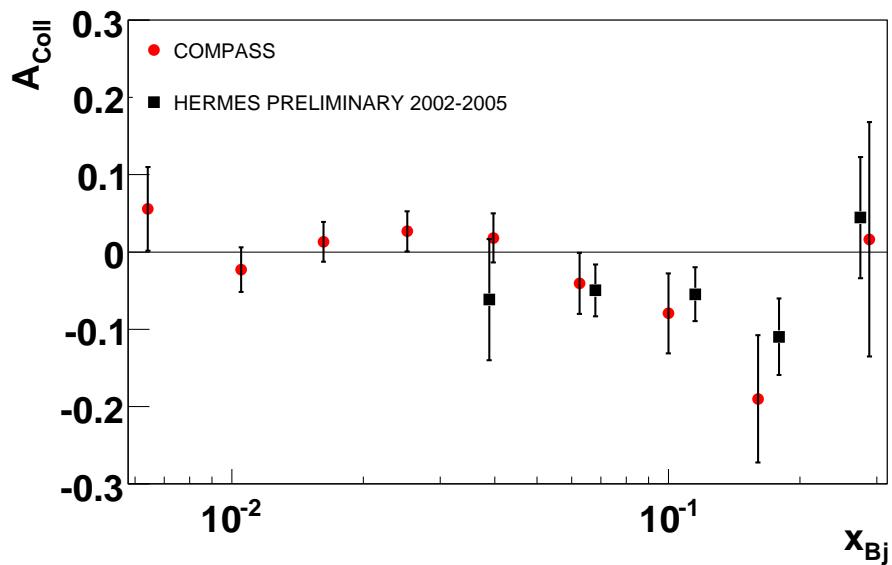
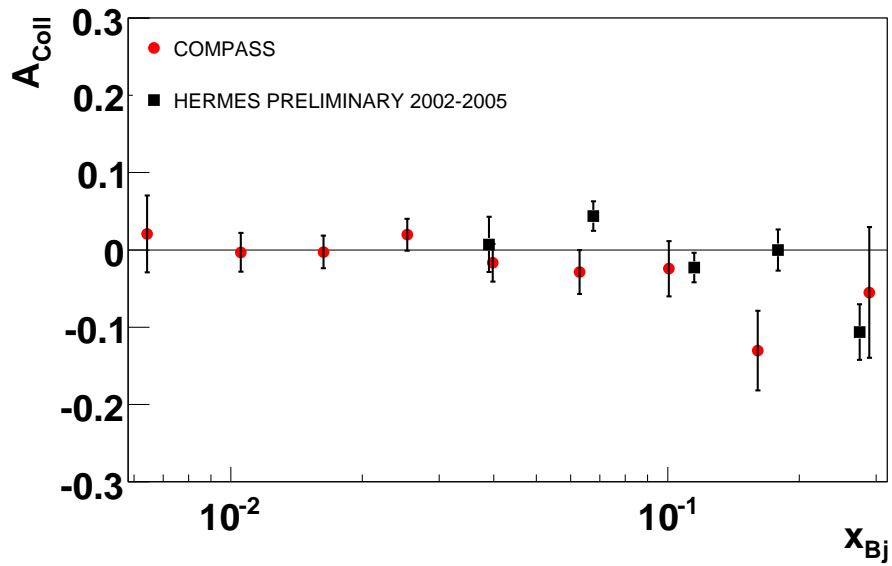


**Figure 5.25:** Collins asymmetries for identified  $K^+$  (top) and  $K^-$  (bottom) measured by HERMES and COMPASS. The sign of the HERMES asymmetries has been reversed to match COMPASS conventions and only statistical errors are shown. They have been shown at DIS07 [113].

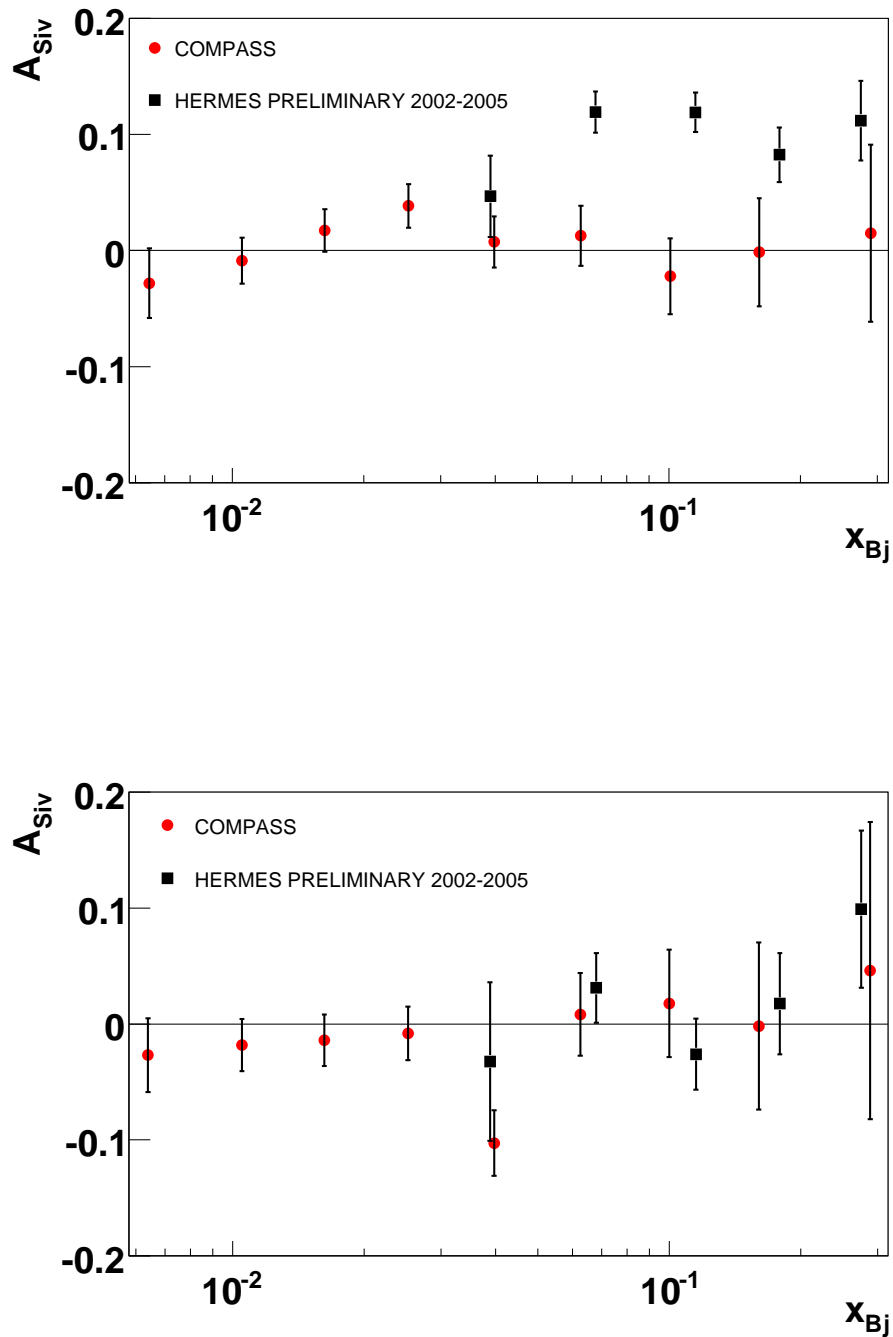


**Figure 5.26:** Sivers asymmetries for identified  $K^+$  (top) and  $K^-$  (bottom) measured by HERMES and COMPASS. Only statistical errors are shown. The HERMES asymmetries have been shown at DIS07 [113].

started [114]. HERMES found first hints for two hadron single spin asymmetries, thus confirming the existence of the fragmentation function. These are shown in fig. 5.27. Compared with the COMPASS results, the collected statistics is again significantly lower. Furthermore, only identified pions could be used, limiting the possibilities for a flavor decomposition. Concluding, experimental evidence suggests, that the most

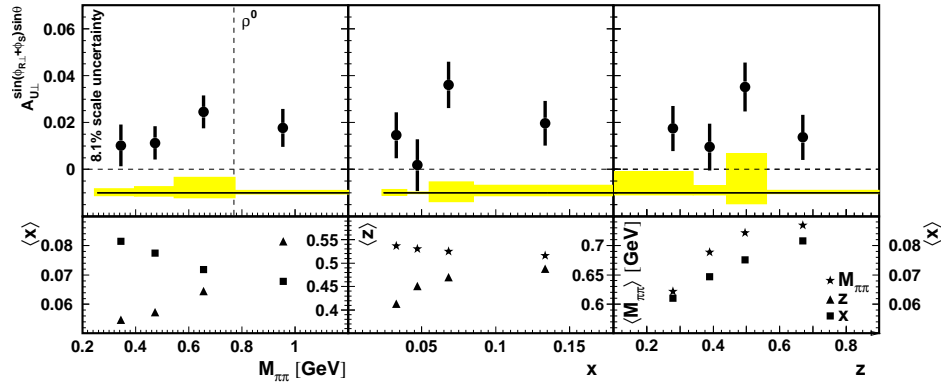


**Figure 5.27:** Measurement of two hadron single spin asymmetries by the HERMES experiment. The top panel shows the two hadron asymmetry. In comparison with the asymmetry extracted in this work, which is defined in eq. 2.56, the  $\sin \theta$  term originating from the partial wave expansion introduced in sec. 2.8.1 is not considered part of the asymmetry and  $\theta$  is fitted separately. The lower panel shows the mean values of the variables that were integrated out. The variable  $z$  is defined as the sum of  $z_1$  and  $z_2$ . Figure taken from [115].

promising way in the interpretation of the COMPASS results will be to consider a cancellation between contributions from neutron and proton within the deuterium. This will be done in the next section.

## 5.5 Interpretation and Conclusion

The results shown in chapter 5 and listed in the appendix all show small asymmetries, they can even be considered compatible with zero. Even though this was not expected, the results can be explained and interpreted by certain simplifying assumptions, by taking into account the data on the quark helicity distributions e.g. from [99], which coincide with the transversity distribution in the non-relativistic case. Then it can be expected, that the contribution of the strange quarks is very small and that the u- and d-quark distribution have opposite signs. Furthermore, the transversity of nucleons will be dominated by the valence quarks. Following this line of thought the Collins asymmetry of pions on a deuteron target can be written as

$$A_{\text{Coll}}^{\pi^+} \approx \frac{4h_{1u}H_1^1 + h_{1d}H_1^2 + 4h_{1d}H_1^1 + h_{1u}H_1^2}{4uD_1 + dD_2 + 4dD_2 + uD_2} = \frac{h_{1u} + h_{1d}}{u + d} \frac{4H_1^1 + H_1^2}{4D_1 + D_2} \quad (5.1)$$

and

$$A_{\text{Coll}}^{\pi^-} \approx \frac{h_{1u} + h_{1d}}{u + d} \frac{H_1^1 + 4H_1^2}{D_1 + 4D_2}. \quad (5.2)$$

In the above equations,  $H_1^1$  and  $H_1^2$  signify the favored and unfavored Collins fragmentation function, respectively. A fragmentation function is favored, if the quark content of the produced meson contains the fragmenting quark. The unpolarized fragmentation functions are called  $D_1$  and  $D_2$ . For the transversity distribution functions of u and d quarks,  $h_{1u}$  and  $h_{1d}$  are used, whereas  $u$  and  $d$  signify the unpolarized distribution functions. The  $K^-$  meson is a pure sea object, therefore no significant asymmetry is expected and the  $K^+$  can be treated similarly to the  $\pi^+$  because it consists also of a valence and a sea quark. Equations 5.1 and 5.2 suggest two possible sources for the small asymmetries measured by COMPASS. Firstly, the isoscalar deuteron target leads to a cancellation between u- and d-quark contributions. But considering the amplitudes of u- and d-quark helicity amplitudes, also the favored and unfavored Collins fragmentation function should partially cancel, which implies opposite signs. This is an interesting result, since in the unpolarized case the favored and unfavored fragmentation functions are not of the same magnitude. These findings are supported by recent fits to COMPASS, HERMES and BELLE data, which are shown in fig. 5.28 [52][116]. Figure 5.29 depicts the Collins fragmentation function which was extracted by [116] and fig. 5.30 the extracted transversity function. In these fits Gaussian factorization of the quark transverse momentum<sup>3</sup> was assumed. The ansatz for the transversity distribution function is based on a polynomial fit and a linear dependence on  $(f_1 + g_1)$ . The values for quark intrinsic transverse momentum and the unpolarized and helicity distribution functions are taken from the literature. Similarly, the model for the Collins fragmentation function is based on the unpolarized fragmentation function.

COMPASS measurements contribute significantly to this result, especially to determine the d-quark contribution to the Collins effect [118].

If two hadrons are detected, models for the two hadron interference fragmentation function  $H_1^{\langle}$  that were presented in sec. 2.8.2, predict, that a signal can be measured, if

<sup>3</sup>A mean square value of quark transverse momentum of 0.25 GeV<sup>2</sup> in the PDF and of 0.2 GeV<sup>2</sup> in the fragmentation was assumed.

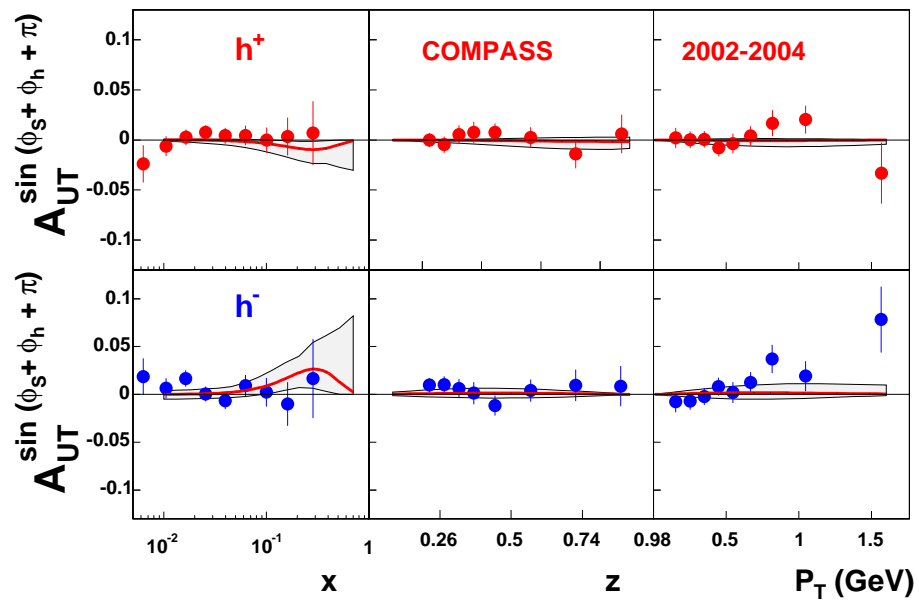


**Figure 5.28:** Global fit of [116] to Collins asymmetries measured by HERMES and COMPASS and Collins fragmentation function measured by BELLE. COMPASS data is shown. The fit was performed to the unidentified hadron sample, which consists mainly of pions. The shaded area represents the theoretical uncertainties.

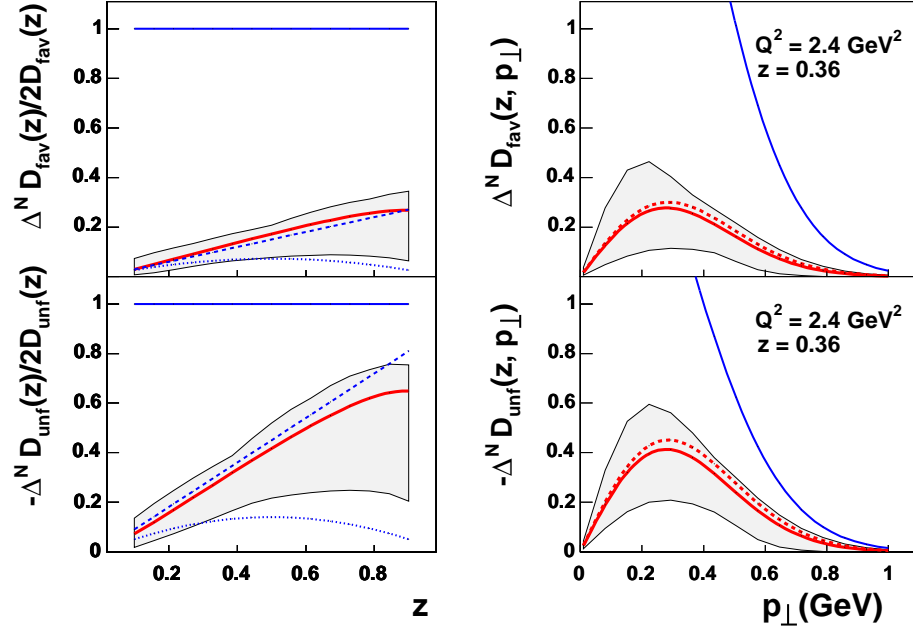


**Figure 5.29:** Collins fragmentation function normalized by two times the unpolarized fragmentation function extracted by [116]. Positivity requires  $|\Delta^N D_{h/q^\uparrow}| \leq |2D_{h/q}|$  therefore with this normalization the positivity bound plotted in blue is unity. The upper plots show the favored, the lower the unfavored function. Notice the sign change. In the plots on the left,  $P_\perp$  was integrated out to obtain the  $z$  dependence. On the right the  $P_\perp$  dependence is shown at a fixed value of  $z$ . The dashed lines are obtained by using the model of [52], the dotted line by using [117]. The shaded area represents the theoretical uncertainties. Instead of  $H_1$  the notation  $\Delta^N D$  is used for the Collins and  $D$  for the unpolarized fragmentation function.

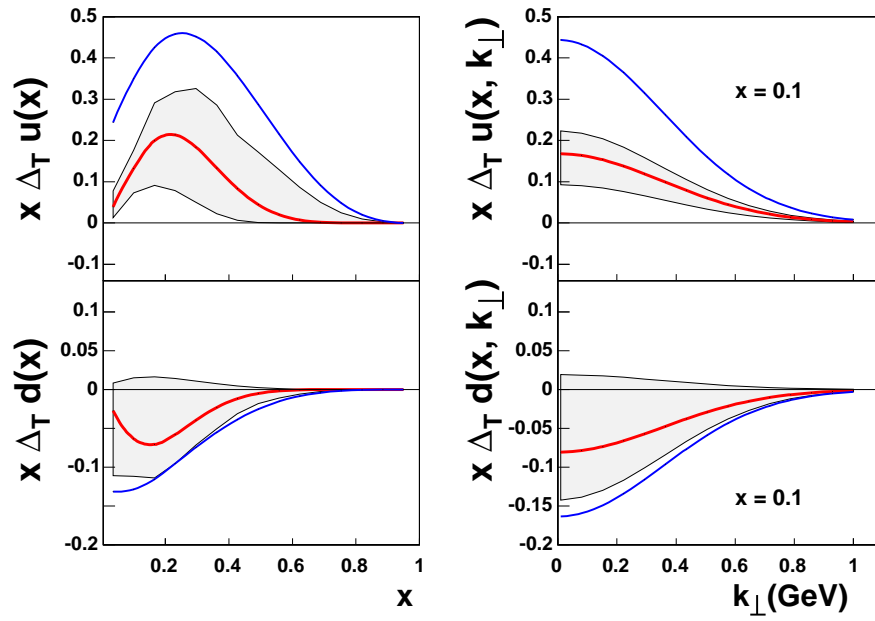


**Figure 5.30:** Transversity distribution function extracted from the fits in [116]. Shaded areas represent theoretical uncertainties, blue lines the Soffer bound. The notation  $\Delta_T u$ ,  $\Delta_T d$  for u- and d-quark transversity distributions was chosen.

the two hadrons come from the decay of a vector meson. In this case the interference between p- and s-wave background can allow a chiral odd fragmentation function. Looking at the quark content of the resonances that are relevant in the kinematic range covered by the COMPASS experiment,  $\rho$ ,  $K^*$  and  $\Phi$ , the similar arguments can be made as for pions and kaons using the simple valence quark model from above. The different resonances are visible in the invariant mass plots shown in fig. 4.10.

For the Sivers asymmetry the same approach can be used. The difference to the Collins case is, that signal and background hadrons fragment via the same function. Therefore the Sivers asymmetry in the simple valence quark model can be written as

$$A_{\text{Siv}}^{\pi^+} = \frac{u_{1T}^\perp + d_{1T}^\perp}{u + d} \quad (5.3)$$

and

$$A_{\text{Siv}}^{\pi^-} = \frac{u_{1T}^\perp + d_{1T}^\perp}{u + d}. \quad (5.4)$$

Thus it is suggested, that the Sivers functions for u and d quarks,  $u_{1T}^\perp$  and  $d_{1T}^\perp$ , are of equal magnitude and have opposite signs. This behavior is affirmed by recent global fits to COMPASS and HERMES data shown in fig. 5.31 from which the Sivers function in fig. 5.32 was extracted [119]. Like the approach for the transversity distribution function, the model for the Sivers function uses Gaussian factorization for the dependence on the quark intrinsic transverse momentum and a linear dependence on the unpolarized distribution function taken from the literature.

The opposite signs of u and d quark contributions could be a consequence of the opposite charges of the quarks: Since the Sivers effect is connected to quark orbital angular momentum, it is reasonable to assume, that the dependence on the polarization of the parent nucleon is due to the orientation of the magnetic momentum of the quark parallel to the spin of the nucleon. However, this is dependent on the charge of the quark. Moreover, the smallness of the effect measured by COMPASS points to a small Sivers effect for gluons [120] and therefore suggest that the contribution from gluon orbital angular momentum to the nucleon spin is small. This finding can be made plausible in a simple picture: Due to the isoscalar nature of the target, the contribution of the valence quarks is canceled, leaving the contribution from the sea. If the gluons carried a sizable fraction of orbital angular momentum, this would be transferred to the sea quarks in the splitting of a gluon into two quarks. The gluon contribution to the nucleon spin puzzle can thus only be by its spin. This contribution is currently being measured by COMPASS and other experiments [121][122].

The contribution of the d-quark to the asymmetries measured by COMPASS with a deuterium target is higher than for experiments using a proton target. In addition, the precision of the measurements is significantly higher than measurements published by other experiments so far. Therefore the importance of the COMPASS data especially to the precise determination of the d-quark contribution to the Sivers effect is obvious.

Both, the global fits to the Collins and Sivers asymmetries fit the data well. Since the identified asymmetries, which were presented in this thesis, were not published at the time the global fits were performed, unidentified asymmetries were taken as

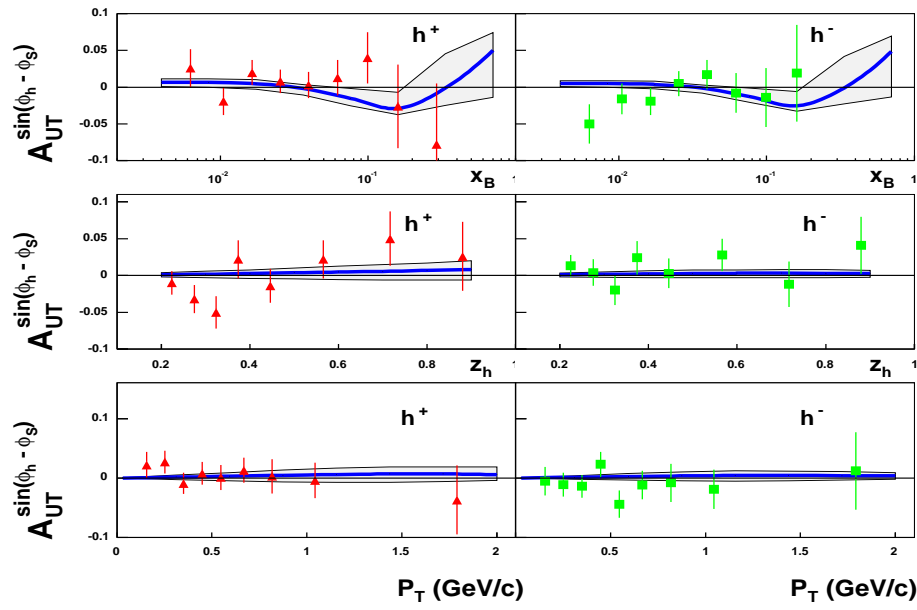


**Figure 5.31:** Global fit of [119] to Sivers asymmetries measured by the HERMES and COMPASS collaborations. The COMPASS data is shown. Theoretical uncertainties are represented by the shaded gray area. The fit is performed to unidentified positive and negative hadrons.

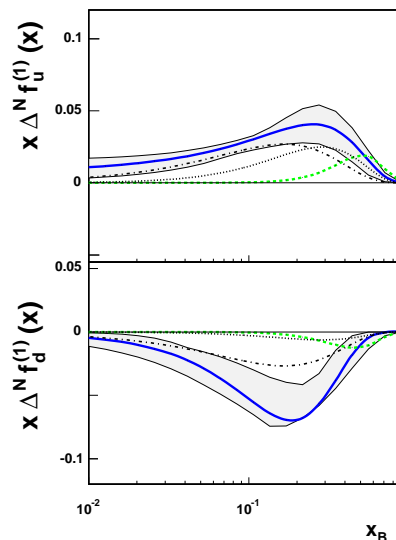


**Figure 5.32:** The first  $k_{\perp}$  moment of the Sivers function extracted from [119]. The u- and d-quark functions have different signs. The dot-dashed, dashed and dotted lines refer to the theoretical models of [123][124][125]. The notation  $\Delta^N f_u^{(1)}$ ,  $\Delta^N f_d^{(1)}$  for the first  $k_{\perp}$  moments of u- and d-quark Sivers function was chosen. It is defined as  $\Delta^N f_q^{(1)} \equiv \int d^2 k_{\perp} \frac{k_{\perp}}{4M_N} q_{1T}^{\perp}(x, k_{\perp})$ .

input. It was assumed, that the unidentified hadron sample consists mainly of pions, which is true to almost 80% as shown in table 4.4 in the identified all single hadron case. Therefore, one can be confident, that the identified asymmetries presented here will further our understanding of the nucleon structure even more. In the year 2007 COMPASS started taking data with a proton target. The collected statistics will lead to statistical errors which are of the same order as the ones for the deuterium target. By the time this thesis is written, the analysis of this data is well under way. From the fits to COMPASS and Sivers asymmetries presented at the beginning of this section, it is possible to make predictions for the amplitudes of the respective asymmetries. These predictions are again taken from [116] and [119] and are shown in figs. 5.33 and 5.34. They show significant asymmetries in the COMPASS data for both, Collins and Sivers asymmetries.

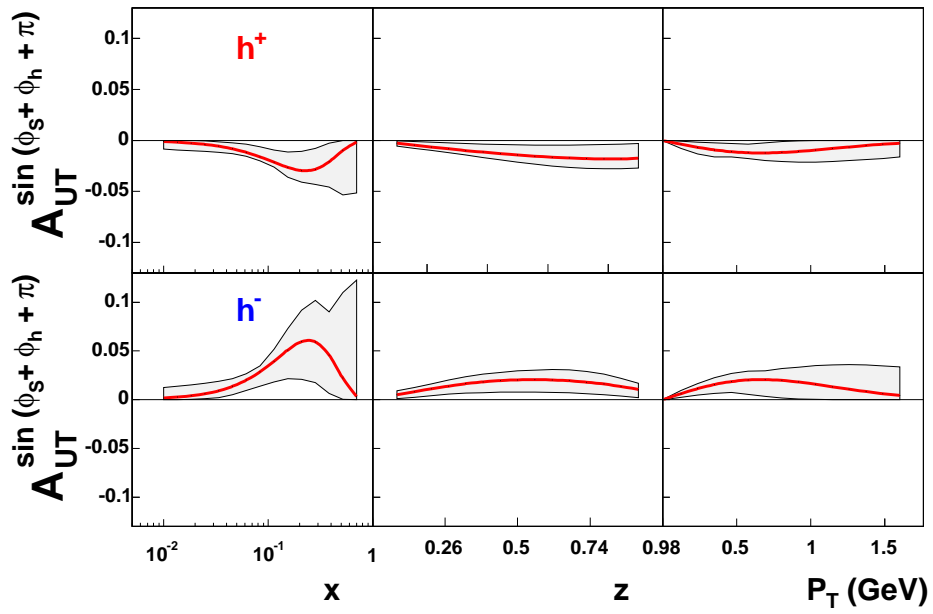


**Figure 5.33:** Predictions of [116] for Collins asymmetries at current COMPASS kinematics with a proton target.

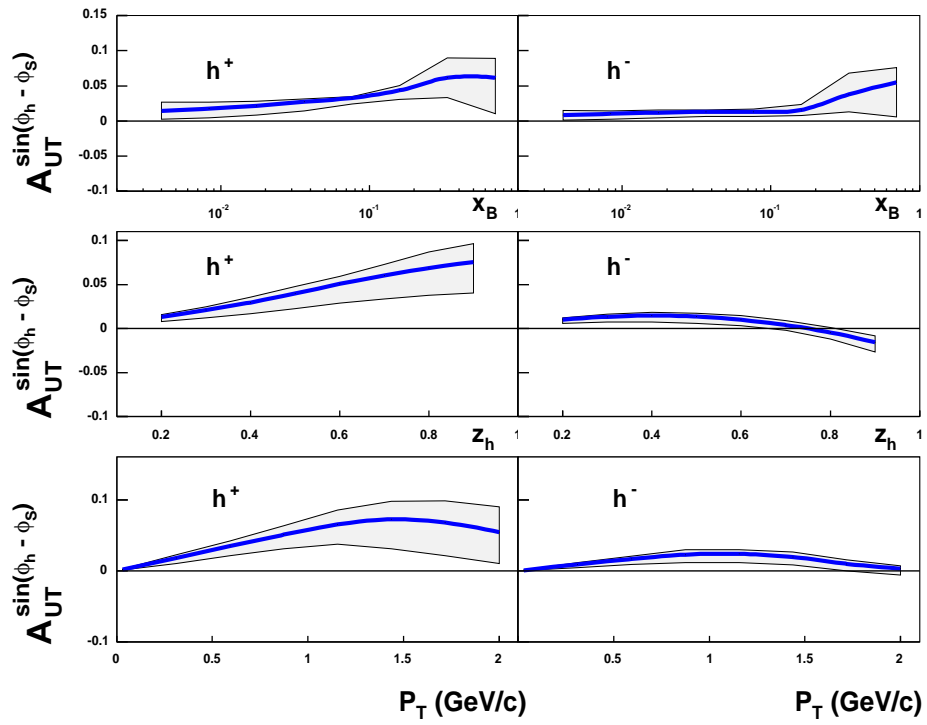


**Figure 5.34:** Predictions of [119] for Sivers asymmetries at current COMPASS kinematics with a proton target.



## 6. Summary

In the years 2003-2004 the COMPASS experiment collected data from DIS events from a high energy muon beam scattering off a deuterium target. From this data Collins and Sivers asymmetries have been extracted in samples containing identified pions and kaons. To access the transversity distribution of the nucleon also identified two hadron correlations were measured. Since, based on the string fragmentation model, an enhanced signal is expected for leading hadrons and hadron pairs, the analyses were additionally performed for particles only with the highest energy in an event. The extracted Collins asymmetries are small, suggesting a cancellation of the u- and d-quark contributions. Measured Sivers asymmetries are also small which can be attributed to the isoscalar deuterium target. The smallness of the Sivers asymmetries also constrain the contribution of gluon orbital angular momentum to the nucleon spin. With the current statistical errors it is not possible to verify predictions of recent models of the fragmentation into two hadrons, in which a signal is expected in the invariant mass region of vector meson production.

Only recently first global fits to results by COMPASS and other experiments have been made to extract Sivers and transversity distribution functions along with the Collins fragmentation function. Here, the precise COMPASS measurements are an indispensable constraint due to its deuterium target and kinematic domain which are complementary to other experiments. For the Collins asymmetry, the data supports the finding, that unfavored and favored Collins fragmentation functions are of equal magnitude and of opposite signs. Thus COMPASS data is very important for the understanding of the nucleon structure.

The topic of this work was the first extraction of the above mentioned single spin asymmetries. To this end several estimators have been developed that ensure a bias-free extraction of the physical signal from data even in the presence of low count rates. In addition to binned methods implementing Gaussian and Poissonian statistics a description of the spectrometer acceptance by Fourier series was devised. This allowed the formulation and construction of an unbinned maximum likelihood estimator. With this novel approach, the groundwork for future analyses has been laid. On specially prepared simulated data, the performance of the new estimators has been demonstrated. Another focus of this analysis was the identification of pions and kaons. Several approaches have been implemented to arrive at the optimal solution. Attribute selection has been done by information gain and in connection with several multivariate methods. A grid search for optimal cuts has been performed on Monte Carlo data and real data. To this end the first full detector simulation with a correct treatment of particle identification and transversely polarized target has been done. The findings were consistent and stable.



# A. Appendix

## A.1 One Hadron Asymmetries

### A.1.1 Binning

The one hadron asymmetries were computed in bins of  $x_{Bj}$ ,  $z$  and  $P_T$ . In the following, the respective bin borders are listed:

$x_{Bj}$	$z$	$P_T$
$0 < x_{Bj} < 0.008$	$0.20 \leq z < 0.25$	$0.10 < P_T[\text{GeV}] \leq 0.20$
$0.008 \leq x_{Bj} < 0.013$	$0.25 \leq z < 0.30$	$0.20 < P_T[\text{GeV}] \leq 0.30$
$0.013 \leq x_{Bj} < 0.020$	$0.30 \leq z < 0.35$	$0.30 < P_T[\text{GeV}] \leq 0.40$
$0.020 \leq x_{Bj} < 0.032$	$0.35 \leq z < 0.40$	$0.40 < P_T[\text{GeV}] \leq 0.50$
$0.032 \leq x_{Bj} < 0.050$	$0.40 \leq z < 0.50$	$0.50 < P_T[\text{GeV}] \leq 0.60$
$0.050 \leq x_{Bj} < 0.080$	$0.50 \leq z < 0.65$	$0.60 < P_T[\text{GeV}] \leq 0.75$
$0.080 \leq x_{Bj} < 0.130$	$0.65 \leq z < 0.80$	$0.75 < P_T[\text{GeV}] \leq 0.90$
$0.130 \leq x_{Bj} < 0.210$	$0.80 \leq z < 1.00$	$0.90 < P_T[\text{GeV}] \leq 1.30$
$0.210 \leq x_{Bj} < 1.000$		$1.30 < P_T[\text{GeV}] \leq \infty$

## A.1.2 Siverts Asymmetries

### A.1.2.1 Leading one Hadron

$\langle x_{Bj} \rangle$	Number of Events	Asymmetry	Error
0.0065	141339	-0.03	0.02
0.0106	372610	-0.023	0.013
0.0165	570183	-0.01	0.011
0.0257	793655	0.001	0.009
0.0397	655286	0.005	0.01
0.0625	424801	0.007	0.012
0.1005	255415	-0.02	0.016
0.1608	123427	-0.03	0.02
0.2796	45763	0	0.04

**Table A.1:**  $\pi^+$  asymmetries in  $x_{Bj}$  binning

$\langle x_{Bj} \rangle$	Number of Events	Asymmetry	Error
0.0065	137617	0.01	0.02
0.0106	346614	-0.012	0.014
0.0164	503167	-0.019	0.011
0.0256	673310	-0.004	0.01
0.0396	536305	0	0.011
0.0625	334453	0.002	0.014
0.1003	190991	-0.025	0.019
0.1605	86647	-0.02	0.03
0.2803	30518	-0.04	0.05

**Table A.2:**  $\pi^-$  asymmetries in  $x_{Bj}$  binning

$\langle P_T \rangle$ [GeV]	Number of Events	Asymmetry	Error
0.155	356313	0.016	0.014
0.252	510867	-0.009	0.011
0.35	569159	-0.007	0.011
0.449	523591	-0.011	0.011
0.548	428756	0.002	0.013
0.669	447153	-0.01	0.012
0.817	258494	0.001	0.016
1.044	236563	-0.036	0.017
1.553	51583	-0.02	0.04

**Table A.3:**  $\pi^+$  asymmetries in  $P_T$  binning

$\langle P_T \rangle$ [GeV]	Number of Events	Asymmetry	Error
0.154	301551	0.018	0.015
0.252	431346	-0.02	0.012
0.35	478663	-0.009	0.012
0.449	437282	-0.012	0.012
0.548	358760	-0.008	0.014
0.669	373099	-0.01	0.013
0.818	215493	0.008	0.018
1.044	198538	-0.024	0.018
1.557	44890	-0.05	0.04

**Table A.4:**  $\pi^-$  asymmetries in  $P_T$  binning

$\langle z \rangle$	Number of Events	Asymmetry	Error
0.274	781359	-0.017	0.009
0.324	638742	-0.013	0.01
0.374	495100	-0.009	0.012
0.445	643518	-0.002	0.01
0.565	481092	0.014	0.012
0.717	223306	0.007	0.017
0.873	119362	-0.02	0.02

**Table A.5:**  $\pi^+$  asymmetries in  $z$  binning

$\langle z \rangle$	Number of Events	Asymmetry	Error
0.274	683037	-0.01	0.01
0.324	545096	-0.006	0.011
0.374	415056	0.008	0.013
0.445	526464	-0.026	0.011
0.564	388788	0.001	0.013
0.717	180659	-0.036	0.019
0.873	100522	0.03	0.02

**Table A.6:**  $\pi^-$  asymmetries in  $z$  binning

$\langle x_{B_j} \rangle$	Number of Events	Asymmetry	Error
0.0065	42799	-0.06	0.04
0.0106	104506	-0.04	0.02
0.0164	139937	0.02	0.02
0.0254	152172	0.03	0.02
0.0398	111051	0.01	0.02
0.0629	79958	0.03	0.03
0.1008	52312	-0.01	0.04
0.1608	25731	-0.01	0.05
0.2885	10744	0.03	0.09

**Table A.7:**  $K^+$  asymmetries in  $x_{B_j}$  binning

$\langle x_{Bj} \rangle$	Number of Events	Asymmetry	Error
0.0065	35480	-0.02	0.04
0.0105	79693	-0.03	0.03
0.0163	95559	-0.04	0.03
0.0253	91757	0.01	0.03
0.0397	60018	-0.1	0.03
0.0625	38752	-0.03	0.04
0.0999	21623	0.06	0.05
0.1598	8714	-0.01	0.08
0.2846	3178	0.24	0.15

**Table A.8:**  $K^-$  asymmetries in  $x_{Bj}$  binning

$\langle P_T \rangle$	Number of Events	Asymmetry	Error
0.154	61835	0.03	0.03
0.252	88259	0.02	0.03
0.351	101347	-0.01	0.02
0.449	100831	-0.01	0.03
0.549	90027	0.04	0.03
0.671	106434	-0.01	0.02
0.819	70731	0.02	0.03
1.052	77593	-0.01	0.03
1.574	22153	-0.01	0.06

**Table A.9:**  $K^+$  asymmetries in  $P_T$  binning

$\langle P_T \rangle$ [GeV]	Number of Events	Asymmetry	Error
0.154	38440	-0.02	0.04
0.252	54457	0.01	0.03
0.35	62675	-0.03	0.03
0.449	61040	0.01	0.03
0.549	54061	0.03	0.04
0.67	62916	-0.04	0.03
0.819	41519	0	0.04
1.053	46023	-0.14	0.04
1.578	13643	-0.15	0.06

**Table A.10:**  $K^-$  asymmetries in  $P_T$  binning

$\langle z \rangle$	Number of Events	Asymmetry	Error
0.275	113359	-0.04	0.02
0.325	113441	0	0.02
0.374	102611	0.06	0.03
0.447	159221	0	0.02
0.566	143600	0.01	0.02
0.714	62128	0	0.03
0.869	24850	0.04	0.05

**Table A.11:**  $K^+$  asymmetries in  $z$  binning

$\langle z \rangle$	Number of Events	Asymmetry	Error
0.275	82876	-0.01	0.03
0.325	78371	-0.03	0.03
0.374	66796	-0.02	0.03
0.446	95401	-0.03	0.03
0.563	77023	-0.01	0.03
0.711	26278	-0.14	0.05
0.865	8029	0.1	0.09

**Table A.12:**  $K^-$  asymmetries in  $z$  binning

## A.1.2.2 All one Hadron

$\langle x_{Bj} \rangle$	Number of Events	Asymmetry	Error
0.0065	271477	-0.012	0.016
0.0106	645537	-0.014	0.01
0.0164	937539	-0.008	0.008
0.0256	1220507	0.003	0.007
0.0397	959170	-0.001	0.008
0.0625	622601	-0.001	0.01
0.1005	374620	-0.018	0.014
0.1608	179942	-0.03	0.02
0.2814	68810	0	0.03

**Table A.13:**  $\pi^+$  asymmetries in  $x_{Bj}$  binning

$\langle x_{Bj} \rangle$	Number of Events	Asymmetry	Error
0.0065	265812	0.003	0.016
0.0106	606322	-0.003	0.01
0.0164	844904	-0.023	0.009
0.0255	1062497	-0.008	0.008
0.0396	809273	-0.006	0.009
0.0625	508454	-0.01	0.011
0.1003	293522	-0.017	0.015
0.1606	132972	0	0.02
0.2818	48831	-0.03	0.04

**Table A.14:**  $\pi^-$  asymmetries in  $x_{Bj}$  binning

$\langle P_T \rangle$ [GeV]	Number of Events	Asymmetry	Error
0.155	606398	0	0.01
0.252	875289	-0.011	0.009
0.35	955097	-0.006	0.008
0.448	838004	-0.003	0.009
0.547	651557	0.001	0.01
0.668	640763	-0.008	0.01
0.817	348993	0.008	0.014
1.042	301295	-0.033	0.015
1.55	62807	-0.01	0.03

**Table A.15:**  $\pi^+$  asymmetries in  $P_T$  binning

$\langle P_T \rangle$ [GeV]	Number of Events	Asymmetry	Error
0.155	523662	0.006	0.011
0.252	757068	-0.01	0.009
0.35	828375	-0.015	0.009
0.448	726528	-0.018	0.01
0.547	565991	-0.002	0.011
0.668	555322	-0.018	0.011
0.817	300511	-0.003	0.015
1.042	259899	-0.01	0.016
1.552	55231	-0.03	0.03

**Table A.16:**  $\pi^-$  asymmetries in  $P_T$  binning

$\langle z \rangle$	Number of Events	Asymmetry	Error
0.224	1436744	-0.011	0.007
0.274	1038609	-0.003	0.008
0.324	754822	-0.013	0.009
0.374	546584	-0.011	0.011
0.445	678115	-0.004	0.01
0.564	482569	0.015	0.012
0.717	223383	0.007	0.017
0.873	119377	-0.02	0.02

**Table A.17:**  $\pi^+$  asymmetries in  $z$  binning

$\langle z \rangle$	Number of Events	Asymmetry	Error
0.224	1303614	-0.014	0.007
0.274	921384	-0.012	0.008
0.324	653027	-0.004	0.01
0.374	463590	0.007	0.012
0.444	559433	-0.024	0.011
0.564	390265	0.002	0.013
0.717	180735	-0.034	0.019
0.873	100539	0.03	0.02

**Table A.18:**  $\pi^-$  asymmetries in  $z$  binning

$\langle x_{Bj} \rangle$	Number of Events	Asymmetry	Error
0.0065	72842	-0.03	0.03
0.0105	158627	-0.009	0.02
0.0163	187628	0.017	0.018
0.0253	187823	0.038	0.019
0.0398	134384	0.01	0.02
0.0628	96867	0.01	0.03
0.1006	62676	-0.02	0.03
0.1609	30826	0	0.05
0.2897	13306	0.01	0.08

**Table A.19:**  $K^+$  asymmetries in  $x_{Bj}$  binning

$\langle x_{Bj} \rangle$	Number of Events	Asymmetry	Error
0.0064	61235	-0.03	0.03
0.0105	125011	-0.02	0.02
0.0162	134722	-0.01	0.02
0.0252	120860	-0.01	0.02
0.0397	78010	-0.1	0.03
0.0625	51302	0.01	0.04
0.0999	28522	0.02	0.05
0.1602	11824	0	0.07
0.2882	4742	0.05	0.13

**Table A.20:**  $K^-$  asymmetries in  $x_{Bj}$  binning

$\langle P_T \rangle$ [GeV]	Number of Events	Asymmetry	Error
0.154	87499	0.01	0.03
0.252	122630	0.01	0.02
0.35	138527	-0.01	0.02
0.449	134383	0.01	0.02
0.549	117352	0.04	0.02
0.67	135534	-0.02	0.02
0.819	87941	0.02	0.03
1.051	94718	0.01	0.03
1.57	26395	0.01	0.05

**Table A.21:**  $K^+$  asymmetries in  $P_T$  binning

$\langle P_T \rangle$ [GeV]	Number of Events	Asymmetry	Error
0.154	58895	-0.03	0.03
0.252	82550	-0.01	0.03
0.35	92673	-0.03	0.03
0.449	87683	0.01	0.03
0.549	76065	0.03	0.03
0.67	86616	-0.03	0.03
0.819	55565	-0.03	0.03
1.051	59348	-0.08	0.03
1.571	16833	-0.14	0.06

**Table A.22:**  $K^-$  asymmetries in  $P_T$  binning

$\langle z \rangle$	Number of Events	Asymmetry	Error
0.225	155104	0.01	0.02
0.275	147432	-0.02	0.02
0.324	131899	0	0.02
0.374	112572	0.06	0.02
0.446	167074	-0.001	0.02
0.566	143898	0.01	0.02
0.714	62146	0	0.03
0.869	24854	0.04	0.05

**Table A.23:**  $K^+$  asymmetries in  $z$  binning

$\langle z \rangle$	Number of Events	Asymmetry	Error
0.225	123840	-0.01	0.02
0.274	110237	-0.02	0.02
0.324	93156	-0.02	0.03
0.374	74795	-0.02	0.03
0.445	102583	-0.03	0.03
0.563	77289	0	0.03
0.711	26295	-0.13	0.05
0.865	8033	0.1	0.09

**Table A.24:**  $K^-$  asymmetries in  $z$  binning

### A.1.3 Collins Asymmetries

#### A.1.3.1 Leading Hadrons

$\langle x_{Bj} \rangle$	Number of Events	Asymmetry	Error
0.0065	141339	-0.08	0.03
0.0106	372610	-0.009	0.016
0.0165	570183	0.015	0.012
0.0257	793655	0.004	0.01
0.0397	655286	0.008	0.011
0.0625	424801	0.012	0.013
0.1005	255415	0.001	0.017
0.1608	123427	0.03	0.03
0.2796	45763	0	0.05

**Table A.25:**  $\pi^+$  asymmetries in  $x_{Bj}$  binning

$\langle x_{Bj} \rangle$	Number of Events	Asymmetry	Error
0.0065	137617	0.04	0.04
0.0106	346614	0.002	0.017
0.0164	503167	0.014	0.013
0.0256	673310	-0.003	0.01
0.0396	536305	-0.004	0.012
0.0625	334453	0.001	0.015
0.1003	190991	0.014	0.02
0.1605	86647	0.01	0.03
0.2803	30518	-0.01	0.06

**Table A.26:**  $\pi^-$  asymmetries in  $x_{Bj}$  binning

$\langle P_T \rangle$ [GeV]	Number of Events	Asymmetry	Error
0.155	356313	0.031	0.015
0.252	510867	-0.005	0.012
0.35	569159	-0.006	0.012
0.449	523591	-0.001	0.012
0.548	428756	-0.004	0.014
0.669	447153	-0.001	0.013
0.817	258494	0.024	0.018
1.044	236563	0.031	0.019
1.553	51583	-0.03	0.04

**Table A.27:**  $\pi^+$  asymmetries in  $P_T$  binning

$\langle P_T \rangle$ [GeV]	Number of Events	Asymmetry	Error
0.154	301551	-0.023	0.016
0.252	431346	-0.001	0.013
0.35	478663	-0.018	0.013
0.449	437282	0.014	0.014
0.548	358760	0.003	0.015
0.669	373099	0.02	0.015
0.818	215493	0.029	0.02
1.044	198538	0.01	0.02
1.557	44890	0.13	0.05

**Table A.28:**  $\pi^-$  asymmetries in  $P_T$  binning

$\langle z \rangle$	Number of Events	Asymmetry	Error
0.274	781359	0.004	0.01
0.324	638742	-0.004	0.011
0.374	495100	0.011	0.013
0.445	643518	0.008	0.011
0.565	481092	0.01	0.012
0.717	223306	-0.005	0.018
0.873	119362	-0.01	0.02

**Table A.29:**  $\pi^+$  asymmetries in  $z$  binning

$\langle z \rangle$	Number of Events	Asymmetry	Error
0.274	683037	0.018	0.011
0.324	545096	0.002	0.012
0.374	415056	-0.007	0.014
0.445	526464	-0.009	0.012
0.564	388788	0.009	0.014
0.717	180659	0.012	0.02
0.873	100522	-0.02	0.03

**Table A.30:**  $\pi^-$  asymmetries in  $z$  binning

$\langle x_{Bj} \rangle$	Number of Events	Asymmetry	Error
0.0065	42799	0.02	0.06
0.0106	104506	-0.02	0.03
0.0164	139937	0.03	0.02
0.0254	152172	0.03	0.02
0.0398	111051	-0.03	0.03
0.0629	79958	-0.03	0.03
0.1008	52312	-0.03	0.04
0.1608	25731	-0.18	0.06
0.2885	10744	-0.09	0.09

**Table A.31:**  $K^+$  asymmetries in  $x_{Bj}$  binning

$\langle x_{Bj} \rangle$	Number of Events	Asymmetry	Error
0.0065	35480	0.05	0.07
0.0105	79693	-0.03	0.04
0.0163	95559	0.01	0.03
0.0253	91757	0.03	0.03
0.0397	60018	0.01	0.04
0.0625	38752	0.01	0.04
0.0999	21623	-0.07	0.06
0.1598	8714	-0.16	0.09
0.2846	3178	0.07	0.17

**Table A.32:**  $K^-$  asymmetries in  $x_{Bj}$  binning

$\langle P_T \rangle$ [GeV]	Number of Events	Asymmetry	Error
0.154	61835	-0.07	0.04
0.252	88259	0.02	0.03
0.351	101347	-0.01	0.03
0.449	100831	-0.03	0.03
0.549	90027	0.02	0.03
0.671	106434	0.01	0.03
0.819	70731	-0.05	0.03
1.052	77593	0.04	0.03
1.574	22153	-0.04	0.07

**Table A.33:**  $K^+$  asymmetries in  $P_T$  binning

$\langle P_T \rangle$ [GeV]	Number of Events	Asymmetry	Error
0.154	38440	0	0.05
0.252	54457	-0.08	0.04
0.35	62675	0.04	0.04
0.449	61040	-0.02	0.04
0.549	54061	0	0.04
0.67	62916	0.02	0.04
0.819	41519	0	0.04
1.053	46023	0.09	0.04
1.578	13643	-0.03	0.08

**Table A.34:**  $K^-$  asymmetries in  $P_T$  binning

$\langle z \rangle$	Number of Events	Asymmetry	Error
0.275	113359	0	0.03
0.325	113441	0.01	0.03
0.374	102611	-0.01	0.03
0.447	159221	-0.02	0.02
0.566	143600	0	0.02
0.714	62128	-0.01	0.03
0.869	24850	-0.05	0.05

**Table A.35:**  $K^+$  asymmetries in  $z$  binning

---

$\langle z \rangle$	Number of Events	Asymmetry	Error
0.275	82876	-0.02	0.04
0.325	78371	0.03	0.03
0.374	66796	0.03	0.04
0.446	95401	-0.05	0.03
0.563	77023	0.02	0.03
0.711	26278	0.07	0.05
0.865	8029	0.08	0.09

---

**Table A.36:**  $K^-$  asymmetries in  $z$  binning

## A.1.3.2 All Hadrons

$\langle x_{Bj} \rangle$	Number of Events	Asymmetry	Error
0.0065	271477	-0.06	0.03
0.0106	645537	-0.004	0.012
0.0164	937539	0.008	0.009
0.0256	1220507	-0.001	0.008
0.0397	959170	0.013	0.009
0.0625	622601	0.008	0.011
0.1005	374620	0.002	0.015
0.1608	179942	0.02	0.02
0.2814	68810	-0.01	0.04

**Table A.37:**  $\pi^+$  asymmetries in  $x_{Bj}$  binning

$\langle x_{Bj} \rangle$	Number of Events	Asymmetry	Error
0.0065	265812	0.03	0.03
0.0106	606322	0.013	0.013
0.0164	844904	0.019	0.01
0.0255	1062497	-0.002	0.008
0.0396	809273	-0.012	0.01
0.0625	508454	0.015	0.012
0.1003	293522	0.002	0.016
0.1606	132972	0.01	0.03
0.2818	48831	0.01	0.05

**Table A.38:**  $\pi^-$  asymmetries in  $x_{Bj}$  binning

$\langle P_T \rangle$ [GeV]	Number of Events	Asymmetry	Error
0.155	606398	0.021	0.011
0.252	875289	0	0.01
0.35	955097	-0.005	0.009
0.448	838004	-0.003	0.01
0.547	651557	-0.004	0.011
0.668	640763	-0.004	0.011
0.817	348993	0.024	0.016
1.042	301295	0.026	0.017
1.55	62807	-0.04	0.04

**Table A.39:**  $\pi^+$  asymmetries in  $P_T$  binning

$\langle P_T \rangle$ [GeV]	Number of Events	Asymmetry	Error
0.155	523662	-0.006	0.012
0.252	757068	-0.001	0.01
0.35	828375	-0.011	0.01
0.448	726528	0.014	0.011
0.547	565991	0.003	0.012
0.668	555322	0.014	0.012
0.817	300511	0.037	0.017
1.042	259899	0.014	0.019
1.552	55231	0.12	0.04

**Table A.40:**  $\pi^-$  asymmetries in  $P_T$  binning

$\langle z \rangle$	Number of Events	Asymmetry	Error
0.224	1436744	0.001	0.008
0.274	1038609	-0.005	0.009
0.324	754822	0.001	0.011
0.374	546584	0.013	0.012
0.445	678115	0.009	0.011
0.564	482569	0.011	0.012
0.717	223383	-0.005	0.018
0.873	119377	-0.01	0.02

**Table A.41:**  $\pi^+$  asymmetries in  $z$  binning

$\langle z \rangle$	Number of Events	Asymmetry	Error
0.224	1303614	0.014	0.008
0.274	921384	0.014	0.01
0.324	653027	0	0.011
0.374	463590	-0.006	0.013
0.444	559433	-0.011	0.012
0.564	390265	0.009	0.014
0.717	180735	0.012	0.02
0.873	100539	-0.02	0.03

**Table A.42:**  $\pi^-$  asymmetries in  $z$  binning

$\langle x_{Bj} \rangle$	Number of Events	Asymmetry	Error
0.0065	72842	0.02	0.05
0.0105	158627	0	0.02
0.0163	187628	0	0.02
0.0253	187823	0.02	0.02
0.0398	134384	-0.02	0.02
0.0628	96867	-0.03	0.03
0.1006	62676	-0.02	0.04
0.1609	30826	-0.13	0.05
0.2897	13306	-0.06	0.08

**Table A.43:**  $K^+$  asymmetries in  $x_{Bj}$  binning

$\langle x_{Bj} \rangle$	Number of Events	Asymmetry	Error
0.0064	61235	0.06	0.05
0.0105	125011	-0.02	0.03
0.0162	134722	0.01	0.03
0.0252	120860	0.03	0.03
0.0397	78010	0.02	0.03
0.0625	51302	-0.04	0.04
0.0999	28522	-0.08	0.05
0.1602	11824	-0.19	0.08
0.2882	4742	0.02	0.15

**Table A.44:**  $K^-$  asymmetries in  $x_{Bj}$  binning

$\langle P_T \rangle$ [GeV]	Number of Events	Asymmetry	Error
0.154	87499	-0.11	0.03
0.252	122630	0.03	0.03
0.35	138527	0	0.03
0.449	134383	-0.02	0.03
0.549	117352	0	0.03
0.67	135534	0.03	0.03
0.819	87941	-0.03	0.03
1.051	94718	0.02	0.03
1.57	26395	-0.04	0.06

**Table A.45:**  $K^+$  asymmetries in  $P_T$  binning

$\langle P_T \rangle$ [GeV]	Number of Events	Asymmetry	Error
0.154	58895	-0.02	0.04
0.252	82550	-0.05	0.03
0.35	92673	0.04	0.03
0.449	87683	-0.02	0.03
0.549	76065	-0.01	0.03
0.67	86616	0.01	0.03
0.819	55565	0	0.04
1.051	59348	0.08	0.04
1.571	16833	-0.08	0.08

**Table A.46:**  $K^-$  asymmetries in  $P_T$  binning

$\langle z \rangle$	Number of Events	Asymmetry	Error
0.225	155104	-0.01	0.03
0.275	147432	-0.01	0.03
0.324	131899	0	0.03
0.374	112572	0	0.03
0.446	167074	-0.01	0.02
0.566	143898	0	0.02
0.714	62146	-0.01	0.03
0.869	24854	-0.05	0.05

**Table A.47:**  $K^+$  asymmetries in  $z$  binning

---

$\langle z \rangle$	Number of Events	Asymmetry	Error
0.225	123840	-0.01	0.03
0.274	110237	-0.03	0.03
0.324	93156	0.03	0.03
0.374	74795	0.03	0.04
0.445	102583	-0.05	0.03
0.563	77289	0.02	0.03
0.711	26295	0.08	0.05
0.865	8033	0.08	0.09

---

**Table A.48:**  $K^-$  asymmetries in  $z$  binning

## A.2 Two Hadron Asymmetries

### A.2.1 All Two Hadron pairs

#### A.2.1.1 Binning

The asymmetries represent the product of a  $z$  and  $M_{\text{Inv}}$ -dependent fragmentation function and an  $x$ -dependent quark distribution function. The asymmetry is calculated separately in bins over the range of  $x_{Bj}$ ,  $z$  and  $M_{\text{inv}}$ . The selected binning for the identified pion-pion analysis in  $x_{Bj}$ ,  $z$  and  $M_{\text{inv}}$  is:

$x_{Bj}$		$z$		$M_{\text{Inv}}$ [Gev]
				$0.00 < M_{\text{Inv}} < 0.40$
				$0.40 \leq M_{\text{Inv}} < 0.50$
				$0.50 \leq M_{\text{Inv}} < 0.60$
				$0.60 \leq M_{\text{Inv}} < 0.70$
				$0.70 \leq M_{\text{Inv}} < 0.80$
				$0.80 \leq M_{\text{Inv}} < 0.90$
				$0.90 \leq M_{\text{Inv}} < 1.00$
				$1.00 \leq M_{\text{Inv}} < 1.10$
				$1.10 \leq M_{\text{Inv}} < 1.20$
				$1.20 \leq M_{\text{Inv}} < 1.30$
				$1.30 \leq M_{\text{Inv}} < 1.40$
				$1.40 \leq M_{\text{Inv}} < 1.50$
				$1.50 \leq M_{\text{Inv}} < 1.60$
				$1.60 \leq M_{\text{Inv}} < 1.80$
				$2.00 \leq M_{\text{Inv}} < \infty$
$0 < x_{Bj} < 0.008$		$0.20 \leq z < 0.30$		
$0.008 \leq x_{Bj} < 0.013$		$0.30 \leq z < 0.35$		
$0.013 \leq x_{Bj} < 0.020$		$0.35 \leq z < 0.40$		
$0.020 \leq x_{Bj} < 0.032$		$0.40 \leq z < 0.50$		
$0.032 \leq x_{Bj} < 0.050$		$0.50 \leq z < 0.65$		
$0.050 \leq x_{Bj} < 0.080$		$0.65 \leq z < 0.80$		
$0.080 \leq x_{Bj} < 0.130$		$0.80 \leq z < 0.90$		
$0.130 \leq x_{Bj} < 0.210$				
$0.210 \leq x_{Bj} < 1.000$				

Because models for  $H_1^\langle$  are sensitive to the shape of the dependence on the invariant mass, the binning in  $M_{\text{Inv}}$  is chosen finer than for the other kinematic dependencies. For example the model by Jaffe and collaborators predicts a change of sign for the asymmetry. For pion-kaon and kaon-pion analysis a different  $z$  and  $M_{\text{inv}}$  binning was chosen due to the higher invariant mass and the higher relative hadron momentum sum  $z$ . chosen:

$\mathbf{z}$		$M_{\text{Inv}}$ [GeV]
		$0.00 \leq M_{\text{Inv}} < 0.70$
		$0.70 \leq M_{\text{Inv}} < 0.80$
		$0.80 \leq M_{\text{Inv}} < 0.90$
$0.00 \leq z < 0.35$		$0.90 \leq M_{\text{Inv}} < 1.00$
$0.35 \leq z < 0.40$		$1.00 \leq M_{\text{Inv}} < 1.10$
$0.40 \leq z < 0.50$		$1.10 \leq M_{\text{Inv}} < 1.20$
$0.50 \leq z < 0.65$		$1.20 \leq M_{\text{Inv}} < 1.30$
$0.65 \leq z < 0.80$		$1.30 \leq M_{\text{Inv}} < 1.40$
$0.80 \leq z < 0.90$		$1.40 \leq M_{\text{Inv}} < 1.50$
		$1.50 \leq M_{\text{Inv}} < 1.60$
		$1.60 \leq M_{\text{Inv}} < 1.80$
		$1.80 \leq M_{\text{Inv}} < 2.00$
		$2.00 \leq M_{\text{Inv}} < \infty$

For the kaon-kaon analysis the corresponding  $z$  and  $M_{\text{inv}}$  binning is:

$\mathbf{z}$		$M_{\text{Inv}}$ [GeV]
		$0.00 \leq M_{\text{Inv}} < 1.10$
		$1.10 \leq M_{\text{Inv}} < 1.20$
$0.20 \leq z < 0.40$		$1.20 \leq M_{\text{Inv}} < 1.30$
$0.40 \leq z < 0.50$		$1.30 \leq M_{\text{Inv}} < 1.40$
$0.50 \leq z < 0.60$		$1.40 \leq M_{\text{Inv}} < 1.50$
$0.60 \leq z < 0.70$		$1.50 \leq M_{\text{Inv}} < 1.60$
$0.70 \leq z < 0.80$		$1.60 \leq M_{\text{Inv}} < 1.80$
$0.80 \leq z < 0.90$		$1.80 \leq M_{\text{Inv}} < 2.20$
		$2.20 \leq M_{\text{Inv}} < \infty$

### A.2.1.2 Asymmetries

$\langle x_{Bj} \rangle$	Number of Events	Asymmetry	Error
0.0065	252029	-0.02	0.03
0.0106	590365	0.011	0.013
0.0164	780868	-0.03	0.01
0.0253	847815	0.004	0.01
0.0396	568096	0.005	0.012
0.0625	364587	0.026	0.015
0.1	207139	0.04	0.02
0.1602	86304	-0.03	0.04
0.2833	32355	-0.08	0.06

**Table A.49:** All  $\pi^+/\pi^-$  pairs asymmetries in  $x_{Bj}$  binning

$\langle z \rangle$	Number of Events	Asymmetry	Error
0.238	100344	0.03	0.03
0.277	431522	-0.014	0.015
0.325	568722	0.017	0.013
0.375	557233	-0.003	0.013
0.447	892495	-0.008	0.01
0.565	761570	-0.003	0.011
0.714	319335	0.008	0.016
0.846	98337	0.01	0.03

**Table A.50:** All  $\pi^+/\pi^-$  pairs asymmetries in  $z$  binning

$\langle M_{\text{Inv}} \rangle$ [GeV]	Number of Events	Asymmetry	Error
0.354	539823	0.005	0.013
0.45	617925	0.004	0.012
0.549	578257	-0.009	0.012
0.649	499303	0.017	0.013
0.749	502309	-0.012	0.014
0.846	332048	-0.016	0.017
0.947	217930	-0.02	0.02
1.046	136909	0.01	0.03
1.147	95578	-0.01	0.03
1.247	70277	0.04	0.04
1.346	45671	0	0.05
1.446	28885	-0.02	0.06
1.547	18928	0.03	0.07
1.687	22936	0.01	0.07
2.112	22779	-0.02	0.07

**Table A.51:** All  $\pi^+/\pi^-$  pairs asymmetries in  $M_{\text{Inv}}$  binning

$\langle x_{Bj} \rangle$	Number of Events	Asymmetry	Error
0.0064	31588	0	0.08
0.0104	54821	-0.05	0.05
0.0161	51291	0.02	0.04
0.0251	41454	-0.04	0.05
0.0397	25848	-0.04	0.06
0.0624	17168	-0.05	0.07
0.0995	9690	0.13	0.09
0.16	3916	0.26	0.16
0.2906	1706	0.1	0.2

**Table A.52:** All  $\pi^+/K^-$  pairs asymmetries in  $x_{Bj}$  binning

$\langle z \rangle$	Number of Events	Asymmetry	Error
0.306	44487	0.06	0.06
0.375	32135	0.06	0.06
0.449	62442	-0.02	0.04
0.567	62475	-0.02	0.04
0.714	28112	-0.13	0.05
0.844	7831	-0.08	0.1

**Table A.53:** All  $\pi^+/K^-$  pairs asymmetries in  $z$  binning

$\langle M_{\text{Inv}} \rangle$ [GeV]	Number of Events	Asymmetry	Error
0.752	42202	-0.06	0.05
0.854	52676	-0.01	0.05
0.944	42154	0.02	0.05
1.047	25974	0.08	0.06
1.147	18019	0.12	0.07
1.247	12972	-0.03	0.09
1.349	9563	-0.3	0.1
1.447	7224	-0.13	0.11
1.547	4545	0	0.15
1.688	5243	-0.19	0.13
2.113	5887	-0.15	0.15

**Table A.54:** All  $\pi^+/K^-$  pairs asymmetries in  $M_{\text{Inv}}$  binning

$\langle x_{Bj} \rangle$	Number of Events	Asymmetry	Error
0.0064	36222	0.03	0.07
0.0104	64212	0.01	0.04
0.0162	63935	-0.06	0.04
0.0252	53631	-0.01	0.04
0.0398	35223	0.04	0.05
0.0628	25042	0.04	0.06
0.1003	15353	-0.02	0.07
0.161	6986	-0.11	0.12
0.2884	3032	-0.51	0.19

**Table A.55:** All  $K^+/\pi^-$  pairs asymmetries in  $x_{Bj}$  binning

$\langle z \rangle$	Number of Events	Asymmetry	Error
0.307	49313	-0.05	0.05
0.376	38254	0.03	0.06
0.449	78214	0.04	0.04
0.568	84946	-0.04	0.03
0.714	41062	0	0.04
0.844	11847	-0.1	0.07

**Table A.56:** All  $K^+/\pi^-$  pairs asymmetries in  $z$  binning

$\langle M_{\text{Inv}} \rangle$ [GeV]	Number of Events	Asymmetry	Error
0.752	51385	-0.01	0.04
0.855	66565	0.02	0.04
0.944	53926	-0.09	0.04
1.047	33367	0.03	0.06
1.147	23304	-0.03	0.07
1.247	16960	0.17	0.08
1.348	12777	-0.08	0.09
1.446	9705	0.04	0.1
1.546	6012	-0.03	0.12
1.688	7095	0.1	0.13
2.117	7897	0.08	0.11

**Table A.57:** All  $K^+/\pi^-$  pairs asymmetries in  $M_{\text{Inv}}$  binning

$\langle x_{Bj} \rangle$	Number of Events	Asymmetry	Error
0.0089	32193	-0.01	0.07
0.0161	17479	0.06	0.08
0.0252	13471	0.03	0.09
0.0399	9058	-0.03	0.1
0.0627	6769	0.02	0.12
0.1005	4113	0.06	0.14
0.2074	3154	0.39	0.18

**Table A.58:** All  $K^+/K^-$  pairs asymmetries in  $x_{Bj}$  binning

$\langle z \rangle$	Number of Events	Asymmetry	Error
0.343	16288	0.05	0.1
0.45	18814	-0.02	0.08
0.549	18598	0.28	0.08
0.648	15026	-0.15	0.08
0.747	10411	-0.07	0.09
0.847	7100	0.08	0.11

**Table A.59:** All  $K^+/K^-$  pairs asymmetries in  $z$  binning

$\langle M_{\text{Inv}} \rangle$ [GeV]	Number of Events	Asymmetry	Error
1.041	25859	-0.02	0.07
1.148	15535	-0.02	0.08
1.249	12224	0.22	0.1
1.347	8947	0.06	0.1
1.448	6357	0.1	0.13
1.547	4929	0.01	0.15
1.685	5941	0.1	0.13
1.961	4444	-0.01	0.16
2.559	2001	-0.3	0.2

**Table A.60:** All  $K^+/K^-$  pairs asymmetries in  $M_{\text{Inv}}$  binning

## A.2.2 Leading Two Hadron Asymmetries

### A.2.2.1 Binning

If only pairs of leading and subleading hadron in an event are considered, the statistics is considerably lower. Therefore the binning for this analysis is chosen in the following way for the  $\pi^- \pi$  combinations:

$\mathbf{x_{Bj}}$		$\mathbf{z}$	$\mathbf{M_{Inv}}$
$0 < x_{Bj} < 0.008$			$0.00 \leq M_{Inv} < 0.40$
$0.008 \leq x_{Bj} < 0.013$			$0.40 \leq M_{Inv} < 0.50$
$0.013 \leq x_{Bj} < 0.020$			$0.50 \leq M_{Inv} < 0.60$
$0.020 \leq x_{Bj} < 0.032$			$0.60 \leq M_{Inv} < 0.70$
$0.032 \leq x_{Bj} < 0.050$			$0.70 \leq M_{Inv} < 0.80$
$0.050 \leq x_{Bj} < 0.080$			$0.80 \leq M_{Inv} < 0.90$
$0.080 \leq x_{Bj} < 0.130$			$0.90 \leq M_{Inv} < 1.00$
$0.130 \leq x_{Bj} < 0.210$			$1.00 \leq M_{Inv} < 1.10$
$0.210 \leq x_{Bj} < 1.000$			$1.10 \leq M_{Inv} < 1.20$
		$0.25 \leq z < 0.35$	$1.20 \leq M_{Inv} < 1.30$
		$0.35 \leq z < 0.40$	$1.30 \leq M_{Inv} < 1.40$
		$0.40 \leq z < 0.50$	$1.40 \leq M_{Inv} < 1.50$
		$0.50 \leq z < 0.65$	$1.50 \leq M_{Inv} < 1.60$
		$0.65 \leq z < 0.80$	$1.60 \leq M_{Inv} < 2.00$
		$0.80 \leq z < 0.90$	$2.00 \leq M_{Inv} < \infty$

For  $\pi$ -kaon and kaon- $\pi$  analysis the binning is:

$\mathbf{x_{Bj}}$		$\mathbf{z}$	$\mathbf{M_{Inv}}$
$0 < x_{Bj} < 0.008$			$0.70 \leq M_{Inv} < 0.80$
$0.008 \leq x_{Bj} < 0.013$			$0.80 \leq M_{Inv} < 0.90$
$0.013 \leq x_{Bj} < 0.020$			$0.90 \leq M_{Inv} < 1.00$
$0.020 \leq x_{Bj} < 0.032$			$1.00 \leq M_{Inv} < 1.10$
$0.032 \leq x_{Bj} < 0.050$			$1.10 \leq M_{Inv} < 1.20$
$0.050 \leq x_{Bj} < 0.080$			$1.20 \leq M_{Inv} < 1.30$
$0.080 \leq x_{Bj} < 0.130$			$1.30 \leq M_{Inv} < 1.40$
$0.130 \leq x_{Bj} < 0.210$			$1.40 \leq M_{Inv} < 1.50$
$0.210 \leq x_{Bj} < 1.000$			$1.50 \leq M_{Inv} < 1.60$
		$0.25 \leq z < 0.35$	$1.60 \leq M_{Inv} < 1.80$
		$0.35 \leq z < 0.40$	$1.80 \leq M_{Inv} < \infty$
		$0.40 \leq z < 0.50$	
		$0.50 \leq z < 0.65$	
		$0.65 \leq z < 0.80$	
		$0.80 \leq z < 0.90$	

For the kaon-kaon analysis, the statistics is sufficient only to compute a single asymmetry for each combination, shown in table A.97 for each charge combination.

### A.2.2.2 Asymmetries

$\langle x_{Bj} \rangle$	Number of Events	Asymmetry	Error
0.0065	67058	-0.05	0.05
0.0106	161130	-0.01	0.02
0.0164	221863	-0.029	0.019
0.0254	256401	-0.008	0.018
0.0396	178128	0.01	0.02
0.0625	113778	0.04	0.03
0.1001	65524	0.09	0.04
0.16	27500	-0.06	0.06
0.2812	9712	0.08	0.1

**Table A.61:** Leading  $\pi^+/\pi^-$  pairs asymmetries in  $x_{Bj}$  binning

$\langle z \rangle$	Number of Events	Asymmetry	Error
0.278	74164	-0.03	0.04
0.326	120038	-0.01	0.03
0.375	140633	-0.02	0.03
0.449	274447	-0.012	0.018
0.568	295908	0.017	0.017
0.715	147572	0.01	0.02
0.846	48332	-0.01	0.04

**Table A.62:** Leading  $\pi^+/\pi^-$  pairs asymmetries in  $z$  binning

$\langle M_{\text{Inv}} \rangle$ [GeV]	Number of Events	Asymmetry	Error
0.354	144438	0.02	0.02
0.451	169954	-0.01	0.02
0.549	162439	0	0.02
0.65	142696	0	0.02
0.75	149476	-0.01	0.02
0.846	103285	0	0.03
0.947	70318	-0.02	0.04
1.047	46188	0.02	0.05
1.148	33017	0.01	0.05
1.247	25329	0.07	0.06
1.346	17061	0.07	0.08
1.446	10931	-0.16	0.09
1.547	7272	-0.08	0.11
1.755	13692	-0.17	0.09
2.332	4998	0.01	0.15

**Table A.63:** Leading  $\pi^+/\pi^-$  pairs asymmetries in  $M_{\text{Inv}}$  binning

$\langle x_{Bj} \rangle$	Number of Events	Asymmetry	Error
0.0064	7230	-0.29	0.15
0.0103	11016	-0.07	0.1
0.016	8702	0.22	0.1
0.025	6178	-0.08	0.12
0.0733	8908	-0.04	0.09

**Table A.64:** Leading  $\pi^+/K^-$  pairs asymmetries in  $x_{Bj}$  binning

$\langle z \rangle$	Number of Events	Asymmetry	Error
0.312	5549	-0.09	0.17
0.376	4911	0.02	0.16
0.45	10972	-0.02	0.1
0.569	12741	-0.1	0.08
0.74	7861	0.02	0.1

**Table A.65:** Leading  $\pi^+/K^-$  pairs asymmetries in  $z$  binning

$\langle M_{\text{Inv}} \rangle$ [GeV]	Number of Events	Asymmetry	Error
0.776	2638	-0.08	0.16
0.856	9279	0.03	0.11
0.945	8216	0.07	0.11
1.048	5834	-0.09	0.12
1.147	4204	-0.1	0.15
1.247	3125	-0.18	0.16
1.349	2334	-0.1	0.2
1.447	1802	-0.1	0.2
1.547	1228	0	0.3
1.688	1476	0.3	0.2
2.136	1898	-0.1	0.2

**Table A.66:** Leading  $\pi^+/K^-$  pairs asymmetries in  $M_{\text{Inv}}$  binning

$\langle x_{Bj} \rangle$	Number of Events	Asymmetry	Error
0.0065	13680	0.12	0.12
0.0105	28490	-0.04	0.06
0.0163	33048	-0.09	0.05
0.0252	30394	-0.06	0.05
0.075	48278	0	0.04

**Table A.67:** Leading  $K^+/\pi^-$  pairs asymmetries in  $x_{Bj}$  binning

$\langle z \rangle$	Number of Events	Asymmetry	Error
0.312	14554	-0.03	0.09
0.376	14452	-0.02	0.09
0.451	36039	0.01	0.05
0.571	50152	-0.09	0.04
0.746	38693	-0.01	0.04

**Table A.68:** Leading  $K^+/\pi^-$  pairs asymmetries in  $z$  binning

$\langle M_{\text{Inv}} \rangle$ [GeV]	Number of Events	Asymmetry	Error
0.75	29650	-0.09	0.05
0.854	32355	0.02	0.05
0.943	25621	-0.12	0.06
1.047	15916	0.06	0.07
1.147	11170	-0.02	0.09
1.248	8376	0.03	0.1
1.348	6416	-0.05	0.13
1.445	4884	-0.03	0.14
1.547	3011	-0.3	0.14
1.688	3550	-0.09	0.16
2.114	3844	0.12	0.15

**Table A.69:** Leading  $K^+/\pi^-$  pairs asymmetries in  $M_{\text{Inv}}$  binning

$\langle x_{Bj} \rangle$	Number of Events	Asymmetry	Error
0.0065	68434	-0.02	0.05
0.0106	162250	-0.02	0.02
0.0164	217815	0.03	0.019
0.0254	249273	0.02	0.018
0.0396	172063	-0.03	0.02
0.0625	108669	-0.01	0.03
0.1001	61283	0.05	0.04
0.16	25760	0.08	0.06
0.2804	9151	-0.03	0.1

**Table A.70:** Leading  $\pi^-/\pi^+$  pairs asymmetries in  $x_{Bj}$  binning

$\langle z \rangle$	Number of Events	Asymmetry	Error
0.278	73670	0.04	0.04
0.326	118132	-0.01	0.03
0.375	136730	0.03	0.03
0.449	267739	0.009	0.018
0.568	284609	0.008	0.017
0.715	145238	-0.01	0.02
0.847	48580	-0.03	0.04

**Table A.71:** Leading  $\pi^-/\pi^+$  pairs asymmetries in  $z$  binning

$\langle M_{\text{Inv}} \rangle$ [GeV]	Number of Events	Asymmetry	Error
0.354	139429	0.03	0.02
0.451	164963	0.01	0.02
0.549	158365	0.01	0.02
0.65	139526	-0.02	0.02
0.75	148663	0.01	0.02
0.846	101523	0.04	0.03
0.947	68839	0.06	0.04
1.047	44589	-0.04	0.05
1.148	32508	0.01	0.05
1.247	24349	0	0.06
1.346	16149	-0.01	0.08
1.447	10627	-0.15	0.1
1.547	7074	-0.22	0.11
1.756	13234	-0.03	0.08
2.339	4860	-0.1	0.16

**Table A.72:** Leading  $\pi^-/\pi^+$  pairs asymmetries in  $M_{\text{Inv}}$  binning

$\langle x_{Bj} \rangle$	Number of Events	Asymmetry	Error
0.0064	8537	-0.26	0.14
0.0104	13153	-0.05	0.09
0.0161	10378	0.04	0.1
0.0251	7587	-0.1	0.11
0.077	11906	-0.06	0.09

**Table A.73:** Leading  $\pi^-/K^+$  pairs asymmetries in  $x_{Bj}$  binning

---

$\langle z \rangle$	Number of Events	Asymmetry	Error
0.312	6106	0.06	0.15
0.376	5646	-0.11	0.15
0.45	13001	-0.27	0.1
0.57	15971	-0.07	0.08
0.744	10837	0.19	0.09

---

**Table A.74:** Leading  $\pi^-/K^+$  pairs asymmetries in  $z$  binning

$\langle M_{\text{Inv}} \rangle$ [GeV]	Number of Events	Asymmetry	Error
0.776	2905	0.06	0.16
0.857	10894	0.01	0.1
0.944	10185	-0.02	0.11
1.048	6933	0.02	0.14
1.148	5210	0.11	0.14
1.247	3785	-0.46	0.16
1.349	3002	-0.02	0.18
1.447	2397	-0.17	0.18
1.547	1573	0	0.2
1.687	2000	-0.1	0.2
2.148	2677	-0.49	0.19

**Table A.75:** Leading  $\pi^-/K^+$  pairs asymmetries in  $M_{\text{Inv}}$  [GeV] binning

$\langle x_{Bj} \rangle$	Number of Events	Asymmetry	Error
0.0065	11759	0.05	0.12
0.0105	23788	0.09	0.07
0.0162	25544	0.01	0.06
0.0252	22304	0.06	0.06
0.0695	30388	0.08	0.05

**Table A.76:** Leading  $K^-/\pi^+$  pairs asymmetries in  $x_{Bj}$  binning

---

$\langle z \rangle$	Number of Events	Asymmetry	Error
0.311	12654	-0.04	0.11
0.376	11829	0.07	0.09
0.451	28102	0.08	0.06
0.569	35431	-0.01	0.05
0.746	25767	0.15	0.06

---

**Table A.77:** Leading  $K^-/\pi^+$  pairs asymmetries in  $z$  binning

$\langle M_{\text{Inv}} \rangle$ [GeV]	Number of Events	Asymmetry	Error
0.75	23016	0.09	0.06
0.854	23891	0.03	0.06
0.944	18820	0.07	0.07
1.046	11546	-0.05	0.09
1.148	8270	-0.15	0.11
1.248	6042	-0.05	0.12
1.348	4483	0.22	0.13
1.446	3448	0.15	0.14
1.547	2177	0.11	0.18
1.687	2560	0.68	0.14
2.119	2901	0.42	0.2

**Table A.78:** Leading  $K^-/\pi^+$  pairs asymmetries in  $M_{\text{Inv}}$  binning

$\langle x_{B_j} \rangle$	Number of Events	Asymmetry	Error
0.0065	37473	0.03	0.07
0.0106	90643	0.04	0.03
0.0164	124180	-0.01	0.03
0.0254	142274	-0.01	0.02
0.0397	101194	-0.01	0.03
0.0626	67667	0.07	0.03
0.1004	41139	0	0.05
0.1605	18787	-0.1	0.07
0.28	6862	0.06	0.13

**Table A.79:** Leading  $\pi^+/\pi^+$  pairs asymmetries in  $x_{B_j}$  binning

---

$\langle z \rangle$	Number of Events	Asymmetry	Error
0.278	52284	0.02	0.04
0.326	80739	0.03	0.03
0.375	90497	-0.03	0.03
0.448	167206	0	0.02
0.566	160425	0.02	0.02
0.711	65262	0.03	0.03
0.84	13806	0.03	0.07

---

**Table A.80:** Leading  $\pi^+/\pi^+$  pairs asymmetries in  $z$  binning

$\langle M_{\text{Inv}} \rangle$ [GeV]	Number of Events	Asymmetry	Error
0.352	109010	0.02	0.03
0.449	109023	0.02	0.03
0.549	98538	0.05	0.03
0.648	83660	-0.04	0.03
0.748	65090	-0.04	0.04
0.848	48498	-0.03	0.04
0.947	35211	0.01	0.05
1.047	24918	-0.02	0.06
1.147	17057	-0.04	0.07
1.247	11722	0.04	0.09
1.347	8173	0.14	0.1
1.447	5639	0.15	0.11
1.547	3886	-0.02	0.15
1.755	7091	0.12	0.12
2.358	2703	0.08	0.19

**Table A.81:** Leading  $\pi^+/\pi^+$  pairs asymmetries in  $M_{\text{Inv}}$  binning

$\langle x_{Bj} \rangle$	Number of Events	Asymmetry	Error
0.0064	4981	0.12	0.17
0.0104	7719	0.26	0.12
0.016	6324	0.15	0.12
0.0251	4606	-0.02	0.13
0.0802	8374	-0.19	0.1

**Table A.82:** Leading  $\pi^+/K^+$  pairs asymmetries in  $x_{Bj}$  binning

$\langle z \rangle$	Number of Events	Asymmetry	Error
0.313	4132	-0.01	0.18
0.376	3758	0.16	0.18
0.45	8504	0.21	0.12
0.569	9996	0.04	0.09
0.733	5614	0.04	0.13

**Table A.83:** Leading  $\pi^+/K^+$  pairs asymmetries in  $z$  binning

$\langle M_{\text{Inv}} \rangle$ [GeV]	Number of Events	Asymmetry	Error
0.776	2335	-0.4	0.18
0.85	6368	0.09	0.12
0.948	5787	0.28	0.13
1.047	4687	0.18	0.15
1.147	3368	-0.23	0.15
1.247	2511	-0.07	0.18
1.347	1723	-0.2	0.2
1.447	1258	0.3	0.2
1.546	956	-0.1	0.3
1.69	1337	0.1	0.2
2.167	1674	0.2	0.2

**Table A.84:** Leading  $\pi^+/K^+$  pairs asymmetries in  $M_{\text{Inv}}$  binning

$\langle x_{Bj} \rangle$	Number of Events	Asymmetry	Error
0.0064	8155	-0.43	0.14
0.0105	16819	-0.09	0.08
0.0162	18591	0.08	0.07
0.0252	16604	0.11	0.07
0.0781	28131	0.04	0.05

**Table A.85:** Leading  $K^+/\pi^+$  pairs asymmetries in  $x_{Bj}$  binning

$\langle z \rangle$	Number of Events	Asymmetry	Error
0.312	10027	0.13	0.11
0.376	9459	0.04	0.1
0.451	22899	-0.02	0.06
0.569	28820	0.04	0.05
0.735	17095	-0.04	0.07

**Table A.86:** Leading  $K^+/\pi^+$  pairs asymmetries in  $z$  binning

$\langle M_{\text{Inv}} \rangle$ [GeV]	Number of Events	Asymmetry	Error
0.75	20208	-0.08	0.07
0.848	16626	-0.01	0.08
0.948	12840	0.18	0.08
1.048	9655	0.05	0.09
1.147	7013	-0.02	0.11
1.247	4712	-0.04	0.14
1.347	3269	0.14	0.15
1.446	2296	0.05	0.18
1.547	1634	-0.2	0.2
1.69	1924	0.2	0.2
2.142	2206	0.1	0.2

**Table A.87:** Leading  $K^+/\pi^+$  pairs asymmetries in  $M_{\text{Inv}}$  binning

$\langle x_{B_j} \rangle$	Number of Events	Asymmetry	Error
0.0065	35829	0	0.07
0.0105	79514	0	0.04
0.0163	101954	0.05	0.03
0.0253	110028	0.01	0.03
0.0397	74982	0.02	0.03
0.0626	48026	-0.05	0.04
0.1	26851	0.11	0.05
0.1597	11075	-0.19	0.09
0.28	3827	-0.04	0.15

**Table A.88:** Leading  $\pi^-/\pi^-$  pairs asymmetries in  $x_{B_j}$  binning

$\langle z \rangle$	Number of Events	Asymmetry	Error
0.278	45211	-0.07	0.05
0.326	67555	-0.04	0.04
0.375	74201	0.06	0.03
0.448	130925	0.01	0.03
0.565	118141	0.04	0.03
0.711	46358	0	0.04
0.84	9695	0.01	0.08

**Table A.89:** Leading  $\pi^-/\pi^-$  pairs asymmetries in  $z$  binning

$\langle M_{\text{Inv}} \rangle$ [GeV]	Number of Events	Asymmetry	Error
0.351	86254	-0.03	0.03
0.449	85698	0	0.03
0.549	76042	0.01	0.03
0.648	64154	-0.03	0.04
0.748	50313	0.01	0.04
0.847	37932	0.06	0.05
0.948	27469	0.04	0.06
1.047	19343	-0.01	0.07
1.147	13399	0.14	0.08
1.247	9283	0.27	0.1
1.347	6428	0.06	0.13
1.447	4518	0.14	0.13
1.547	3105	0.02	0.16
1.758	5798	-0.01	0.13
2.35	2350	0.3	0.2

**Table A.90:** Leading  $\pi^-/\pi^-$  pairs asymmetries in  $M_{\text{Inv}}$  binning

$\langle x_{Bj} \rangle$	Number of Events	Asymmetry	Error
0.0064	3985	-0.1	0.2
0.0103	5678	0.03	0.15
0.016	4196	0.03	0.14
0.0251	2912	0	0.2
0.069	3867	-0.12	0.15

**Table A.91:** Leading  $\pi^-/K^-$  pairs asymmetries in  $x_{Bj}$  binning

$\langle z \rangle$	Number of Events	Asymmetry	Error
0.311	3381	0.36	0.19
0.375	2823	0.09	0.19
0.45	5772	0.03	0.16
0.567	6073	-0.13	0.12
0.727	2589	-0.09	0.18

**Table A.92:** Leading  $\pi^-/K^-$  pairs asymmetries in  $z$  binning

$\langle M_{\text{Inv}} \rangle$ [GeV]	Number of Events	Asymmetry	Error
0.776	1577	-0.1	0.2
0.85	4170	-0.09	0.16
0.949	3807	0.09	0.16
1.047	3007	0.01	0.17
1.146	2167	-0.36	0.2
1.246	1608	0.1	0.3
1.348	1063	-0.3	0.3
1.444	768	-0.1	0.2
1.547	597	-1.7	0.4
1.691	796	0.2	0.3
2.17	1078	0.1	0.3

**Table A.93:** Leading  $\pi^-/K^-$  pairs asymmetries in  $M_{\text{Inv}}$  binning

$\langle x_{Bj} \rangle$	Number of Events	Asymmetry	Error
0.0064	6604	0.06	0.16
0.0105	11710	-0.03	0.09
0.0162	11445	0.14	0.09
0.0251	9235	-0.07	0.09
0.0682	12050	0	0.08

**Table A.94:** Leading  $K^-/\pi^-$  pairs asymmetries in  $x_{Bj}$  binning

$\langle z \rangle$	Number of Events	Asymmetry	Error
0.311	7416	-0.14	0.13
0.376	6472	0.1	0.13
0.449	14069	0.03	0.08
0.566	15310	0.12	0.08
0.731	7777	-0.06	0.09

**Table A.95:** Leading  $K^-/\pi^-$  pairs asymmetries in  $z$  binning

$\langle M_{\text{Inv}} \rangle$ [GeV]	Number of Events	Asymmetry	Error
0.75	11729	0.12	0.09
0.848	9632	0.04	0.09
0.948	7369	0.11	0.11
1.047	5577	0.08	0.13
1.147	3887	0.04	0.14
1.248	2861	-0.03	0.2
1.348	1898	-0.11	0.17
1.447	1376	0.25	0.19
1.547	907	0.2	0.3
1.69	1262	-0.47	0.19
2.141	1390	0.3	0.2

**Table A.96:** Leading  $K^-/\pi^-$  pairs asymmetries in  $M_{\text{Inv}}$  binning

Charge Combination	$\langle x_{Bj} \rangle$	$\langle z \rangle$	$\langle M_{\text{Inv}} \rangle$ [GeV]	Number of Events	Asymmetry	Error
-/+	0.0314	0.586	1.312	32450	-0.09	0.06
+/-	0.0336	0.588	1.321	35549	0.03	0.06
+/+	0.0312	0.518	1.347	5857	0.25	0.14
-/-	0.022	0.489	1.329	3042	0.43	0.18

**Table A.97:** Asymmetries for leading kaon pairs



# List of Figures

2.1	Deep Inelastic Scattering . . . . .	4
2.2	Coordinate System for the one hadron asymmetries . . . . .	5
2.3	Kinematic regimes in lepton-nucleon scattering . . . . .	7
2.4	Illustration of the Optical Theorem . . . . .	9
2.5	Handbag diagrams . . . . .	10
2.6	Symbolic denotation of the spin averaged SIDIS hadronic tensor . . . . .	20
2.7	Illustration of the Collins mechanism . . . . .	22
2.8	Illustration of the Sivers effect . . . . .	23
2.9	Definition of the angle $\theta$ in the center of mass system of the hadron pair	25
2.10	Phase shifts from p-wave resonances and non-resonant s-wave background	27
2.11	Diagrams considered in the predictions for $H_{1,ut}^{\triangleleft,sp}$ . . . . .	27
2.12	Predictions for $H_1^{\triangleleft}$ for a deuterium target . . . . .	28
2.13	Predictions for $H_1^{\triangleleft}$ for a proton target . . . . .	29
2.14	Distribution of the kinematic factor $\gamma$ . . . . .	31
2.15	Coordinate System for the two hadron asymmetries . . . . .	32
3.1	COMPASS setup . . . . .	38
4.1	$z_h$ Distributions for correctly and incorrectly identified leading hadrons	42
4.2	Correlation between energy measured in HCAL1 and momentum measured in the spectrometer . . . . .	43
4.3	Correlation between energy measured in HCAL2 and momentum measured in the spectrometer . . . . .	44
4.4	$Q^2$ vs. $x_{Bj}$ distribution of the all one hadron sample . . . . .	45
4.5	$P_T$ spectrum of the all one hadron sample . . . . .	45

4.6	$y$ spectrum of the all one hadron sample . . . . .	46
4.7	$z$ spectrum of the all one hadron sample . . . . .	46
4.8	Distribution of sum of $z$ of the hadron pair before $z_1 + z_2$ cut . . . . .	47
4.9	$R_T$ spectrum . . . . .	47
4.10	Invariant mass spectrum of the two hadron analysis for different particle combinations . . . . .	48
4.11	$D^{\cos(\Phi_h+\Phi_S)}$ spectrum of the all one hadron sample . . . . .	49
4.12	$D^{\cos(\Phi_h+\Phi_S)}$ VS. $x_{Bj}$ distribution of the all one hadron sample . . . . .	49
4.13	$\sin^2(\theta)$ spectrum for different particle combinations . . . . .	50
4.14	Feynman diagrams contributing to the Born and radiative corrected cross-sections in lepton-nucleon scattering . . . . .	55
4.15	Comparison of data and Monte Carlo for values important to the PID . . . . .	56
4.16	CORAL reconstruction scheme . . . . .	59
4.17	measured momentum VS Čerenkov angle . . . . .	61
4.18	Signal efficiency vs. background rejection curves using neural networks for PID . . . . .	65
4.19	Exemplary fit to the $\rho$ and $\phi$ signal and background . . . . .	67
4.20	Purities of kaon identification evaluated on data . . . . .	69
4.21	Purities of kaon and pion samples after PID . . . . .	70
4.22	Purities of pions and kaon samples after PID, invariant mass binning . . . . .	71
4.23	Distribution of $\Phi_S$ for all events after cuts in the weeks 33 and 34. . . . .	76
4.24	Distribution of the factor $DR' = DR \frac{k_U^\uparrow k_D^\uparrow}{k_U^\downarrow k_D^\downarrow}$ . . . . .	80
4.25	Normalized difference of errors on the asymmetry between weighted and standard method . . . . .	80
4.26	Variation of the double ratio of the global factor $\frac{1}{xyQ^2}$ . . . . .	81
4.27	Artificial acceptance function generated by $1+0.25\cdot\cos(2\Phi_S)+0.6\sin(\phi_S)$ and $\Phi_S$ distribution of all events after cuts in the weeks 33 and 34. . . . .	90
4.28	Results for 1D double ratio, 2D double ratio and least squares fit on Monte Carlo with artificial asymmetries . . . . .	91
4.29	Acceptances extracted from least squares fit . . . . .	92
4.30	Deviation of the mean of $\Phi_h$ and $\Phi_S$ from the center of each bin . . . . .	93
5.1	Collins asymmetries for leading and all $\pi^+$ and $K^+$ in $x_{Bj}$ binning . . . . .	96

5.2	Collins asymmetries for leading and all $\pi^-$ and $K^-$ in $x_{Bj}$ binning . . .	97
5.3	Sivers asymmetries for leading and all $\pi^+$ and $K^+$ in $x_{Bj}$ binning . . . .	98
5.4	Sivers asymmetries for leading and all $\pi^-$ and $K^-$ in $x_{Bj}$ binning . . . .	99
5.5	Collins asymmetries for leading and all $\pi^+$ and $K^+$ in $z$ binning . . . .	100
5.6	Collins asymmetries for leading and all $\pi^-$ and $K^-$ in $z$ binning . . . .	101
5.7	Sivers asymmetries for leading and all $\pi^+$ and $K^+$ in $z$ binning . . . .	102
5.8	Sivers asymmetries for leading and all $\pi^-$ and $K^-$ in $z$ binning . . . .	103
5.9	Collins asymmetries for leading and all $\pi^+$ and $K^+$ in $p_T$ binning . . . .	104
5.10	Collins asymmetries for leading and all $\pi^-$ and $K^-$ in $p_T$ binning . . . .	105
5.11	Sivers asymmetries for leading and all $\pi^+$ and $K^+$ in $p_T$ binning . . . .	106
5.12	Sivers asymmetries for leading and all $\pi^-$ and $K^-$ in $p_T$ binning . . . .	107
5.13	Two hadron asymmetries in $x_{Bj}$ binning . . . . .	108
5.14	Two hadron asymmetries in $z$ binning . . . . .	109
5.15	Two hadron asymmetries in $M_{\text{Inv}}$ binning . . . . .	110
5.16	Leading two hadron asymmetries in $x_{Bj}$ binning . . . . .	111
5.17	Leading two hadron asymmetries in $x_{Bj}$ binning . . . . .	112
5.18	Leading two hadron asymmetries in $z$ binning . . . . .	113
5.19	Leading two hadron asymmetries in $z$ binning . . . . .	114
5.20	Leading two hadron asymmetries in $M_{\text{Inv}}$ binning . . . . .	115
5.21	Leading two hadron asymmetries in $M_{\text{Inv}}$ binning . . . . .	116
5.22	Collins fragmentation function measured by the BELLE experiment . .	119
5.23	Collins asymmetries for identified pions measured by the HERMES experiment . . . . .	120
5.24	Sivers asymmetries for identified pions measured by the HERMES experiment . . . . .	121
5.25	Comparison of Collins asymmetries by HERMES and COMPASS for identified kaons . . . . .	122
5.26	Comparison of Sivers asymmetries by HERMES and COMPASS for identified kaons . . . . .	123
5.27	Measurement of two hadron single spin asymmetries by the HERMES experiment . . . . .	124
5.28	Global fit to extract transversity . . . . .	126

5.29	Extracted Collins fragmentation function . . . . .	127
5.30	Extracted transversity distribution function . . . . .	128
5.31	Global fit to Sivers asymmetries . . . . .	130
5.32	Extracted Sivers function . . . . .	131
5.33	Prediction for Collins asymmetries for COMPASS with proton target . .	132
5.34	Prediction for Sivers asymmetries for COMPASS with proton target . .	133

# List of Tables

2.1	Definition of kinematic variables relevant for the DIS process . . . . .	4
4.1	Data taking periods . . . . .	40
4.2	Events statistics for the period W35-36 . . . . .	51
4.3	Hadron statistics for the period W35-36 . . . . .	51
4.4	RICH statistics for the period W35-36 . . . . .	52
4.5	Final statistics for pions for the years 2003, 2004 . . . . .	52
4.6	Final statistics for kaons for the years 2003, 2004 . . . . .	52
4.7	Statistics for all identified hadron-pairs in comparison with the statistics for the unidentified case. . . . .	53
4.8	Statistics for leading $\pi/\pi$ and $\pi/K$ pairs . . . . .	53
4.9	Statistics for leading $K/\pi$ and $K/K$ pairs . . . . .	53
4.10	Optimal parameter set for pions and kaons . . . . .	66
4.11	Optimal cuts as computed from data. . . . .	68
4.12	Cuts used for the analysis. . . . .	68
4.13	Results for the different cuts to identify kaons . . . . .	71
A.1	$\pi^+$ asymmetries in $x_{Bj}$ binning . . . . .	138
A.2	$\pi^-$ asymmetries in $x_{Bj}$ binning . . . . .	138
A.3	$\pi^+$ asymmetries in $P_T$ binning . . . . .	139
A.4	$\pi^-$ asymmetries in $P_T$ binning . . . . .	139
A.5	$\pi^+$ asymmetries in $z$ binning . . . . .	139
A.6	$\pi^-$ asymmetries in $z$ binning . . . . .	140
A.7	$K^+$ asymmetries in $x_{Bj}$ binning . . . . .	140

A.8	$K^-$ asymmetries in $x_{Bj}$ binning . . . . .	141
A.9	$K^+$ asymmetries in $P_T$ binning . . . . .	141
A.10	$K^-$ asymmetries in $P_T$ binning . . . . .	141
A.11	$K^+$ asymmetries in $z$ binning . . . . .	142
A.12	$K^-$ asymmetries in $z$ binning . . . . .	142
A.13	$\pi^+$ asymmetries in $x_{Bj}$ binning . . . . .	143
A.14	$\pi^-$ asymmetries in $x_{Bj}$ binning . . . . .	143
A.15	$\pi^+$ asymmetries in $P_T$ binning . . . . .	144
A.16	$\pi^-$ asymmetries in $P_T$ binning . . . . .	144
A.17	$\pi^+$ asymmetries in $z$ binning . . . . .	144
A.18	$\pi^-$ asymmetries in $z$ binning . . . . .	145
A.19	$K^+$ asymmetries in $x_{Bj}$ binning . . . . .	145
A.20	$K^-$ asymmetries in $x_{Bj}$ binning . . . . .	146
A.21	$K^+$ asymmetries in $P_T$ binning . . . . .	146
A.22	$K^-$ asymmetries in $P_T$ binning . . . . .	146
A.23	$K^+$ asymmetries in $z$ binning . . . . .	147
A.24	$K^-$ asymmetries in $z$ binning . . . . .	147
A.25	$\pi^+$ asymmetries in $x_{Bj}$ binning . . . . .	148
A.26	$\pi^-$ asymmetries in $x_{Bj}$ binning . . . . .	148
A.27	$\pi^+$ asymmetries in $P_T$ binning . . . . .	149
A.28	$\pi^-$ asymmetries in $P_T$ binning . . . . .	149
A.29	$\pi^+$ asymmetries in $z$ binning . . . . .	149
A.30	$\pi^-$ asymmetries in $z$ binning . . . . .	150
A.31	$K^+$ asymmetries in $x_{Bj}$ binning . . . . .	150
A.32	$K^-$ asymmetries in $x_{Bj}$ binning . . . . .	150
A.33	$K^+$ asymmetries in $P_T$ binning . . . . .	151
A.34	$K^-$ asymmetries in $P_T$ binning . . . . .	151
A.35	$K^+$ asymmetries in $z$ binning . . . . .	151
A.36	$K^-$ asymmetries in $z$ binning . . . . .	152
A.37	$\pi^+$ asymmetries in $x_{Bj}$ binning . . . . .	153
A.38	$\pi^-$ asymmetries in $x_{Bj}$ binning . . . . .	153

A.39 $\pi^+$ asymmetries in $P_T$ binning . . . . .	154
A.40 $\pi^-$ asymmetries in $P_T$ binning . . . . .	154
A.41 $\pi^+$ asymmetries in $z$ binning . . . . .	154
A.42 $\pi^-$ asymmetries in $z$ binning . . . . .	155
A.43 $K^+$ asymmetries in $x_{Bj}$ binning . . . . .	155
A.44 $K^-$ asymmetries in $x_{Bj}$ binning . . . . .	155
A.45 $K^+$ asymmetries in $P_T$ binning . . . . .	156
A.46 $K^-$ asymmetries in $P_T$ binning . . . . .	156
A.47 $K^+$ asymmetries in $z$ binning . . . . .	156
A.48 $K^-$ asymmetries in $z$ binning . . . . .	157
A.49 All $\pi^+/\pi^-$ pairs asymmetries in $x_{Bj}$ binning . . . . .	160
A.50 All $\pi^+/\pi^-$ pairs asymmetries in $z$ binning . . . . .	160
A.51 All $\pi^+/\pi^-$ pairs asymmetries in $M_{\text{Inv}}$ binning . . . . .	161
A.52 All $\pi^+/K^-$ pairs asymmetries in $x_{Bj}$ binning . . . . .	161
A.53 All $\pi^+/K^-$ pairs asymmetries in $z$ binning . . . . .	162
A.54 All $\pi^+/K^-$ pairs asymmetries in $M_{\text{Inv}}$ binning . . . . .	162
A.55 All $K^+/\pi^-$ pairs asymmetries in $x_{Bj}$ binning . . . . .	162
A.56 All $K^+/\pi^-$ pairs asymmetries in $z$ binning . . . . .	163
A.57 All $K^+/\pi^-$ pairs asymmetries in $M_{\text{Inv}}$ binning . . . . .	163
A.58 All $K^+/K^-$ pairs asymmetries in $x_{Bj}$ binning . . . . .	163
A.59 All $K^+/K^-$ pairs asymmetries in $z$ binning . . . . .	164
A.60 All $K^+/K^-$ pairs asymmetries in $M_{\text{Inv}}$ binning . . . . .	164
A.61 Leading $\pi^+/\pi^-$ pairs asymmetries in $x_{Bj}$ binning . . . . .	166
A.62 Leading $\pi^+/\pi^-$ pairs asymmetries in $z$ binning . . . . .	166
A.63 Leading $\pi^+/\pi^-$ pairs asymmetries in $M_{\text{Inv}}$ binning . . . . .	167
A.64 Leading $\pi^+/K^-$ pairs asymmetries in $x_{Bj}$ binning . . . . .	167
A.65 Leading $\pi^+/K^-$ pairs asymmetries in $z$ binning . . . . .	167
A.66 Leading $\pi^+/K^-$ pairs asymmetries in $M_{\text{Inv}}$ binning . . . . .	168
A.67 Leading $K^+/\pi^-$ pairs asymmetries in $x_{Bj}$ binning . . . . .	168
A.68 Leading $K^+/\pi^-$ pairs asymmetries in $z$ binning . . . . .	168
A.69 Leading $K^+/\pi^-$ pairs asymmetries in $M_{\text{Inv}}$ binning . . . . .	169

A.70	Leading $\pi^-/\pi^+$ pairs asymmetries in $x_{Bj}$ binning . . . . .	169
A.71	Leading $\pi^-/\pi^+$ pairs asymmetries in $z$ binning . . . . .	169
A.72	Leading $\pi^-/\pi^+$ pairs asymmetries in $M_{\text{Inv}}$ binning . . . . .	170
A.73	Leading $\pi^-/K^+$ pairs asymmetries in $x_{Bj}$ binning . . . . .	170
A.74	Leading $\pi^-/K^+$ pairs asymmetries in $z$ binning . . . . .	171
A.75	Leading $\pi^-/K^+$ pairs asymmetries in $M_{\text{Inv}}$ [GeV]binning . . . . .	172
A.76	Leading $K^-/\pi^+$ pairs asymmetries in $x_{Bj}$ binning . . . . .	172
A.77	Leading $K^-/\pi^+$ pairs asymmetries in $z$ binning . . . . .	173
A.78	Leading $K^-/\pi^+$ pairs asymmetries in $M_{\text{Inv}}$ binning . . . . .	174
A.79	Leading $\pi^+/\pi^+$ pairs asymmetries in $x_{Bj}$ binning . . . . .	174
A.80	Leading $\pi^+/\pi^+$ pairs asymmetries in $z$ binning . . . . .	175
A.81	Leading $\pi^+/\pi^+$ pairs asymmetries in $M_{\text{Inv}}$ binning . . . . .	176
A.82	Leading $\pi^+/K^+$ pairs asymmetries in $x_{Bj}$ binning . . . . .	176
A.83	Leading $\pi^+/K^+$ pairs asymmetries in $z$ binning . . . . .	177
A.84	Leading $\pi^+/K^+$ pairs asymmetries in $M_{\text{Inv}}$ binning . . . . .	177
A.85	Leading $K^+/\pi^+$ pairs asymmetries in $x_{Bj}$ binning . . . . .	177
A.86	Leading $K^+/\pi^+$ pairs asymmetries in $z$ binning . . . . .	178
A.87	Leading $K^+/\pi^+$ pairs asymmetries in $M_{\text{Inv}}$ binning . . . . .	178
A.88	Leading $\pi^-/\pi^-$ pairs asymmetries in $x_{Bj}$ binning . . . . .	178
A.89	Leading $\pi^-/\pi^-$ pairs asymmetries in $z$ binning . . . . .	179
A.90	Leading $\pi^-/\pi^-$ pairs asymmetries in $M_{\text{Inv}}$ binning . . . . .	179
A.91	Leading $\pi^-/K^-$ pairs asymmetries in $x_{Bj}$ binning . . . . .	179
A.92	Leading $\pi^-/K^-$ pairs asymmetries in $z$ binning . . . . .	180
A.93	Leading $\pi^-/K^-$ pairs asymmetries in $M_{\text{Inv}}$ binning . . . . .	180
A.94	Leading $K^-/\pi^-$ pairs asymmetries in $x_{Bj}$ binning . . . . .	180
A.95	Leading $K^-/\pi^-$ pairs asymmetries in $z$ binning . . . . .	181
A.96	Leading $K^-/\pi^-$ pairs asymmetries in $M_{\text{Inv}}$ binning . . . . .	181
A.97	Asymmetries for leading kaon pairs . . . . .	181

# References

- [1] Vincenzo Barone, Alessandro Drago, and Philip G. Ratcliffe. Transverse Polarisation of Quarks in Hadrons. *Physics Reports*, **359**:1–169, March 2002.
- [2] Alessandro Bacchetta. *Probing the transverse spin of quarks in deep inelastic scattering*. Ph.d. thesis, Vrije Universiteit Amsterdam, October 2002.
- [3] R.L. Jaffe. Spin, Twist and Hadron Structure in Deep Inelastic Scattering. August 1995. Notes for Lectures Presented at the International School of Nucleon Structure The Spin Structure of the Nucleon, Erice, 2-10 August 1995.
- [4] Fetze Pijlman. *Single spin asymmetries and gauge invariance in hard scattering processes*. Phd thesis, Vrije Universiteit Amsterdam, January 2006.
- [5] W. Greiner, S. Schramm, and E. Stein. *Quantum Chromodynamics*. Springer, 2002. ISBN 354067610.
- [6] F. Halzen and A.D. Martin. *Quarks and Leptons*. Wiley, 1984. ISBN 0471887412.
- [7] L.H. Ryder. *Quantum Field Theory, Second Edition*. Cambridge University Press, 1996. ISBN 0521478146.
- [8] The CTEQ Collaboration. Handbook of perturbative QCD. *Rev. Mod. Phys.*, **67**(1):157–248, 1995.
- [9] Y.L. Dokshitzer. Calculation of Structure Functions of Deep-Inelastic Scattering and  $e^+e^-$  Annihilation by Perturbation Theory in Quantum Chromodynamics. *Sov. Phys. JETP*, **46**:641, 1997.
- [10] V.N. Gribov and L.N. Lipatov. Deep Inelastic ep Scattering in Perturbation Theory. *Sov. J. Nucl. Phys*, **15**:438, 1972.
- [11] G. Altarelli and G. Parisi. Asymptotic Freedom in Parton Language. *Nucl. Phys.*, **B126**:298, 1977.
- [12] Alessandro Bacchetta. private communication, 2007.
- [13] E. Leader. *Spin in Particle Physics*. Cambridge University Press, 2001. ISBN 0521352819.

- 
- [14] P.J. Mulders and R.D. Tangerman. The complete tree-level result up to order  $1/Q$  for polarized deep-inelastic lepton production. *Nucl. Phys.*, **B461**(1):197–237(41), 1996.
- [15] D. Boer and P.J. Mulders. Time-reversal odd distribution functions in lepton production. *Phys. Rev.*, **D57**:5780–5786, 1998.
- [16] J. Soffer. Positivity Constraints for Spin-Dependent Parton Distributions. *Phys. Rev. Lett.*, **74**:1292, 1995.
- [17] A. Hayashigaki, Y. Kanazawa, and Y. Koike. Next-to-leading order  $Q^2$  evolution of the transversity distribution  $h_1(x, Q^2)$ . *Phys. Rev.*, **D56**:7350–7360, 1997.
- [18] S. Aoki et al. Tensor Charge of the Nucleon in Lattice QCD. *Phys. Rev.*, **D56**:433–436, 1997.
- [19] R.C. Brower et al. Calculation of Moments of Nucleon Structure Function. *Nucl. Phys. Proc. Suppl.*, **53**:318–320, 1997.
- [20] M. Göckeler et al. The Drell-Yan process and Deep Inelastic Scattering from the lattice. *Nucl. Phys. Proc. Suppl.*, **53**:315–317, 1997.
- [21] S. Capitani et al. Towards a lattice calculation of  $\Delta q$  and  $\delta q$ . *Nucl. Phys. Proc. Suppl.*, **79**:548–550, 1999.
- [22] D. Dolgov et al. Moments of Structure Functions in Full QCD. *Nucl. Phys. Proc. Suppl.*, **94**:303–306, 2001.
- [23] R. Jakob. *Transverse Momenta in Hard Scattering Processes*. Habilitation, University of Wuppertal, November 2002.
- [24] D. Sivers. Single-spin production asymmetries from the hard scattering of point-like constituents. *Phys.Rev.*, **D41**:83–90, 1990.
- [25] D. Sivers. Hard-scattering scaling laws for single-spin production asymmetries. *Phys.Rev.*, **D43**:261–263, 1991.
- [26] J.C. Collins. Fragmentation of transversely polarized quarks probed in transverse momentum distributions. *Nucl. Phys.*, **B396**:161, 1993.
- [27] M. Anselmino and F. Murgia. Single spin asymmetries in transversely polarized proton(antiproton)-proton inclusive processes. *Phys.Lett.*, **B442**:470, 1998.
- [28] M. Anselmino, M. Boglione, and F. Murgia. Single spin asymmetry for  $p^\uparrow p \rightarrow \pi X$  in perturbative QCD. *Phys.Lett.*, **B362**:164, 1995.
- [29] M Burkardt and D.S. Hwang. Sivers effect and generalized parton distributions in impact parameter space. *Phys. Rev.*, **D69**:074032, 2004.
- [30] M. Anselmino et al. Non-standard time reversal for particle multiplets and the spin-flavor structure of hadrons. *Nucl. Phys. B Proc. Suppl.*, **105**:132–133, February 2002.

- 
- [31] A. Airapetian and others HERMES collab. Evidence for a Single-Spin Azimuthal Asymmetry in Semi-inclusive Pion Electroproduction. *Phys. Rev. Lett.*, **84**:4047, 2000.
- [32] M. Anselmino et al. Non-Standard Time Reversal and Transverse Single-Spin Asymmetries. 2002.
- [33] X. Ji, J.-P. Ma, and F. Yuan. QCD factorization for spin-dependent cross sections in DIS and Drell-Yann processes at low transverse momentum. *Phys. Lett.*, **B597**:299–308, 2004.
- [34] A. Bacchetta and M. Radici. Two-hadron semi-inclusive production including subleading twist. *Phys. Rev.*, **D69**(074026), 2004.
- [35] M. Radici and G. van der Steenhoven. The new transversity council of Trento. *Cern Courier*, **44**(8):51–53, 2004.
- [36] M. Gökeler et al. Transverse spin structure of the nucleon from lattice QCD. *Phys. Rev. Lett.*, **98**:222001, 2007.
- [37] M. Radici, R. Jakob, and A. Bianconi. Accessing transversity with interference fragmentation functions. *Phys. Rev.*, **D65**:074031, 2002.
- [38] A. Bianconi et al. Two-hadron interference fragmentation functions. I: General framework. *Nucl. Phys.*, **B536**:303–317, 1998.
- [39] J.C. Collins, S.F. Heppelmann, and G.A. Ladinsky. Measuring transversity densities in singly polarized hadron-hadron and lepton-hadron collisions. *Nucl. Phys.*, **B420**:565, 1994.
- [40] R.L. Jaffe, X. Jin, and J. Tang. Interference fragmentation functions and nucleon’s transversity. *Phys. Rev. Lett.*, **80**:1166–1169, 1998.
- [41] R.L. Jaffe, X. Jin, and J. Tang. Interference fragmentation functions and valence quark spin distributions in the nucleon. *Phys. Rev.*, **D57**:5920–5922, 1998.
- [42] J.C. Collins and G.A. Ladinsky. On pi-pi Correlations in Polarized Quark Fragmentation Using the Linear Sigma Model. *PSU-TH-114*, page 18, 1994.
- [43] A. Bianconi et al. Two-hadron interference fragmentation functions. II: A model calculation. *Phys. Rev.*, **D62**:034009, 2000.
- [44] R.L. Jaffe, X. Jin, and J. Tang. Interference Fragmentation Functions and the Nucleon’s Transversity. *Phys. Rev. Lett.*, **80**:1166, 1998.
- [45] P. Estabrooks and A.D. Martin.  $\pi$ - $\pi$  phase shift analysis below the K anti-K threshold. *Nucl. Phys.*, **B79**:301, 1974.
- [46] A. Bacchetta and M. Radici. Modeling dihadron fragmentation functions. *Phys. Rev.*, **D74**:114007, 2006.

- [47] J. Soffer, M. Stratmann, and W. Vogelsang. Accessing Transversity in Double-Spin Asymmetries at the BNL-RHIC. *Phys. Rev.*, **D65**, 2002.
- [48] M. Wakamatsu. Chiral-odd distribution functions in the chiral quark soliton model. *Phys. Lett.*, **B509**, 2001.
- [49] V.A. Korotkov, W.D. Nowak, and A. Oganessyan. Transversity Distribution and Polarized Fragmentation Function from Semi-inclusive Pion Electroproduction. *Eur. Phys. J.*, **C18**, 2001.
- [50] P. Schweitzer et al. Transversity distributions in the nucleon in the large- $N_c$  limit. *Phys. Rev.*, **D64**, 2001.
- [51] COMPASS Collaboration. A new measurement of the Collins and Sivers asymmetries on a transversely polarised deuteron target. *Nucl. Phys.*, **B765**:31–70, Januar 2006. arXiv:0610068 [hep-ex].
- [52] A.V. Efremov, K. Goeke, and P. Schweitzer. Collins effect in semiinclusive deeply inelastic scattering and in electron-positron-annihilation. *Phys. Rev.*, **D73**:094025, 2006.
- [53] J.C. Collins et al. Sivers effect in semiinclusive deeply inelastic scattering. *Phys. Rev.*, **D73**:014021, 2006.
- [54] A. Kotzinian et al. *Release note on extraction of target transverse spin dependent asymmetries on identified pions and kaons from COMPASS 2003-2004 runs*. June 2007, COMPASS internal report.
- [55] A. Kotzinian (on behalf of the COMPASS collaboration). *Beyond Collins and Sivers: further measurements of the target transverse spin-dependent azimuthal asymmetries in semi-inclusive DIS from COMPASS*. Talk given at the XV International Workshop on Deep-Inelastic Scattering and Related Subjects.
- [56] A. Bacchetta et al. Semi-inclusive deep inelastic scattering at small transverse momentum. *Journal of High Energy Physics*, **2007**(02), 2007.
- [57] COMPASS Collaboration. The COMPASS Experiment at CERN. *Nucl. Instr. Meth.*, **A577**:455–518, Januar 2007. arXiv:0703049 [hep-ex].
- [58] N. Doble et al. The upgraded muon beam at the SPS. *Nucl. Instr. Meth.*, **A343**:351, 1994.
- [59] SMC Collaboration. The Polarized Double Cell Target of the SMC. *Nucl. Instr. Meth.*, **A437**:23, 1999.
- [60] K. Gustafsson. *Computation of the Dilution Factor for the Year 2002 COMPASS Data*. July 2003, COMPASS-note 2003-3.
- [61] G. Abragam and M. Goldman. Principles of Dynamic Nuclear Polarisation. *Rep. Prog. Phys.*, **41**:395, 1978.

- [62] X. Artru and J.C. Collins. Measuring transverse spin correlations by 4-particle correlation in  $e^+e^- \rightarrow 2$  jets. *Z. Phys*, **C69**:277, 1996.
- [63] S. Koblitz, A. Korzenev, and F. Robinet. *COMPASS STABILITY PAGE* <http://wwwcompass.cern.ch/compass/software/offline/input/stab/index.html>.
- [64] F. Sozzi. *Status of identified hadron asymmetries*, 2006. Presentation at the COMPASS analysis meeting March 2006.
- [65] F. Sozzi. *Some studies on RICH stability for transversity data*, 2006. Presentation at the COMPASS analysis meeting January 2006.
- [66] Paolo Pagano. *Preliminary measurement of Transversity at COMPASS experiment*. Ph.d. thesis, Università degli studi di Trieste, 2001.
- [67] V. Alexakhin et al. *Vertex reconstruction in the COMPASS spectrometer. Part I. Monte Carlo studies*. December 2001, COMPASS-note 2001-17.
- [68] A. Bressan. *Origin and cure of the peak in  $\gamma$* . April 2007, COMPASS-note 2006-13.
- [69] B. Andersson. *The Lund Model*. Cambridge University Press, 1998. Contributor T. Ericson, P.Y. Landshoff, ISBN 0521420946.
- [70] H. L. Lai et al. Global QCD analysis of parton structure of the nucleon: CTEQ5 parton distributions. *The European Physical Journal C - Particles and Fields*, **12**(3), 2000.
- [71] G. Ingelman, A. Edin, and J. Rathsman. *LEPTO 6.5 A Monte - Carlo generator for Deep Inelastic Lepton Nucleon Scattering*.
- [72] G. Ingelman, A. Edin, and J. Rathsman. *lepto web page* <http://www.isv.uu.se/theo/MC/lepto/>.
- [73] T. Sjostrand et al. Pythia 6.3, physics and manual. *Journal of High Energy Physics*, 0605:026, 2006. arXiv:0308153 [hep-ex].
- [74] I.V. Akushevich, H. Böttcher, and D. Ryckbosch. RADGEN 1.0, Monte Carlo Generator for Radiative Events in DIS on Polarized and Unpolarized Targets. *Proc. of the Workshop on Monte Carlo Generators for HERA Physics*, 1998.
- [75] I.V. Akushevich and N.M. Shumeiko. Radiative effects in deep inelastic scattering of polarized leptons by polarized light nuclei. *J.Phys. G: Nucl Part. Phys.*, **20**:513–531, 1994.
- [76] S. Hedicke. *Determination of the Gluon Polarisation in the Nucleon using Hadron Pairs with High Transverse Momentum at COMPASS*. Doktorarbeit, Physikalisches Institut Freiburg, 2005.
- [77] M. Frhr. v. Hodenberg. *First Measurement of the Gluon Polarisation in the Nucleon using D Mesons at COMPASS*. Doktorarbeit, Physikalisches Institut Freiburg, November 2005.

- 
- [78] V. Alexakhin. *COMgeant web page* <http://valexakh.web.cern.ch/valexakh/wwwcomg/index.html>.
- [79] CERN. *GEANT – Detector Description and Simulation Tool*. CERN Program Library Long Writeup W5013.
- [80] CERN IT Division. *Geant web page* <http://wwwasd.web.cern.ch/wwwasd/geant/index.html>, 1993.
- [81] CERN IT Division. *The ZEBRA system*, 1995. CERN Program Library Long Writeups Q100/Q101.
- [82] B. Gobbo. *coral web page* <http://coral.web.cern.ch/coral/>.
- [83] K. Kurek et al. An algorithm for track reconstruction in the large angle spectrometer of the COMPASS experiment. *Nucl. Instr. Meth.*, **A485**:720–738, 2002.
- [84] Ivan Kisel. *Application of the cellular automaton and neural networks methods for the COMPASS off-line event reconstruction program and on-line trigger*. June 1998, COMPASS-note 1998-4.
- [85] Y. Bedfer et al. *COMPASS’s track reconstruction algorithm*. January 2004, COMPASS-note 2004-01.
- [86] R. Frühwirth et al. *Data Analysis Techniques for High-Energy Physics*. Cambridge University Press, 2000. ISBN 0521632196.
- [87] E. Albrecht et al. Status and characterisation of COMPASS RICH-1. *Nucl. Instr. Meth.*, **553**:215–219, 2005.
- [88] P. Schiavon. *Particle identification in COMPASS RICH-1, Progress Report*. September 2001, COMPASS-note 2001-12.
- [89] P. Schiavon. *Hints for PID in RICH-1*. May 2003, COMPASS-note 2003-02.
- [90] W. Käfer. *Azimuthal Asymmetries in Unpolarized Semi-Inclusive DIS*. Diplomarbeit, Physikalisches Institut Freiburg, 2008.
- [91] M. Diehl. Generalized Parton Distributions. *Phys. Rept.*, **388**:41–277, 2003. arXiv:0307382 [hep-ph].
- [92] A. Vossen. Basics of Feature Selection and Statistical Learning for High Energy Physics. *Prepared for CERN Yellow Reports*, 2008. arXiv:0803.2344v1 [physics.data-an], CERN-2008-002.
- [93] C.E. Shannon. A Mathematical Theory of Communication. *Bell Systems Technical Journal*, **27**:379–423, 1948.
- [94] I.A. Witten and E. Frank. *Data Mining: Practical machine learning tools and techniques, 2nd Edition*. Morgan Kaufmann, San Francisco, 2005.
- [95] A. Höcker et al. *TMVA web page* <http://tmva.sourceforge.net>.

- 
- [96] R. Brun et al. *Root Users Guide 5.17*, <http://root.cern.ch/>.
- [97] A. Vossen. Support Vector Machines in High Energy Physics. *Prepared for CERN Yellow Reports*, 2008. arXiv:0803.2345v1 [physics.data-an], CERN-2008-002.
- [98] N. et. al. Barabino. Support Vector Machines vs. Multi-Layer Perceptrons in Particle Identification. *Proc. European Symposium on Artificial Neural Networks '99*, page 257, 1999.
- [99] W.-M. Yao et al. Review of Particle Physics. *Journal of Physics G*, **33**, 2006. <http://pdg.lbl.gov>.
- [100] F. Sozzi. *Update on RICH purity for transversity identified 1h analysis*, 2006. Presentation at the COMPASS analysis meeting November 2006.
- [101] A. Kotzinian. *Remarks on acceptance effects in asymmetry extraction*. February 2007, COMPASS-note 2007-2.
- [102] F. Bradamante and A. Martin. *Comparison between different proposed methods for the extraction of transverse spin asymmetries*. May 2005, COMPASS-note 2005-05.
- [103] G. Mallot. *Principle of a bias-free "2D" transverse asymmetry fit*, 2007. Presentation at the COMPASS analysis meeting September 2007.
- [104] D. Levenberg. A Method for the Solution of Certain Problems in Least Squares. *Quart. Appl. Math.* **2**, pages 164–168, 1944.
- [105] D. Marquardt. An Algorithm for Least-Squares Estimation of Nonlinear Parameters. *SIAM J. Appl. Math.*, **11**:431–441, 1963.
- [106] M. Celis, J.E. Dennis, and R.A. Tapia. *A trust region strategy for nonlinear equality constrained optimization*, 1985. in Numerical Optimization 1994, (P. Boggs, R.H. Byrd and R.B. Schnabel eds.) Philadelphia SIAM 1985 .pp. 71-82.
- [107] R.H. Byrd, R.B. Schnabel, and G.A. Schultz. A trust region algorithm for nonlinearly constrained optimization. *SIAM J. Numer. Anal.*, pages 1152–1170, 1987.
- [108] B.Editor Gough. *GNU Scientific Library Reference Manual -2nd Edition*. Network Theory Ltd., 2006. ISBN 0954161734.
- [109] L. Lyons. *Statistics for Nuclear and Particle Physicists*. Cambridge University Press, 1989. ISBN 0521379342.
- [110] R. Fletcher and C.M. Reeves. Function minimization by conjugate gradients. *The Computer Journal*, **2**:149–154, 1964.
- [111] COMPASS Collaboration. First Measurement of the Transverse Spin Asymmetries of the Deuteron in Semi-Inclusive Deep Inelastic Scattering. *Phys. Rev. Lett.*, **94**:202002, 2005.

- [112] R. Seidl et al. Measurement of Azimuthal Asymmetries in Inclusive Production of Hadron Pairs in  $e^+e^-$  Annihilation at Belle. *Phys. Rev. Lett.*, **96**, 2006.
- [113] M. Diefenthaler et al. Hermes measurements of Collins and Sivers asymmetries from a transversely polarised hydrogen target. *To appear in the proceedings of the XV International Workshop on Deep Inelastic Scattering, Munich, Germany, April 16th - April 20th.*
- [114] R. Seidl. *Spin dependent fragmentation analysis at Belle*, 2007. Presentation at DIS 07.
- [115] A. Airapetian et al. Evidence for a Transverse Single-Spin Asymmetry in Lepto-production of  $\pi^+\pi^-$  Pairs. *submitted to JHEP*, 2008.
- [116] M. Anselmino et al. Transversity and Collins functions from SIDIS and  $e^+e^-$  data. *Phys. Rev.*, **D75**, 2007.
- [117] W. Vogelsang and F. Yuan. Single-transverse-spin asymmetries: From deep inelastic scattering to hadronic collisions. *Phys. Rev.*, **72**, 2005.
- [118] The COMPASS Collaboration. Collins and Sivers Transverse Spin Asymmetries for Pions and Kaons on Deuterons. *submitted to Phys. Rev. Lett.*, 2008. [hep-ex/0802.3023].
- [119] M. Anselmino et al. Extracting the Sivers function from polarized semi-inclusive deep inelastic scattering data and making predictions. *Phys. Rev.*, **D72**, 2005.
- [120] S.J. Brodsky and S. Gardner. Evidence for the Absence of Gluon Orbital Angular Momentum in the Nucleon. *Phys. Lett.*, **B643**:22–28, 2006.
- [121] COMPASS Collaboration. Direct Measurement of the Gluon Polarisation in the Nucleon via Charm Meson Production. *subm. PRL*, 2008.
- [122] COMPASS Collaboration. Gluon polarization in the nucleon from quasi-real photoproduction of high-pT hadron pairs. *Phys. Lett.*, **B633**, 2006.
- [123] A.V. Efremov et al. Sivers effect in semi-inclusive DIS and in the Drell-Yan process. *Phys. Lett.*, **B612**:233, 2005.
- [124] U. D'Alesio and F. Murgia. Parton intrinsic motion in inclusive particle production: unpolarized cross sections, single spin asymmetries, and the Sivers effect. *Phys. Rev.*, **D70**, 2004.
- [125] F. Yuan. Sivers Function in the MIT Bag Model. *Phys. Lett*, **B575**:45–54, 2003.

## B. Acknowledgements

This work would not have been possible without the people supporting me. Therefore I would like to thank

- Prof. Kay Königsmann for giving me the opportunity to perform my PhD thesis in his group and putting faith in an outsider to particle physics. I will never forget the fruitful discussions in various seminars nor his generous support.
- Prof. Horst Fischer for constant support, helpful discussions and sharing his knowledge about the various aspects of the COMPASS experiment and the physics involved with me.
- Wolfgang Käfer for helpful discussions, filling the gaps in my knowledge about theoretical physics and carefully proofreading this thesis.
- The Freiburg group for good company and help in all aspects of the daily life of a physicist. A special thank goes to Heiner Wollny, Jochen Barwind, Frank Nerling and Christian Schill for the effort of reading this thesis and Sonja Hedicke, who helped make me feel at home on the 7th floor.
- Rainer Joosten for patiently introducing me to the world of transversity.
- The COMPASS collaboration, especially the transversity subgroup for the communicative atmosphere and the valuable input I got.
- Ellen Frey for all the things that cannot be said here. Life would've been difficult without her. Let's make it work.
- Cornelia Steinmetz for everything she has done for me.

Finally, I would like to thank Sabine, Rainer and Hartmut and the rest of my family. They were there for me whenever I needed them. Not only during my thesis.

Anselm Vossen, April 2008